UNIVERSITY OF BELGRADE
FACULTY OF TECHNOLOGY AND METALLURGY

Walid Mukhtar Musrati

CHARACTERISATION OF DAMAGE AND FRACTURE OF PIPELINE MATERIAL USING RING-SHAPED SPECIMENS

- Doctoral Dissertation -

Belgrade, 2019

UNIVERZITET U BEOGRADU
TEHNOLOŠKO-METALURŠKI FAKULTET

Walid Mukhtar Musrati

KARAKTERIZACIJA OŠTEĆENJA I LOMA MATERIJALA CEVOVODA KORIŠĆENJEM EPRUVETA OBLIKA PRSTENA

- doktorska disertacija -

Beograd, 2019.

Supervisor:

_____

Dr. Marko Rakin, Full Professor
University of Belgrade, Faculty of Technology and Metallurgy

Commission Members:

_____

Dr. Bojan Međo, Assistant Professor
University of Belgrade, Faculty of Technology and Metallurgy

_____

Dr. Nenad Gubeljak, Full Professor
University of Maribor, Faculty of Mechanical Engineering

_____

Dr. Slaviša Putić, Full Professor
University of Belgrade, Faculty of Technology and Metallurgy

_____

Dr. Ivana Cvijović Alagić, Research Associate
University of Belgrade, Institute for Nuclear Sciences "Vinča"

Ph.D. Candidate: Walid Musrati, M.Sc.

Date of defense: _____

Strane sa podacima o doktorskoj disertaciji (na engleskom jeziku):

Title of doctoral dissertation: Characterisation of Damage and Fracture of Pipeline Material using Ring-Shaped Specimens

Abstract

Having in mind the great importance of integrity assessment and ensuring the safe service of pipelines in different industries, the subject of this thesis is analysis and characterisation of damage and fracture by using recently proposed ring-shaped bending specimens. The main deficiency of standard fracture mechanics specimens in this field is difficult or impossible fabrication of geometries with sufficient thickness for testing in plane strain conditions. Therefore, different research groups introduced some new testing geometries; however, most specimens with axial stress concentrator are too complex to prepare or test. Therefore, ring-shaped specimens are applied in this thesis, with the focus on analysis of damage and fracture development in thin-walled steel pipes. Due to the thin walls, such pipes are characterised by low weight and lack of the plane strain state. The examination of the possibility for pipe testing by using these specimens required a thorough experimental and numerical analysis of both seamless and seam (longitudinally welded) pipes. The stress concentrators were fabricated in axial direction, which is the critical direction for fracture initiation and development in cylindrical structures exposed to internal fluid pressure. Experimental-numerical procedure, based primarily on the micromechanical approach, is developed for prediction of damage development in the pipeline material until final fracture by application of specimens convenient for use in engineering practice. Also, it is optimised for use on pipes with different dimensions and produced from different materials. Finally, the effect of heterogeneity of seam pipes on the fracture behaviour is assessed. It is concluded that PRNB specimens can be successfully applied in assessment of failure resistance of the materials of seam and seamless pipes.

Keywords: *Pipe failure, Steel pipes, Pipe ring notched bending specimen, Ductile fracture, Micromechanical analysis, Finite element method*

Scientific field: Technology Engineering

Scientific subfield: Materials Engineering

UDK number:

Strane sa podacima o doktorskoj disertaciji (na srpskom jeziku):

Naslov doktorske disertacije: Karakterizacija oštećenja i loma materijala cevovoda korišćenjem epruveta oblika prstena

Rezime

Imajući u vidu veliki značaj procene integriteta i obezbeđenja sigurnog rada cevovoda u različitim granama industrije, tema ovog rada je analiza i karakterizacija oštećenja i loma primenom epruveta za savijanje oblika prstena predloženih u prethodnom periodu. Osnovni nedostatak standardnih epruveta mehanike loma u ovoj oblasti je teška ili nemoguća izrada geometrija sa debljinom dovoljnom za ispitivanje u uslovima ravnog stanja deformacije. Stoga, više istraživačkih grupa je predložilo nove geometrije za ispitivanje; međutim, većina epruveta sa koncentratorom napona u uzdužnim pravcu se odlikuje komplikovanim postupkom izrade ili ispitivanja. Stoga, u ovom radu su primenjene epruvete oblika prstena, sa naglaskom na analizu oštećenja i loma u tankozidnim čeličnim cevima. Zbog tankih zidova, odlikuju se malom težinom i nemogućnošću postizanja ravnog stanja napona. Istraživanje mogućnosti ispitivanja cevi primenom ovih epruveta je zahtevalo detaljnu eksperimentalnu i numeričku analizu bešavnih i šavnih (uzdužno zavarenih) cevi. Koncentratori napona su izrađeni u uzdužnom pravcu, koji je kritičan za nastanak loma u cilindričnim strukturama izloženim unutrašnjem pritisku fluida. Razvijen je eksperimentalno-numerički postupak, koji se zasniva pre svega na mikromehaničkom pristupu, za predviđanje razvoja oštećenja u materijalu cevovoda do konačnog loma primenom epruveta pogodnih za korišćenje u inženjerskoj praksi. Takođe, urađena je optimizacija za primenu na cevima različitih dimenzija i izrađenim od različitih materijala. Konačno, procenjen je uticaj heterogenosti šavnih cevi na ponašanje materijala pri lomu. Zaključeno je da se PRNB epruvete mogu uspešno primeniti u oceni otpornosti prema otkazu materijala šavnih i bešavnih cevi.

Ključne reči: Otkaz cevi, Čelične cevi, Epruveta za savijanje oblika prstena, Žilav lom, Mikromehanička analiza, Metoda konačnih elemenata

Naučna oblast: Tehnološko inženjerstvo

Uža naučna oblast: Inženjerstvo materijala

UDK broj:

Acknowledgments

To my family

I gratefully acknowledge my supervisor, Professor Marko Rakin, for offering me an interesting and up-to-date topic for my PhD thesis. During work on experimental and numerical part of the thesis I learned a lot of advanced characterisation of pipeline materials.

Many thanks to Professor Nenad Gubeljak and research associate Primož Štefane for providing me conditions for experimental part of the thesis, which is mainly done in their laboratory.

I immensely acknowledge Dr. Bojan Medjo, assistant professor, who helped me a lot in micromechanical modelling using finite element method (FEM). He had enough patience to guide my models, computation and post-processing of results in FEM software package. Also, together with my supervisor, he helped me a lot in discussion of obtained results.

I am very thankful to Dr. Ivana Cvijović Alagić for help in microstructural analysis and professor Putić for suggestions in presenting the results.

Many thanks to Dr. Zijah Burzić and Professor Željko Kamberović for providing me access to their laboratories with the aim to complete experimental work.

Contents

1. INTRODUCTION

Pipelines are the most commonly used transportation means for both fluids and granular solid materials in almost all industry branches. Their safety, integrity and working life is of crucial importance and is a topic of many studies in the literature. Among the first practical applications of fracture mechanics on pipelines was analysis of a large number of cracks, observed by non destructive evaluation (NDE) methods on the pipeline between Alaska and the rest of the USA. Criteria for acceptance of the size and position of a crack are determined by application of the Crack Tip Opening Displacement - CTOD concept, decreasing the amount of repair welding.

Most pipes, especially thin-walled ones, do not fulfil the requirements imposed on the geometry of standard fracture specimens - primarily compact tensile (CT) and single edge notched bending (SENB) specimens. Therefore, studies are conducted with an aim to define some new geometries which are more convenient for determining the pipeline fracture resistance than the standard ones. A few studies confirmed the better properties of SENT or single edge tensile specimen in comparison with the same geometry exposed to bending load (SENB) if the stress concentrator is positioned circumferentially. An example would be a long vertical pipe loaded by its own weight.

Recently, ring-shaped specimens have been the topic of several published papers; it was shown that it is necessary to understand and analyse a large amount of configurations in order to successfully utilise the advantages of such geometries. However, the main emphasis in the previous work was correlation of the results obtained by experimental and numerical examinations of the new geometry - pipe ring specimens (PRNB) and standard bending specimens (SENB), both exposed to three-point bending. Similar stress and strain distributions are obtained close to the stress concentrator (machined notch or fatigue pre-crack), as well as fracture behaviour assessed through crack resistance curves (CTOD-δ_5). But, it is important to emphasize that the specimens were produced from a plate, i.e. not from the pipeline, which enabled an ideal geometry regarding the size and circularity. Obtained results are, however, important because they

preliminary show the possibility of the application of the new geometry for fracture resistance analysis of the pipelines. It should be noted that some examinations of the ring-specimens cut from the pipes have also been published recently, containing primarily analysis of the residual stresses and their influence on fracture behaviour. The walls were relatively thick (ratio D_o/D_i had values around 1.2), which enabled the plane strain conditions comparable to those occurring in SENB specimens. There was no material heterogeneity due to the welding, since the pipes were seamless.

Some other specimens which contain the cracks in axial pipe direction (in addition to PRNB specimens considered in this Thesis) were also proposed by other authors in the previous period. However, most of these specimens are characterised by a relatively complicated fabrication and/or testing.

In this Thesis, the focus is on analysis of damage and fracture development in thin-walled steel pipes by using PRNB specimens; the ratio of external to internal diameter has value close to one. Such pipes have a significant role in chemical industry and many other industry branches (excluding the applications on very high pressures and temperatures). Due to the thin walls, they are characterised by low weight and lack of the plane strain state. The examination of the possibility for pipe testing by using these specimens required a thorough experimental and numerical analysis of both seamless and seam (longitudinally welded) pipes. The stress concentrators were fabricated in axial direction, which is the critical direction for fracture initiation and development in cylindrical structures exposed to internal fluid pressure.

The main topic was development of experimental-numerical procedure, based primarily on the micromechanical approach, for prediction of damage development in the pipeline material until final fracture by application of specimens convenient for use in engineering practice. Also, the procedure is optimised for use on pipes with different dimensions and produced from different materials. Finally, the effect of heterogeneity of seam pipes (longitudinally welded) on the fracture behaviour is assessed.

The Thesis consists of 8 chapters. In the first one, Introduction, a brief overview about the topic of the work is given. Basic considerations about the stress and strain in solid bodies are covered in chapter 2, as well as a brief historical overview of the scientific field of fracture mechanics starting from the basic notions and observations.

Basic concepts and parameters of fracture mechanics are covered in chapter 3, with an emphasis on elastic-plastic fracture mechanics, EPFM, because the ductile mechanism of damage development is observed in the examined steel pipes. The influence of the stress and strain state on fracture resistance is discussed. The most often used fracture mechanics parameters of EPML are introduced: J integral, crack mouth opening displacement (CMOD) and crack tip opening displacement (CTOD). Also, δ_5 approach for experimental and numerical determination of CTOD is presented, because it is applied in this work.

Detailed overview of ductile damage and fracture mechanism in metallic materials, occurring through nucleation of voids, followed by their growth and final coalescence, is presented in chapter 4. Basic considerations are given about micromechanical models for ductile fracture prediction and assessment in geometries with or without the initial cracks. They can be categorised into the models of uncoupled and coupled approach; emphasis is on the coupled models stemming from the Gurson flow rule (i.e. Gurson plastic potential), because the model applied in this work belongs to this group. Techniques for numerical modelling the development of macroscopic damage in the material - crack growth, are also given in this chapter.

Since the pipelines can be exposed to different mechanical or thermal loads, as well as to aggressive media, in exploitation, chapter 5 contains a brief overview of damage mechanisms in pipes. Subsequently, an overview of the proposed non-standard specimens from the literature is given, with the comments on their properties regarding the fabrication, testing procedure and obtained results.

Chapter Materials and methods summarises the research procedure and gives an insight into techniques and, to some extent, to used equipment. It contains the brief overview of applied experimental and numerical techniques. Experimental examinations include the hardness measurement, microstructural analysis and fracture surface analysis, as well as tensile and fracture mechanics testing including the non-contact measurement of strain (stereometric system with two cameras). Special part of this chapter is devoted to the testing of the pipe ring specimens, both experimentally and by application of numerical analysis.

In the Results and discussion chapter, a detailed presentation of all results obtained during the work on the Thesis is given. It is split into the results from experimental examinations and numerical/micromechanical one. The results are discussed, with a special emphasis on the applicability on fracture testing of new and exploited pipelines.

Conclusions from the presented research work are listed in chapter 8, while the chapter Literature contains all the cited references, including those published from the results of this Thesis.

2. STRESS, STRAIN AND FRACTURE

2.1 Stress

A solid deformable body exposed to external forces is analysed, figure 2.1a. If the body is hypothetically divided into two parts, internal forces can be introduced at both sides. They replace the influence of the other half of the body. Due to the equilibrium conditions, forces in the right surface have the same magnitude and opposite direction, figure 2.1b. When all the internal forces on a section (on either left or right half) are taken into account, a force and a moment (*F* and *M)* are obtained as resultant. Although they are variable from point to point, it can be said that internal force has a homogeneous distribution in an infinitesimal area *dΩ*, figure 2.2a. When it is divided by the infinitesimal area, the stress is obtained:

$$T = dF/d\Omega \tag{2.1}$$

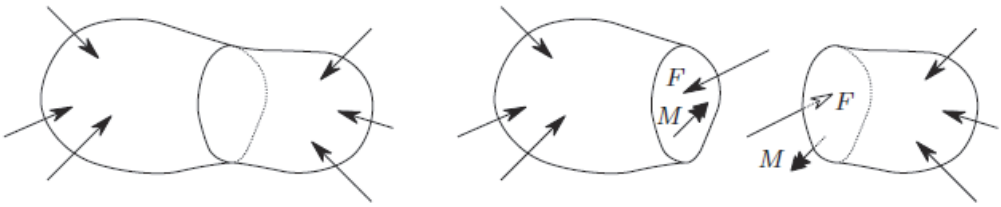

(a) *(b)*

Figure 2.1. Division of a body and internal forces [1]

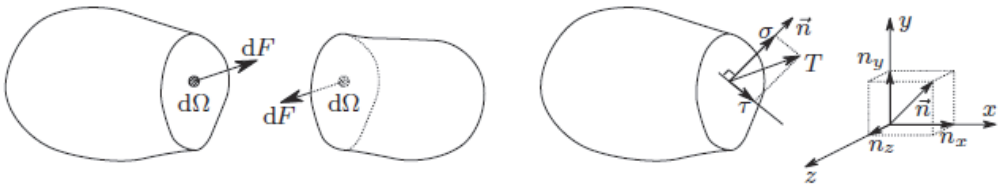

(a) *(b)*

Figure 2.2. Stress vector [1]

In figure 2.2b, the vector *n* is unit normal to the surface dΩ, and its components are [1]:

$$N_x = \cos(n, x) = l$$

$$N_y = \cos(n, y) = m$$

$$N_z = \cos(n, z) = n$$

Having in mind the dimension of the vector (i.e. its unit length), it can be written:

$$l^2 + m^2 + n^2 = 1 \qquad (2.2)$$

Stress components on infinitesimal surface are defined by using the angle α; this angle is the angle between the normal n and the stress vector: *normal* component ($\sigma = T \cos \alpha$), and *shear* component ($\tau = T \sin \alpha$).

Normal stresses with directions parallel x, y and z coordinate axes are marked as σ_x, σ_y and σ_z. Shear components have different indexes: τ_{ij} . The first index (here: i) stands for the normal of the surface, while the other (here: j) is the shear stress vector direction. In this way, τ_{xy} stands for the shear stress in y direction, within the plane which is normal to the x direction, i.e. in y-z plane. Figure 2.3 shows all stress components on an infinitesimal cubic element, which surrounds the point P.

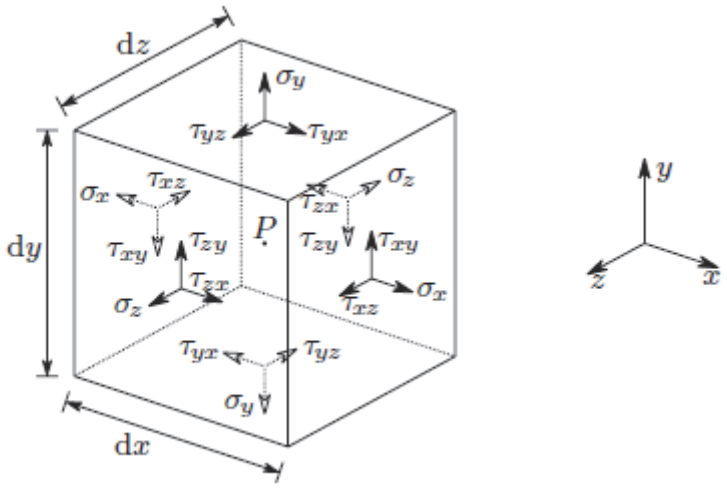

Figure 2.3. Stress components

Equilibrium conditions establish the balance between the external and internal forces; in static conditions this means that the resulting force and moment have zero values.

2.2 Stress tensor

2.2.1 Principal stresses

In mathematical terms, the stress tensor, often denoted as [σ], can be considered as a linear operator. When this operator is applied to the unit vector n (see figure 2.2b), the stress vector T is obtained.

An important feature of the stress tensor is the following: at any point of the body, one can determine the system of three orthogonal directions (i.e. normals, which define three planes) where stress vector directions coincide with the normals. As a consequence, the shear stress is equal to zero. The term used for these directions is *principal directions*, while corresponding stresses are the *principal stresses*.

As mentioned, principal stress does not have the shear components, but only the normal ones σ; this results in the following terms: $T_x = l\sigma$, $T_y = m\sigma$ and $T_z = n\sigma$. This can be represented as:

$$\underbrace{\begin{bmatrix} \sigma_x - \sigma & \tau_{xy} & \tau_{xz} \\ \tau_{yx} & \sigma_y - \sigma & \tau_{yz} \\ \tau_{zx} & \tau_{zy} & \sigma_z - \sigma \end{bmatrix}}_{[C]} \begin{bmatrix} l \\ m \\ n \end{bmatrix} = \begin{bmatrix} 0 \\ 0 \\ 0 \end{bmatrix} \tag{2.3}$$

Of course, a trivial solution for this system is: all three values (*l,m* and *n*) are zero. More importantly, solutions which are not equal to zero will exist in case the equations are linearly dependent on each other. This can be mathematically expressed by the requirement that the system matrix has determinant which is equal to zero:

$$\begin{vmatrix} \sigma_x - \sigma & \tau_{xy} & \tau_{xz} \\ \tau_{yx} & \sigma_y - \sigma & \tau_{yz} \\ \tau_{zx} & \tau_{zy} & \sigma_z - \sigma \end{vmatrix} = -\sigma^3 + \mathrm{I}_1\sigma^2 - \mathrm{I}_2\sigma + \mathrm{I}_3 = 0 \tag{2.4}$$

In this expression the quantities I_1, I_2 and I_3 are the stress tensor invariants:

$$\mathrm{I}_1 = \sigma_x + \sigma_y + \sigma_z$$

$$\mathrm{I}_2 = \begin{vmatrix} \sigma_x & \tau_{xy} \\ \tau_{xy} & \sigma_y \end{vmatrix} + \begin{vmatrix} \sigma_x & \tau_{xz} \\ \tau_{xz} & \sigma_z \end{vmatrix} + \begin{vmatrix} \sigma_y & \tau_{yz} \\ \tau_{yz} & \sigma_z \end{vmatrix}$$

$$= \sigma_z\sigma_y + \sigma_x\sigma_z + \sigma_y\sigma_z - \tau_{xy}^2 - \tau_{xz}^2 - \tau_{yz}^2$$

$$\mathrm{I}_3 = \begin{vmatrix} \sigma_x & \tau_{xy} & \tau_{xz} \\ \tau_{xy} & \sigma_y & \tau_{yz} \\ \tau_{xz} & \tau_{yz} & \sigma_z \end{vmatrix} = \sigma_x\sigma_y\sigma_z + 2\tau_{xy}\tau_{xz}\tau_{yz} - \sigma_x\tau_{yz}^2 - \sigma_y\tau_{xz}^2 - \sigma_z\tau_{xy}^2$$

2.2.2 Stress tensor - isotropic and deviatoric part

An often applied decomposition of the stress tensor considers the difference between the change of volume and the change of shape of the material exposed to external loading. The results of such decomposition are isotropic part of the tensor (responsible for change of volume) and deviatoric part of the tensor (which changes the shape). The quantity σ_m is denoted as mean stress; this value is very important for ductile fracture analysis, which will be considered in the following chapters.

$$\begin{bmatrix} \sigma_m & 0 & 0 \\ 0 & \sigma_m & 0 \\ 0 & 0 & \sigma_m \end{bmatrix} \quad \text{with} \quad \sigma_m = \frac{\sigma_x + \sigma_y + \sigma_z}{3} = \frac{\mathrm{I}_1}{3} \tag{2.5}$$

This is the matrix representation of the decomposition of the stress tensor:

$$\begin{bmatrix} \sigma_x & \tau_{yx} & \tau_{zx} \\ \tau_{xy} & \sigma_y & \tau_{zy} \\ \tau_{xz} & \tau_{yz} & \sigma_z \end{bmatrix} = \underbrace{\begin{bmatrix} \sigma_m & 0 & 0 \\ 0 & \sigma_m & 0 \\ 0 & 0 & \sigma_m \end{bmatrix}}_{\text{isotropic tensor component}} + \underbrace{\begin{bmatrix} \sigma_x - \sigma_m & \tau_{yx} & \tau_{zx} \\ \tau_{xy} & \sigma_y - \sigma_m & \tau_{zy} \\ \tau_{xz} & \tau_{yz} & \sigma_z - \sigma_m \end{bmatrix}}_{\text{deviatoric tensor component}} \tag{2.6}$$

As mentioned previously, deviatoric component does not cause volume change; its first invariant is equal to zero: $\dot{I}_1 = \sigma_x + \sigma_x + \sigma_z - 3\sigma_m = 0$.

2.3 Failure theories

Failure of different types of materials exposed to static loading can generally be classified into ductile and brittle. Many metallic materials exhibit ductile behaviour, an their failure is related to elastic-plastic deformation of the structure. Some other materials, such as glass, ceramics and some metals (more pronounced at low temperatures), exhibit brittle behaviour. In these materials, fracture occurs without significant plastic deformation, which corresponds to the reaching of a critical stress level.

In a ductile material, yielding typically occurs through the movement of dislocations, i.e. sliding of the atomic planes, figure 2.4. The energy, or amount of mechanical work, which is necessary for yielding is much smaller in comparison with the energy needed for separation of the atomic planes. Therefore, the consequence is that maximum shear stress causes/controls the yielding process in ductile materials.

Figure 2.4. Relative sliding of atomic planes

Since atomistic models which take this mechanism into account are too complex for application on structures and mechanical parts, phenomenological failure theories have been developed and improved for a long time. The purpose is to apply the experimentally obtained values (which are typically obtained by testing in one direction) in analysis of failure in complex stress state, i.e. in materials exposed to multi-axial loading.

2.3.1 Strain energy

The work which is performed by external force acting on the considered solid structure is stored within the material as potential energy. Since this energy corresponds to material deformation, it is denoted as *strain energy* (U). Instead of this quantity, strain energy density $\mathcal{W}$ is more often used. It is actually strain energy for a unit volume; The relation between them can be formulated as:

$$U = \iiint_v \mathcal{W}(x, y, z)dv \tag{2.7}$$

In this equation, v is body/structure volume. For one-dimensional loading (e.g. tensile loading of a cylindrical specimen), $\mathcal{W}$ is determined based on the engineering stress - strain curve, figure 2.5:

$$\mathcal{W} = \frac{1}{2}\sigma\varepsilon \tag{2.8}$$

while for 3-D stress state it is:

$$\mathcal{W} = \frac{1}{2}\sigma_x\varepsilon_x + \sigma_y\varepsilon_y + \sigma_z\varepsilon_z + \tau_{yz}\gamma_{yz} + \tau_{zx}\gamma_{zx} + \tau_{xy}\gamma_{xy} \tag{2.9}$$

For elastic materials, the strain energy after the removal of the external loading is fully recovered.

The Eq. (2.9) can be expressed in a more simple manner, if principal stress directions 1,2,3 are used (which means that the shear stress components are equal to zero).

$$\mathcal{W} = \frac{1}{2}(\sigma_1\varepsilon_1 + \sigma_2\varepsilon_2 + \sigma_3\varepsilon_3) \tag{2.10}$$

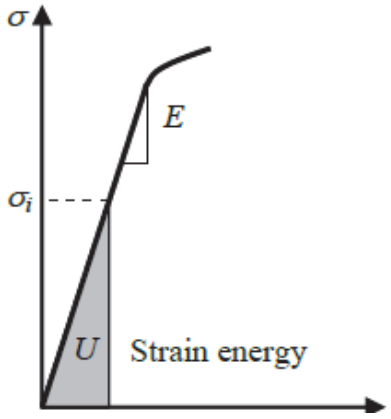

Figure2.5. Strain energy

For principal stresses and strains, it can be written:

$$\begin{cases} \varepsilon_1 = \dfrac{1}{E}(\sigma_1 - \nu\sigma_2 - \nu\sigma_3) \\ \varepsilon_2 = \dfrac{1}{E}(\sigma_2 - \nu\sigma_1 - \nu\sigma_3) \\ \varepsilon_3 = \dfrac{1}{E}(\sigma_3 - \nu\sigma_1 - \nu\sigma_2) \end{cases} \tag{2.11}$$

When the strains are from Eq. (2.11) are substituted in Eq. (2.10), strain energy density can be obtained from principal stresses:

$$\mathcal{W} = \frac{1}{2E}\left[\sigma_1^2 + \sigma_2^2 + \sigma_3^2 - 2\nu(\sigma_1\sigma_2 + \sigma_2\sigma_3 + \sigma_1\sigma_3)\right] \tag{2.12}$$

Similar to the decomposition of the strain tensor, strain energy density can also be split in accordance with the deformation modes. This results in dilatational component $\mathcal{W}_h$ and distortional one, $\mathcal{W}_d$. Mentioned stress components can be derived as follows:

$$\begin{bmatrix} \sigma_1 & 0 & 0 \\ 0 & \sigma_2 & 0 \\ 0 & 0 & \sigma_3 \end{bmatrix} = \begin{bmatrix} \sigma_h & 0 & 0 \\ 0 & \sigma_h & 0 \\ 0 & 0 & \sigma_h \end{bmatrix} + \begin{bmatrix} \sigma_{1d} & 0 & 0 \\ 0 & \sigma_{2d} & 0 \\ 0 & 0 & \sigma_{3d} \end{bmatrix} \tag{2.13}$$

The dilatational component σ_h is defined as:

$$\sigma_h = \frac{\sigma_1 + \sigma_2 + \sigma_3}{3} = \frac{\sigma_{xx} + \sigma_{yy} + \sigma_{zz}}{3} \tag{2.14}$$

Now, the stress values can be substituted into Eq. (2.12), thus giving the dilatational energy density:

$$\mathcal{W}_h = \frac{1}{2E}\sigma_h^2 + \sigma_h^2 + \sigma_h^2 - 2\nu(\sigma_h\sigma_h + \sigma_h\sigma_h + \sigma_h\sigma_h) \tag{2.15}$$

$$= \frac{3}{2}\frac{(1-2\nu)}{E}\sigma_h^2$$

or, by application of the principal stresses:

$$\mathcal{W}_h = \frac{3}{2}\frac{(1-2\nu)}{E}\frac{\left(\sigma_1+\sigma_2+\sigma_3\right)^2}{3} \tag{2.16}$$

$$= \frac{(1-2\nu)}{6E}\sigma_1^2 + \sigma_2^2 + \sigma_3^2 + 2(\sigma_1\sigma_2 + \sigma_2\sigma_3 + \sigma_1\sigma_3)$$

2.3.2 Distortion energy

If the dilatational energy, given in previous section, is subtracted from the total energy, distortion energy is obtained.

$$\mathcal{W}_d = \mathcal{W} - \mathcal{W}_h$$

$$= \frac{1+\nu}{3E}\sigma_1^2 + \sigma_2^2 + \sigma_3^2 - \sigma_1\sigma_2 - \sigma_2\sigma_3 - \sigma_1\sigma_3 \tag{2.17}$$

$$= \frac{1+\nu}{3E}\frac{\sigma_1 - \sigma_2{}^2 + \sigma_2 - \sigma_3{}^2 + \sigma_3 - \sigma_1{}^2}{2}$$

Component $\mathcal{W}_d$ can be expressed in dependence on an equivalent stress - von Mises stress σ_{VM} :

$$\mathcal{W}_d = \frac{1+\nu}{3E}\sigma_{VM}^2 \tag{2.18}$$

Von Mises stress can then be written depending on the principal stresses:

$$\sigma_{VM} = \sqrt{\frac{\sigma_1 - \sigma_2{}^2 + \sigma_2 - \sigma_3{}^2 + \sigma_3 - \sigma_1{}^2}{2}} \tag{2.19}$$

2.3.3 Distortion energy theory

This theory, often referred to as von Mises's one, states that the material yields upon reaching the critical value of distortion energy density. Having in mind that this formulation is also valid for uniaxial loading, this critical value (for the considered material) can be determined by uniaxial testing. When the yielding occurs during the testing under unaxial loading (such as tensile testing), the following relations are valid: $\sigma_1 = \sigma_Y$ and $\sigma_2 = \sigma_3 = 0$ (σ_Y represents the yield stress). At the onset of yielding, distortion component of energy density is:

$$\mathcal{W}_d = \frac{1+\nu}{3E}\sigma_Y^2 \tag{2.20}$$

Therefore, this value of $\mathcal{W}_d$ is critical for the considered material. In the conditions of multi-axial loading conditions, the yielding will take place when $\mathcal{W}_d$ exceeds the critical value:

$$\frac{1+\nu}{3E}\sigma_{VM}^2 \geq \frac{1+\nu}{3E}\sigma_Y^2$$

$$\text{i.e:} \quad \sigma_{VM} \geq \sigma_Y \tag{2.21}$$

In other words, according to this theory the condition for material yielding is that von Mises stress exceeds the uniaxial critical stress σ_Y. Von Mises stress can then be rewritten in the following way:

$$\sigma_{VM} = \sqrt{\frac{(\sigma_{xx}-\sigma_{yy})^2 + (\sigma_{yy}-\sigma_{zz})^2 + (\sigma_{zz}-\sigma_{xx})^2 + 6(\tau_{xy}^2 + \tau_{yz}^2 + \tau_{zx}^2)}{2}} \tag{2.22}$$

The expression for plane stress state ($\sigma_3 = 0$):

$$\sigma_{VM} = \sqrt{\sigma_1^2 - \sigma_1\sigma_2 + \sigma_2^2} \tag{2.23}$$

Eq. (2.23) is based on the principal stresses; if general stress components are considered, then it can be formulated as:

$$\sigma_{VM} = \sqrt{\sigma_{xx}^2 - \sigma_{yy}^2 - \sigma_{xx}\sigma_{yy} + 3\tau_{xy}^2} \tag{2.24}$$

In 2D plane of principal stresses, Eq. (2.23) represents an elliptical line, figure 2.6. If the current stress state, represented as a point with coordinates (σ_1, σ_2), is inside this ellipse, the material is considered safe with respect to yielding.

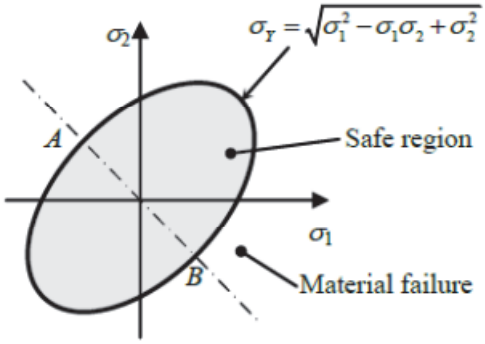

Figure 2.6. Failure envelope of the distortion energy theory

2.4 Fracture mechanics - history and basic considerations

Fracture of different materials is a problem which exists ever since man-made structures have been produced. With the advance of technology, engineering disciplines and industrial production, the fracture problems also become more and more pronounced. More complex structures and machines pose a challenge for ensuring the integrity and safe operation. The progress of fracture assessment techniques and methods enables a better understanding of materials failure, as well as development of procedures for prevention of failure.

Development of fracture mechanics has started more than hundred years ago; two works which are often considered as its foundations are the papers of Inglis about the stress concentration [2] and Griffith about the energy release rate [3]. These works made the basis for linear elastic fracture mechanics (LEFM), with the stress intensity factor as the main parameter. An important turning point in fracture mechanics history was around 1960, when the fracture mechanics research started to incorporate the influence of crack tip plasticity. Several researchers in early sixties considered the plastic deformations at the crack tip, typical for ductile materials, [4-6]. An important work was published by Rice [7]; in this paper, material behaviour is characterised by a contour integral - *J* integral. Eshelby [8] had previously formulated some conservation integrals, but did not deal with applications in fracture mechanics. Through the works of Hutchinson [9] and Rice and Rosengren [10], it has been generalised as a fracture mechanics parameter. A

very important application of this approach was motivated by the requirements of the nuclear industry, with an aim to provide safer design of facilities. To characterise the fracture properties of the used materials (which had high toughness, i.e. could not be described by using LEFM), Begley and Landes [11] applied the Rice’s approach only a few years after it was published.

The fracture mechanics has been significantly developed as a scientific discipline in the previous period. Also, its application in many engineering fields made it a very useful tool in the hands of mechanical and other engineers.

New models for assessment and prediction of damage and fracture of materials are continuously developed, further extending the fracture mechanics applicability. For example, analysis of the influence of material non-linearity started around 60 years ago, and resulted in a significant improvement of fracture assessment. In the more recent period, some new phenomena came into focus, such as time-dependent behaviour: viscoplasticity (high temperatures, creep) and viscoelasticity (e.g. for polymers), fracture in dynamic conditions (low- and high-cycle fatigue), complex damage mechanisms, etc. Also, fracture of composite materials is gaining more and more attention and increasing number of studies worldwide deals with this topic. Problems which occur in the microelectronics industry have led to significant development of at least two branches of fracture mechanics, dealing with interface fracture and nanoscale fracture. An important aspect in development and practical use of fracture mechanics is rapid development of computer technology.

A significant role in the current studies is development of micromechanical models, which predict the macroscopic behaviour and fracture of structures based on the analysis of material damage on the local level. Such approach is applied in this work, i.e. fracture development in the ring-shaped specimens is analysed by application of a micromechanical model for prediction of damage development.

In addition to failure by fracture, structures exposed to static loading can also exhibit plastic collapse, i.e. plastic strains can become so high that the structure cannot be exploited any more (even though fracture did not occur). This mode of failure is also considered in this work.

3. ELASTIC-PLASTIC FRACTURE MECHANICS

Ductile damage mechanism includes a significant deformation of the material exposed to external loading. With this in mind, it is very important to understand, as much as possible, the behaviour of materials, including plastic deformation, under external load in the presence of cracks. Focus in this chapter is therefore on elastic-plastic fracture mechanics (EPFM).

3.1 Stress field around the crack tip in a linear-elastic material

Introducing a singular dominant zone in the region of the crack tip allows a single parameter presentation of the state of the material. Namely, if one considers an isotropic, linearly elastic-material containing a crack, for certain geometries it is possible in a closed form to calculate the stress components σ_{ij} [12-15]:

$$\sigma_{ij} = \left(\frac{k}{\sqrt{r}} \right) f_{ij}(\theta) + \sum_{m=0}^{\infty} A_m r^{\frac{m}{2}} g_{ij}^{(m)}(\theta) \tag{3.1}$$

where r and θ are the polar coordinates which determine the position of the observed location with respect to the crack tip, f_{ij} is a dimensionless function of angle θ, and k is the constant (figure 3.1). A_m and $g_{ij}^{(m)}$ are elements of the higher order (order m) which depend on the geometry and angle θ. Regardless of the considered geometry the formulation for the stress field contains an element proportional to $1/\sqrt{r}$. Then follows a known stress singularity $1/\sqrt{r}$ around the crack tip, which represents one of the basic principles of linear elastic fracture mechanics (LEFM).

The parameter with which it is possible for all three of the basic forms of occurrence of fracture (crack opening, in-plane and out-of-plane shear) to present the material state around the crack tip, in view of the singularity $1/\sqrt{r}$, is the stress intensity factor K. It defines the overall state (stress, displacement and strain) around the tip corresponding to observed external loading, which forms the basis of single-parameter presentation of the state of the material. Detailed formulations for stresses and displacements depending on the known value of K can be found in literature which discusses the LEFM [16 -18].

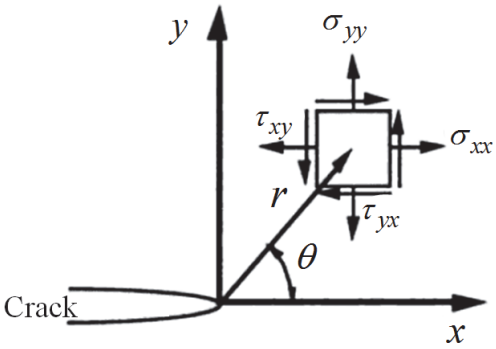

Figure 3.1. Stresses around the crack tip

It is logical to assume that in a certain combination of values of stress and strain the crack begins to grow. Based on the above, to the said combination corresponds an unambiguous value of K. This value may be referred to as critical, K_{crit}, and represents the fracture toughness for a given material. Under certain conditions in defined standard examinations of fracture toughness (see ASTM E399, [19,20]), K_{crit} can be considered a material parameter - fracture toughness in plane strain state.

The LEFM approach predicts infinite stresses at the tip of the crack. For construction materials used in industrial practice, these stresses have a finite value. Even in extremely brittle materials, where the phenomenon of plastic deformation is negligible, stresses around the crack front have a finite value, because an ideally sharp crack corresponds more to mathematical formulation than reality.

3.2 Formulation of elastic-plastic fracture mechanics (EPFM)

Plastic strains cause a decrease of stress values in the vicinity of the crack in comparison with linear-elastic case (figure 3.2).

For determining the plastic zone dimensions, the most commonly used analytical methods are the Irwin [4] and the Dugdale method [5]. Irwin's solution, relying on linear-elastic consideration, gives a value for the radius r_y:

$$r_y = \frac{1}{2\pi}\left(\frac{K_I}{\sigma_Y}\right)^2 \tag{3.2}$$

This formulation represents the so-called evaluation of the first order, and is derived taking into account the conditions of plane stress state (PS) and neglecting material

hardening. The stress values in the previous analysis cannot be higher than the yield stress σ_Y.

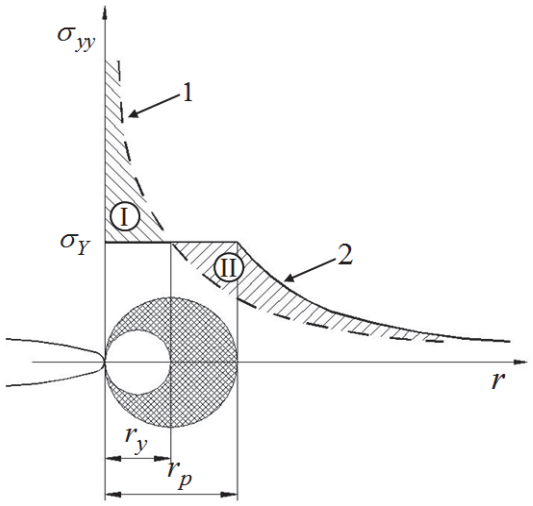

Figure 3.2. The distribution of the stress component σ_{yy} for linear-elastic (curve 1) and perfectly plastic material (curve 2) [21]

The onset of plastic yielding causes redistribution of stress values; with the assumption of ideal plastic material behaviour, these values cannot be found in the area defined by the upper part of curve 1 and marked with the Roman numeral I (figure 3.2).Therefore, in order to achieve a balanced state, the redistribution is performed in the part below the line σ_Y = const, by adding curve 2, thereby forming area II with a surface equal to the surface of area I. Analytically, using the method of equilibrium of forces:

$$\sigma_Y r_p = \int_0^{r_y} \sigma_{yy} dr = \int_0^{r_y} \frac{K_I}{\sqrt{2\pi r}} dr \tag{3.3}$$

a corrected - expanded dimension of the plastic zone r_p is:

$$r_p = \frac{1}{\pi}\left(\frac{K_I}{\sigma_Y}\right)^2 \tag{3.4}$$

In plane strain state (PE), plastic yielding is partially prevented due to the stress state triaxiality, that way the values for the radii r_p and r_y are three times smaller. These formulations are suitable to quickly and easily determine the approximate plastic zone size.

Irwin [13] used the given analysis to propose an actual crack length, which also includes the influence of the plastic zone defined by the radius r_y:

$$a_{eff} = a + r_y \tag{3.5}$$

and the actual stress intensity factor:

$$K_{eff} = Y(a_{eff})\sigma\sqrt{\pi\, a_{eff}} \tag{3.6}$$

Where in $Y(a_{eff})$ is a coefficient, which depends on the crack geometry, while σ is nominal stress (far from the crack, see figure 3.3). When r_y tends to zero, $a_{eff} = a$ and the formulation (3.6) is reduced to the definition of K. K_{eff} is most commonly determined by an iterative process, and for certain geometries, and forms of cracks there is a solution in the closed form. More about the application of K_{eff} can be found in [16, 21].

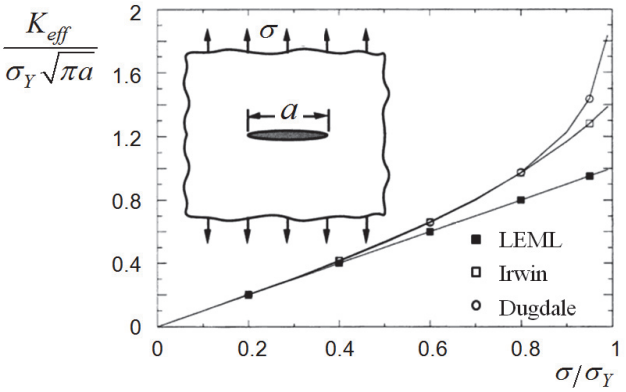

Figure 3.3. Dependence of normalised value of K_{eff} on the ratio σ/σ_Y [16]

Solutions obtained by the analytical methods discussed above are not without practical importance; for example, they are used for the prediction of failure occurrence in structural parts using the failure assessment diagram - FAD.

3.3 The effect of triaxiality

Most of the results in classical fracture mechanics are obtained by applying two-dimensional (2D) analysis. There are problems where such an analysis is sufficient, for special cases which can be represented in plane stress (PS), plane strain (PE) or axisymmetrical conditions. However, there are also problems that cannot be reduced to these 2D simplifications and which require resolution by taking into account all three dimensions (3D).

So far, considered was the value of the greatest component that occurs during crack opening - σ_{yy}, figure 3.2. Due to tension along direction y, the material tends to shrink in the other two directions. This is not possible in the measure that is due to the value of

stress σ_{yy}. Therefore, limited displacements in the other two directions lead to stress triaxiality in the crack tip area.

Figure 3.4 schematically shows the change in stress component σ_{zz} in a plate with a crack. In the interior, far from the surface, this component has higher values relative to the values close to the outer surfaces. This also means that the level of triaxiality is higher in the central part of the plate. The result is that the conditions that apply in this area correspond to the PE. In the vicinity of the side surfaces of the plate, the triaxiality level decreases, but the conditions of pure PS occur only on the surface.

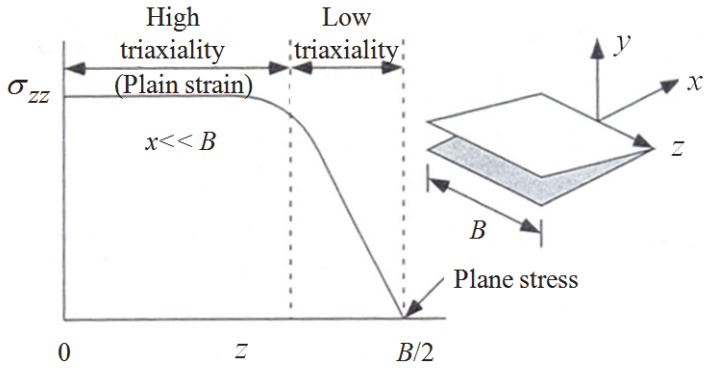

Figure 3.4. Change of stress component σ_{zz} along the crack front [16]

Therefore, in analytical and numerical analysis such geometries are considered in PE conditions, particularly if the thickness of the plate is sufficient.

If we observe the stress state at certain distance from the crack front, it goes from PE to PS condition, which is even more pronounced if the plate is less thick. Narasimhan and Rosakis [22] showed this using detailed 3D numerical calculations, by varying the value of z/B and x/B. Finally, if tension of the plate without cracks is analysed, plane stress conditions can be applied.

Stress triaxiality becomes crucial in the case of ductile fracture. In the following chapter, which presents the models used for prediction of the occurrence of ductile fracture, the ratio σ_m/σ_{eq} (stress state triaxiality) is explicitly used in formulations.

Therefore, there is no doubt that the stress distribution has major influence on fracture. By simple analysis given in [16], it can be shown that the stress component σ_{yy}, with the occurrence of plastic yielding of the material, is 2.5 times higher in PE conditions as compared to the value obtained in PS conditions.

3.4 Parameters describing the change in crack geometry in EPFM

Crack opening displacement - COD, which is often marked δ, is particularly important to be defined precisely at the tip region. Then, this parameter becomes the crack tip opening displacement or CTOD.

When Wells attempted to measure K_{Ic} values (fracture toughness) on different structural steels, he found that "these materials were too tough to be characterised by LEFM", [6]. He concluded that the existing solutions of fracture mechanics (which relied on linear-elastic behaviour of material and stress intensity factor as parameter) should be extended. In particular, the main finding was the displacement of the entire crack faces before the growth initiation, which lead to blunting, figure 3.5. Materials with higher toughness had more pronounced blunting, and therefore Wells proposed CTOD as the new parameter for determination of fracture toughness (designation CTOD was proposed later).

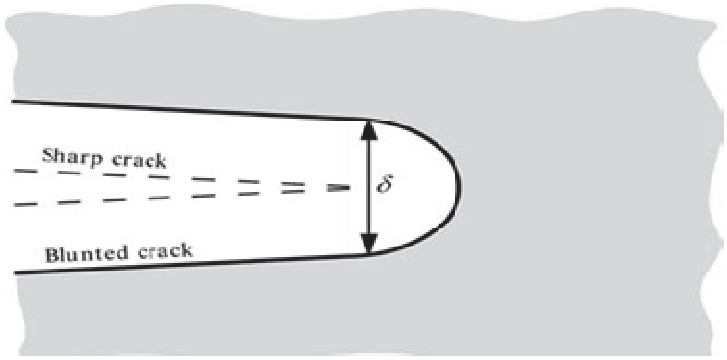

Figure 3.5. Crack tip opening displacement (CTOD)[8]

In figure 3.6, geometrical values important for this analysis are given, for plate with a central crack exposed to tension loading. The dashed line shows the contours of the actual crack at the tip of which was introduced a polar coordinate r. Given that the tip (solid line) is defined by coordinates (a, 0), the actual displacement of the crack at point $r=r_y$ defines the CTOD:

$$\delta(r = r_y) = \text{CTOD} = \frac{4K_I}{m\sigma_Y E} \tag{3.7}$$

Where m is a dimensionless measure, the value of which depends on the stress state (PS or PE) and material deformation hardening. Values for m are available in literature [16,17,21].

The formulation (3.7) is an approximate solution for CTOD in proportionally small scale yielding - SSY conditions. If CTOD defines the minimum value of crack opening δ, determined at its tip, then crack mouth opening displacement - CMOD provides its highest value (for central crack, CMOD represents its opening in the middle, figure 3.6).

The fact that there are several possible definitions of CTOD is due to the lack of physical interpretation of this measure. In this thesis the concept δ_5 was used [23]. Figure 3.7 shows a scheme for δ_5 measurement; measuring points are positioned at ±2.5 mm from the crack tip, perpendicular to its direction of propagation.

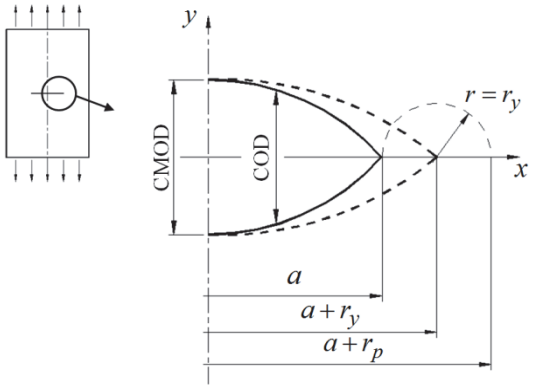

Figure 3.6. Crack opening displacement - schematic presentation

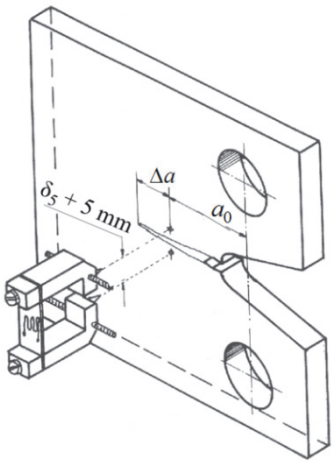

Figure 3.7. Measuring of δ_5 on the compact tension specimen [23]

One of the benefits of using this method is the possibility of determining the CTOD in structures containing cracks in the welded joint or on the boundary surfaces of the materials comprising the bimaterial joint.

The presented concept is also simple for use in FEM numerical calculations. In contrast to measuring the CTOD according to the BSI BS5762 standard, which is limited to passing-through cracks and is applied only on compact tension specimens and bending specimens, the δ_5 concept is also suitable for determining of the opening of the tip of surface cracks. For the practical application of δ_5 it is also important that there is a correlation between δ_5 and the CTOD value defined by the process according to BSI. Examples of correlations for the two geometries are given in [24].

Andersson [25], and de Koning [26] proposed the parameter CTOA - crack tip opening angle for stable growth description. Newman et al. presented the development and application of parameter CTOA in [27].

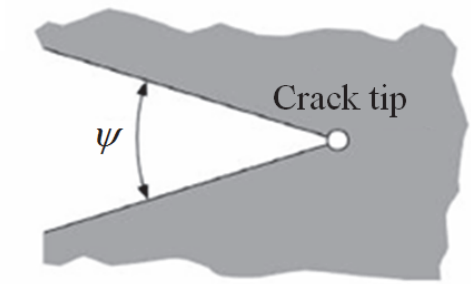

Figure 3.8. Determining CTOA [28]

3.5 Energetic aspect of fracture

An important feature of the fracture occurrence characterised by local plastic strain is that the energy is consumed during the entire process of failure. This is one of the basic features of ductile fracture - damage of material develops gradually, through the mechanism of nucleation, growth and coalescence of voids.

During the action of external load, component or specimen deforms for a certain value of du. In addition, due to the work of external load P is $dU=Pdu$. P is the resultant of forces or torques, and u is the so-called component response when exposed to external loading: displacement, angle, etc. Further on, these two values will be referred to as force and displacement, and will keep the marks P and u to highlight the general approach in the analysis.

Work due to the force P on displacement of u_1 is derived by integration:

$$U = \int_0^{u_1} P du \tag{3.8}$$

and represents the surface under the force-displacement diagram (interval from 0 to u_1). If the connection between force and displacement is linear, $P = k \cdot u$ is valid, where k stands for stiffness. Work due to external force is then:

$$U = \int_0^{u_1} k \cdot u \, du \tag{3.9}$$

and represents the area of the triangle in the part of curve P-u where the strain is elastic.

Work caused by external force corresponds to the strain energy of the deformed component, as outlined in detail in [16,29] (when ignoring the losses, the values are equal).

Strain energy density $\mathcal{W}$ can be calculated as:

$$\mathcal{W} = \frac{U}{A \cdot L} = \int_0^{u_1} \frac{P}{A \cdot L} du = \int_0^{u_1} \frac{P}{A} \frac{du}{L} = \int_0^{\varepsilon_1} \sigma d\varepsilon \tag{3.10}$$

The obtained value represents the surface of the area under the stress-strain curve; the interval is (0 - ε_1). For elastic strain of the material, it becomes:

$$\mathcal{W} = \frac{\sigma^2}{2E} \tag{3.11}$$

in this equation, E is elasticity modulus, while yield stress is denoted as σ_Y.

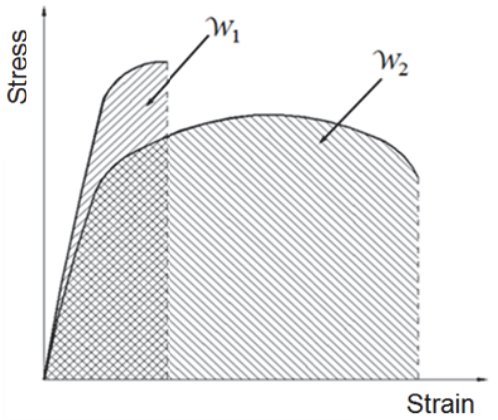

Figure 3.9. Nominal stress - strain curves with marked strain energy density ($\mathcal{W}_1$ for brittle and $\mathcal{W}_2$ for ductile behaviour)

On the basis of the stress - strain curves obtained using uniaxial tension of standard specimens, it is possible to see the extent of plastic deformation before final fracture. These curves are known in literature as nominal [30] or engineering [29,31]. In figure 3.9, nominal stress - strain curves for two materials, which are characterised by brittle and ductile behaviour, are shown. The measure of plastic strain of the material before final fracture in engineering practice is determined by simple formulations:

$$e_f = \frac{L_f - L_0}{L_0} \cdot 100 \tag{3.12a}$$

$$\psi_f = \frac{A_0 - A_f}{A_0} \cdot 100 \tag{3.12b}$$

Where L_0 and A_0 are measurement length and cross-section area of the specimen for determining properties of a material during uniaxial tension, and L_f and A_f the appropriate values at specimen fracture. The values of nominal strains defined by terms (3.12a) and (3.12b) are identified in literature as relative elongation and contraction at fracture.

During the ductile fracture of the specimen, the largest plastic strains are concentrated in the narrow zone (so-called specimen neck - occurs in the final stage of deformation); therefore the value e_f depends on the initial measurement length, L_0. The smaller the measuring length, the proportion of the elongation generated in the neck is higher, which increases the value e_f. Therefore, the size of the elongation at fracture should contain information at which value L_0 was determined.

Reduction of the cross section is not dependent on A_0; also, actual strain defined via the current cross section value is suitable for tracking plastic strain of the specimen up until fracture, as opposed to the true strain defined via the current length of the specimen, which is used up to the appearance of the neck.

3.6 J integral

3.6.1 General notions

Path-independent, which has later become known as *J* integral, was developed and introduced by Cherepanov [32] and Rice [7]. In relation to an arbitrarily selected path (contour), figure 3.10, *J* integral can be formulated:

$$J = \int_{\Gamma} \left(\mathcal{W} dy - T_i \frac{\partial u_i}{\partial x} ds \right) \tag{3.13}$$

$\mathcal{W}$ is strain energy density, ds is path length segment, $T_i = \sigma_{ij} n_j$ tenile stress on the contour, u_i displacement and n_i the unit normal to the contour, figure 3.10.

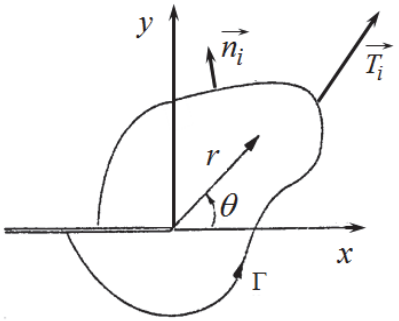

Figure 3.10. Path for J integral calculation [16]

Such definition of *J* integral allows it to be defined according to the path close to the crack, but also for the paths which are further from this zone. Therefore, it should be kept in mind that path independence implies the absence of processes that are time sensitive, as well as volume and inertial forces.

Budiansky and Rice [33] have shown that *J* integral corresponds to the energy release rate in a non-linear elastic medium:

$$J = -\frac{1}{B} \frac{d\Pi}{da} \tag{3.14}$$

Π stands for potential energy, a is crack length and B is thickness.

If the plastic deformation in the crack tip region is not pronounced (within the radius specified by r_y), equality $J=G$ can be stated, which directly links the stress intensity factor *K* and *J* integral. This means that this integral can express the stress intensity

around the crack for a nonlinear-elastic form, in the same way that through K the linear-elastic stress field amplitude can be defined.

This was shown by Hutchinson [9], Rice and Rosengren [10], by analysing the material with non-linear Ramberg-Osgood behaviour. According to them, this field is typically denoted as HRR. The amplitude of this field is actually the value of J integral.

Knowledge of HRR fields allows a connection between the J integral and CTOD if the material's strain hardening exponent is known, [34]. However, the application of J integral in analysis of local fracture process zone implies not only a theoretical base in continuum mechanics, but also taking into account the mechanism of ductile fracture.

3.6.2 Application in ductile fracture analysis

Exposed to a monotonically increasing external load, the sharp initial crack becomes blunt and moves slowly forward, as represented in diagram J-Δa, where Δa is the increase of crack length (figure 3.11). Around the crack tip, due to particle fracture or their decohesion from the base material, voids are formed. The voids grow and join with the rounded crack tip; the blunting process is then over, and the stable crack growth begins.

J integral value at the moment when the crack starts to grow is indicated by J_i. This can be related with the observation on fracture surface: rather small growth (significantly smaller than 1 mm for metals) which corresponds to the value of J_i is visible as a relatively smooth strip along the crack front and characterises the material stretch zone. Δa_B is used in literature for marking crack length increase due to its blunting, though the more commonly used term is Δa_{SZW}, which is the final stretch zone width. This quantity is measured after the final fracture of the specimen and separation into two parts, on the fracture surfaces.

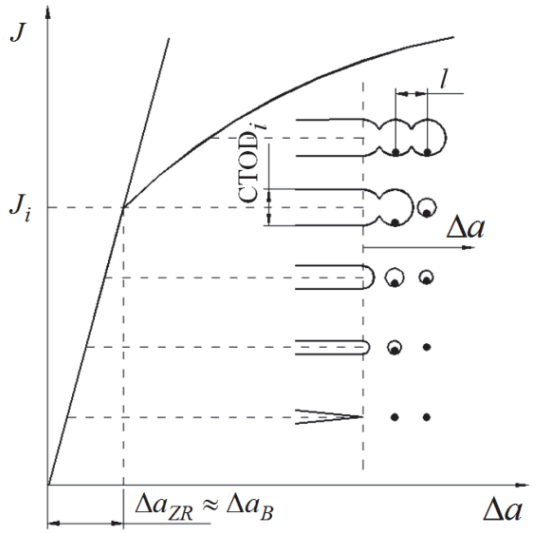

Figure 3.11. Change in J integral value at stable crack growth by ductile fracture mechanism

By increasing the external loading, there is an increase in number of voids (at the mean mutual spacing *l*), which in time coalesce with the existing voids. This phenomenon represents stable crack growth. Nucleation of the voids is influenced by the shape, dimensions and direction of particles (in case they are non-spherical), while distance between the voids and the localisation of the stress and strain determines the coalescence mechanism.

3.7 Failure by plastic collapse

Besides failure by fracture, which can occur by ductile, brittle or cleavage mechanism in metallic materials, mechanical components/structures can also fail due to excessive plastic deformation - which is denoted as plastic collapse.

The load-carrying capacity of a mechanical part, machine or structure can be expressed through the limit load or plastic collapse load. Together with fracture resistance, it can be used for integrity assessment of a structure, with an aim to ensure safe service under the exploitation loads. Some structures are more sensitive to fracture, while others have plastic collapse as more pronounced failure mechanism. In engineering practice, failure is typically caused by a combination of these two.

Limit analysis is a procedure which enables determination of the loading which can be applied to the considered structure, assuming that the material behaviour is perfectly plastic (i.e. without hardening). Such loading is denoted as the limit load.

In general, the condition for plastic collapse is that the entire ligament in front of the crack tip is plastically deformed. The load value (force, pressure, moment, etc.) at that moment is denoted as plastic collapse load. Unfortunately, it cannot be precisely determined experimentally. Instead, it is often determined based on the loading-displacement curves, like in figure 3.12. Three presented methods are: twice elastic slope (TES) method, based on the linear part slope, twice elastic displacement (TED), based on determination of elastic displacement, and tangent inter-section (TIM) method, which requires determination of two tangent directions. This is considered in several studies in literature, including [35], and the first mentioned method is applied here. The remaining two methods are more susceptible to subjective estimate, since the elastic slope can be determined much more precisely in comparison with the elastic displacement or the slope of the plastic part of the curve.

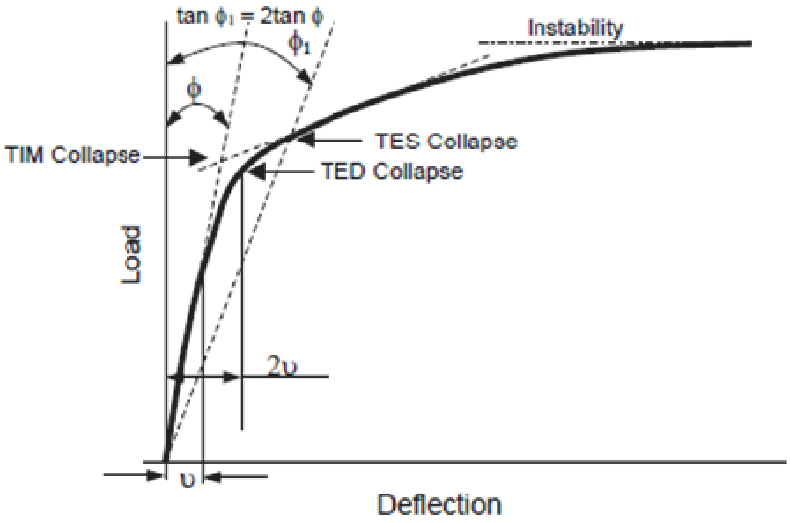

Figure 3.12. Various definitions of plastic collapse load [35]

4. ANALYSIS OF DUCTILE FRACTURE

Determination of failure conditions and prediction of damage development in structures produced from different materials require the approach which will take into account different aspects of fracture, from small scale yielding to large scale plasticity, mixed mode cracking, thermo-mechanical loading, etc. There are two main approaches to tackle these problems, and in the literature they are often named as global and local approach to fracture.

4.1 Global and local approach

Classical, or global, approach to fracture relies on the methodology of LEFM and EPFM, continually developed during the past decades. Application relies on the assumption that one parameter is sufficient to quantify the resistance of material to fracture. Depending on the prevailing stress conditions, the fracture initiation resistance can be critical value of: stress intensity factor K_{Ic}, J integral J_{Ic} or CTOD (CTOD$_c$). Standard procedures for measurement of fracture resistance, however, do not contain the influence of the damage mechanism, i.e. the process which leads to macroscopic fracture.

Global approach has certain limitations, which are especially emphasized in large scale yielding conditions. One of the main problems is so-called size effect - fracture toughness of the material is dependent on specimen size, i.e. typically depends on the material thickness. This dependence causes problems in transferring of the results from the laboratory specimens to structures in exploitation. Most often consequence is too conservative assessment of structure’s fracture resistance, based on the fracture mechanics specimens with large thickness.

However, the global approach has its important role in fracture analysis, and it is not ‘replaced’ by the local approach, but they are rather applied together.

Development of the local approach began around 40-50 years ago, and since then it has constantly been improved and applied in different types of fracture problems. Even

some older contributions, such as those of McClintock [37,38] can also be categorised as local approaches. Rather than taking the macroscopic behaviour of the structure with a crack (as in the global approach), local approach aims at establishing the criteria for damage development on the local level. Then, these criteria are valid regardless of the specimen size, stress concentrator size and shape, and even for geometries without an initial crack. Development of this methodology requires appropriate micromechanical models, which require the knowledge of stress-strain field on the local level and contain the parameter or parameters which describe the damage development in the material. Numerical methods are typically used for both determining the stress/strain and damage parameter fields.

There are two main types of micromechanical models. The first group describes the behaviour of the material conventionally (e.g. as elastic-plastic material), and the damage variable is subsequently determined through a post-processing procedure. This is referred to as uncoupled approach. On the other hand, coupled approach includes constitutive equations with a softening effect caused by damage development, i.e. damage parameter is incorporated into the constitutive relations and is calculated during the processing procedure.

As mentioned in [36], “application of so-called global criteria of fracture mechanics such as CTOD and *J* integral in characterisation of ductile fracture does not provide satisfactory results for all geometries and external loading types”. For example, it cannot be applied in failure prediction of geometries without an initial crack, and does not take the damage mechanism into account.

The main advantage of micromechanical modelling of damage and fracture (i.e. local approach) in comparison with the global one is that the parameters of these models are material-dependant, rather than geometry-dependant. From this, an important property arises - transferability of parameters between different geometries produced from the same material. Application of micromechanical models typically includes a combined experimental-numerical procedure, consisting of mechanical testing, fracture mechanics testing, microstructural analysis and numerical calculations. The main aim is to model/predict the fracture process by taking into account the damage mechanism within the material.

4.2 Ductile fracture mechanism

Ductile fracture in metallic materials is a process consisting of nucleation, growth and coalescence of voids. If we analyse a round tensile specimen made from a ductile material, without stress concentrators, localisation of deformation in the form of a neck will occur around maximum load. This precedes the separation of the specimen in two pieces. The fracture typically initiates inside the specimen, and develops towards the surface to form typical cup-cone shape of the fracture. The voids in the material nucleate around particles/inclusions, grow and eventually coalesce, which leads to macroscopic damage by ductile fracture mechanism. Theoretically, if the material could be produced as perfectly homogeneous, the neck diameter could decrease to zero before fracture.

4.2.1 Void nucleation

In metallic materials, the voids nucleate under external loading primarily around different particles. These are typically non-metallic inclusions (MnS, oxides, silicates, etc.) or second phase particles. In very pure metallic materials, the process of void nucleation is not related to any particles, but the voids nucleate homogeneously. An example for such behaviour is shown in [39], on Ti alloys. The work of Goods and Brown [40] summarises many results obtained by examining different ductile materials.

Nucleation of voids is typically related to the inhomogeneity in strain field caused by the existence of a particle in material matrix. Different methods were developed with the aim to simulate this mechanism. Some of them are based on dislocation theory, but most of them rely on the application of continuum mechanics. According to [40], the particle dimensions are the key parameter for selection of one of these approaches; they stated that the minimum radius for application of continuum mechanics approach is around 1μm.

Also, it should be mentioned that the nucleation does not have to be instantaneous - it can happen at different loading levels, continuously, typically more intensive with the increase of plastic strain.

Particle fracture and particle-matrix debonding are dependent on plastic properties of the materials. It is shown in [41] on the example of aluminium and Al2124 alloy. In Al matrix (lower strength and non-pronounced hardening) decohesion is dominant, figure 4.1a. Aluminium alloy 2124 has better tensile properties (figure 4.1b); hence, particle fracture is more frequently observed. Of course, these two mechanisms can be active at the same time, depending on the matrix and particle material properties.

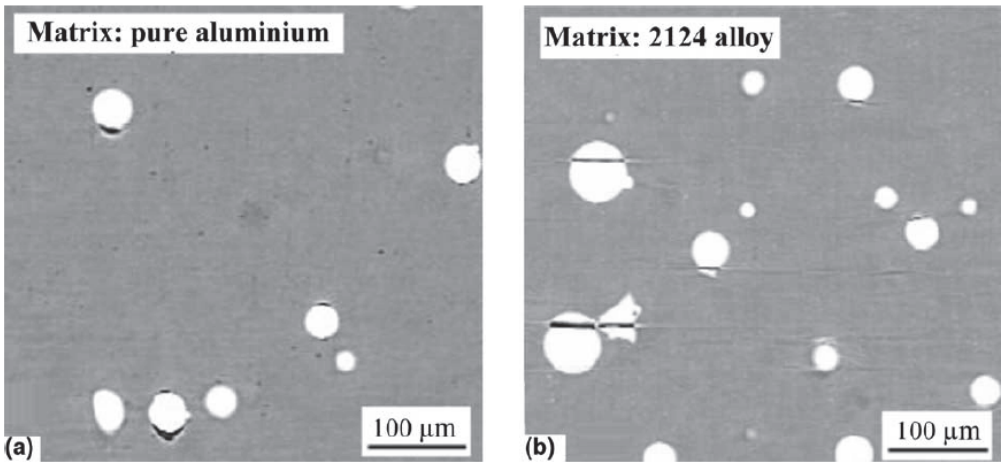

Figure 4.1. X-ray tomography (in situ) - matrix contains 4% ZrO2/SiO2 particles: particle debonding from Al matrix (a) particle fracture in Al2124(T6) matrix [41]

Figure 4.1 presents an image of spherical particles, in an artificially produced metal matrix composite (MMC). Of course, particles or inclusions in different alloys can have different, irregular shape. Fracture of such (cementite) particle in steel is shown in figure 4.2. Another example involving irregular shape of the particle, which exhibits decohesion from the matrix, is shown in figure 4.3.

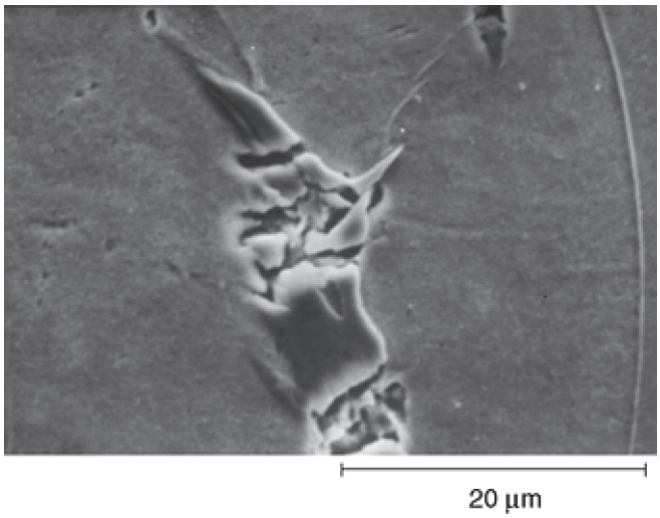

Figure 4.2. Cracked cementite particle in low-carbon steel (cca. 0.1% C) [42]

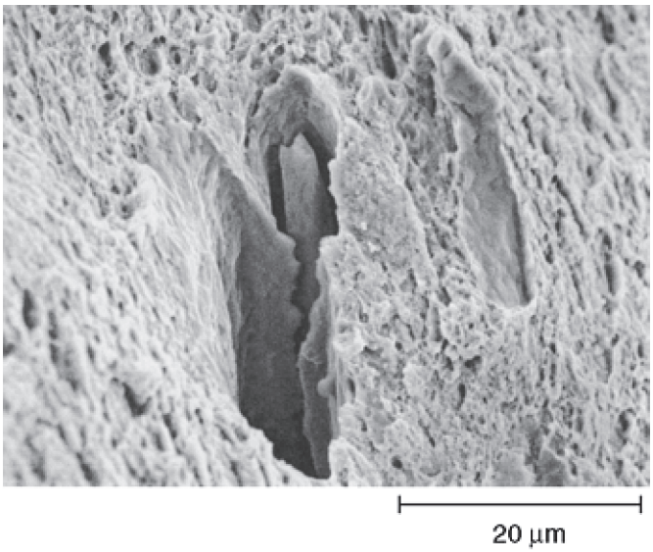

Figure 4.3. Debonding of MnS particle in a 4140 quenched and tempered steel [42]

4.2.2 Void growth

Some of the first studies which dealt with the void growth description resulted in publication of theoretical models by McClintock [38], Berg [43] and Rice and Tracey [44]. The main common point of these analyses was the dependence of void growth on plastic strain in the material matrix, as well as on the stress triaxiality. Of course, in order to derive the expressions for the void growth, the authors of these models had to impose some assumptions, and therefore the models are not necessarily reflection of the real materials behaviour. One of the most significant assumptions is neglecting the influence of the other voids in the vicinity of the analysed one.

4.2.3 Void coalescence

Coalescence of nucleated voids is a complex process which results in formation of macroscopic damage in a ductile material. It can generally be said that there are two different types of coalescence. The first type occurs in case the material does not have a population of smaller voids, typically nucleated around smaller particles. In other words, the voids grow continuously until their coalescence, figure 4.4a. This can sometimes be clearly visible on fracture surfaces, i.e. these joined voids are seen as connected dimples. If a second class of smaller voids, nucleated around smaller particles, exists - the growth of larger voids is interrupted by joining these smaller voids

in the manner shown in figure 4.4b - shear bands. For example, carbide particles are often found in steels and they represent a nucleation sites for the smaller voids (large ones typically nucleate around non-metallic inclusions).

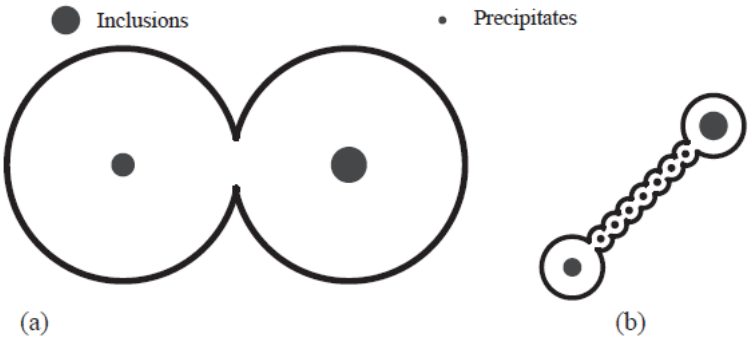

Figure 4.4. Coalescence of large voids (a) and shear band formation (b)

In figure 4.5, SEM microphotographs showing inclusions within dimples on steel fracture surfaces are presented. These inclusions were clearly initiation spots for voids in the material. They are also typically present below the fracture surface, because high triaxiality and plastic strain are also present in this zone. A schematic representation and SEM microphotograph of such voids are shown in figure 4.6.

Finally, microphotographs in figures 4.7 and 4.8 show the existence of two populations of dimples on ductile fracture surface. Large particles are observed in larger dimples, while smaller dimples can be found in the ligaments between them.

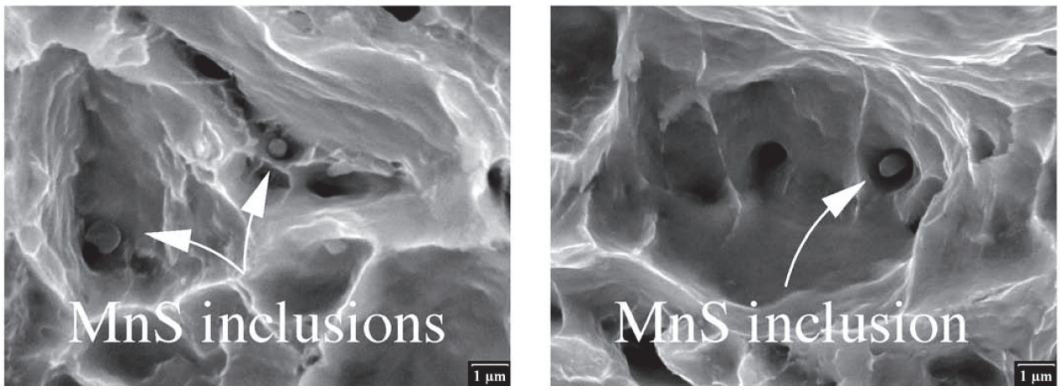

Figure 4.5. SEM microphotograph of MnS inclusions in dimples on fracture surface of a ferritic–pearlitic steel [45]

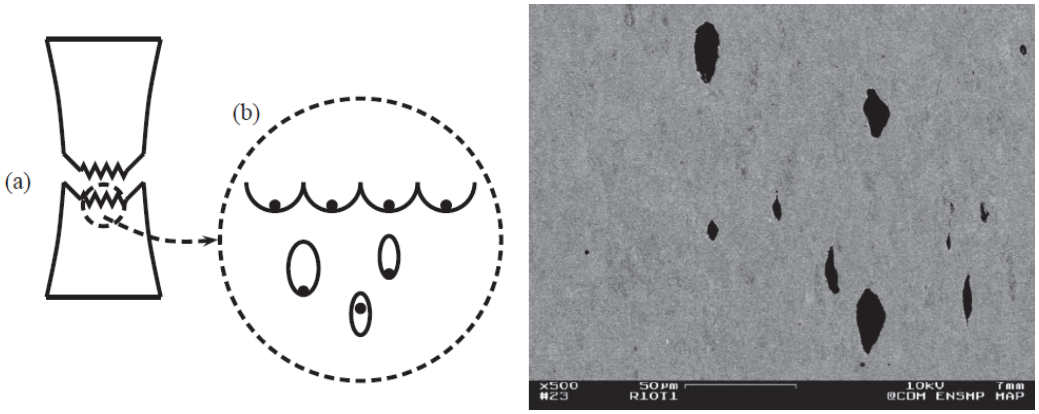

Figure 4.6. Voids positioned right under the fracture surface: scheme (a) [46] and SEM microphotograph of such voids (b) [47]

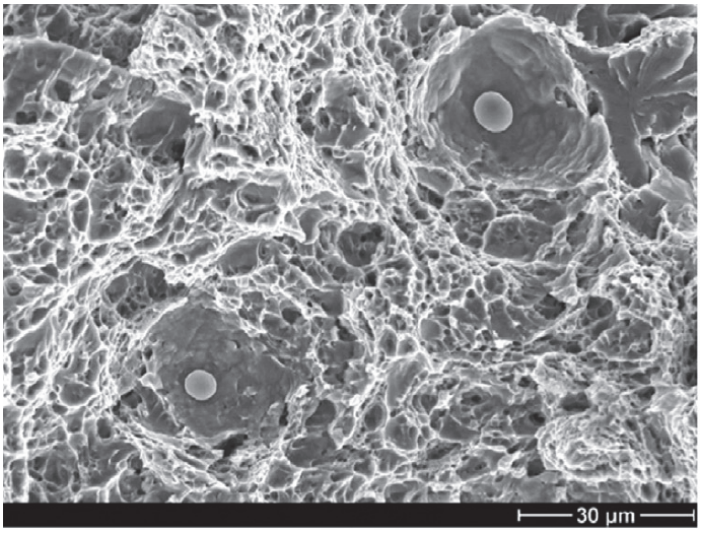

Figure 4.7. Fracture surface - 22NiMoCr3-7 [48]

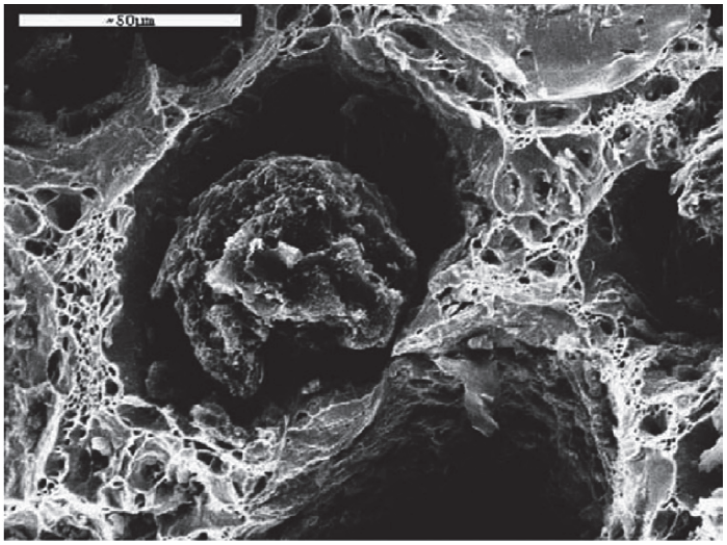

Figure 4.8. Fracture surface with dimples originating from primary and secondary voids in nodular cast iron [49]

4.3 Micromechanical models

As mentioned previously, ductile fracture of metallic materials exposed to external loading begins by formation of voids around different inclusions or second phase particles. Also, this process is accompanied by significant plastic deformation on the local level. The shapes and dimensions of particles/inclusions depends on the particular material; their shape can be regular (sphere, ellipsoid, etc.) or irregular [50,51].

There are several models which describe and predict the process of void nucleation; most of them have one thing in common - the void nucleation is predicted at the moment when critical stress is reached. This can happen either inside the inclusion (particle fracture) or at the boundary particle - matrix (debonding). For both mechanisms, the void is nucleated and starts to grow under the external loading. For non-spherical shapes of the particles, the position of the particle (in comparison to some characteristic direction, e.g. principal one) should be taken into account [51].

4.3.1 Void growth models

"According to the **uncoupled micromechanical** damage models, the damage parameter is calculated in the post-processing phase of the finite element (FE) analysis", [36]. Examples of the models which belong to this group are developed by: Rice and Tracey (with modification by Beremin group) [44,52], Huang [53], Chaouadi [54]. The first two mentioned models consider the same damage parameter - void growth ratio R/R_0, and its value is calculated in a post-processing procedure. The model developed in [54] considers the work necessary for local damage development.

4.3.2 Uncoupled approach - Rice-Tracey model

After the void is formed, its growth is affected by stress/strain distribution in its vicinity. Most studies have shown the key role of the stress triaxiality and plastic strain. This represents the basic premise of uncoupled approach to ductile fracture: behaviour of material is typically modelled by using von Mises plasticity (yielding criterion), i.e. damage does not change/influence the elastic-plastic deformation process.

Consideration of a single void (influence of other voids is neglected) lead to development of the Rice-Tracey micromechanical model [44,52]. The following text about this model is mostly based on [36].

$$\ln\left(\frac{R}{R_0}\right) = 0.283 \cdot \int_0^{\varepsilon_{eq}^p} \exp\left(\frac{3}{2}\frac{\sigma_m}{\sigma_{eq}}\right) d\varepsilon_{eq}^p \qquad (4.1)$$

Using the Rice-Tracey model and taking into account material hardening proposed by Beremin [52], critical void growth ratio $(R/R_0)_c$, corresponding to void coalescence, can be written as:

$$\ln\left(\frac{R}{R_0}\right)_c = \int_{\varepsilon_0=0}^{\varepsilon_c} 0.283 \cdot \exp\left(\frac{3}{2}\frac{\sigma_m}{\sigma_{eq}}\right) d\varepsilon_{eq}^p$$

where R stands for the actual mean void radius, R_0 is its initial value, σ_m/σ_{eq} represents stress triaxiality, and $d\varepsilon_{eq}^p$ is the equivalent plastic strain increment. The upper limit, σ_c, in the integral corresponds to the critical void growth ratio, i.e. when their coalescence initiates a crack in material.

According to this group of models, void presence does not significantly alter the behaviour of the material [55], and therefore the damage parameter is not represented in the yield criterion. The major advantage of such an approach may be simple numerical procedure and the possibility to use the results of a single FE calculation for many post-processing routines. However, the treatment of a void as totally isolated from other voids may be rather unrealistic in some cases, for example in materials containing large number of voids nucleated from larger and smaller particles.

In metallic materials, voids are often remote, and therefore it can be said that the change of stress and strain field around one void does not influence the neighbouring ones during the early stage of the void growth, [56].

After significant void growth, the next phase of ductile fracture is coalescence of voids, which leads to local instability of the material; this cannot be successfully captured by the models which consider an isolated void. In some studies, e.g. [57], the application of the void growth models is justified by declaring that the void growth is dominant phase of ductile fracture initiation (this work was performed on steel 22NiMoCr-3-7).

However, in more accurate analyses it is important to consider two remaining phases - void nucleation and coalescence.

4.3.3 Coupled approach – Gurson-Tvergaard-Needleman model – GTN

In the recent past, much more effort has been devoted to micromechanical models of the **coupled approach**, which incorporate the damage parameter into the constitutive equation. Therefore, damage development in the material also influences the yielding, which is not the case in uncoupled models. Also, the value of the damage parameter is calculated during each step/increment of the analysis.

In GTN model, nucleation is often taken into account by using the initial value of damage parameter, which corresponds to the larger or primary voids, and additionally by volume fraction of secondary voids formed around smaller particles under external loading. It should be noted that primary voids are assumed to exist even in the unloaded state, because they are formed around larger particles, which easily break or separate from the matrix material in early loading stages (i.e. at low external loads).

The models of coupled approach describe the material as porous; the existence of voids influences the distributions of mechanical quantities, and the most important in this case are the stress and strain. The Gurson yield criterion [58] essentially represents the extension of von Mises plasticity, with added influence of the existence of voids on material behaviour. The parameter which quantifies the damage is the void volume fraction or porosity *f*. "This variable is introduced into the expression for plastic potential; eq. (4.2) corresponds to one of the most-often used micromechanical models - GTN or Gurson-Tvergaard-Needleman model", [36]:

$$\phi = \frac{3S_{ij}S_{ij}}{2\sigma^2} + 2q_1 f^* \cosh\left(\frac{3q_2\sigma_m}{2\sigma}\right) - \left[1 + \left(q_1 f^*\right)^2\right] = 0 \tag{4.2}$$

σ is the current flow stress of the material matrix, σ_m is the mean stress, S_{ij} is the stress deviator, q_1 and q_2 constitutive parameters, and f^* is the damage function, or modified void volume fraction:

$$f^* = \begin{cases} f & \text{for } f \le f_c \\ f_c + K(f - f_c) & \text{for } f > f_c \end{cases}; \quad K = \frac{f_u^* - f_c}{f_F - f_c} \tag{4.3}$$

K is parameter that represents the loss of load-carrying capacity of the material (sudden drop of force at the force - diameter reduction diagram). A crucial parameter in this model and its modifications is the critical void volume fraction at void coalescence, denoted as f_c. The value of damage function at the moment of fracture is denoted as $f_u^* = 1/q_1$, while void volume fraction at final fracture is denoted as f_F.

4.3.4 Coupled approach - Complete Gurson model - CGM

There are several modifications of the original Gurson model, and probably the most important one is the GTN, shown in the previous section. Besides modifications of the yield criterion and the model itself, combinations of this model with other methods are also applied by some authors. For example, the GTN model is combined with cohesive zone technique by Scheider in [59].

A modification of the GTN model is applied in this thesis; this modification was proposed by Z.L. Zhang in [60], and it is known as the Complete Gurson model or CGM. The main focus in development of CGM was the treatment of the critical void volume fraction at the onset of coalescence f_c. In GTN, and most of other modifications of the original Gurson model, this value is a material parameter which has to be determined prior to analysis; two most often used ways are transferring from another geometry and unit cell analysis. In the CGM, criterion which defines the void coalescence onset is incorporated into the model itself, i.e. the f_c is calculated in each increment of the finite element analysis and is not a material parameter:

$$\frac{\sigma_1}{\sigma} > \left(\alpha\left(\frac{1}{r} - 1\right) + \frac{\beta}{\sqrt{r}} \right)\left(1 - \pi r^2\right) \tag{4.4}$$

where σ_1 is the maximum principal stress, α and β are constants initially fitted by Thomason [50] (α = 0.1 and β = 1.2), while Zhang et al. [60] proposed a linear dependence of α on hardening exponent n: $\alpha = 0.12+1.68n$. The void space ratio r in eq. (4.4) is defined as:

$$r = \sqrt[3]{\frac{3f}{4\pi} e^{\varepsilon_1+\varepsilon_2+\varepsilon_3}} \Bigg/ \left(\frac{\sqrt{e^{\varepsilon_2+\varepsilon_3}}}{2} \right) \tag{4.5}$$

ε_1, ε_2 and ε_3 are principal strains.

In the initial stage of ductile fracture of steel, the voids nucleate mainly around non-metallic inclusions. In this work, the initial porosity f_0 is therefore set equal to the volume fraction of non-metallic inclusions f_v.

Another parameter will be commented here - f_F or void volume fraction at final fracture, as very important for micromechanical analysis of the crack growth (i.e. ductile damage development) through the material. In general, it could be determined from microstructural observation of the fracture surfaces, but this is a very difficult and uncertain procedure. Zhang et al. [60] have shown, using the unit cell model, that f_F depends on f_0, and can be approximately calculated by Eq. (4.6). This value is applied in the CGM, and this means that failure occurs when the porosity in an integration point within a finite element reaches f_F.

$$f_F \approx 0.15 + 2 f_0 \tag{4.6}$$

The complete Gurson model is applied in this work through user material subroutine (created by Z.L. Zhang, based on [60]).

4.4 Crack growth modelling

4.4.1 Introduction

Modelling of the crack growth results in formation of a curve of resistance to fracture, which is, in case of ductile fracture, related to the growth of voids ahead of the current crack and their successive coupling with the tip.

The tear-breaking mechanism is characterised by a different distribution of stress and deformation for the crack that grows in relation to the stationary (initial) crack. This difference is related to geometry, since cracking tampering has a major impact on the stress of the stress condition in front of its top. Observing the cracks geometry at the beginning and at a later stage of its growth contributes to a more detailed understanding of this phenomenon.

Tip of a stationary crack in Incoloy 800 SGTs (Ni- Cr- Fe) is shown in the figure 4.9a and 4.9b, while the beginning of growth and stable growth are seen in the figure 4.10a and 4.10b.

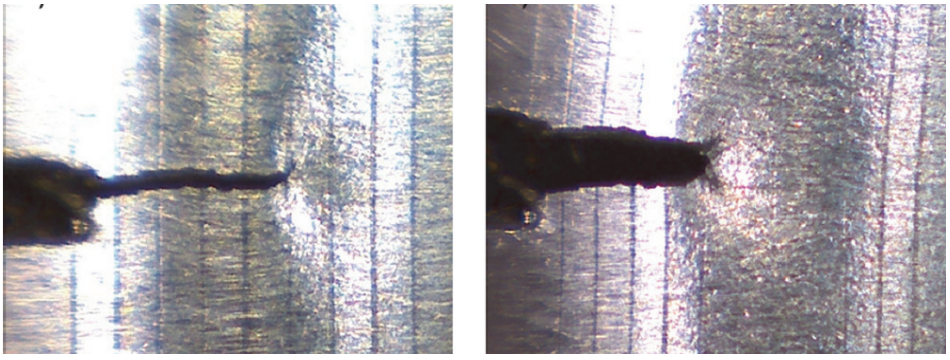

Figure 4.9. Incoloy 800 SGTs: opening of the crack (a) and blunting (b) [61]

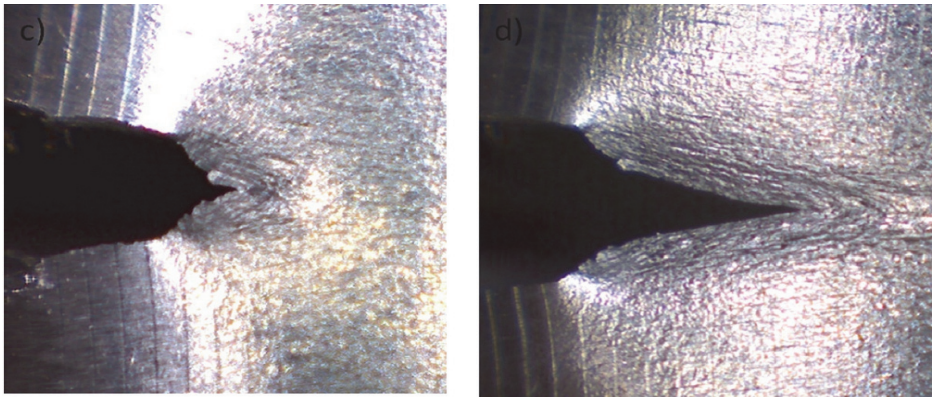

Figure 4.10. Incoloy 800 SGTs: onset of crack growth (a) and growth at a later stage (b) [61]

Figure 4.11 shows stable cracking by tearing mechanism in the aluminium alloy Al6056. Apart from cracks, there are inclusions that have significant influence on the crack development, as it grows up by joining the current top of the crack and voids in front of the tops created around the inclusions or particles in the material.

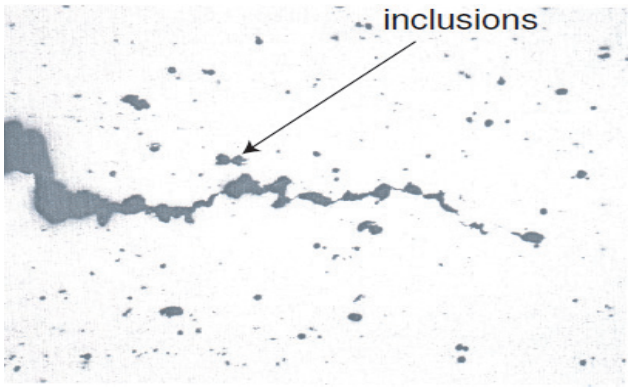

Figure 4.11. Ductile crack growth - Al6056 [62]

4.4.2 The techniques of crack growth modelling

By using the local approach models, it is possible to analyse stable ductile crack growth. For a proper description of this process, one should bear in mind that the damage mechanism requires connecting the model with the microstructure of the material.

4.4.2.1 Release nodes

If an uncoupled approach is applied, the crack growth is modelled using FEM and appropriate node release technique, figure 4.12. The value of the damage parameter in front of the crack, whose critical size is reached as a criterion for node release, is determined during the post-processing procedure.

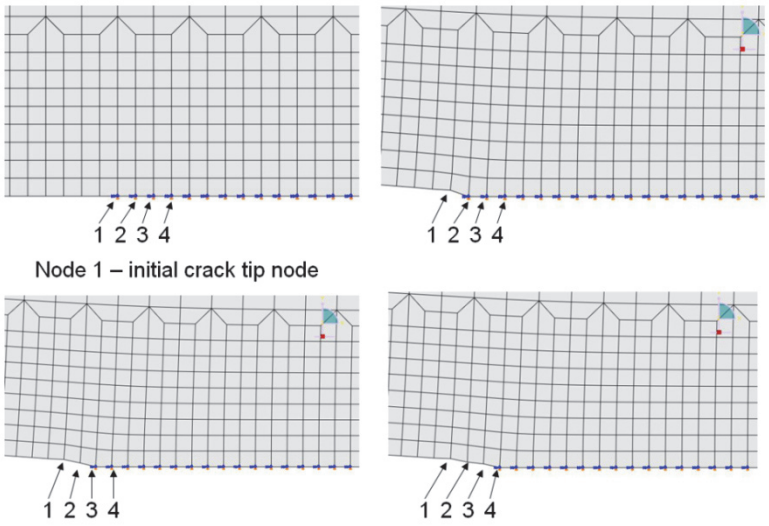

Figure 4.12. Node separation technique - the first three nodes in the ligament in front of the crack [63]

Separation of two nodes corresponds to an advance of the crack that is equal to the length of the edge of the finite element. This procedure is illustrated in figure 4.12. for the first three nodes in the ligament; when the nodes are separated, the boundary conditions of symmetry must be changed, which is also shown in this figure.

This procedure is used in combination with models of coupled approach, but also in a much more complex form for the so-called remeshing techniques, which involve re-forming the FE mesh after achieving the conditions for cracks growth [64-66].

4.4.2.2 Modelling the damage development in the ligament

Coupled approach models can be used to model the growth mechanism by tracking the damage parameter in the region ahead of the crack tip/front. By reaching the critical value f_c, the nodes are released during the FEM calculation, or a simplified procedure is applied with respect to the uncoupled approach - tracking the loss of material load carrying capacity.

Xia and Shih [67] and Gao et al. [68] in their works denoted the finite elements in the fracture zone as *computational cells*, and the dimensions of these elements depend on the microstructure of the material. In doing so, it is assumed that the damage occurs in a relatively narrow zone ahead of the crack, figure 4.13. Material behaviour in this zone (gray elements) is described by applying one of the coupled approach models. On the other hand, ductile damage is not considered in the remaining part of the structure; the material behaviour is often modelled by application of von Mises plasticity.

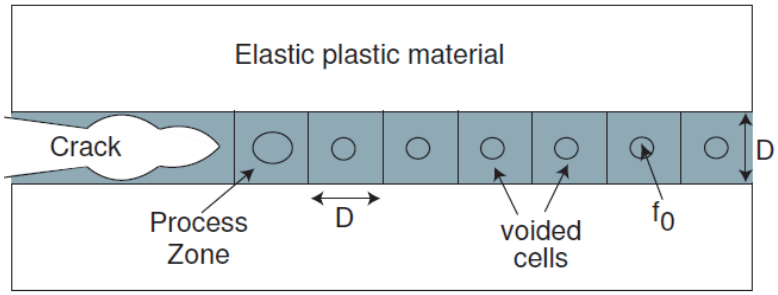

Figure 4.13. Schematic view of the zone in front of the cranial tip with calculating cells [62]

This approach is often used in a slightly altered form. Namely, instead of one layer of elements in which the development of the damage occurs, several layers are used or the whole FE model is considered using a micromechanical model [69-71]. If the cracks growth path is experimentally determined or predictable, the FE mesh is formed to obtain a model with as few elements as possible. Models in which the paths cannot be predicted are more complex and require a fine, regular mesh in areas where cracking can occur or increase, as shown in [69], where it is analyzed by a fracture of specimens made of steel X70. The change in the crack direction is shown in figure 4.14 in the example of a fusion zone in the laser welded joint of aluminium alloy 6000 from the base metal (BM) in the fusion zone (ZS).

In this Thesis, crack growth is modelled in the above manner, i.e. by using the CGM to assess the material behaviour in the entire volume of the structure. Figure 4.15 shows the appearance of predicted surface in a 3D model representing the PRNB specimen.

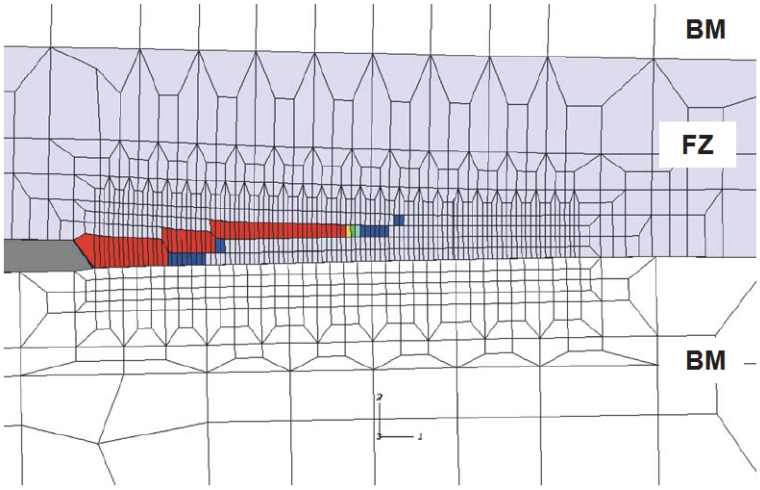

Figure 4.14. Alignment of the crack in the welded joint of the aluminium alloy 6000 - GTN model [69]

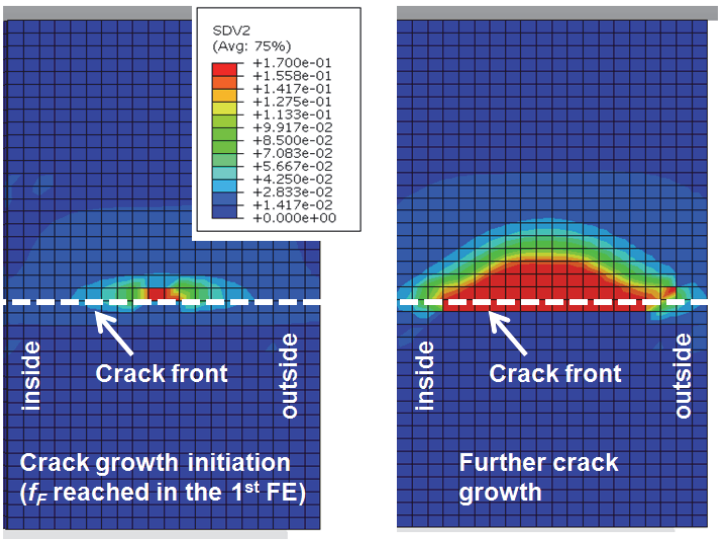

Figure 4.15. Crack growth in the 3D model of PRNB specimens

4.4.2.3 Modelling individual voids in the ligament

Unlike models from previous section, in which the influence of the voids is taken into account indirectly, through damage parameter (volume fraction of the voids), it is possible to consider crack growth and explicitly model the individual voids, with an exceptionally fine FE mesh in the ligaments between them. Tvergaard and Hutchinson

[72] and Tvergaard [73] modelled the voids in front of the cracks in the elastic-plastic material. All voids have the same initial radius R_0, and the distances between the centres of adjacent voids are equal and have the value X_0 (figure 4.16a), so that the initial width of the ligament is X_0 - $2R_0$. The deformed mesh is shown in (figure 4.16b). The initial content of such voids (in terms of volumes) in the ligament length X_0 is given by:

$$f_0 = \pi\left(\frac{R_0}{X_0}\right)^2$$

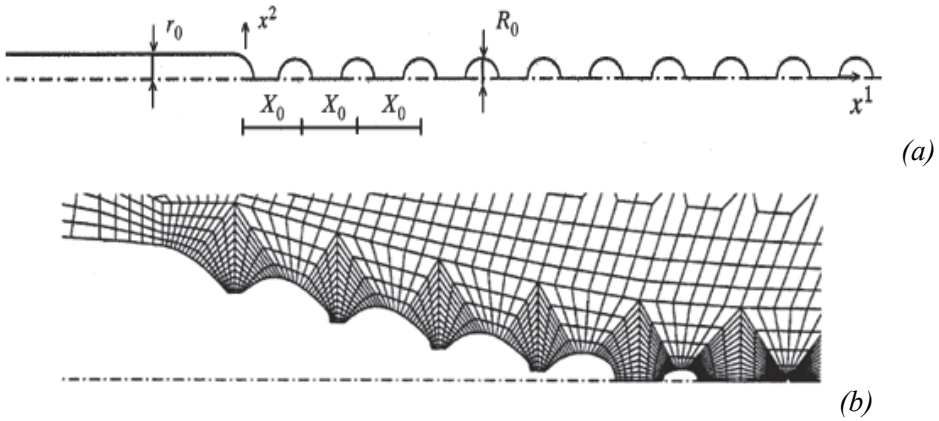

Figure 4.16. Model of the fracture zone with the initial cracks and voids: dimensions (a) and deformed FE mesh (b) [73]

In the model, the crack grows by releasing the of nodes in a ligament at the time when its width decreases to the value $b_c \cdot X_0$, where b_c is the coefficient whose values range from 0.15 to 0.6, given in detail in [34, 72, 73].

This technique is demanding from the point of view of processor time and computer resources, and can take into account a limited number of voids, which makes it difficult to apply in the analysis of real structures with cracks (especially in 3D calculations). However, the results allow a detailed consideration of the impact of distribution of voids on ductile fracture mechanism [74].

4.4.2.4 Cohesive zone model

Although not part of the local approach method, the cohesion zone technique, which is often used to model crack growth, will be briefly presented below. This model implies the use of the so-called cohesion surfaces, [75-77]. The behaviour of the area in which the damage and fracture occurs is modelled using the "Cohesion law", i.e. traction-

separation curves (figure 4.17). Its main features are the separation work J_0 and the highest stress value, which is often denoted as cohesive stress.

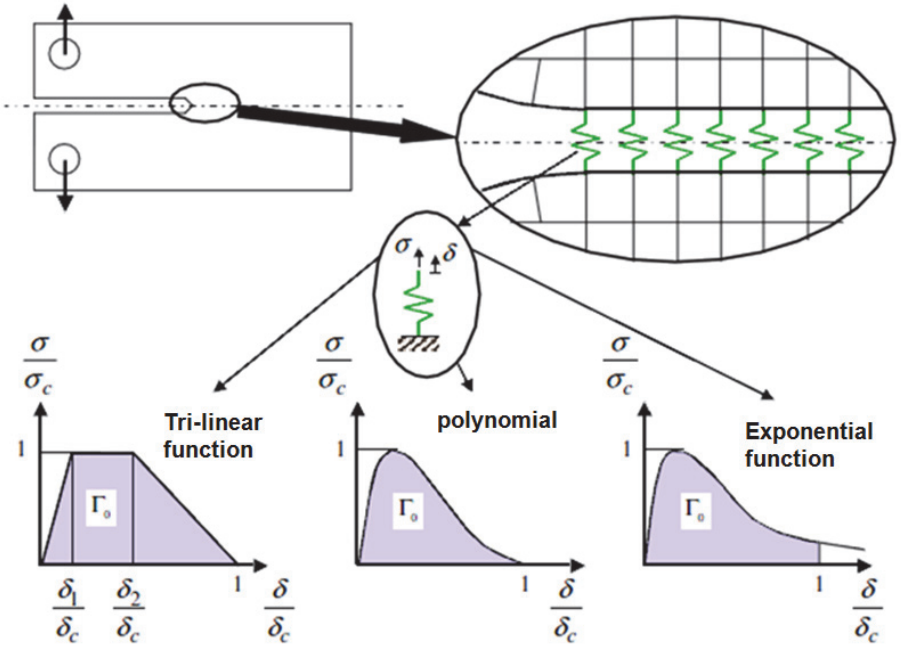

Figure 4.17. Cohesion zone model with three typical shapes of the traction - separation curve [78]

In the cohesion zone, the material in the area where crack growth is expected is modelled with cohesive elements, and remaining part of the considered body is modelled as elastic-plastic material. The crack growth is simulated by the interface elements, figure 4.18. Although on the left-hand side of this figure ductile fracture mechanism is shown, cohesion zone models can also be used to model other fracture mechanisms, using the appropriate strain dependence on deformation, [79]. In fact, the first application of this technique was for brittle fracture.

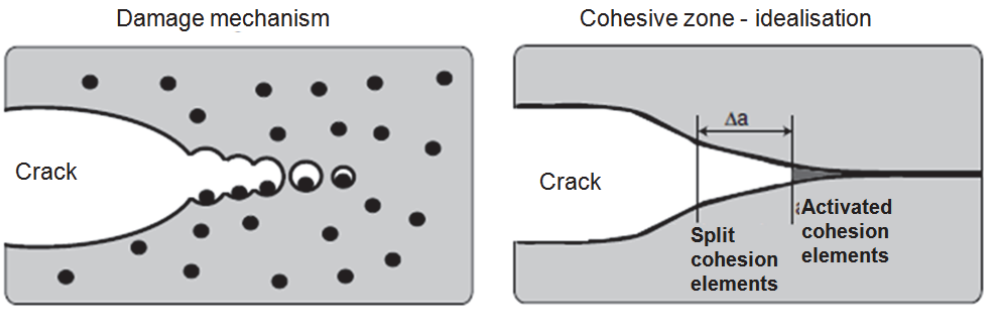

Figure 4.18. Cohesion zone for the modelling of ductile fracture - idealisation [62]

The cohesion elements have no thickness and have a dimension of 1 smaller than the rest of the model (1D for flat and 2D for spatial models). When the damage occurs, the elements in front of the cranks break open, and when the final failure they lose their load capacity.

The cohesion law can refer to a normal-to-crack direction (δ_N, form 1) and / or crack plane (δ_T, form 2 and 3).

Traction stress is another parameter which is used in the cohesive zone technique to model the advance of the crack. After the maximum value of σ_c is reached, cohesive elements start to fail (they lose the load bearing capacity).

The third parameter depends on the two above: cohesion energy J_0. This energy represents the work that is spent on the separation of cohesion elements and corresponds to the surface below the curve σ - δ.

$$J_0 = \int_{\delta}^{\delta_c} \sigma(\delta) d\,\delta = \alpha \sigma_c \delta_c$$

Where parameter α has a value between 0.5 and 1 for most metallic materials, [62].

Bearing in mind that the models of the cohesion zone can be classified into a group of phenomenological models, it is not possible to directly connect the shape of the dependence of the stress from the deformation to the fracture mechanism. Therefore, the form of this dependence is adopted; a few examples are shown in figure 4.17.

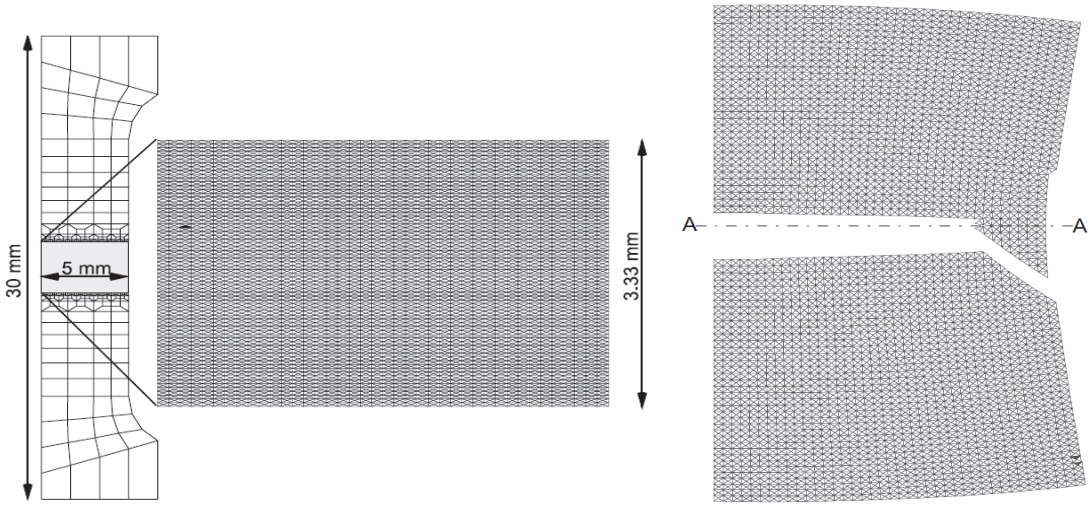

Figure 4.19. Model of a round tensile specimen - cohesion elements at all boundaries of the elements in the neck zone [80]

Since the cracks can only grow along the boundaries between the elements, the crack path must be known before the analysis. Otherwise, it is necessary to anticipate more possible directions of growth and define the cohesion elements along these lines, figure 4.19.

4.4.2.5 Combined models

The cohesion zone model in [59,81] was used in combination with Gurson's plastic yield criterion for crack growth modelling. The main goal of this approach was to overcome a deficiency related to the cohesion zone method; namely, unlike the Gurson model and its modifications, the failure criterion does not depend on the mean stress, which is very important for modelling the ductile fracture.

Also, an interesting combination is shown in [82], figure 4.20: in a three-dimensional model, zone around the crack front is modelled by explicitly taking into account the voids. Then, 2D cohesive elements are used to assess the fracture development, while material further from the crack front has properties defined through GTN model.

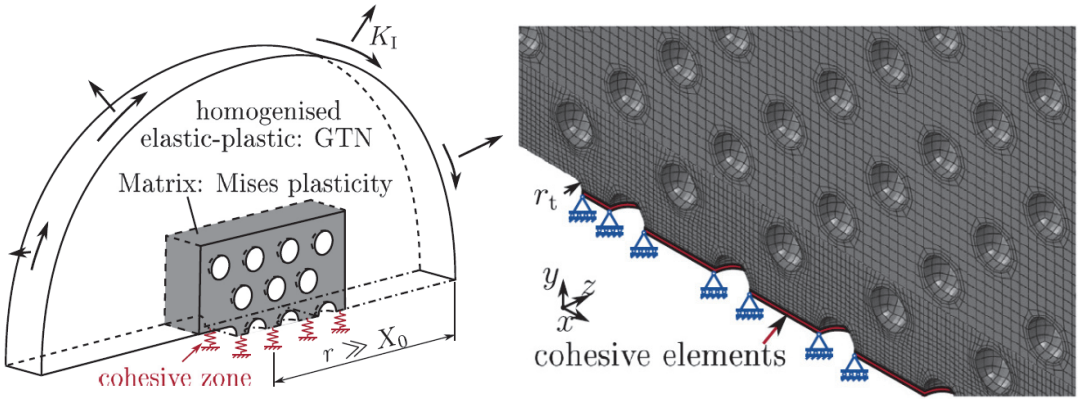

Figure 4.20. Model of a fracture zone - cohesion elements on all boundaries of the elements in the symmetry plane [82]

5. PIPELINE FRACTURE ASSESSMENT

5.1 Defects in metallic materials

5.1.1 Introduction

All metals contain defects, which can be found on different levels: from atomic scale in the crystal lattices to macroscopic ones which can occur during production, assembly or exploitation. With proper technological procedures and control, the second category may be significantly reduced (or even avoided) to such extent that they do not represent a danger to the structure. Defects or inhomogeneities in metallic materials can originate from complex chemical and physical reactions which occur in either molten or solid state. If they are introduced in early stages of production, it is important to prevent their development in the later stages of fabrication or during exploitation, which could lead do macroscopic damage and failure. In some cases, it is very difficult to avoid the occurrence of defects (for example, those which are typical for some processing procedure), and the key task is to decrease their presence and influence on material properties by applying proper control techniques. Some of the most often encountered ones are the pores, cracks, segregation, inclusions, second phase particles and blunt volumetric surface defects.

Besides defects, residual stresses which can occur in any stage of the life-cycle of a metallic structure affect the behaviour in exploitation and can decrease the integrity and load carrying capacity. Examples are residual stresses caused by solidification, welding, surface machining, etc.

The defects can be characterised by both origin and shape, but it can be said that all of them cause more or less intensive stress concentration. Planar defects, including cracks, are the most pronounced stress concentrators, i.e. they have the most significant jump or discontinuity in the stress field. On the other hand, the stress concentration caused by volumetric defects is less intensive, but the stress can also be increased because the load-carrying portion of the section is decreased. When the influence of the defects on

the material and structural behaviour is assessed, these are some important influential factors:

- Size (including distinguishing between 2D defects like cracks, and volumetric or 3D defects),
- Sharpness, or stress concentrator radius,
- Orientation in space, having in mind the load case to which the structure is exposed,
- Proximity to any joints or critical sections of a structural element.

5.1.2 Fabrication and service defects

As mentioned, fabrication and processing of metallic materials inevitably lead to the introduction of defects. The main types of fabrication defects are:

- Porosity,
- Segregation, caused mainly by non-uniform distribution of chemical elements in the material,
- Shrinkage and piping, occurrence caused by different cooling rates of the outer surfaces and inner surface,
- Inclusions, for example oxides, sulphides, etc.
- Surface defects, caused by the contact between the mold and the material that solidified.
- Embrittlement.

Also, subsequent operations after the material has been produced, such as cutting, heat treatment or joining, are also typical sources of defects.

The main causes of defect (damage) initiation in exploitation of a structure are fatigue (i.e. dynamic loading), high temperature, environmental impact, wear, cavitation and erosion. They can also act together; an example is fatigue corrosion, where dynamical loading and action of corrosive fluid lead to development of damage.

Occurrence of cracks is often considered as the most dangerous defect, due to the fact that they cause significant stress concentration and are difficult or impossible to reveal by simple visual inspection. As presented in chapter 3, fracture mechanics represents a

useful tool to determine the effect of sharp defects on integrity and load carrying capacity of a part, construction or machine. Of course, applied assessment procedure depends on the fracture mechanism; for example, in static conditions it can be brittle, cleavage, ductile or combination of these.

5.1.3 Causes of defects in pipes

There are many types of defects which can be found on pipes and other pipeline elements in different industrial branches. These defects can stem from several causes, but regardless of the cause they are a risk for the pipeline integrity. In the literature, there have been some attempts to group these defects or causes; one such division is shown in ASME B31.8S [83]:

1. “External corrosion,
2. Internal corrosion,
3. Stress-corrosion cracking,
4. Manufacturing defects,
5. Construction defects (welding/fabrication),
6. Equipment,
7. Third-party mechanical damage,
8. Incorrect operational procedure,
9. Weather and outside force.”

5.2 Specimens for fracture assessment of pipelines

Fracture toughness tests of metallic materials, which are conducted to determine the fracture resistance, are typically carried out with standard fracture mechanics specimens. Examples of such specimens are SENB and CT specimens, which are already mentioned in chapter 3. These standard specimens can sometimes be cut from the pipes, if the wall thickness is sufficient. An example is shown in this work (figures 5.1 and 6.19), where compact tensile (CT) specimens are cut from the pipe with dimensions Ø133x11 mm. If the pipe cross-section is sufficient, SENB specimen could also be extracted from the pipe, but it is more likely that it couldn’t be used for defects in axial direction.

More details on fracture mechanics testing is shown in the next chapter, while theoretical aspects of fracture mechanics is given in chapters 2 and 3.

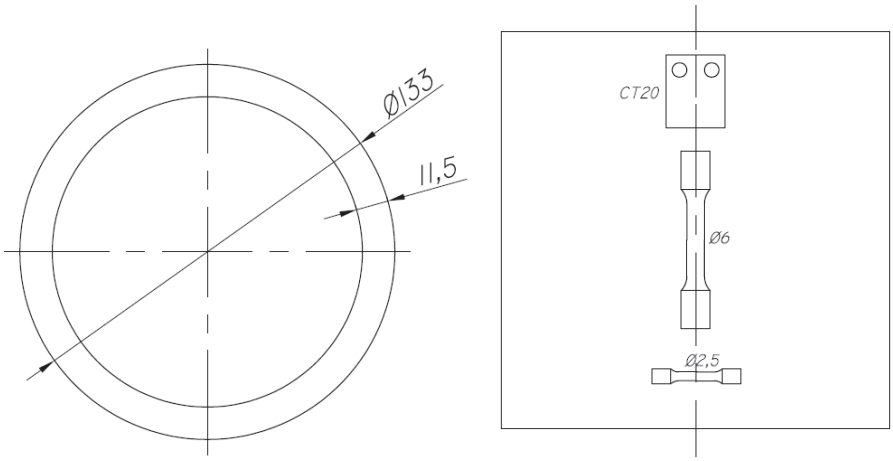

Figure 5.1. Cutting of compact tensile (CT) specimen and round tensile (RT) specimens from a pipe

5.2.1 Curved CT specimens

Both types of typically used standard fracture mechanics specimens (CT and SENB) are plane specimens. If assessment of fracture behaviour of thin-walled pipes and pipeline elements is required, the problem is to achieve the proper (plane) geometry for producing the fracture mechanics specimens. In the study [84], authors propose curved CT specimens (see figure 5.2), with an aim to achieve the stress/strain state similar to those in a pressurised pipe. This way, the forces which are transferred by the testing rig, figure 5.2, correspond to the hoop stresses, which are crucial for axial defects in cylindrical geometries. Unfortunately, the testing rig can be used for only one cross - sectional dimension of a pipe, which is certainly a downside of this specimen.

Two types of CT specimens were examined: the ones which were flattened before testing and the ones which had the original pipe curvature. It turned out that the difference between the straightened and curved specimen is very small, concerning their fracture resistance (toughness).

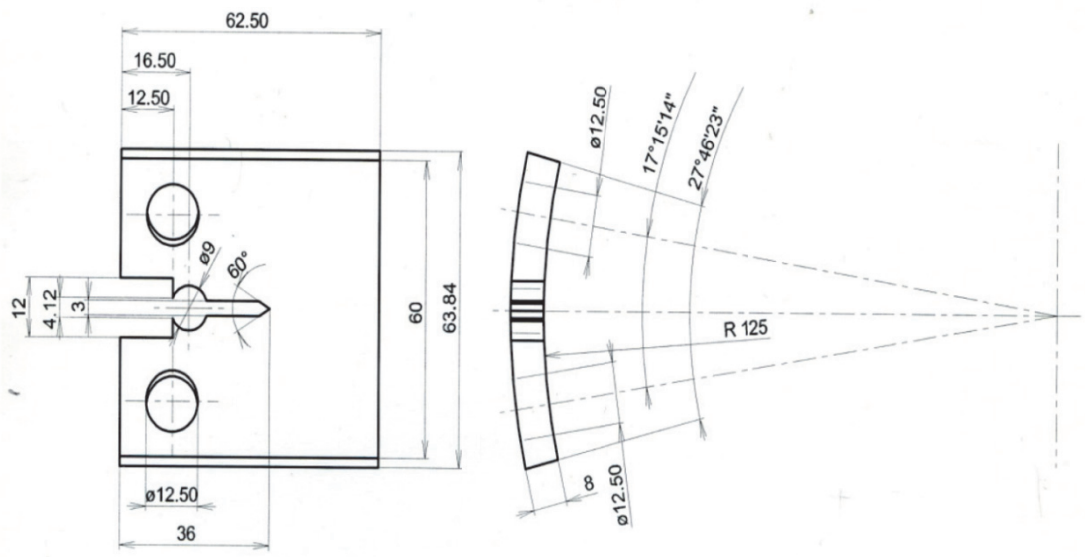

Figure 5.2. Curved CT specimen geometry [84]

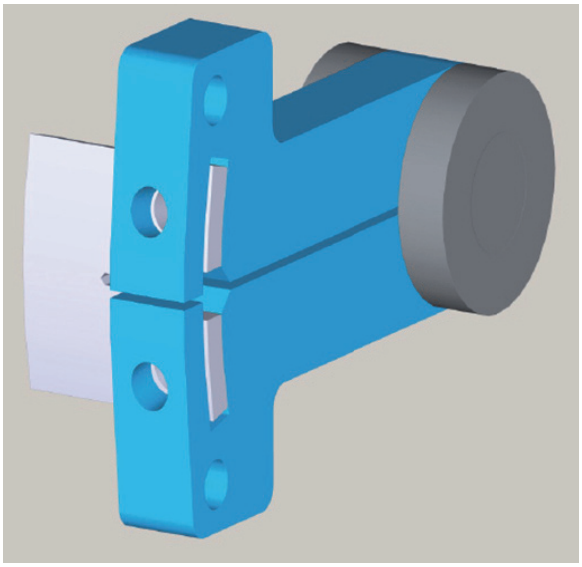

Figure 5.3. Testing rig for load transfer to a curved CT specimen [84]

The authors of [84] also applied the curved CT specimens in examination of the stress corrosion cracking.

Generally, it can be said that this is a specimen which can be useful for examining the influence of axial defects to integrity of pipelines, but a significant downside is the rig (figure 5.3) which is needed for testing and cannot accommodate different pipe sizes.

5.2.2 SENT methodology for pipeline applications

Application of SENT specimens (single edge notched tension) for pipeline applications has been the topic of several recent studies, including the consideration of the crack tip constraint, size effects and weld metal mismatch/misalignment. Namely, it was noticed that SENB specimen testing gives conservative estimates for some loading cases, which is why SENT specimen is often considered a good alternative, figure 5.4a [85- 87].

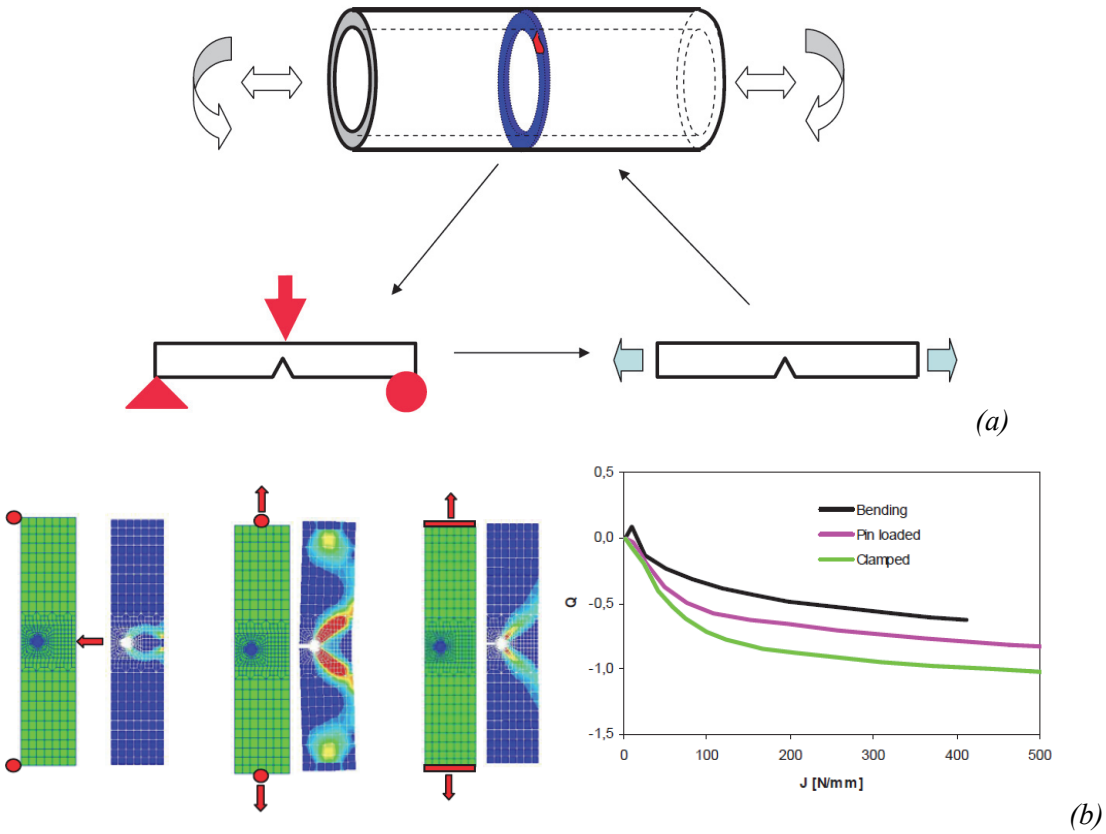

Figure 5.4. Specimens for pipeline fracture assessment: SENB and SENT (a) and deformation modes and crack tip constraints of the SENB and SENT specimen (b) [85]

Constraint levels in SENT specimen can be adjusted by the loading and boundary conditions (clamped versus pin-loaded), crack/depth ratios and the length of the specimens. Figure 5.4b shows the influence of loading modes (bending, clamped tension and pin-loaded tension) on the deformation modes and crack tip constraint (Q).

The authors of the paper [86] conducted an analysis of fracture behaviour of SENB and SENT specimen. Both geometries are presented in figure 5.5; of course, the crucial difference between them is in the loading conditions. In the same figure, the finite element mesh of the model, including a zoomed area at the symmetry line, is shown.

Figure 5.6 shows the comparison of SENT and SENB specimens when critical CTOD values are considered; the authors of [86] state these critical values after the crack has grown for Δa=0.5 mm. For both specimen types, specimen width (W) and ratio a/W are varied. When SENT specimens with small width (W=10 mm) are observed, CTOD values become less sensitive to the crack depth.

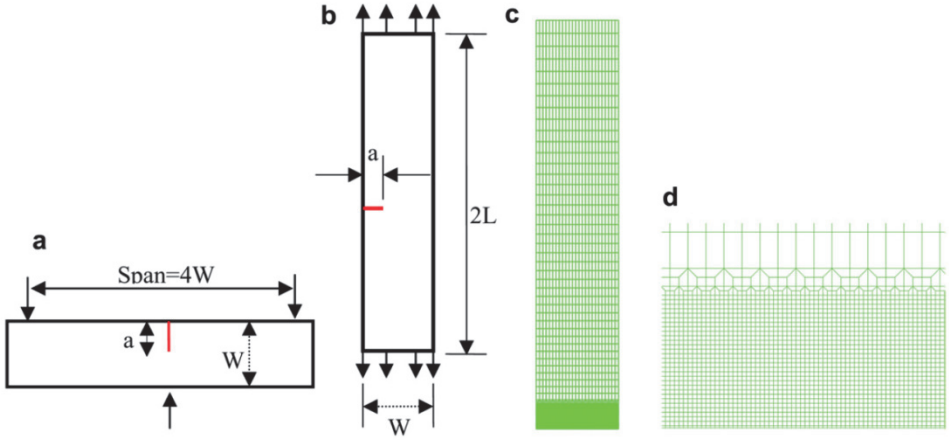

Figure 5.5. Geometries of SENB (a) and SENT specimen (b), FE mesh (c) and detail in the crack region (d) [86]

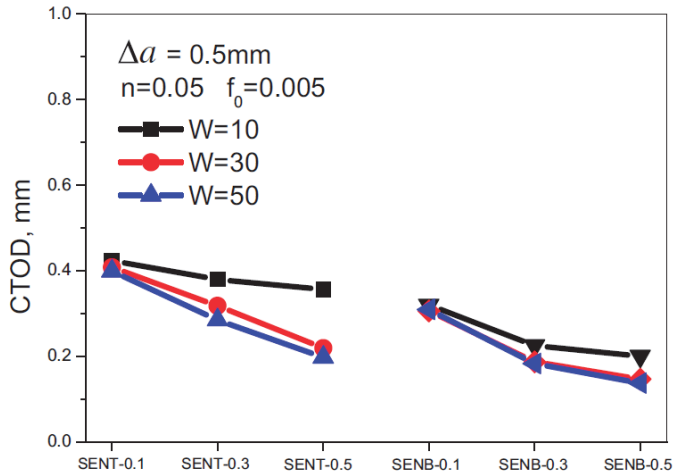

Figure 5.6. Influence of specimen width (W) and crack size (a/W) on critical CTOD [86]

A micromechanical study presented in [87] shows an assessment of ductile fracture behaviour of pipes, through the Complete Gurson model. The crack position was circumferential. The results obtained on pipes are then compared with the ones from tension and bending specimens with the same geometry (of both specimen and crack), see figure 5.5.

The pipe segment with a crack is shown in figure 5.7a, while figure 5.7b illustrates the relation between the axisymmetric geometry and full 3D pipe geometry with an internal crack. Of course, this 2D model represents the case when the entire profile is rotated around the symmetry axis, forming the 3D cylinder, i.e. pipe with a full circumferential crack. The SENT model has the same shape as the axisymmetric model from figure 5.7b, but it is analysed in plane strain conditions.

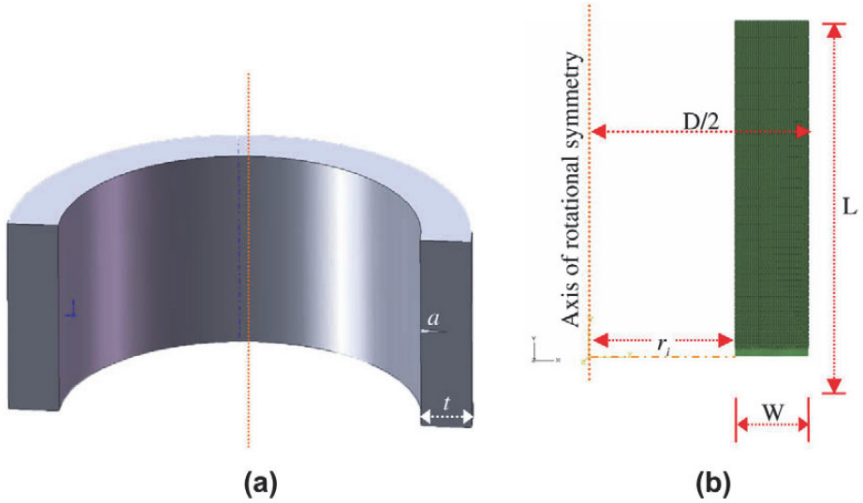

Figure 5.7. Geometry of the pre-cracked pipe (a) and axisymmetric model (b) [87]

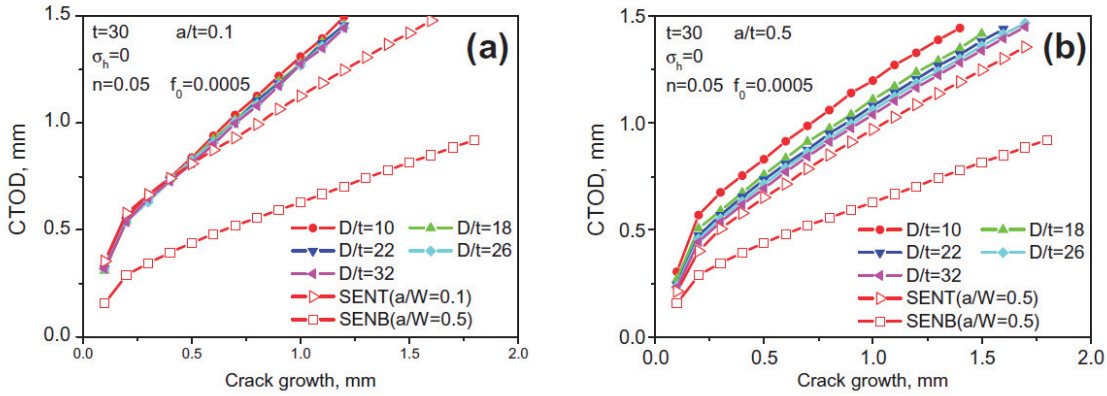

Figure 5.8. CTOD–Δa curves for internally cracked pipes with f_0 = 0.0005: a/t = 0.1(a), a/t = 0.5 (b) [87]

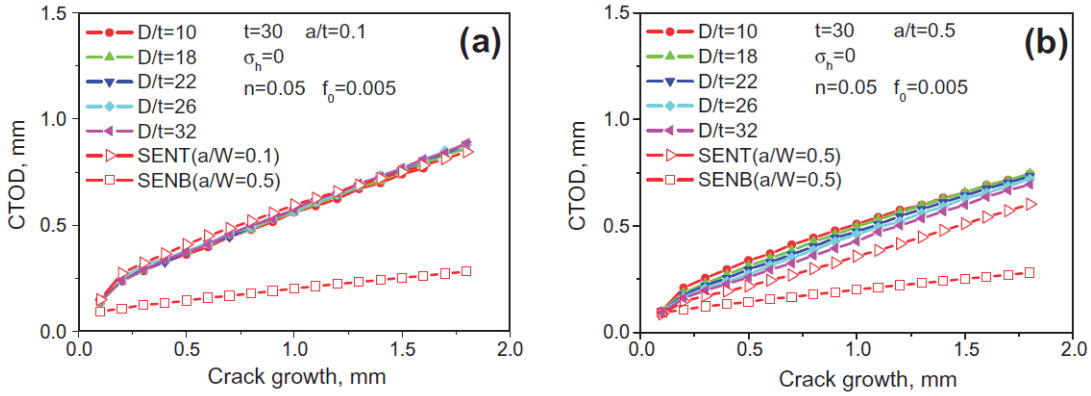

Figure 5.9. CTOD–Δa curves for internally cracked pipes with f_0 = 0.005: a/t = 0.1(a), a/t = 0.5 (b) [87]

Comparison of the fracture resistance curves obtained for pipe, SENT and SENB geometries is given in figures 5.8 and 5.9. The authors of [87] concluded that "*D*/*t*-ratio shows more significant effect for the pipes with deep internal circumferential cracks (*a*/*t* = 0.5) than that with shallow ones (*a*/*t* = 0.1)." Less pronounced effect of ratio *D*/*t* was also obtained for external cracks. As for the crack size *a*, has a low effect in the pipe geometries, and somewhat more pronounced for the SENT specimen.

The authors of [87] concluded that the SENT geometry is appropriate for fracture assessment in the circumferentially cracked pipes, i.e. that it is more adequate for this purpose than SENB specimen. However, this geometry is not convenient for axial cracks, which are critical for the pressurised pipes, i.e. those which have internal pressure as the dominant loading.

5.2.3 Compact pipe specimens

In [88,89], another geometry for fracture testing of pipes is proposed - tensile compact pipe (CP) specimen. According to measures (*D*=168.3 mm, *B*=18.3 mm), the pipes examined in these studies can be categorised as thick-walled, having in mind the ratio of the external and internal diameter which exceeds the value 1.2. Standard CT specimen was produced from the pipe; cutting scheme is shown in figure 5.10, (CT specimen thickness: 15.24 mm).

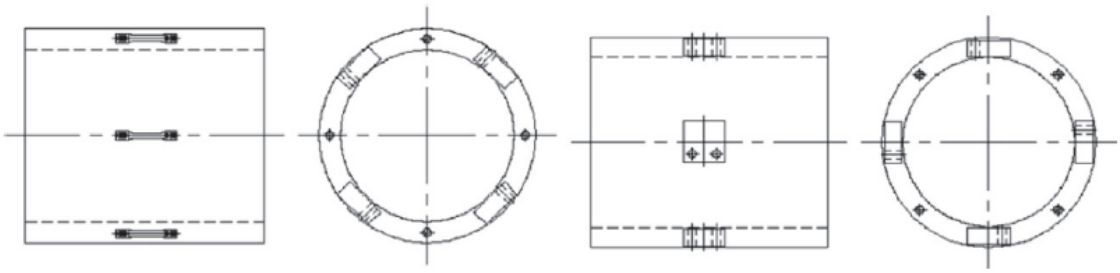

Figure 5.10. Specimen cutting scheme [89]

The specimen drawing is shown in figure 5.11. A downside of this geometry is visible immediately - additional levers have to be welded to each specimen in order to transfer loading.

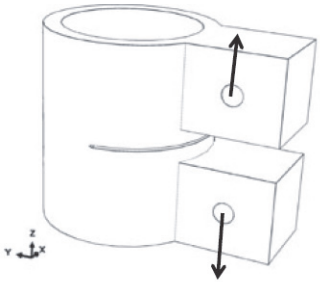

Figure 5.11. Compact pipe (CP) specimen with levers for load transfer ([88]

The FE mesh of the quarter-symmetry model is given in figure 5.12, of course, the model contains the lever, just like in figure 5.11.

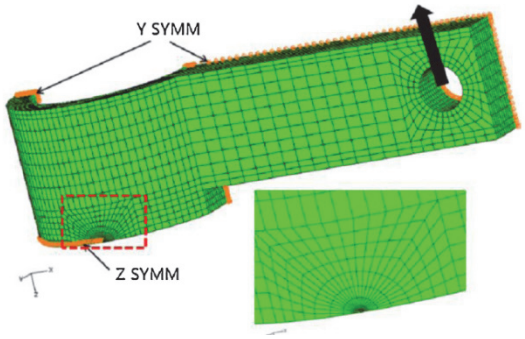

Figure 5.12. FE mesh - quarter-symmetry model of CP specimen [89]

Figure 5.13 contains the crack growth resistance of standard CT specimen and different pipe geometries (crack angle is varied on pipes). For larger crack growth values, there are significant differences among the curves corresponding to different pipe crack geometries. Also, the cracks in pipes experienced significantly larger growth in

comparison with CT specimen. For an initial crack growth of 2 mm, all *J*-R curves are rather similar.

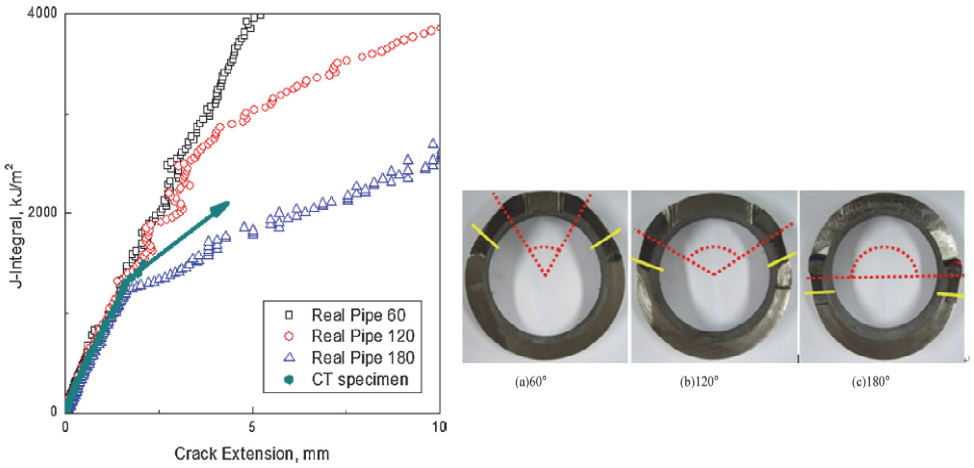

Figure 5.13. Fracture resistance curves - pipes and CT specimen; Different crack angles in pipes [89]

However, when Compact Pipe, CP, specimen is examined, similar crack lengths ad *J*-R curves are obtained when appropriate crack angle is prepared on the specimen. The authors of [89] stated that "tensile CP specimen can simulate various stress conditions if the lever length is controlled".

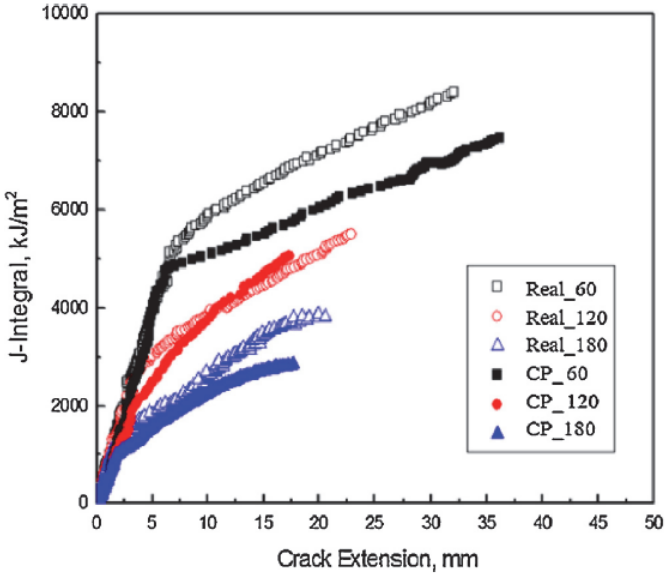

Figure 5.14. Fracture resistance curves - pipes and CP specimens [89]

In another work [88], the same geometry is applied for determination of the critical stretch zone width SZW. CP specimens had different external diameters (OD), while the wall thickness was fixed - 10 mm. The change of the critical value of SZW along the

specimen thickness, obtained by FE analysis, is considered, figure 5.15. Authors of [88] claim that these results correspond to the values obtained for the standard specimen, and also conclude that evaluation of the critical SZW can be independent on geometry if CP specimen is produced with a sufficient wall thickness.

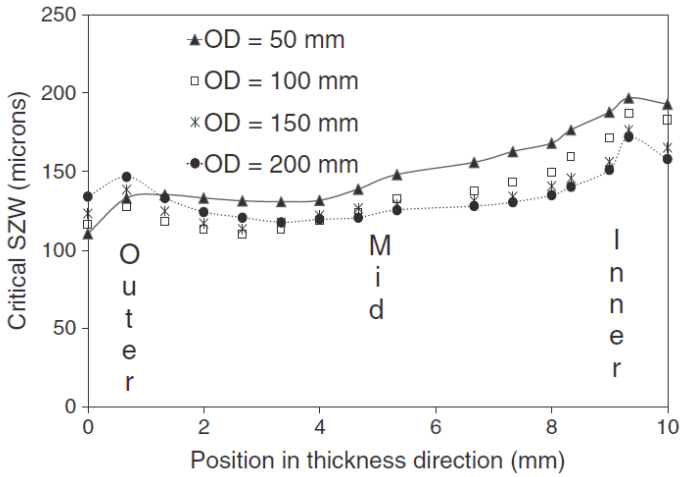

Figure 5.15. Change of the critical SZW along the wall thickness - compact pipe (CP) geometry [88]

5.2.4 Non-standard half- specimens

Some new proposals for non-standard specimens are also shown in [61,90]; all the geometries are shown in figures 5.16 and 5.17, with the most important measures. The first group are the specimens containing one or two circumferential cracks, figure 5.16a; the cracks were produced through the entire thickness (through-cracks). The loading type of these geometries was either tensile or bending, figure 5.16b-5.16d.

Significantly different procedure is proposed for the axial position of cracks, figure 5.17. Of course, all operations shown in the figure make the preparation of these specimens rather complex; however, it is emphasized in [61] that this production method preserves the thermo-mechanical conditions from the actual pipes.

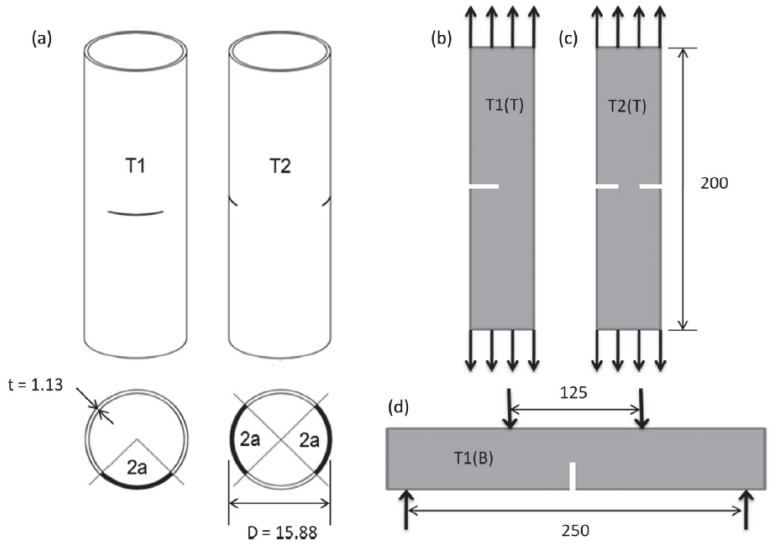

Figure 5.16. Specimens with circumferential crack/cracks (a) and load cases (b)-(d) [61]

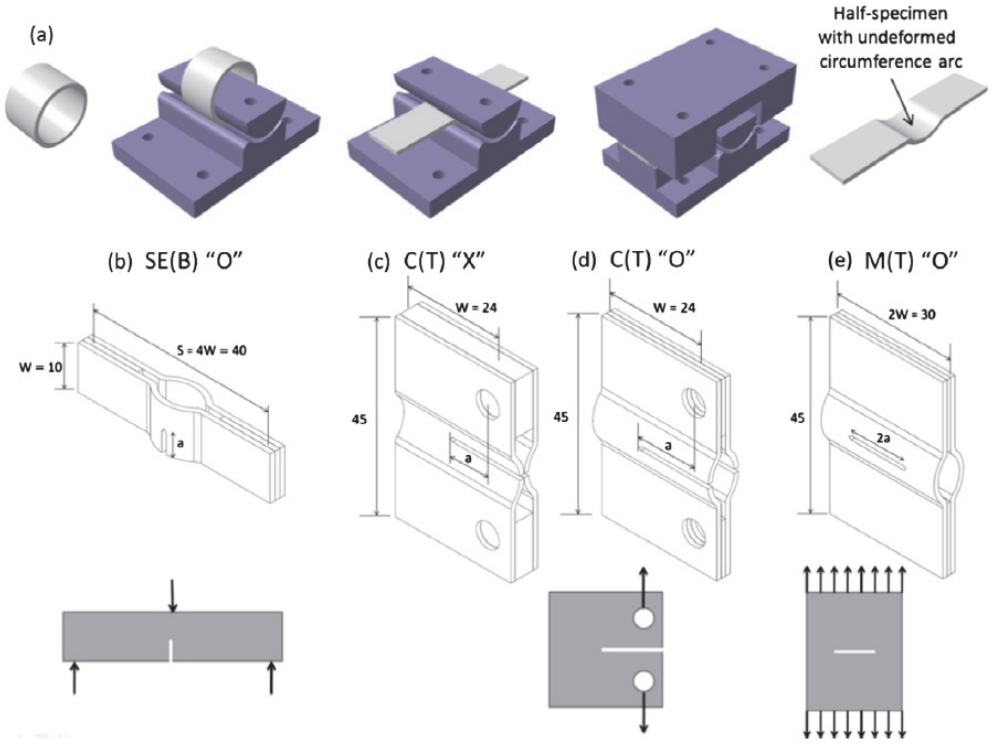

Figure 5.17. Specimen with longitudinal cracks: Fabrication method (a) and different specimen types (b)-(e) [61]

The authors of [61, 90] conclude that "the proposed specimens (exempting the M(T) O) permit a suitable experimental determination of fracture properties that can be used in structural integrity assessment". Fracture resistance curves obtained by testing the previously shown geometries are shown in figure 5.18; the trends and values are rather similar for all cases.

Although many crack geometries are included in this analysis, it is obvious that fabrication of the specimens with axial cracks is rather complex. For example, change of specimen diameter would require a new set of tools for fixing the pipe segment during the specimen fabrication.

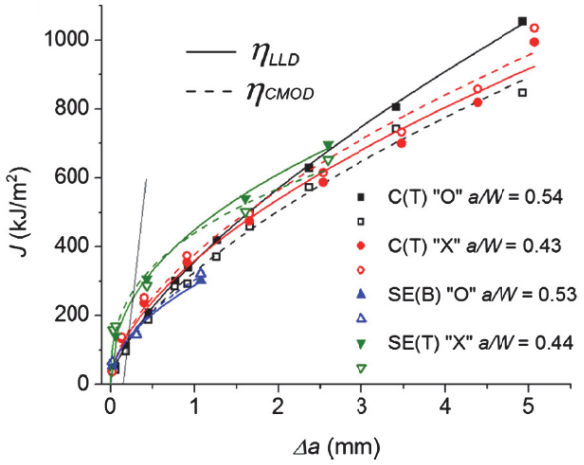

Figure 5.18. Crack resistance curves for longitudinal cracks - different specimen geometries [61]

5.2.5 Curved SENB specimens

In the study [91], the authors evaluated and compared the fracture resistance by cutting standard CT and non-standard curved SENB specimens from the pipes, figure 5.19. The fracture of the longitudinal seam weld of an API 5L X52 is analysed in this work. Of course, this procedure could also be applied to the base metal of the seam pipe, or the seamless pipe.

The fracture toughness in CR (circumferential-radial) direction was around 25% lower in comparison with CL (circumferential-longitudinal) direction; averaged values of K_{Ic} from 3 specimens are given in table 5.1. Besides introducing this new geometry for fracture testing in this work, the authors of [91] discussed the difference between the two directions and between different specimen geometries. They attribute the difference to the microconstituent distribution in the seam zones (ferrite/acicular ferrite) - in CR direction, the crack propagated mainly in acicular ferrite areas, with pronounced cleavage influence. Additionally, it is observed that the porosity is different in two directions, also favouring the crack growth in CR direction.

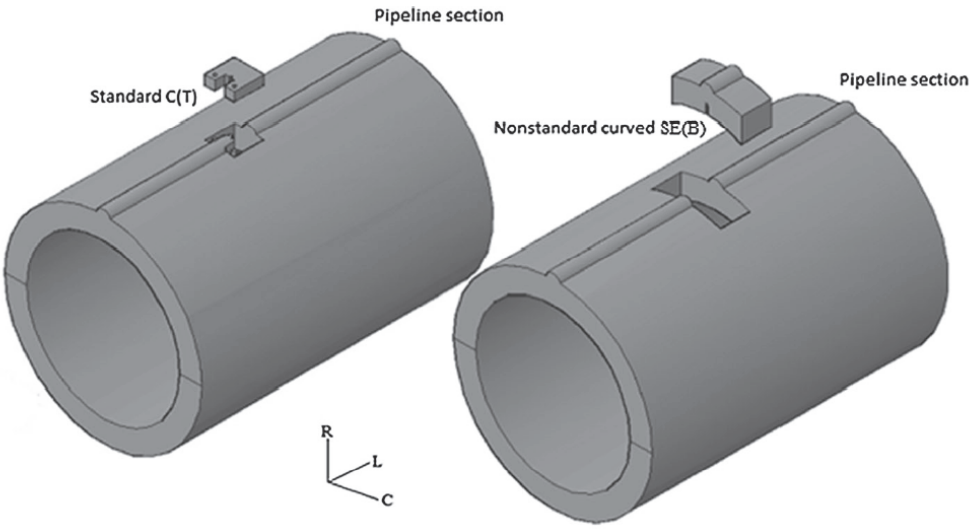

Figure 5.19. Specimens [91]

Table 5.1. Fracture toughness of the weld (seam) - CL and CR direction [91]

Specimen	Test direction	K_{IC} (MPa$\sqrt{m}$)	Standard deviation (MPa$\sqrt{m}$)
C(T)	CL	75.43	3.22
Nonstandard curved SE(B)	CR	56.29	2.93

6. MATERIALS AND METHODS

In this chapter, basic data about the experimental and numerical methods used in this work are given. Also, preparation of specimens for material testing, as well as testing procedures, is considered.

6.1 Tested materials

The first material which is used for examination of the pipe-ring specimens is actually not a pipeline material at all. The specimens were cut from a plate of the high-strength low alloyed steel, as shown in figure 6.1. The tested material is a micro alloyed high strength steel - grade HT50, with commercial mark NIOMOL 490K (producer - Železarna Jesenice, Slovenia). Chemical composition of the material is shown in Table 6.1; based on these properties, it is comparable with S460 steel (according to EN 10025-6 standard).

The idea of such approach is comparison of failure conditions in standard (SENB) and PRNB geometries with the same loading mode (bending). The work is carried out on the specimens cut from a plate in order to ensure the same material state for all of them. Another reason for selection of plate geometry is possibility to select the size of each type of specimen, which is not always possible when pipes are concerned.

Specimens produced from NIOMOL 490K steel were experimentally examined in the thesis [92], while in this work their fracture will be analysed by using the micromechanical model.

Table 6.1. Chemical composition of NIOMOL 490K steel, weight %

C	Si	Mn	P	S	Cr	Ni	Mo
0.123	0.33	0.56	0.003	0.002	0.57	0.13	0.34

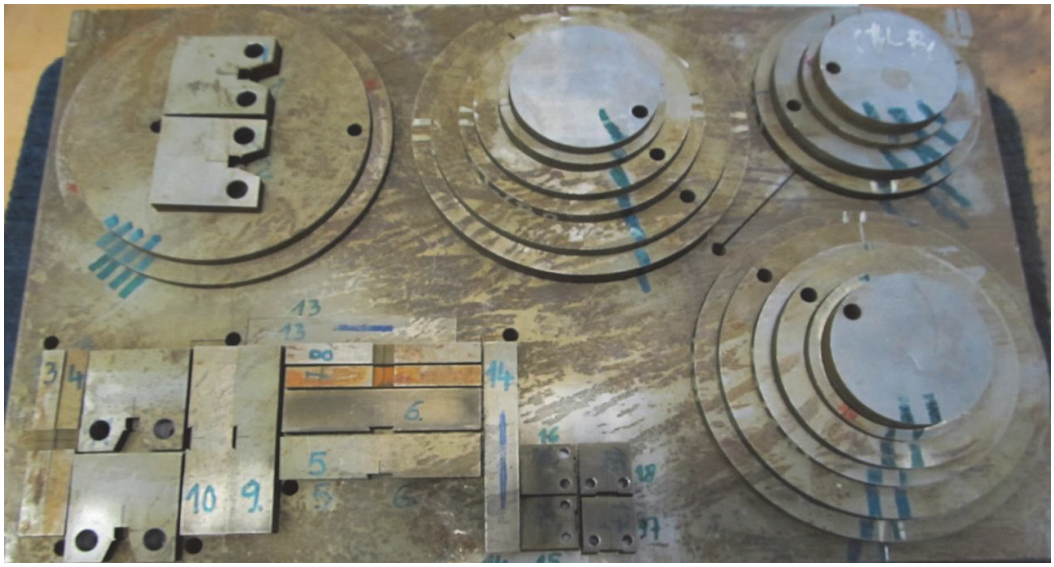

Figure 6.1. Cutting of different specimens from a steel plate [92]

Another group of examined specimens was prepared from actual seam and seamless pipes for high-pressure application, with different radius, wall thickness and other important geometry parameters. Figure 6.2 shows the segments cut from the pipes, prepared for producing (cutting) of the specimens. Examination of thin-walled pipes is emphasised, having in mind that rings cut from NIOMOL plate involved relatively high thicknesses of all ring specimens (although they were still thin walled, having ratio of the external to the internal diameter was around 1.13). Another important reason for analysis of fracture in thin-walled pipes is the fact that it is rather difficult to fabricate standard fracture mechanics specimens from them.

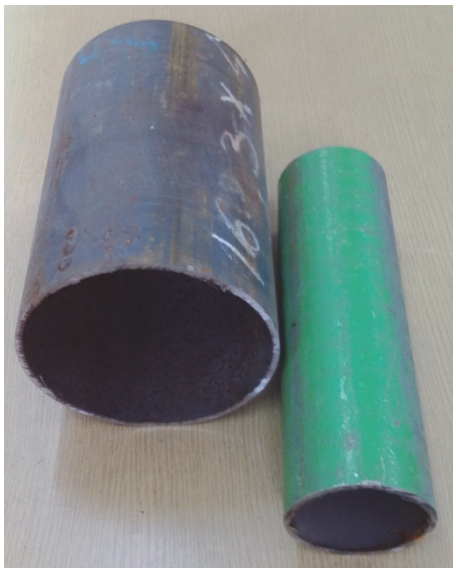

Figure 6.2. Pipe segments with different diameter - prepared for cutting of specimens

Two materials are considered: P235TR1 and P235GH. They are similar by the standard required properties, and the most important difference is the fact that the one denoted as GH has guaranteed mechanical properties on elevated temperature, due to its use for steam lines.

The pipe materials are non-alloy steel tubes for pressure purposes - grades P235TR1 and P235GH (according to EN 10216-1 and 10216-2 standards). Chemical compositions are shown in table 6.2; these are the requirements from the standard. Actual values for different pipes differed slightly, but all of them satisfy the standard requirements.

Table 6.2. Chemical composition of the pipe materials - P235TR1 and P235GH, weight %

	C [%]	Mn [%]	S [%]	P [%]	Si [%]	Ni [%]	Cr [%]	Mo [%]	Cu [%]	Al [%]
P235TR1	max 0.16	max 1.2	max. 0.02	max 0.025	max. 0.35	max. 0.3	max. 0.3	max. 0.08	max. 0.3	
P235GH	max 0.16	0.4-1.2	max. 0.025	max 0.03	max. 0.35	max. 0.3	max. 0.3	max. 0.08	max. 0.3	min. 0.02

6.2 Experimental methods

6.2.1 Hardness

Hardness is typically considered as the resistance to penetration of a solid body made from another material. Measurement of hardness can reveal whether the material is appropriate for the intended application [93]. Further, it is possible to some extent to correlate the results of the hardness testing to some mechanical properties, including strength and brittleness of the material. Such correlations have made the hardness testing an often used technique in material selection and control procedures.

Table 6.3. First appearance of hardness measurement procedures [94]

Test method	Germany	UK	USA	France	ISO	Europe
Brinell (1900)	1942	1937	1924	1946	1981	1955
Rockwell (1919)	1942	1940	1932	1946	1986	1955
Vickers (1925)	1940	1931	1952	1946	1982	1955
Knoop (1939)			1969		1993	

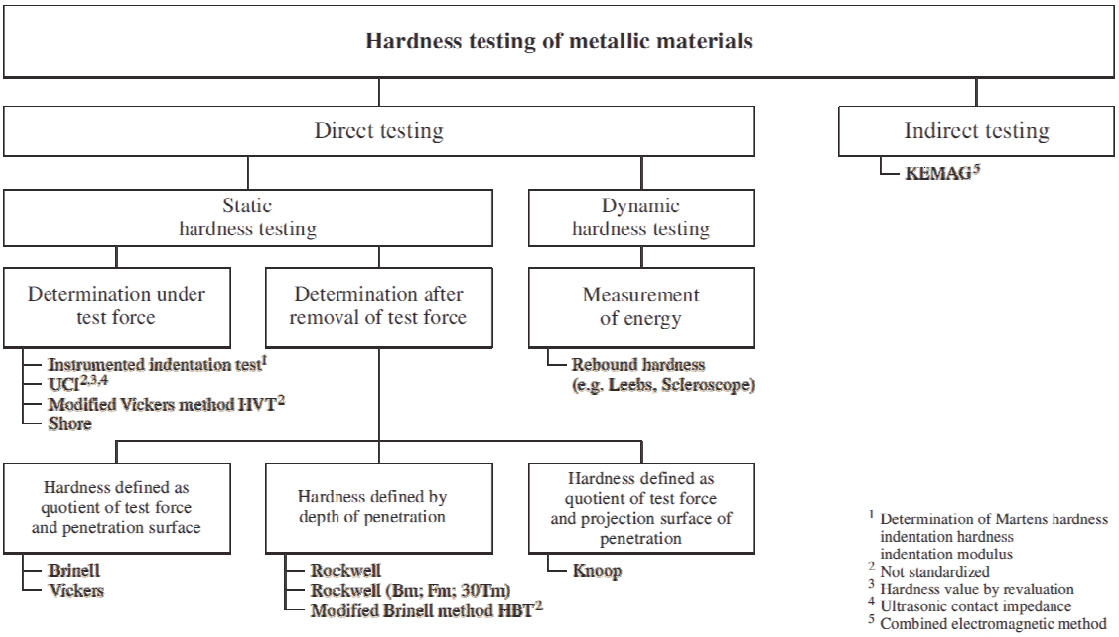

Figure 6.3. Hardness testing methods [94]

Hardness testing has a long history of use, see table 6.3, and it found its application on different material groups. It is fairly simple and inexpensive, and results in minimum damage to the material surface, but the obtained results depend on the measurement system. Therefore, it requires calibration procedures which lead to the hardness scales for practical application. Crucial data regarding the testing are:

1. Measurement technique,
2. Calibration of testing equipment,
3. Testing of the reference samples.

Brinell hardness test is established a long time ago, in 1900, but several other methods were also introduced since then, with the aim to improve the testing for different applications. It is advantageous for materials with rough surface, due to the fact that the loads are relatively high, in comparison with the other methods. The measurement scheme is shown in figure 6.4; it should be noted that the dimension in the surface plane is measured, i.e. diameter of the indentation.

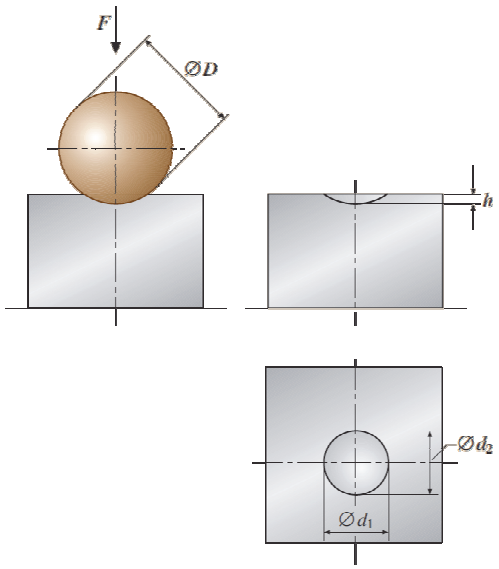

Figure 6.4. Brinell testing

Because the indentation ball is so much larger than indenters in other testing methods, hardness values derived from the test provide a more representative average values. It is characterised by low testing rates, and leaves a large indentation on the surface of metallic materials.

As a less destructive testing technique, Rockwell test decreases the influence of mechanical imperfections. The indenter is a tungsten carbide ball or a sphero-conical diamond indenter. The testing itself can be split into two stages: applying the pre-load (with the aim to decrease the effect of the surface finish) and subsequently the main load. The main load is kept during a certain time period to allow for elastic recovery, and then released, returning to the pre-load value. A significant difference in comparison with the Brinell method is measurement of the indentation depth, instead of the size in the surface plane.

The Vickers test uses the pyramid shape of the indenter, figure 6.5. The shape of the pyramid base is square, while the angle between the faces is 136°. The measurement result is the diagonal d of the indentation; it is calculated as the average of the two diagonals d_1 and d_1, figure 6.5, measured after the removal of the loading.

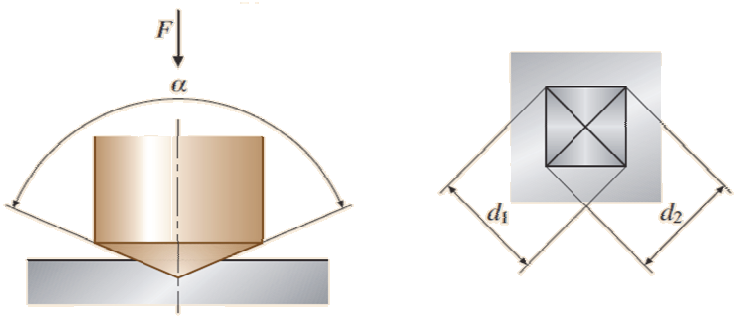

Figure 6.5. Vickers testing

Vickers testing is characterised by lower forces and higher accuracy in comparison with the Brinell method. It can even be applied on small samples, plates with low thickness, coatings, etc. It can even be used to determine the hardness of the microstructural constituents, like ferrite, austenite, etc.

However, Vickers testing also has some disadvantages, some of which are relatively high effort for surface preparation and possible dependence of results on the surface state, sensitivity to effects of vibration (for low forces) and to some extent variation of results depending on the person who analyses the microscope image.

Figure 6.6 shows the schemes for hardness measurement on seam and seamless pipes. Of course, the welded joint zone should be included in examination on seam pipes. Examples of specimens from two seam pipes and one seamless pipe are given; the lines represent the positions of the measurement points. The samples are prepared by etching in nital solution. Figures 6.7 and 6.8 show the pieces cut from the pipes and subsequently used for fabrication of the final samples.

Device: Buehler Microindentation Tester - Micromet 5101;

Loading: 1000 gf (9807 mN);

Indentation time: 15 s;

Hardness determination, Vickers method: $HV = 0.1891 \cdot F/d^2$; F [N], d [mm].

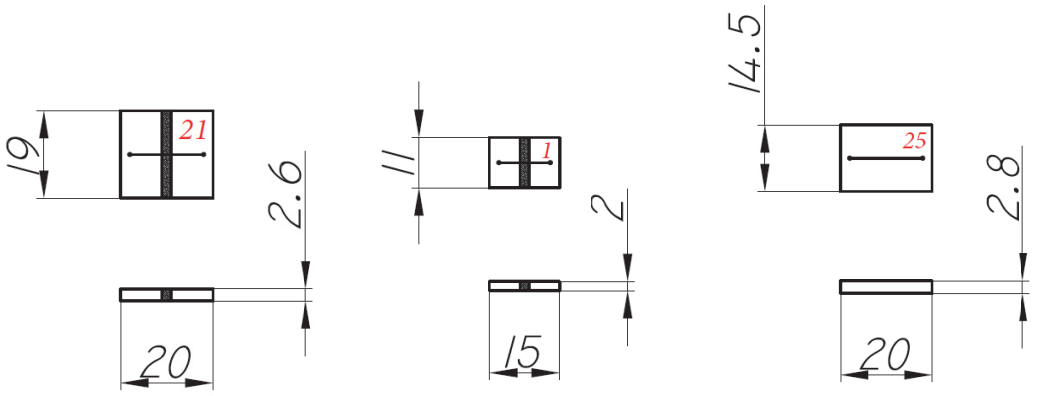

Figure 6.6. Samples for hardness measurements cut from the seam and seamless pipes

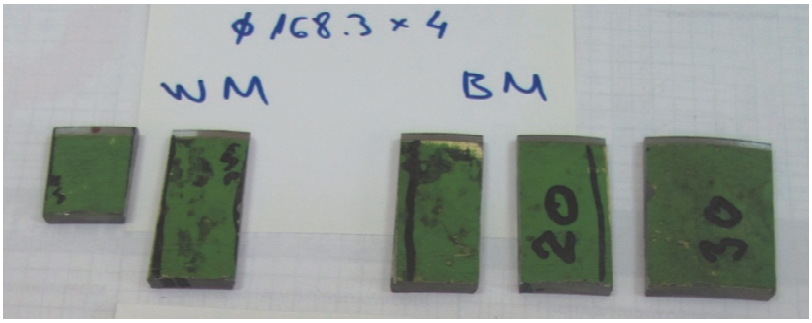

Figure 6.7. Cut samples for hardness testing - seam pipes

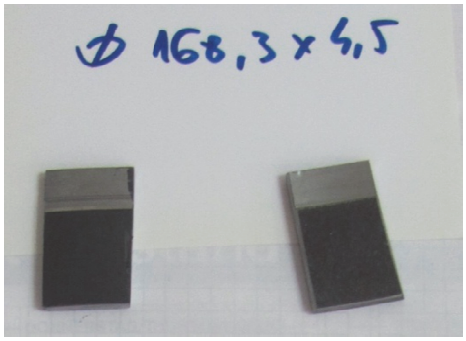

Figure 6.8. Cut samples for hardness testing - seamless pipes

6.2.2 Quantitative microstructural analysis

The volume fraction of non-metallic inclusions f_v in the examined materials is determined by quantitative microstructural analysis, based on the surface fraction of detected inclusions A_A, obtained by optical microscopy [95]:

$$f_v = A_A = \frac{A_i}{A_T}$$

in the previous expression A_i represents the area of inclusions, while A_T is area of the measurement field. Volume fraction f_v is calculated as the mean value for all measurement fields, according to ASTM E1245 standard and [95].

For determining the mean free path between non-metallic inclusions λ in accordance with ASTM E1245 standard, five measurement lines are defined in each measurement field, and the number of interceptions of inclusions per measurement line unit, N_L, is determined. The mean free path is mean edge-to-edge distance between inclusions:

$$\lambda = \frac{1 - A_A}{N_L}$$

The final value of λ is obtained as the mean value for all measurement fields.

Samples for quantitative microstructural analysis of the seamless and seam pipe material are shown in figure 6.9. The samples are prepared for testing by polishing.

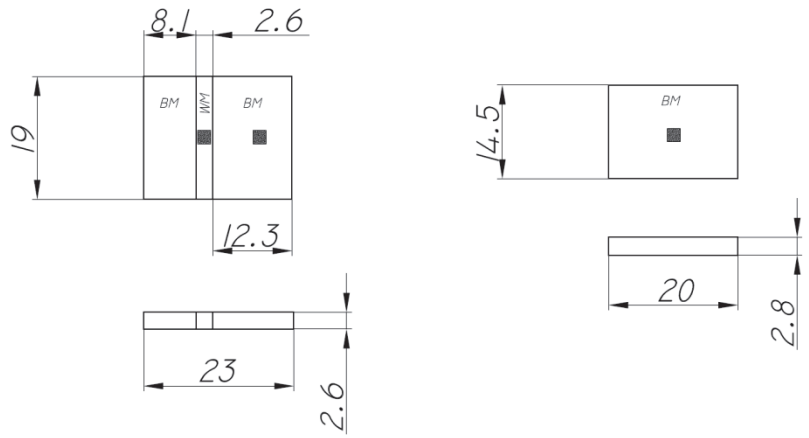

Figure 6.9. Samples from quantitative microstructural analysis from a seam and seamless pipe

6.2.3 Tensile testing

Tensile testing of the specimens enables determination of several material properties, including the modulus of elasticity, upper/lower yield strength (or conventional yield strength, if the material does not exhibit the Lüders plateau on the stress-strain curve), tensile strength, ductility and exponent of hardening. Since mentioned quantities can be influenced by testing temperature and loading rate, tensile testing can also be used to determine this dependence.

Figure 6.10. Geometries of tensile specimens [96]

During the testing, the force and displacement of a gauge length attached to the specimen are measured, which leads to the corresponding dependence (curve). Subsequently, these data are used to obtain the stress-strain curve.

Gauge length (ΔL) can be measured by using the strain gauges, or, some non-contact method such as stereometry can be used (this will be considered further in this chapter). Nominal stress and strain (sometimes also denoted as engineering ones) are defined as:

$$\sigma_n = F/A_0$$

$$e = \Delta L/L_0$$

in this expression, A_0 and L_0 are initial measurement (gauge) length on the specimen and its cross-section area, respectively.

Some of the parameters which can be used to assess the ductility of the material based on the tensile test are uniform elongation (before strain localisation by necking, figure 6.11b) and total elongation after fracture, figure 6.11c. Also, decrease of the cross-section of the specimen can be used as a measure, which is a way to avoid the dependence on the gauge length L_0; decrease of area from A_0 to A_f is considered instead.

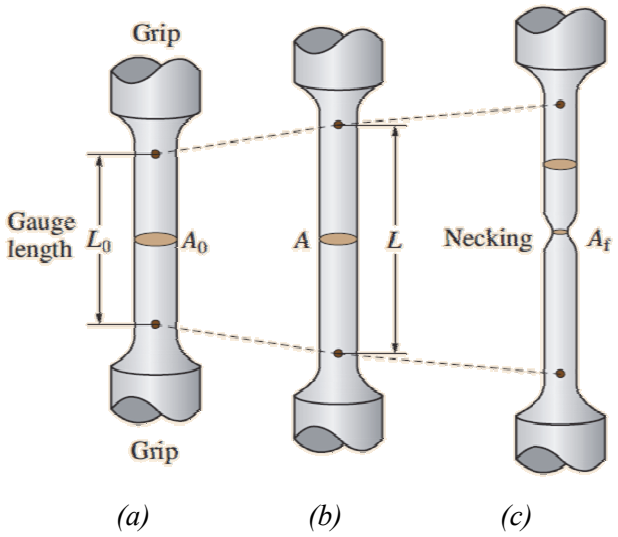

Figure 6.11. Tension specimen: before test (a), uniform deformation (b), localisation of deformation (c) [94]

An example of the nominal stress-strain curve (without pronounced yielding region - Lüders plateau), with true stress - true strain curve obtained from it.

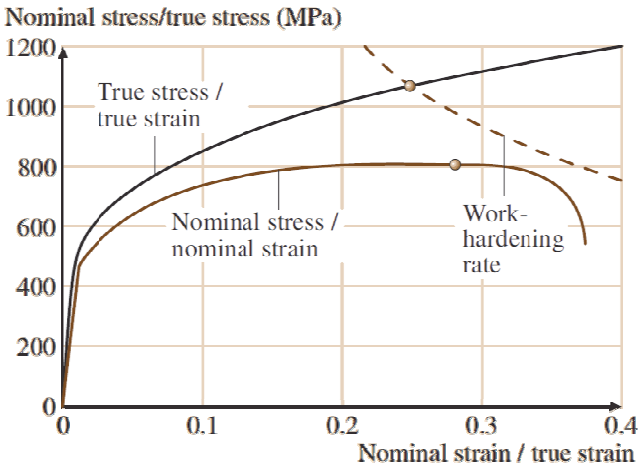

Figure 6.12. True stress - true strain curve [94]

Tensile testing is here performed on round tensile specimens (RT), figure 6.13. The diameter of the specimens was 2 mm; this was the maximum size which could be fabricated from most of examined pipes. Nominal measures are shown in the figure. In addition to this size, larger specimens (with diameter 6 mm in axial direction, and 3 mm in hoop direction) are cut from one of the pipes with much larger wall thickness.

Due to small diameters of most specimens, it was necessary to fabricate fixtures with external and internal thread, as shown in figure 6.14.

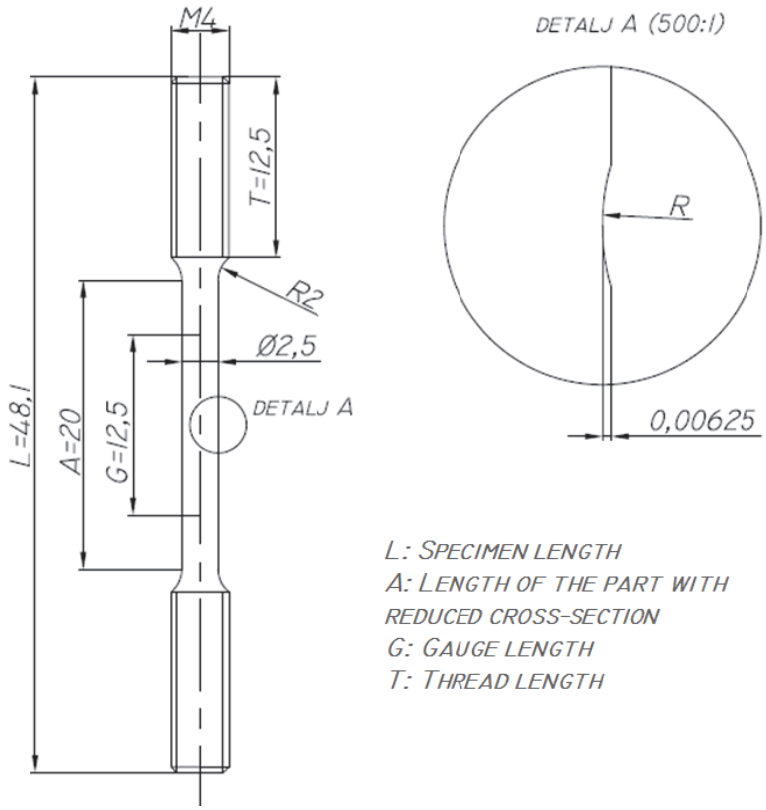

Figure 6.13. Drawing of round tensile (RT) specimen

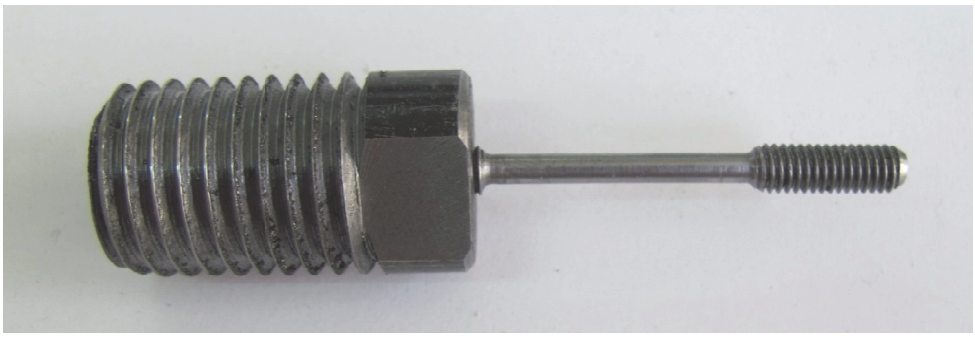

Figure 6.14. RT specimen with fixture on one side

6.2.4 Fracture mechanics testing

As mentioned in the previous chapters, there are different reasons for occurrence of defects in engineering structures. Whether they are initiated during production, assembly process, or in exploitation, an important task is to estimate their effect on the integrity of structure in exploitation, and to predict the maintenance procedures accordingly.

As opposed to the classical approach to design, where the stresses in material, caused by exploitation loads, are compared to some allowed stress, calculated based on the yield/tensile strength, the fracture mechanics introduces another concept. Namely, the quantity which is considered is the fracture mechanics parameter, and the structure is safe while this parameter is below its critical or allowed value (which quantifies the fracture resistance).

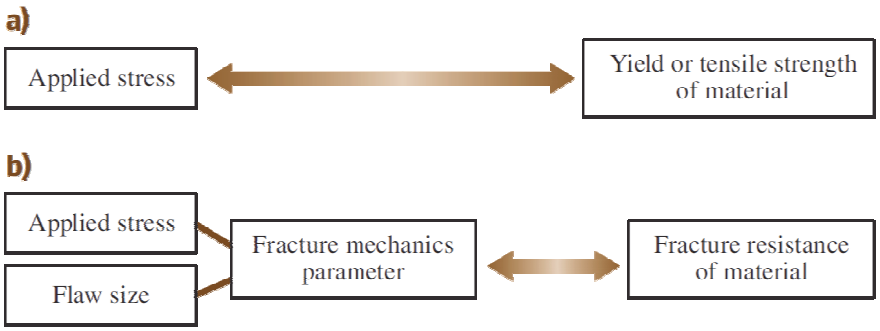

Figure 6.15. Classical design (a) and design in accordance with fracture consideration (b) [94]

Fracture mechanics parameters are previously considered in chapter 3; in case linear-elastic fracture mechanics (LEFM) is applied, stress intensity factor K, is typically used as fracture parameter. However, in case of significant plastic deformation in the crack tip region, elastic-plastic fracture mechanics (EPFM) is more appropriate (typically through J integral and CTOD).

Besides the opening, mode I in figure 6.16, in some situations it is important to consider some other relative movements of the fracture surfaces. These additional modes correspond to shearing, in accordance with figure 6.16; shearing can be either in-plan or out-of-plane.

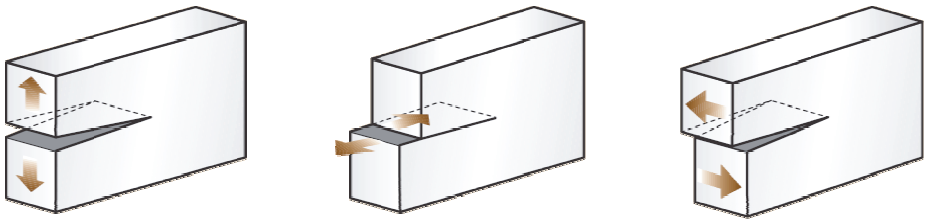

(a) *(b)* *(c)*

Figure 6.16. Crack deformation modes: I (opening) (a) II (in-plane shearing)(b), III (out-of-plane shearing) (c)[94]

For determination of fracture resistance of a material, single-edge notched bending (SENB) specimen or a compact tension (CT) specimen is typically used, figures 6.17 and 6.18.

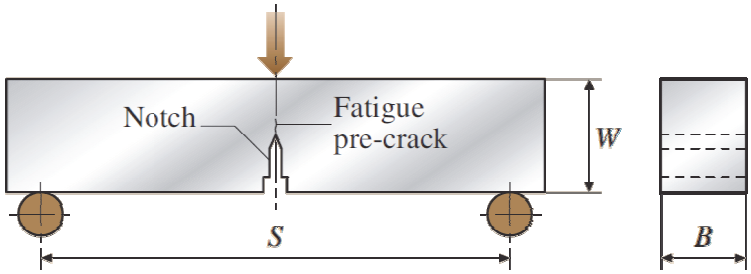

Figure 6.17. Single-edge notched bending (SENB) specimen [94]

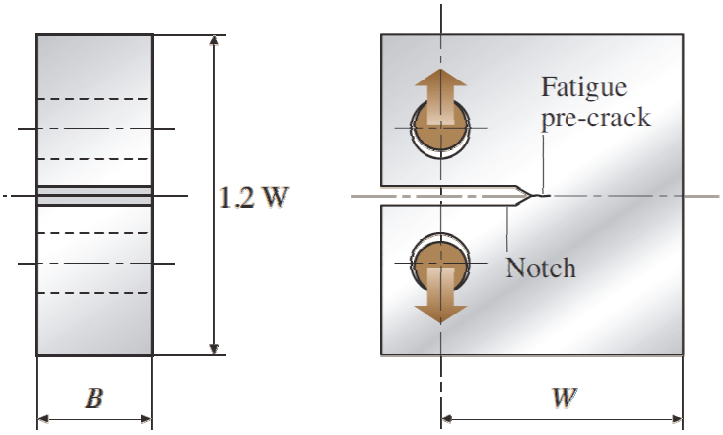

Figure 6.18. Compact tension (CT) specimen [94]

Figure 6.19 contains the drawing of compact tension specimens (nominal measures are given), along with a photo of testing on the tensile testing machine. These specimens are cut from the pipe with dimensions ∅133x11mm. All other pipes had insufficient wall thickness, which is the motive for application and analysis of fracture of PRNB specimens.

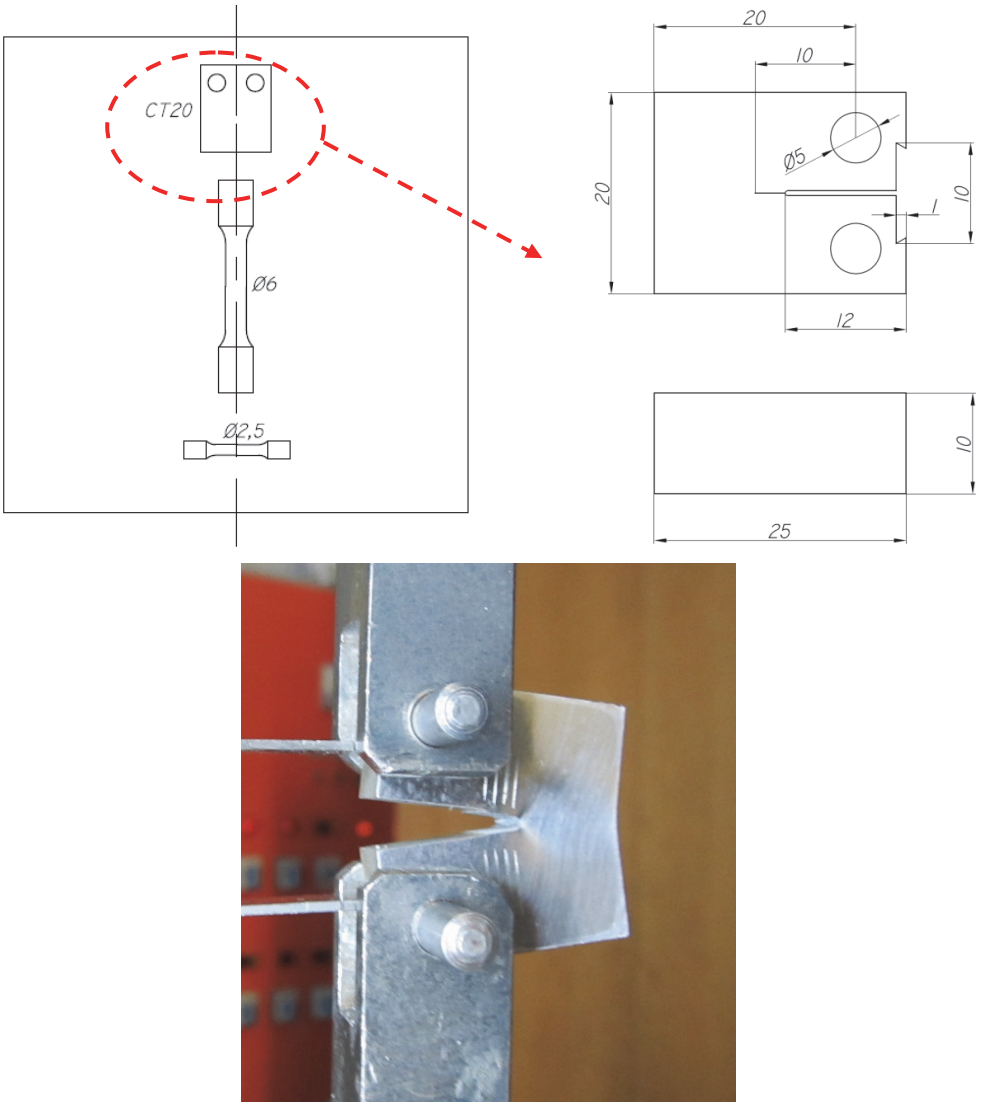

Figure 6.19. Compact tension (CT) specimen - drawing and photograph of testing

6.2.5 Measurement of strain using stereometry

Non-contact measurement of strain using stereometry offers a possibility to track the 3D displacements of points on the surface during the loading, and subsequent calculation of strains in post-processing procedure.

While the concept of strain gauges includes the elongation measurement of small initial measuring length, basic concept of stereometric method is contactless measurement of the points distributed across the selected surface area. This is achieved by contrast spraying, which result in black dots on white surface. These dots are tracked during the

increase of loading, i.e. it is possible to determine the change of their position during time.

The measurement volume is defined depending on dimensions of the object/area to be analysed. It should be selected to ensure that the area of interest lies within the measurement volume during the entire loading period.

Based on the displacement of surface points, recorded by the system with two cameras and stored on a computer, strain field is determined in the software package. One segment of the structural element surface with a points grid in a non-loaded state and their positions after deformation is shown in figure 6.20.

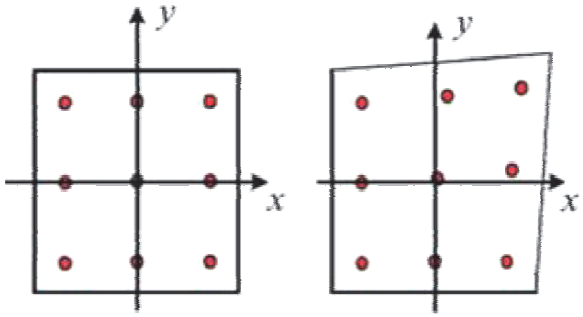

Figure 6.20. Position of points on surface segment in non-loaded and loaded state

The scheme of the measuring system with two video cameras is shown in figure 6.21.

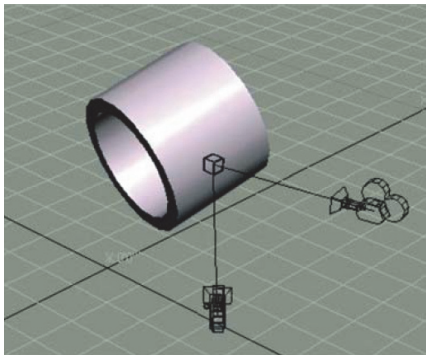

Figure 6.21. Recording of strains on the surface with two video cameras (scheme) [97]

Aramis system is shown in figure 6.22, with a tested specimen at the centre.

The coordinate system is not necessarily related with the geometry of the specimen or structure being monitored. Its position is based on the calibration of the cameras, and it enables the tracking of the position of the points through three coordinates, i.e. in 3D (*x, y, z* coordinates).

Figure 6.22. Cameras of Aramis system with the tested sample at the centre. [97]

However, the user can relate the coordinate directions to the geometry of the structure which is being examined, in order to show the strain fields in a more natural way, aligned with some characteristic axes, edges or surfaces. The software can show the coordinate system; example from Aramis is shown in figure 6.23.

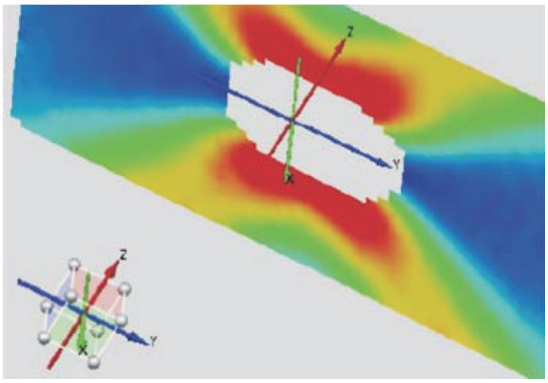

Figure 6.23. Coordinate system in the 3D view [97]

Two models can be used for calculation in the software for data processing. The first one relies on the assumption that a point’s neighbourhood can be represented adequately by a tangential plane. This means that the tangential plane has to be determined first for the undeformed state, and then changed as the structure (and points on its surface) deforms. After that, the points in the neighbourhood are orthogonally projected to this plane.

If the linear model is not sufficient, than it is necessary to include some more adjacent points in the calculation, which leads to so-called spline model. Figure 6.24 shows the adjacent points of the small four-sided surface on a curved surface.

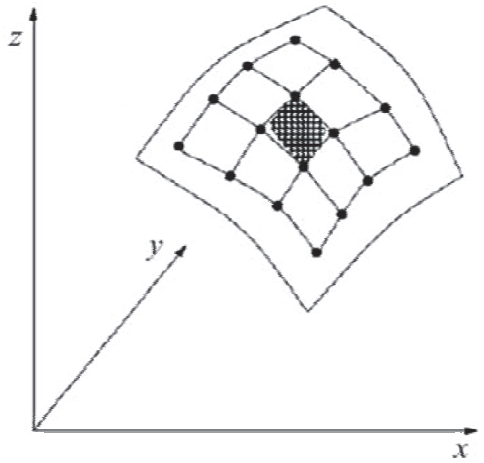

Figure 6.24. Adjacent points on a curved surface

6.2.6 Fracture surface examination

Fracture surfaces of the ring specimens after final fracture are examined by using the stereo microscope Olympus SZX12; the entire system which includes the microscope, digital camera DP12 and image capture software Olympus DP-Soft is shown in figure 6.25.

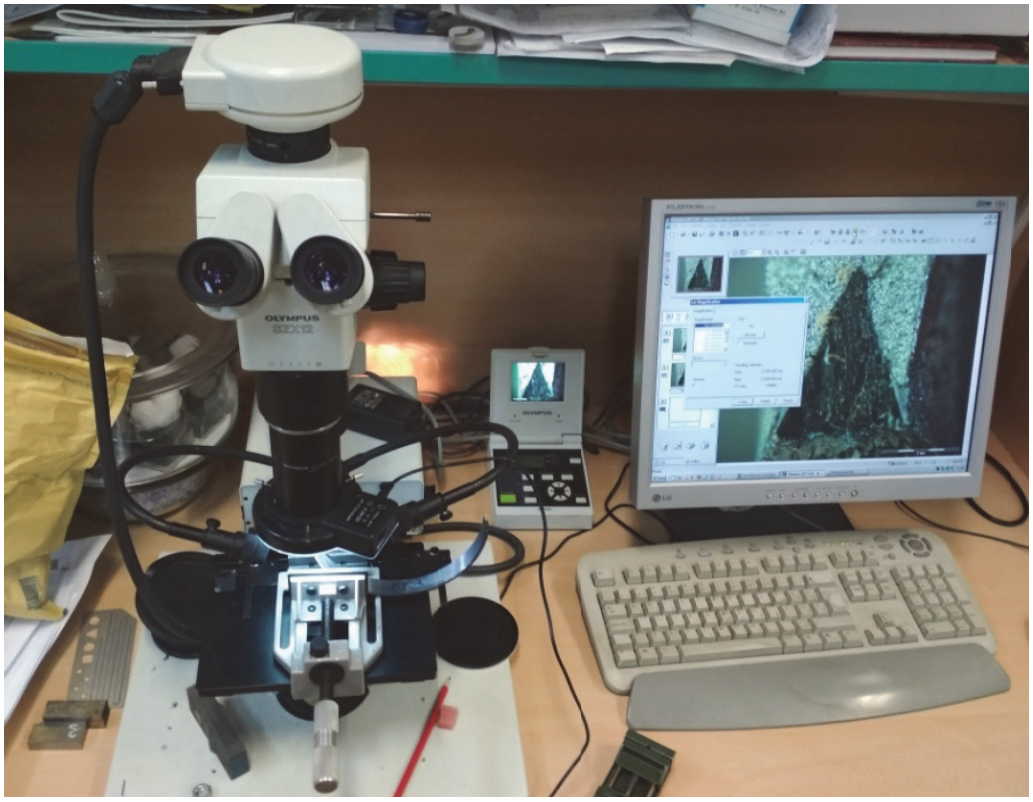

Figure 6.25. Stereo microscope with camera and image capture software

The images obtained by using the microscope were used for fracture surface measurement, i.e. determining the final crack growth. Also, more detailed images contain only a part of fracture surface and illustrate the ductile fracture mechanism, characterised by dimples.

It should be noted that fracture surfaces of some specimens were also observed by using Nikon D90 digital camera; these images were used only for final crack growth measurement.

6.3 Testing of ring-shaped specimens - experimental analysis

A schematic representation of a PRNB specimen exposed to bending is given in figure 6.26; stress concentrator can be either machined notch or fatigue pre-crack.

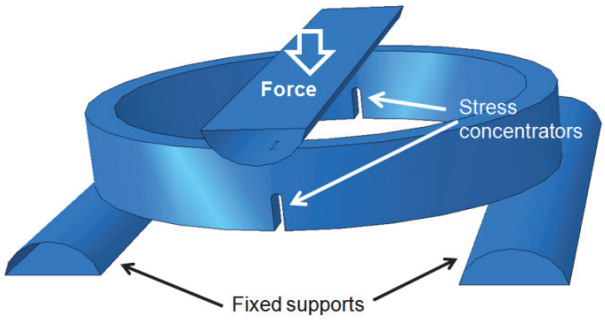

Figure 6.26. PRNB specimen - testing scheme

6.3.1 High strength low alloyed steel NIOMOL 490

As mentioned in the beginning of this chapter, an experimental study has been conducted previously, [92], with an aim to determine the fracture behaviour of PRNB specimens cut from a plate of high strength low alloyed steel NIOMOL 490K. The fracture of these specimens was compared with the fracture of standard SENB specimen; it was chosen for comparison due to the same loading type, i.e. bending, and crack type (passing through thickness). In this work, fracture of these specimens will be analysed by using the micromechanical model. The fact that both types of specimens were made from the same plate of material causes the same fabrication conditions and material history. Dimensions of a group of specimens cut from the plate, is shown in

table 6.4: Ring external radius R, specimen width W and thickness B, as well as crack or notch length a_0. The specimens were either pre-cracked (R60 and R40) or notched (R85 - the notch radius was 0.25 mm). Stable crack growth by ductile fracture mechanism is observed in all specimens, regardless of the shape of the stress concentrator (fatigue pre-crack or machined notch). SENB specimen is also tested, to enable a comparison of the results.

Due to the cylindrical geometry, dynamic loading produced uneven cracks, i.e. the fatigue crack growth was more pronounced on the interior surface of the specimen, left side of figure 6.27. It is discussed and concluded in [98] that machined notch is a suitable stress concentrator for this geometry and that it gives reliable and repeatable results. Namely, notched PRNB specimen without fatigue pre-crack exhibits symmetric blunting, as well as crack growth, with respect to symmetry line of the fracture surface. Therefore, it will be mainly used in the future examinations of the rings cut from the pipes manufactured by different technologies. In addition to the fact that a more precise and straight defect shape can be obtained by notch fabrication (when compared to fatigue pre-cracking), this further simplifies the preparation for testing.

Table 6.4. Dimensions of specimens – NIOMOL 490K

	PRNB R85	PRNB R60	PRNB R40	SENB
R [mm]	85	60	40	-
B [mm]	10.04	7.5	5	10.17
W [mm]	20	15	10	20.02
a/W [-]	0.44 (notch radius=0.25 mm)	0.41 and 0.71 (pre-crack)	0.6 (pre-crack)	0.5

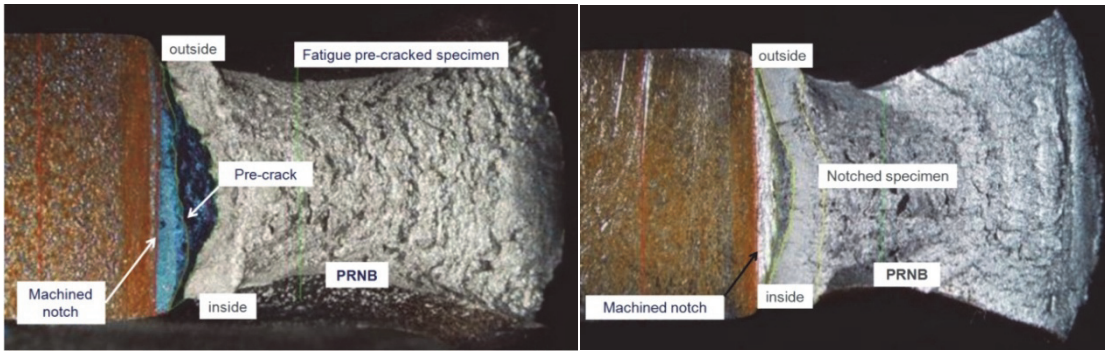

(a) *(b)*

Figure 6.27. Fracture surfaces of fatigue pre-cracked (a) and notched (b) PRNB specimen [98]

Dimensions and testing scheme for PRNB specimens is shown in figure 6.28.

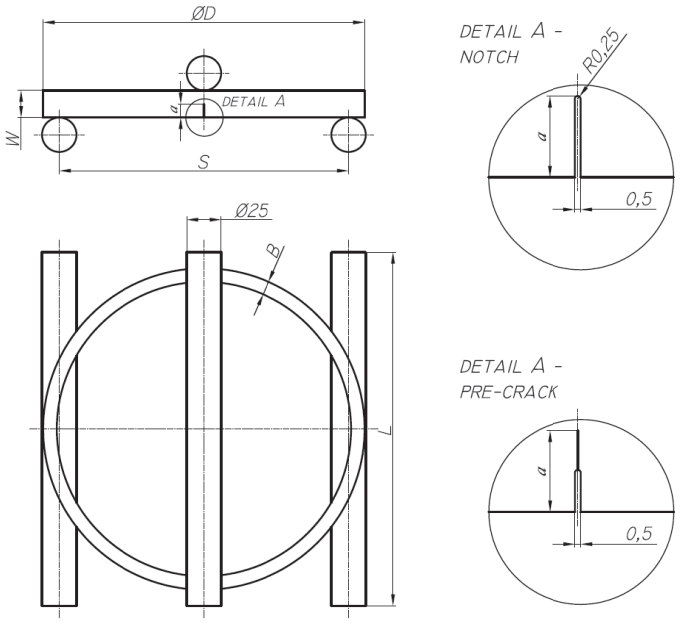

Figure 6.28. Specimen dimensions and testing scheme

6.3.2 Seam and seamless pipes - pressure vessel steel P235GH and P235TR1

The following figures contain the specimens prepared from actual seam and seamless pipes for high-pressure application, with different radius, wall thickness and other important geometry parameters. Figure 6.2 shows the segments cut from the pipes, prepared for producing (cutting) of the specimens. Two materials are considered: P235TR1 and P235GH. They are similar by the standard required properties, and the most important difference is the fact that the one denoted as GH has guaranteed mechanical properties on elevated temperature, due to its use for steamlines.

Several prepared specimens are shown in figure 6.29 - two diameters are used: 168.3 and 88.9 mm. Different wall thicknesses are considered, to account for the constraint effect caused by thickness. Dark lines can be noticed on some of the specimens, representing the position of the welded joint (seam) on the seam pipes.

Different stress concentrators are formed on the specimens: machined notch or fatigue pre-crack. As mentioned previously, both seam and seamless pipes are considered, for both diameters. Seam pipes are produced from P235TR1 material, while P235GH is the material of the seamless pipes.

Figure 6.29. Produced PRNB specimens

Figure 6.30 shows a drawing of a seam pipe and corresponding specimen. Dimensions of specimens cut from the seam and seamless pipes are shown in table 6.5. A larger number of specimens are prepared and considered within this study, but some of them are not in this table, either because they did not exhibit crack growth or they were cut for other tests (such as metallographic examination).

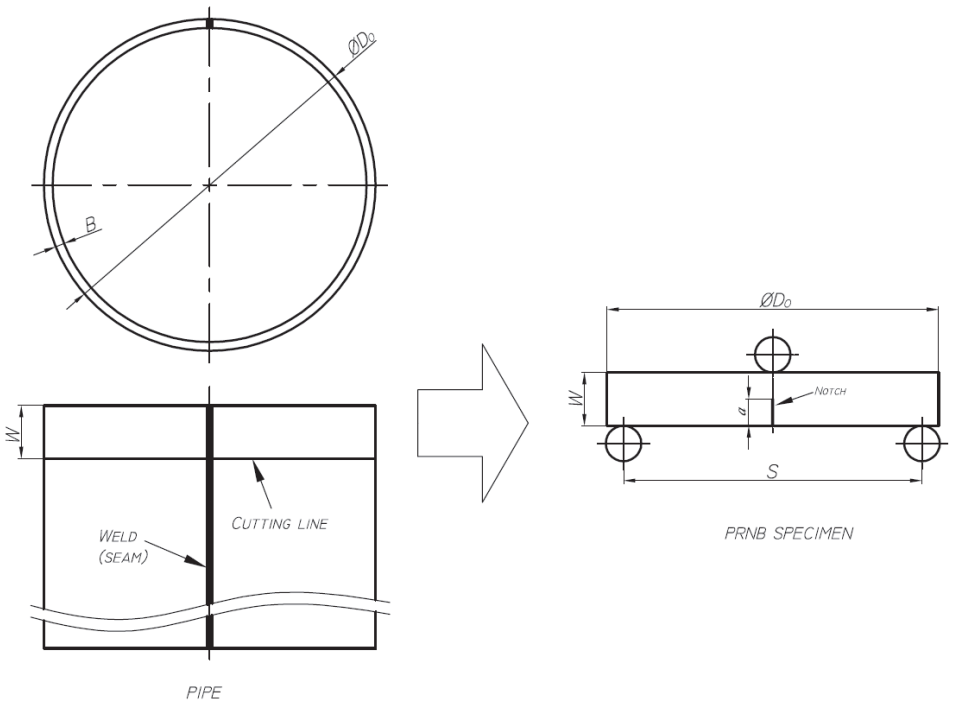

Figure 6.30. Seam pipe and specimen geometry with testing scheme

During the testing, deformation of specimen surface and geometrical fracture mechanics parameters (CMOD and CTOD) are monitored using the stereometric measurement system *Gom Aramis*. Displacement of surface points is measured using two connected cameras. The testing equipment is shown in figure 6.31.

In order to enable this procedure, the surface is sprayed with a contrasting colour (a combination of black and white) before testing, figure 6.32. This leads to a ‘discretised’ surface, and the software package can track the points to determine their displacement, and subsequently calculate strains and other related mechanical quantities. For example, figure 6.33 shows a view of the strain field obtained during testing of a specimen.

Table 6.5. Dimensions of specimens made from seam and seamless pipes

	Pipe type	D_o [mm]	B [mm]	W [mm]	W/B [-]	a/W [-]	S (=0.9 D_o) [mm]
S-WM(168)-1	Seam (notches in WM and BM)	168.18	3.21	12.99	≈ 4	0.5	151.5
S-WM(168)-2	Seam (notches in WM and BM)	168.43	3.46	21.05	≈ 6	0.5	151.5
S-WM(168)-3	Seam (notches in WM and BM)	168.21	3.24	19.26	≈ 6	0.5	151.5
S-WM(168)-5	Seam (notches in WM and BM)	168.3	3.23	19.26	≈ 6	0.75	151.5
S-WM(168)-4	Seam (notches in WM and BM)	168.3	3.3	13.26	≈ 4	0.47	151.5
S-BM(168)-6	Seam (notches in BM)	168.28	3.22	19.23	≈ 6	0.5	151.5
S-WM(89)-7	Seam (notches in WM and BM)	88.28	2.71	11.05	≈ 4	0.5	80
S-WM(89)-8	Seam (notches in WM and BM)	88.59	2.58	10.48	≈ 4	0.5	80
S-BM(89)-9	Seam (notches in BM)	88.62	2.55	10.30	≈ 4	0.45	80
S-BM(89)-10C	Seam (pre-cracks in BM)	88.46	2.63	10.48	≈ 4	0.25 + crack = 0.38/0.46	80
SL(168)-11	Seamless (notches)	168.39	3.52	21.15	≈ 6	0.45	151.5
SL(168)-12C	Seamless (pre-cracks)	168.22	3.61	21.68	≈ 6	0.45 + crack = 0.53	151.5
SL(168)-13C	Seamless (pre-cracks)	168.25	3.58	21.62	≈ 6	0.25 + crack = 0.43	151.5
SL(168)-14C	Seamless (pre-cracks)	168.35	3.57	21.06	≈ 6	0.25 + crack = 0.46	151.5
SL(89)-15	Seamless (notches)	88.39	2.82	11.28	≈ 4	0.45	80
SL(89)-16C	Seamless (pre-cracks)	88.42	2.89	11.70	≈ 4	0.25 + crack = 0.6 / 0.35	80
SL(89T)-17	Seamless (notches)	88.95	4.91	19.66	≈ 4	0.5	80
SL(89T)-18	Seamless (notches)	88.87	4.77	19.27	≈ 4	0.75	80
SL(89T)-19	Seamless (notches)	88.92	4.82	19.22	≈ 4	0.25	80
SL(89T)-20	Seamless (notches)	88.94	4.69	28.74	≈ 6	0.5	80
SL(89T)-21	Seamless (notches)	88.91	4.75	28.67	≈ 6	0.5	80
SL(89T)-22	Seamless (notches)	88.86	4.86	9.29	≈ 2	0.5	80
SL(89T)-23	Seamless (notches)	88.9	4.75	9.24	≈ 2	0.5	80

Figure 6.31. Testing equipment: tensile testing machine and stereometric measurement system

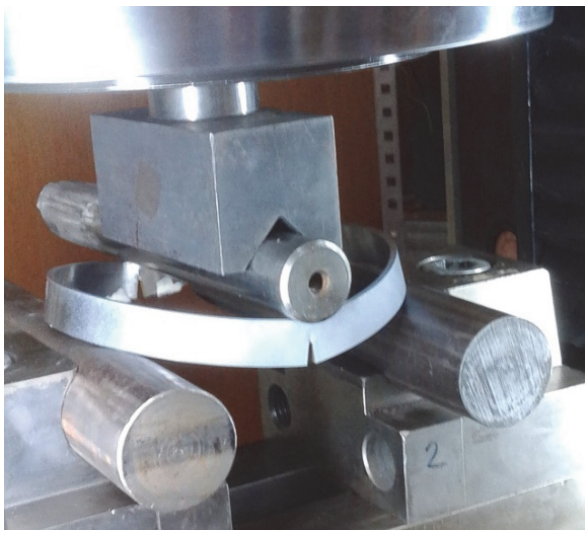

Figure 6.32. Side of the specimen for Aramis measurement, with applied contrast spray (specimen already deformed)

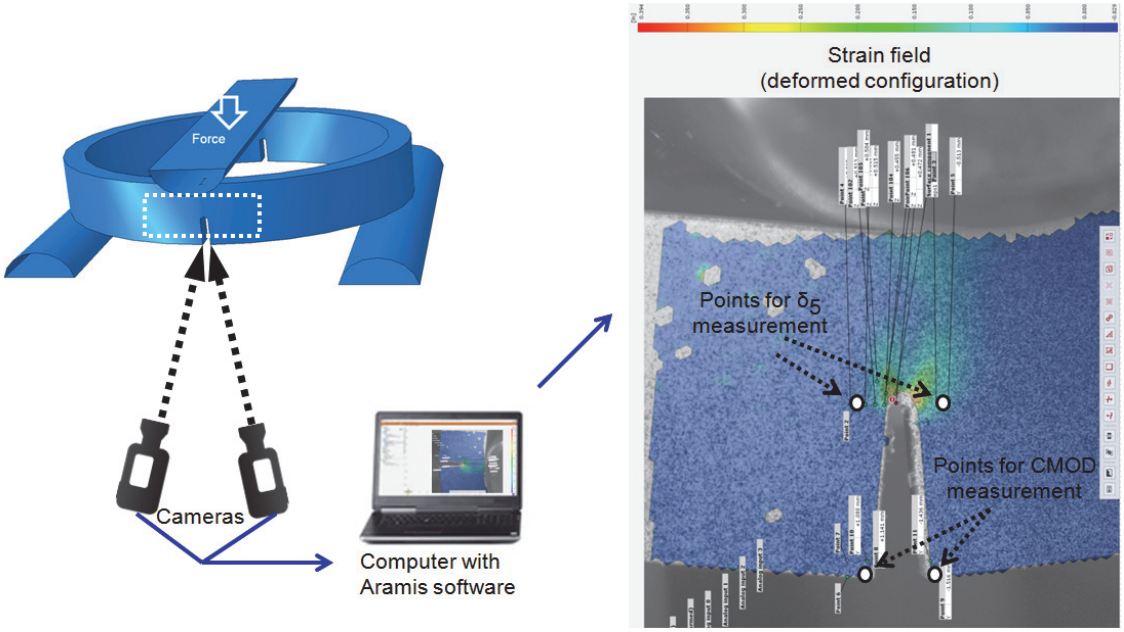

Figure 6.33. Measurement system GOM Aramis - scheme and example of strain field [99]

On the other side of the specimen, at the second notch (or crack), a COD gauge is mounted in order to determine the value of CMOD, figure 6.34.

Figure 6.34. Side of the specimen with COD gauge

6.4 Testing of ring-shaped specimens - numerical analysis

6.4.1 Introduction

Figures 6.35 and 6.36 show an example of the finite element mesh on a model formed by using quarter-symmetry and half-symmetry conditions. Region near the crack front

is enlarged, and it can be seen that the size of elements in this region is rather uniform, in order to enable the tracking of crack growth in the numerical model.

Numerical analysis is performed by the finite element method (FEM), using the software package Simulia Abaqus (www.simulia.com).

Three-dimensional models consist of 8-node full integration elements. Due to the symmetry of the geometry and loading, either one quarter of the PRNB specimen is considered, i.e. two symmetry planes are applied (Figure 6.35) or one half of the specimen (Figure 6.36). In the part of the ligament ahead of the crack front, where the crack growth occurs, finite elements have the same size and similar dimensions in all directions (cubic-shaped), in order to capture the crack growth adequately. As mentioned before, a quarter of the SENB geometry is analysed, having in mind the symmetry, figure 6.37.

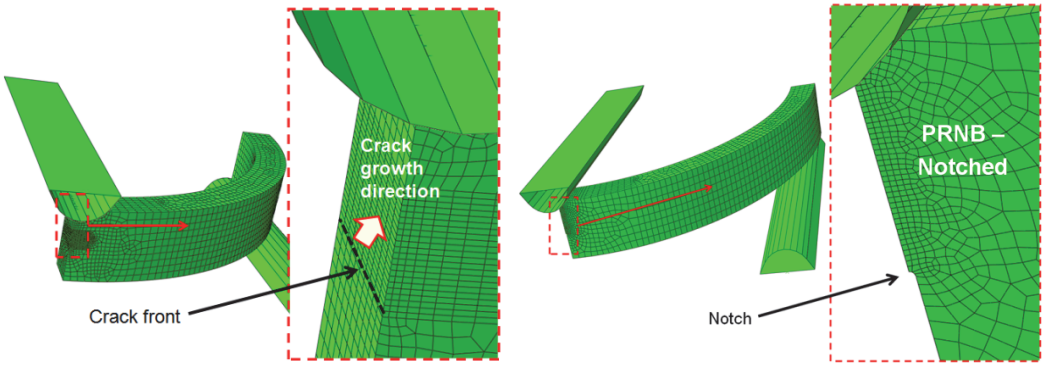

Figure 6.35. Models of PRNB specimen - quarter-geometries

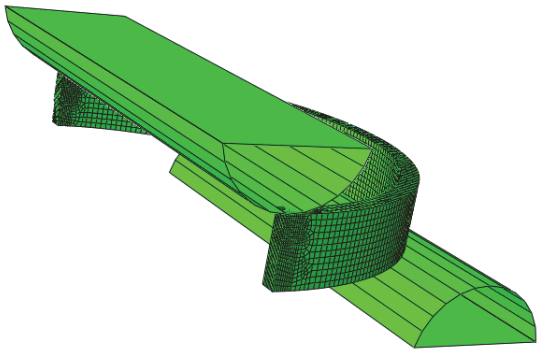

Figure 6.36. Models of PRNB specimen - half-geometry

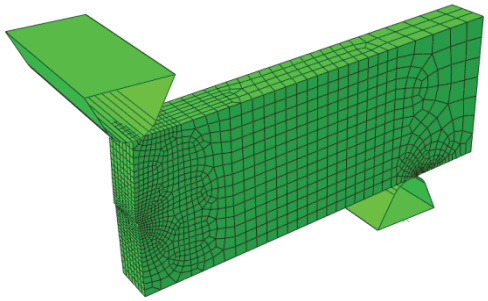

Figure 6.37. Model of SENB specimen - quarter-geometry

Micromechanical material model is applied for determining the crack growth initiation and stable growth. The complete Gurson model is applied in the numerical analysis through user material subroutine (created by Z.L. Zhang, based on [60]).

6.4.2 Creation of a half-symmetric numerical model of the ring specimen

Initially the model has been sketched and created; it represents three-dimensional shape of half of a ring in three dimensions, according to the given dimensions; figure 6.38 shows two models with different dimensions. Of course, very similar procedure is used for the quarter geometry.

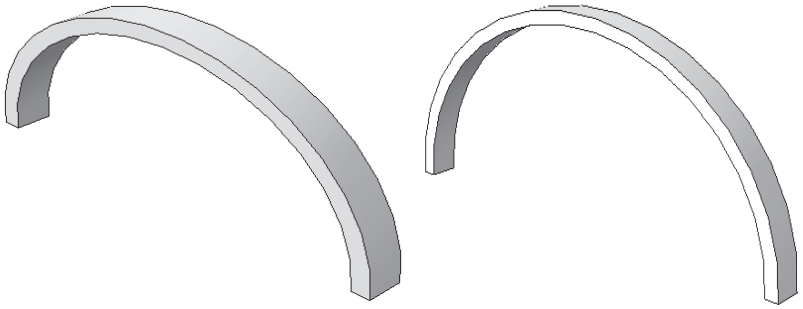

Figure 6.38. Half-symmetrical model of the ring specimen (a) model 1 (b) model 2

Partition tool in Abaqus software package is used to cut the region into different sub-regions, primarily for achieving different mesh densities. These partitions are shown in figure 6.39; two of them which are used as crack fronts are enlarged in the lower part of the figure. The view on the partitions from another angle is shown in figure 6.40.

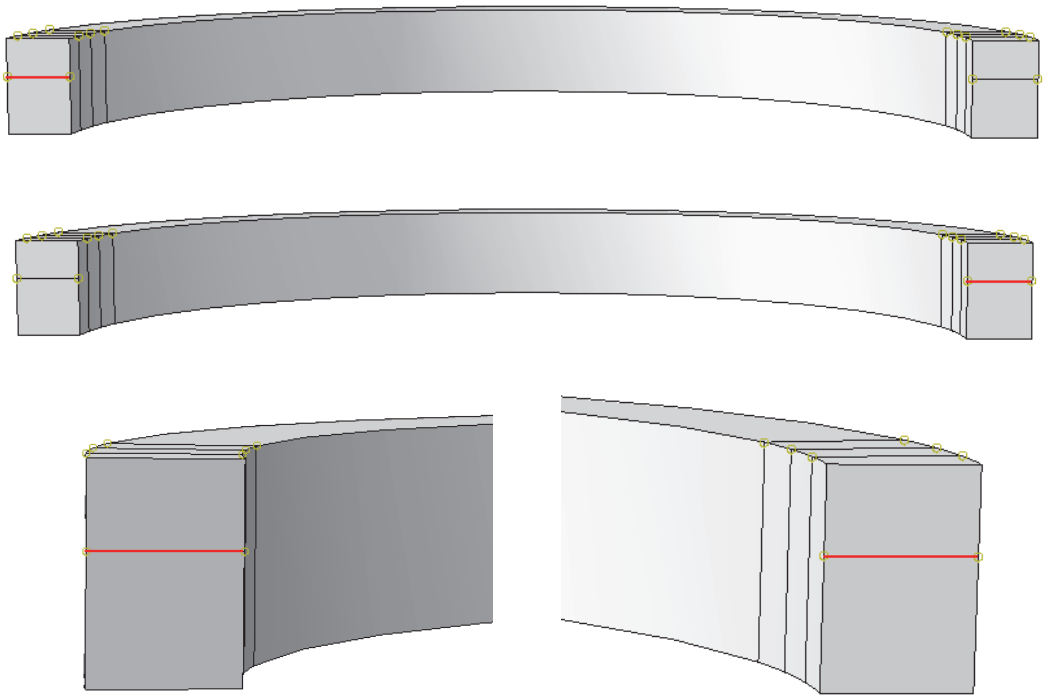

Figure 6.39. Partitions of the model - symmetry plane

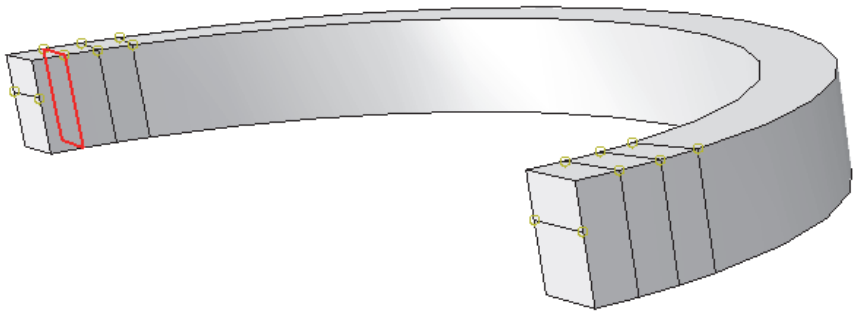

Figure 6.40. Partitions of the model

Then the supports have been sketched and created, as three-dimensional non-deformable bodies. Simplification of the problem by using non-deformable bodies is often used in cases where deformation of one part in the contact (ring, in this case) is dominant, while deformation of the other part (support) can be neglected.

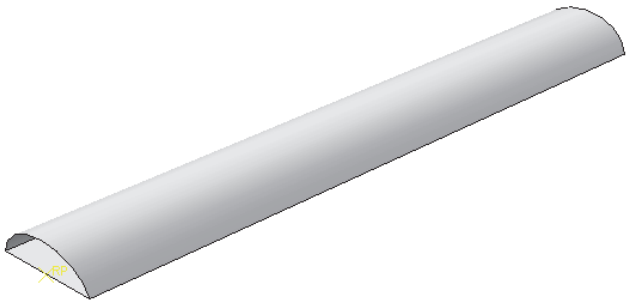

Figure 6.41. Support

After the creation of the geometry for each part, they are imported into the Assembly module, where they are positioned in accordance with figure 6.42. One instance of the ring and two instances of the support (fixed support and loading pin) are imported.

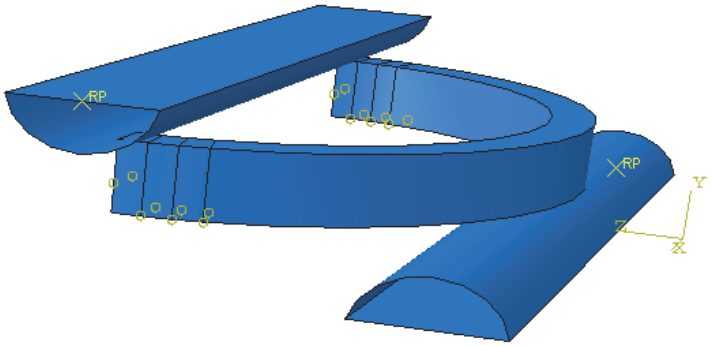

Figure 6.42. Assembly - model and two supports

Definition of the contact surfaces is shown in figures 6.43 and 6.44; two contact pairs are defined, for the interaction of the ring with the upper and lower support.

Finally, the boundary/loading conditions are as follows: the loading pin has one non-fixed degree of freedom - prescribed displacement in the vertical direction, while the support is fixed, i.e. all displacements and rotations of this rigid body are prevented.

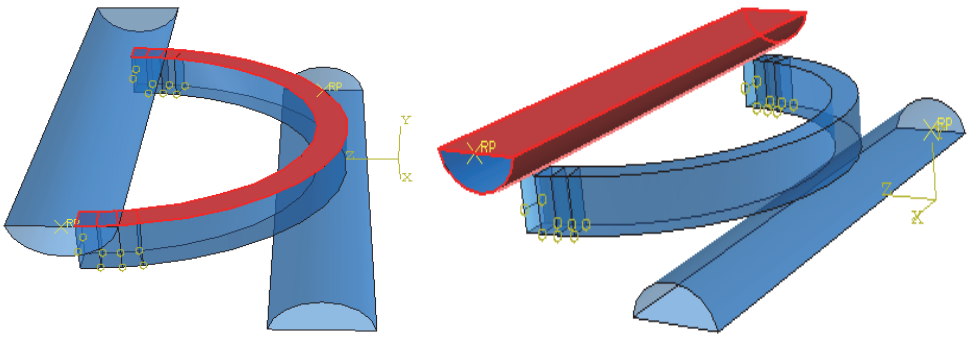

Figure 6.43. Defining contact surfaces - 1

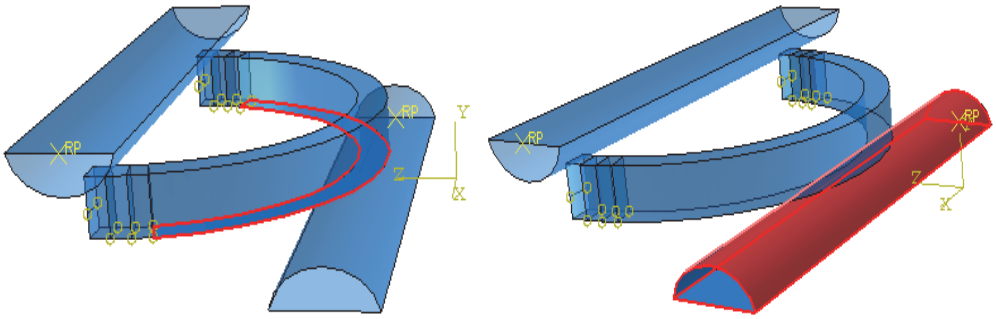

Figure 6.44. Defining contact surfaces – 2

7. RESULTS AND DISCUSSION

In this chapter, all the results obtained by experimental and numerical methods presented in the previous chapter are presented. Experimental data are shown in the beginning; first, the results of the ring specimen testing and afterwards other results - tensile testing, hardness, microstructural analysis, etc. Remainder of the chapter contains the results obtained by application of the finite element method and micromechanical model CGM.

7.1 Ring-shaped specimens - experimental fracture analysis

After testing, the ring specimens were plastically deformed, but not broken into two parts, as shown in figures 7.1 and 7.2. In order to proceed with the analysis, i.e. to determine the crack lengths, it was necessary to break them, but to keep the shape and structure of the fracture surfaces. There are two often-used ways, fatigue loading and brittle fracture of cooled specimens; the second one is applied here.

The results obtained through experimental fracture testing of ring specimens produced from seam and seamless pipes (materials P235GH and P235TR1) are shown in this sub-chapter. As mentioned previously, the specimens cut from the low alloyed high strength steel (NIOMOL 490K) are experimentally examined in [92], and a part of these results will be given along with the micromechanical analysis done within the framework of this thesis.

In order to ensure a good visibility of fracture surface, i.e. clear distinction between the ductile and brittle fracture zones, the specimens are first heated for 30 min at the temperature of 400 °C (so called heat-tinting). Specimens prepared for heating in the metallurgical furnace are shown in figure 7.3. Afterwards, they are cooled down to room temperature, which was recorded by thermal imaging camera. It turned out that the thickness of the specimen can cause certain difference in cooling rate, while stress concentrator influence is not observed. Figure 7.4 shows two images of the same specimen, right after it was removed from the furnace and after about 12 minutes. It can

be seen that the temperature dropped almost instantly to 281°C in the initial state (max. value on the scale), and after 12 minutes the specimen was cooled down to 54°C (again, this is max. value).

Figure 7.1. Several specimens after the static testing

Figure 7.2. One of the specimens with prominent crack growth

Figure 7.3. Specimens prepared for heating in the furnace

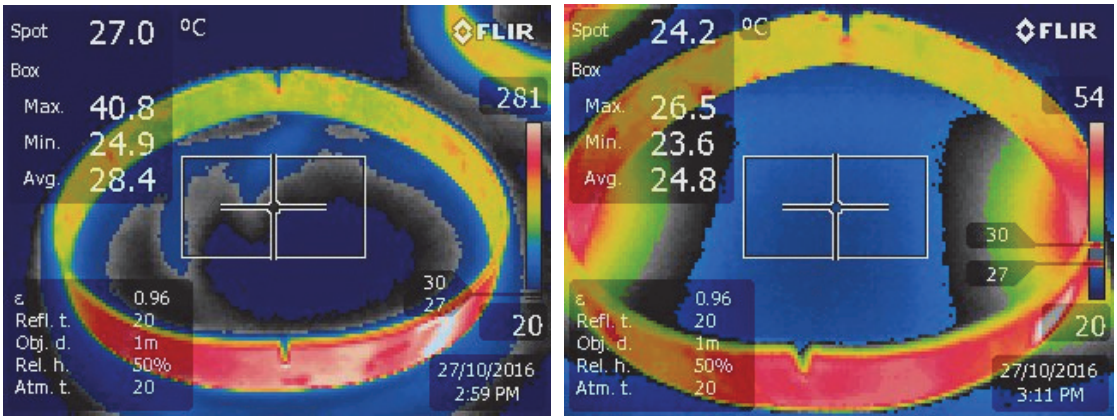

Figure 7.4. Thermovision images obtained during air-cooling of a specimen from 400℃

On ductile fractured specimens, a characteristic final crack shape is observed; most pronounced growth is obtained in the central part, i.e. around mid-thickness, figure 7.5. Darker colour of ductile fracture surface is clearly visible on all specimens, which is the result of the mentioned heat-tinting.

In notched specimens, the final fracture has symmetrical shape with respect to the symmetry axis of the cross section, which points to the fact that the specimen shape (ring) does not affect the uniformity of the crack growth; uniformity is here considered as comparison between the inner and outer surface of the specimen. In figure 7.5, first two specimens have initial notch.

When specimens with fatigue pre-crack are considered (two specimens in the right-hand side of figure 7.5), uneven fatigue crack growth is observed - the crack under dynamic

loading grows more intensively on the internal specimen surface. This non-uniformity is, along with simplicity and precision of fabrication, one of the advantages of the notched specimens, where initial damage (notch) is machined. It should be emphasized that ductile crack growth under static loading is relatively uniform even in the case of uneven fatigue pre-crack, i.e. ductile crack growth is the most pronounced near the middle of thickness, while it is the smallest on the internal and external surfaces.

Crack length measurement on fracture surfaces, such as those in figure 7.5, enabled an initial estimate of the influence of heterogeneity on fracture resistance of the seam pipes. More details about this measurement is shown later in this chapter.

Figure 7.5. Fracture surfaces of ring-shaped specimens

In some specimens, ductile crack growth did not occur, or the crack growth was very small. There are two possible reasons for this: i) specimen geometry does not provide sufficient values of stress triaxiality and/or plastic strain necessary for ductile fracture, ii) ending the test due to the large values of load line displacement - i.e. specimen excessive deformation. The factor which certainly influences the first reason is small thickness, which is related to low stress triaxiality. However, it is shown that higher

ratio *a/W* (e.g. 0.75 in comparison with 0.5) and lower ratio *W/B* (e.g. 4 in comparison with 6) more often does not lead to fracture. As for the second reason, the end of the test depends up to some extent on the subjective estimate of the moment when significant plastic deformation is reached; this moment corresponds to the drop of the force value on the tensile testing machine.

F-CMOD curves for all specimens are formed. These curves are not convenient for direct comparison of the specimens during fracture, because several parameters affect their shape: material properties, fracture behaviour, specimen size (diameter, wall thickness and width) and stress concentrator size. However, they can be used for comparison of the specimens which are different by only one of the mentioned factors. Examples are determining the influence of the wall thickness or specimen width on the load-carrying capacity.

Figure 7.6 shows the curves *F*-CMOD for 10 specimens, with different sizes, both seam and seamless. Next to the specimen number are the basic data, in accordance with figure 6.30 and table 6.5: seam/seamless pipe or seam pipe with notches in base metal only, diameter × wall thickness, ratio *a/W*, ratio *W/B*. For example, notation "*Seam, 168.3x3.2, a0.5, W4*" stands for the specimen from the seam pipe, with diameter 168.3 mm, wall thickness *B*=3.2 mm, ratio *a/W*=0.5 and ratio *W/B*=4. The notch/crack position is schematically shown besides the legend.

On this and next figures, if the specimen mark contains the word *Crack*, the specimen was pre-cracked, otherwise it contains machined notches. Only for the seam pipes, *Seam-norm* means that both notches/cracks are in BM, i.e. that fracture direction is perpendicular to the seam. On the other hand, *Seam* (without *-norm*) stands for the specimens with one notch/crack in the seam (weld).

Some of the mentioned data can be seen from the specimen designation itself. For example, S-WM(168)-1 stands for: specimen 1, cut from seam pipe, with diameter 168.3 mm and one of the notches in the weld metal. Seam pipes with both notches in base metal are marked as S-BM, while seamless pipes are marked as SL. Pre-cracked specimens contain letter C at the end. Seamless pipes with diameter 88.9 mm have two different thicknesses; those with thicker walls are marked as 89T instead of just 89.

In figure 7.6, it can be seen that most of the results belong to a relatively narrow range,

except seamless specimens SL(89T)-17 and SL(89T)-19. This can be attributed to combination of their dimensions - small diameter, large thickness and small stress concentrator length cause higher loads. It should be noted that curves for selected specimens, and not all of them, are shown in this figure. Some other specimens are added in the next figures, where different sub-groups (with similar size, material, etc.) are considered.

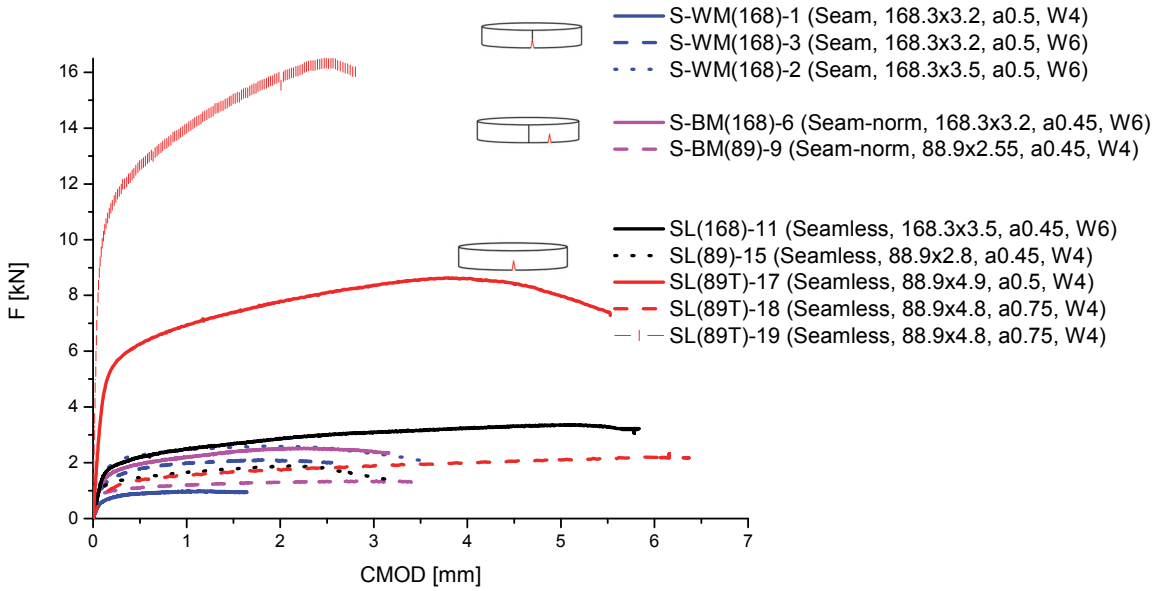

Figure 7.6. F-CMOD curves - different types of specimens

On this diagram, the forces depend significantly on the geometry of the specimen and notch, but it can be noticed that a trend of higher CMOD values is observed for the seamless pipes. (note: testing is stopped after the force drop, i.e. further force drop is not permitted because it leads to extreme plastic deformation).

Figure 7.7 contains the curves for seam pipes with a notch in WM. Besides the obvious influence of the specimen width and notch length, it can be seen that very small difference of thickness causes significant difference in loads (e.g. comparison of pairs S-WM(168)-2 and S-WM(168)-3, as well as S-WM(168)-1 and S-WM(168)-4).

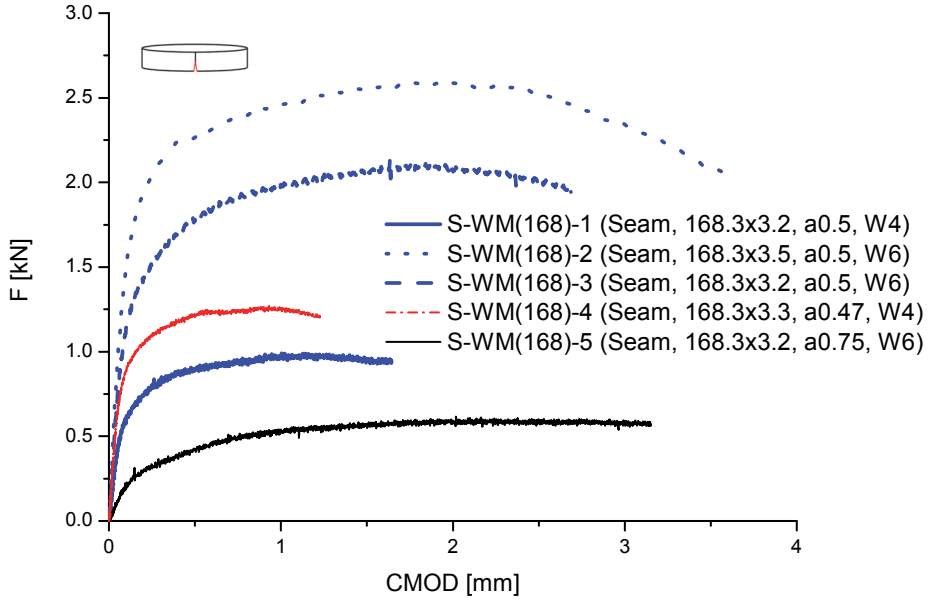

Figure 7.7. F-CMOD curves for seam rings with one of the notches in the weld metal (seam) - diameter 168.3 mm

In figure 7.8., seam pipes with both notches in BM are added, as well as pipes with smaller diameter (represented by red and green colour).

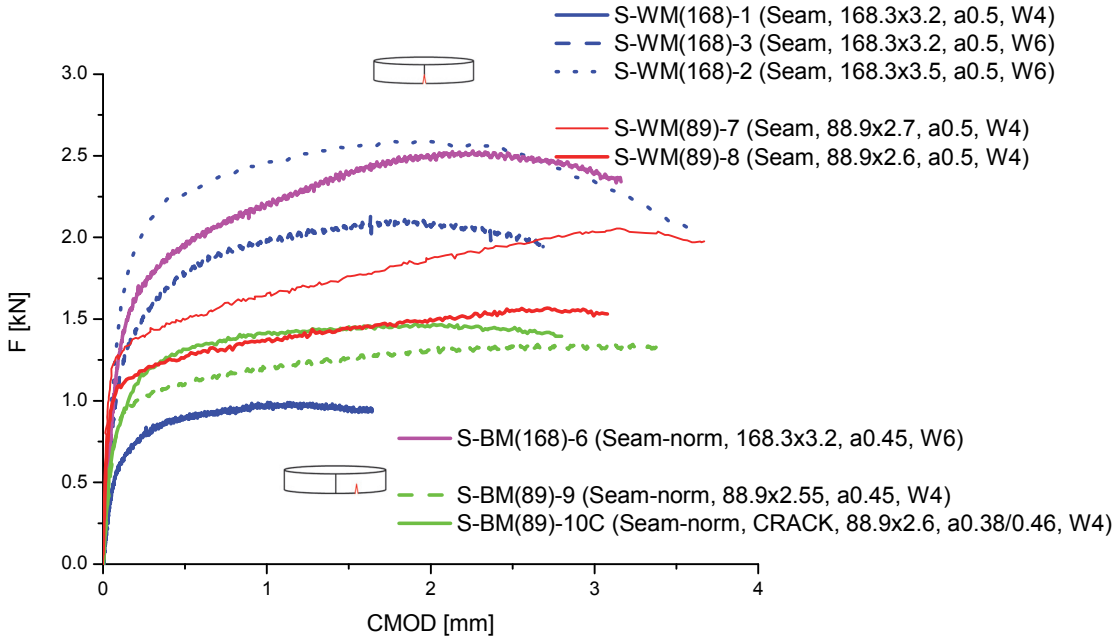

Figure 7.8. F-CMOD curves for seam rings - different diameters and notch positions

Curves for several seamless pipes are shown in figure 7.9. Besides two dimensions which correspond to the seam pipes, there are three specimens (SL(89T)-17, SL(89T)-18 and SL(89T)-19) with a larger *B/W* ratio. Specimen SL(89T)-18 has the largest considered ratio *a/W* (0.75), while the specimen SL(89T)-19 has the smallest ratio (*a/W*

= 0.25). Influence of the notch length is shown in figure 7.9a for three geometries which have similar other dimensions - rings 17, 18 and 19.

The curves in figure 7.9b show the influence of *W/B* ratio for an extended group of seamless specimens with nominal diameter 88.9 mm, wall thickness B = 4.9 mm and ratio a/W = 0.5. The difference between the specimens with varied ratio *W/B* (and all other similar dimensions) can clearly be seen; the values of this ratio were 2, 4 and 6.

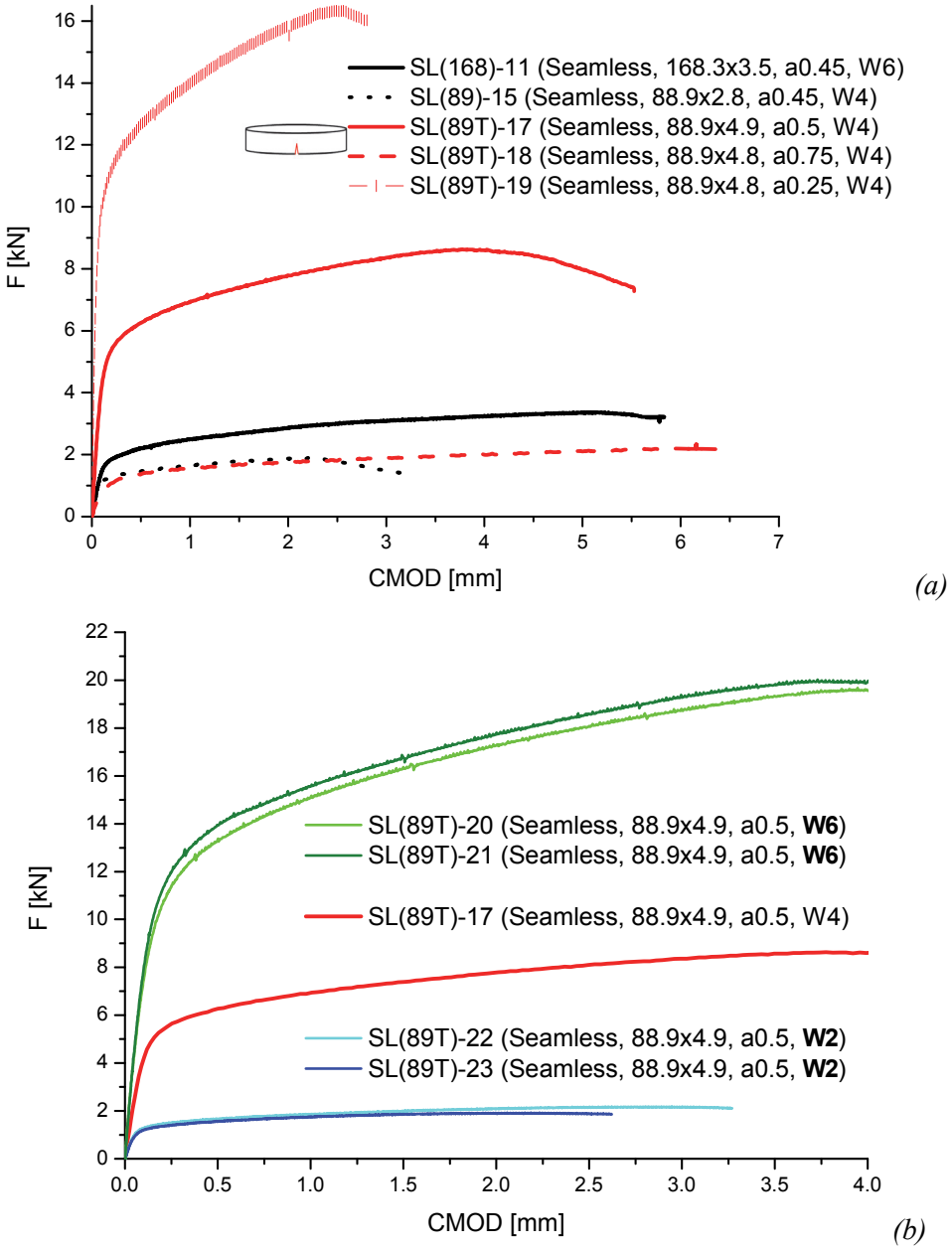

Figure 7.9. F-CMOD curves for seamless rings - different diameters and wall thickness (a) and influence of W/B ratio (b)

Four seamless specimens with similar dimensions, but different stress concentrator shape, are considered in figure 7.10. In addition to notched specimen SL(168)-11, three pre-cracked specimens, SL(168)-14C, SL(168)-12C and SL(168)-13C, are shown. Besides the differences in maximum load, caused primarily by different load-carrying cross sections (wall thickness B and ligament in front of the crack/notch tip $B - a$), it can also be noticed that the CMOD range is smaller than for the notched specimen. Stress concentrator shape effect is also considered later in this chapter, on crack growth curves.

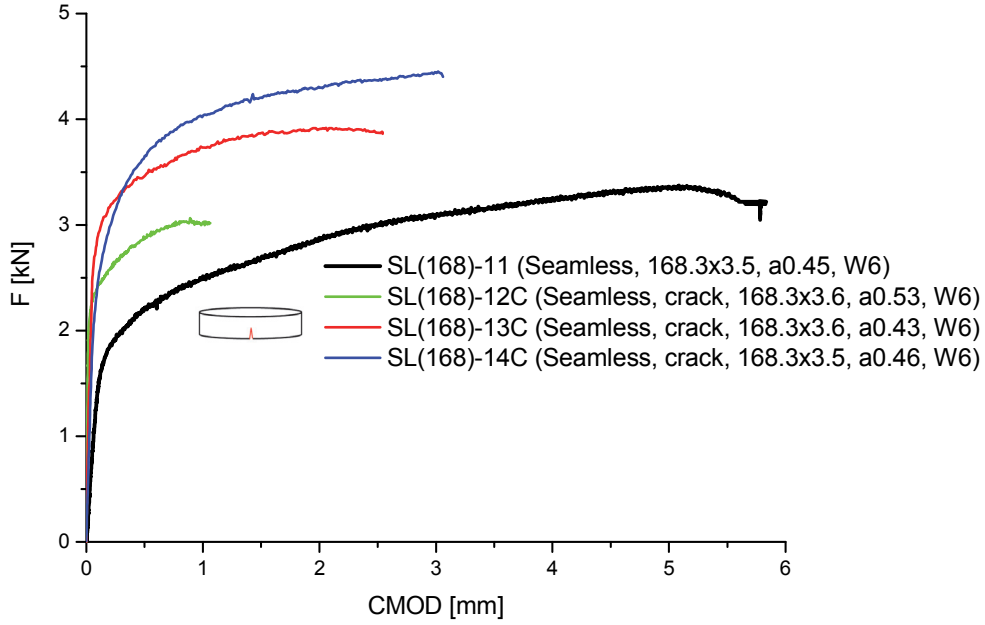

Figure 7.10. F-CMOD curves for seamless rings - diameter 168.3 mm

Unlike the F-CMOD curves, crack growth resistance curves CTOD-Δa depend primarily on the material properties. They are obtained from F-CMOD curves, with the data obtained by fracture surface measurement; normalisation method [100] is applied for determining the crack growth values during the entire test duration.

During the formation of the diagrams in the following text, the value of CTOD is determined by application of δ_5 concept (measurement from Aramis), while the crack growth is obtained by normalisation method, based on the final crack length a_F. Measurement method, from ESIS P2-92 procedure, is schematically shown in figure 7.11, while two examples are shown in figures 7.12 and 7.13 - specimens SL(89T)-17 (notched) and S-BM(89)-10C (pre-cracked).

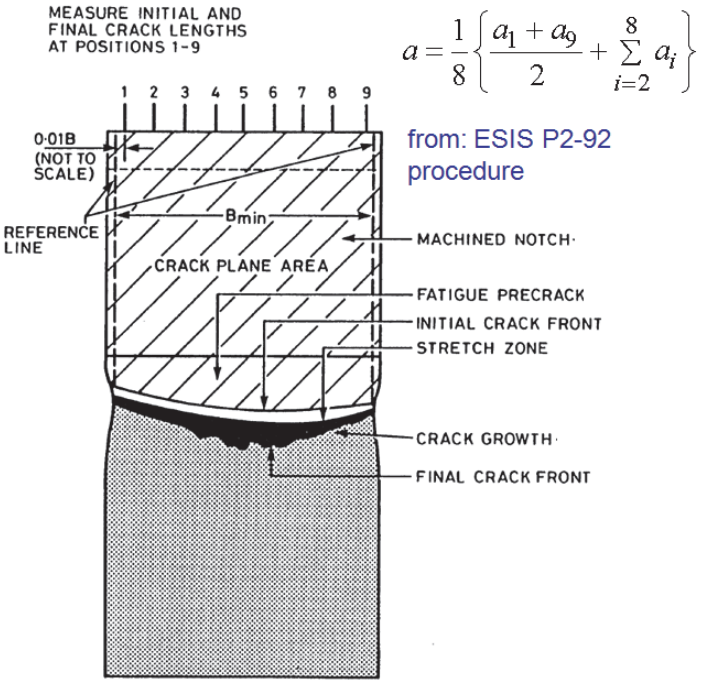

Figure 7.11. Determining the crack length on fracture surface, in accordance with ESIS procedure [19]

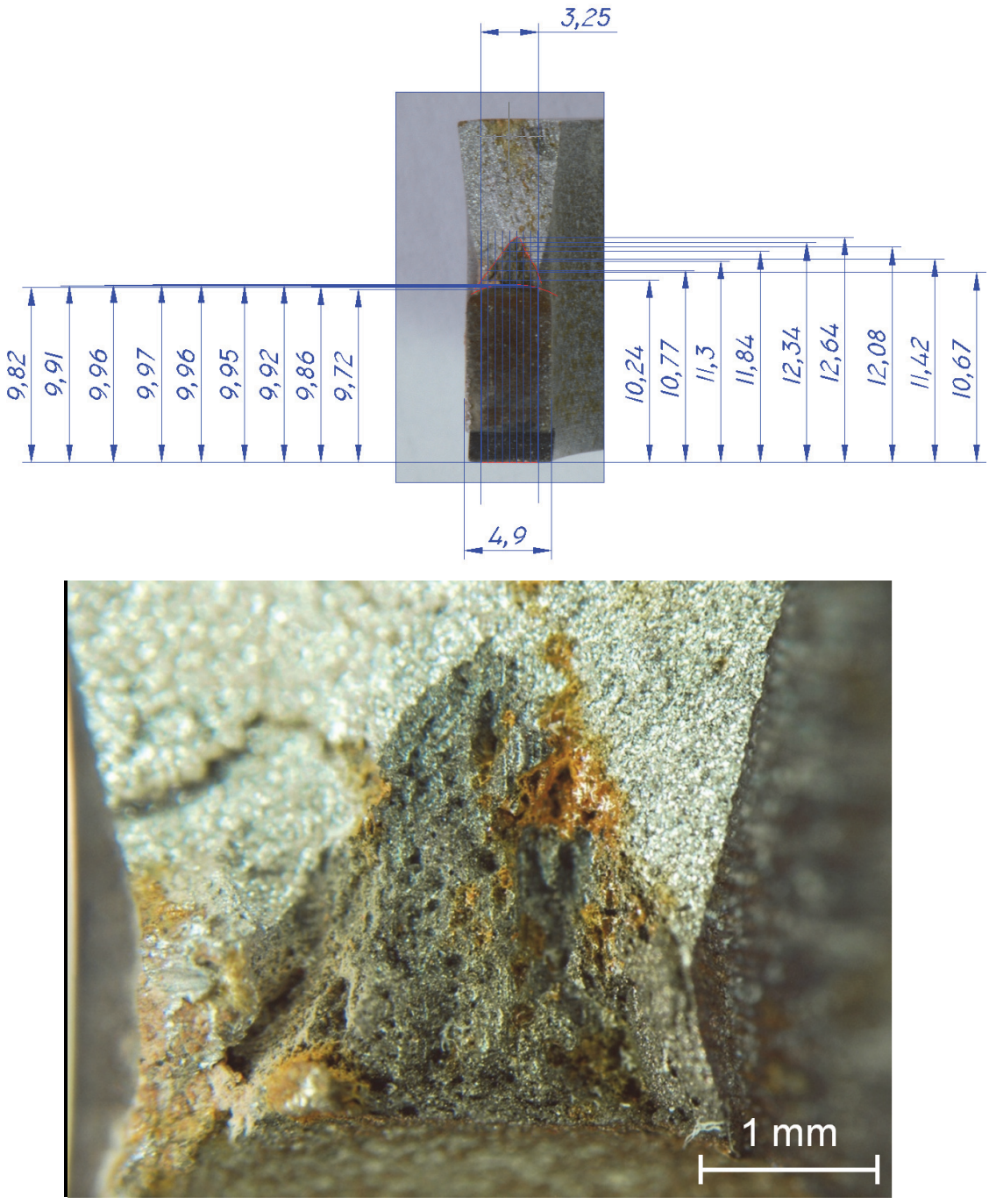

Figure 7.12. Determining the crack length on fracture surface and enlarged view of the crack front - example: specimen SL(89T)-17

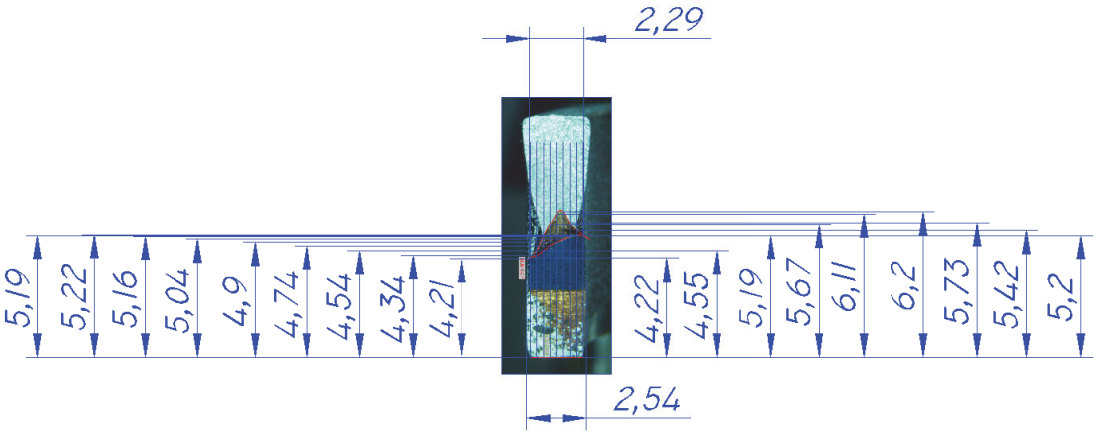

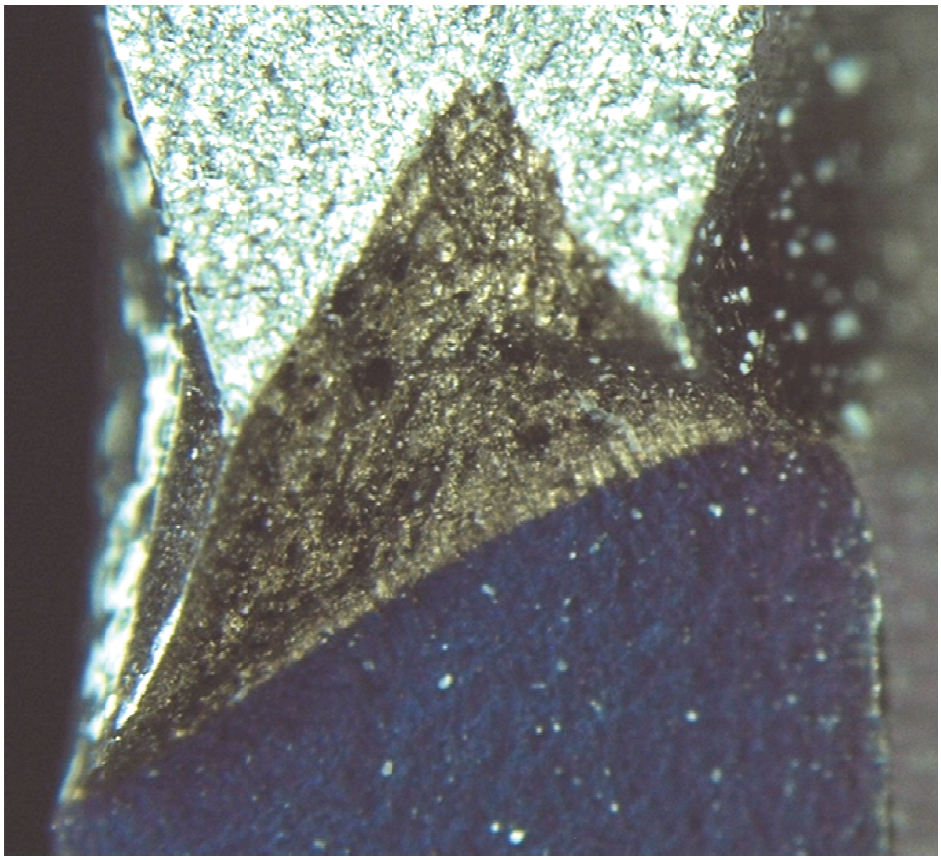

Figure 7.13. Determining the crack length on fracture surface and enlarged view of the final crack front - example: specimen S-BM(89)-10C

Fracture resistance curves (CTOD-Δ*a*) for several specimens which belong to different groups are given in figure 7.14. Generally, the range of the curves for seamless pipes is above the range obtained for the seam pipes. It should be noted that the curves for selected specimens, and not all of them, are shown in this figure.

In the next figures, the curves are grouped for better visibility and more convenient comparison and discussion. Some other specimens are also added, in addition to those shown in figure 7.14.

It should be noted that negative values of the crack growth are obtained by normalisation method for some specimens, in early growth stage. A possible reason is excessive plastic deformation preceding the crack growth and during the early stages of crack growth.

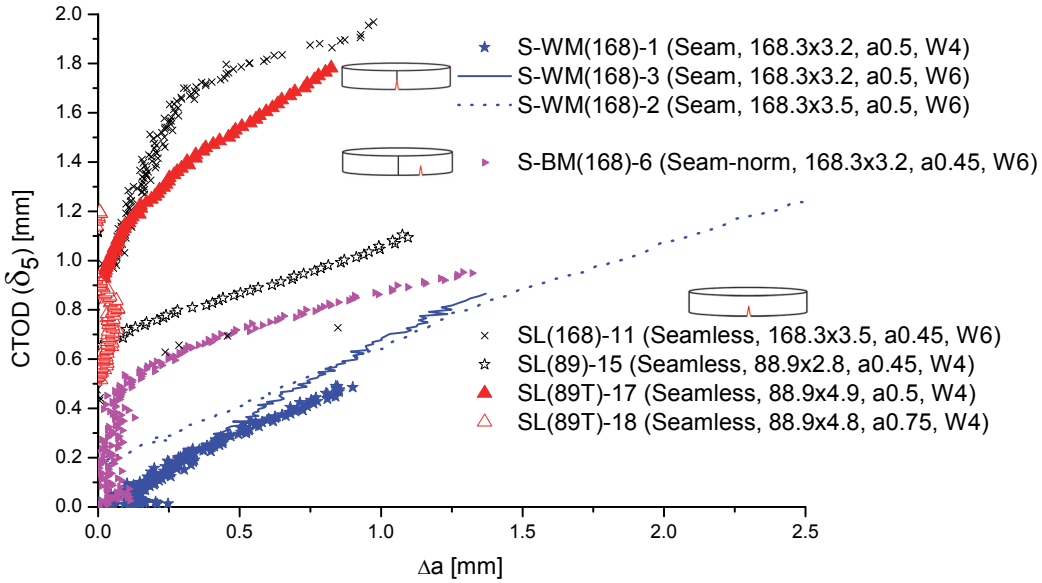

Figure 7.14. CTOD-Δa curves for different ring sizes and materials

Fracture resistance curves for the seam pipes with a notch in WM (seam) are shown in figure 7.15. The curves are very similar, despite the difference in final crack lengths (as mentioned previously, this is partially dependent on the moment when the operator ends the experiment). Another observation is that ratio *W/B* does not significantly influence the fracture resistance. This is important, because the testing results indicate much longer cracks (i.e. more pronounced ductile crack growth) for the increased ratio *W/B*. Repeatability is confirmed - the specimens with one of the notches on the seam exhibit similar results (crack growth resistance curves). Specimen S-WM(168)-5 is represented by one point due to very small crack length.

While the slope of the curve is not affected by the ratio *W/B*, increase of the specimen width *W* causes more pronounced crack growth, i.e. longer cracks.

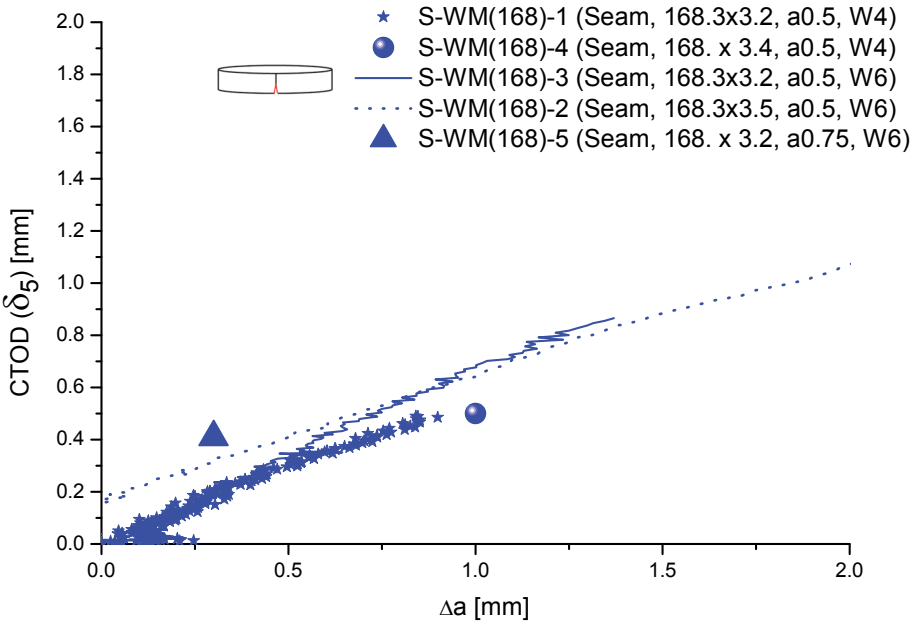

Figure 7.15. CTOD-Δa curves for rings with notches in the seam

Also, on the example of the seam pipes (diameter 168.3 mm), difference between BM and WM (seam) fracture behaviour is obtained, figure 7.16. The seam has lower fracture resistance, which is in agreement with the fact that larger crack length is measured in seam of all specimens from this group, [99, 101].

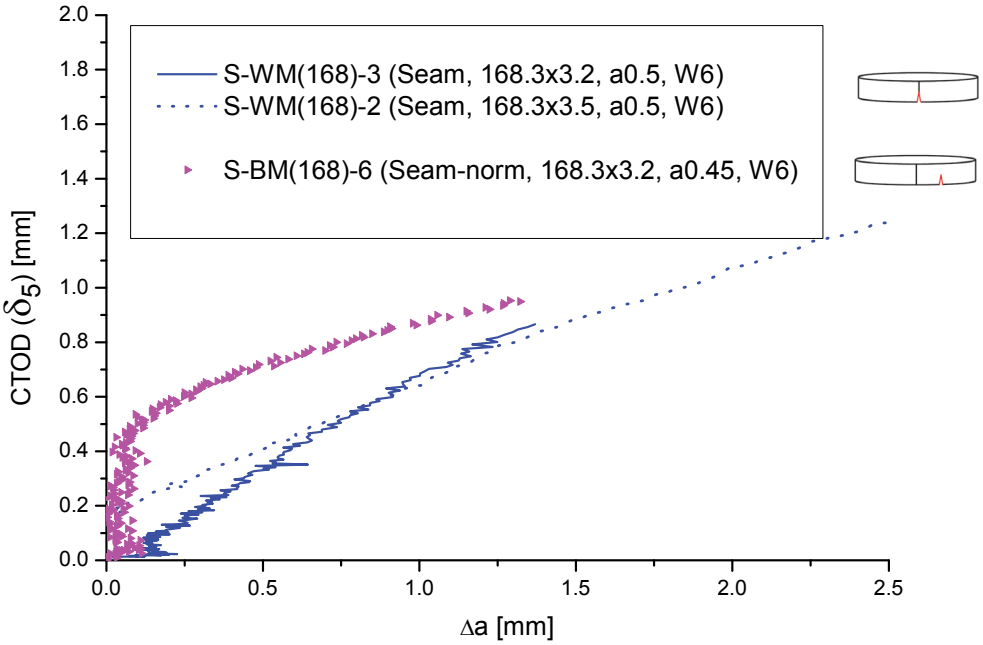

Figure 7.16. CTOD-Δa curves for rings with notches in the seam

Fractured specimen S-WM(168)-3 is shown in figure 7.17, with additionally highlighted crack fronts (initial and final) on each side. The crack in the weld metal is much longer, which is in agreement with the trend in figure 7.16.

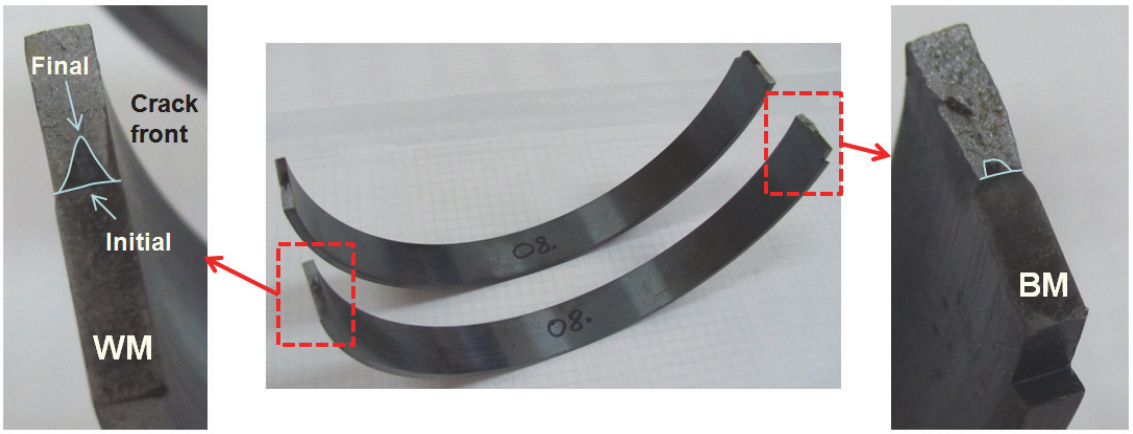

Figure 7.17. Fractured ring specimen S-WM(168)-3, with fracture surfaces in weld metal and base metal

In figure 7.18, a smaller-diameter seam pipe BM is shown, specimen S-BM(89)-9. It exhibits significant difference in comparison with the BM of the seam pipe with larger diameter, specimen S-BM(168)-6.

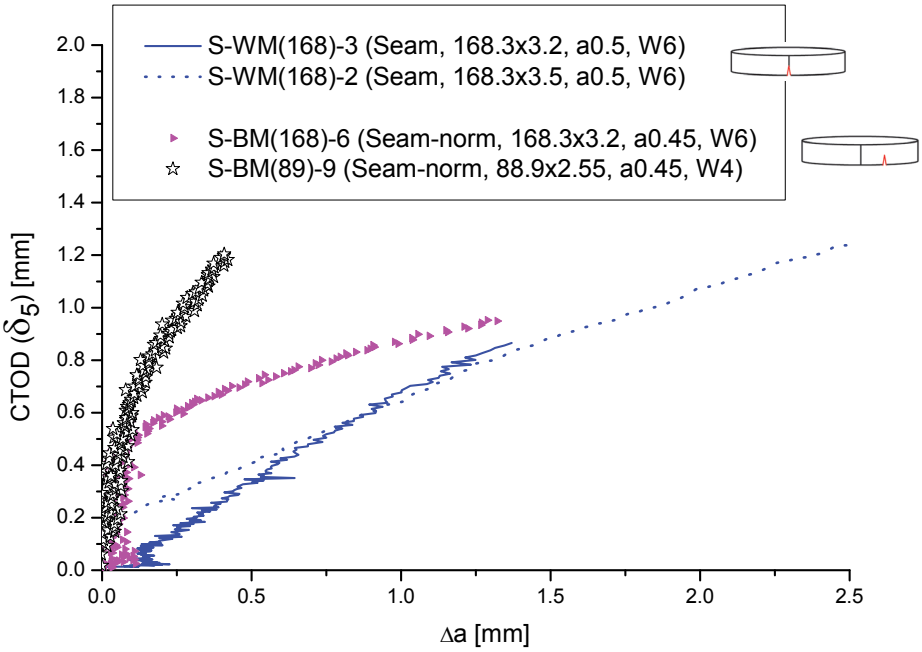

Figure 7.18. Crack growth resistance curves - seam specimen S-BM(89)-9 with notch in BM, D 88.9 (and 3 seam specimens D 168.3 for comparison)

Another specimen from the seam pipe BM (S-BM(89)-10C) with diameter 88.9 mm is added in figure 7.19. It has a pre-crack, unlike the specimen S-BM(89)-9 which is

notched. It can be seen that the difference between them is not so high. Also, the crack growh resistance for the BM of the seam pipe with diameter 88.9 mm (S-BM(89)-9, S-BM(89)-10C) is higher than that of the BM of the seam pipe with larger diameter (S-BM(168)-6).

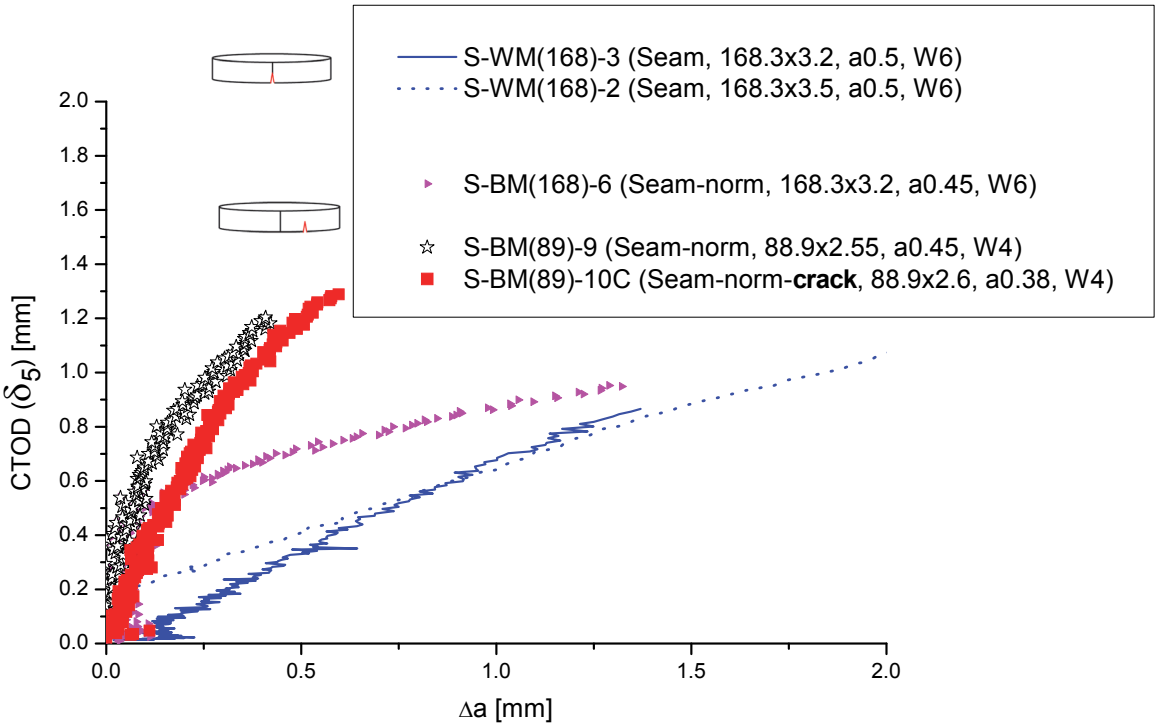

Figure 7.19. Crack growth resistance curves - 2 seam specimens with notch/crack in BM (S-BM(89)-9 and S-BM(89)-10C), D 88.9 (and 3 seam specimens with D 168.3 for comparison)

Next, seam pipes with a notch in WM are considered; specimens S-WM(89)-7 and S-WM(89)-8 in figure 7.20. The curve for the specimen S-WM(89)-7 almost coincides with the one for the BM (S-BM(89)-9), while specimen S-WM(89)-8 exhibit somewhat lower crack growth resistance.

Generally, testing of the pipe ring specimens successfully captured the difference in properties between the seam pipes with diameters 168 and 89 mm, although they were fabricated from the nominally same material, P235TR1. Also, it turned out that the fracture behaviour of the welded joint does not follow the same trend. The same methodology could be used to quickly assess the fracture resistance of the pipes from exploitation, by comparison with the material in as-received state.

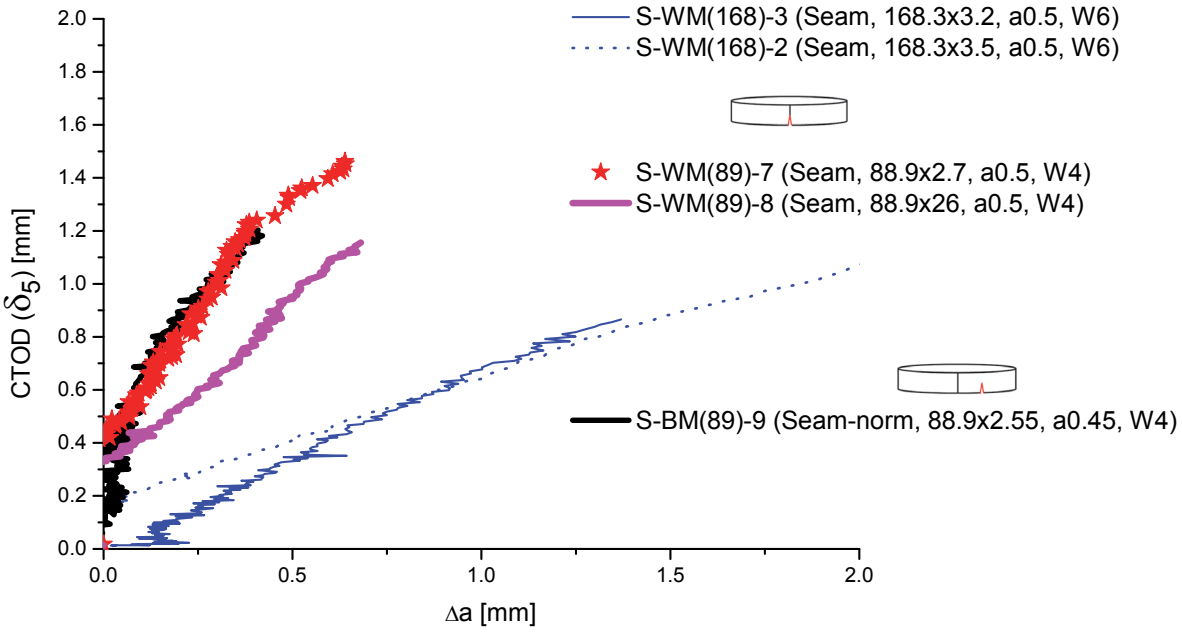

Figure 7.20. Crack growth resistance curves - 1 seam specimen with notch in BM (S-BM(89)-9) and 2 specimens with notch in WM (S-WM(89)-7 and S-WM(89)-8), D 88.9 (and 2 seam specimens D 168.3 for comparison)

Fracture resistance curves for selected seam/seamless rings are given in figure 7.21; it shows generally better fracture resistance of the seamless pipes in comparison with the seam ones with diameter 168.3 mm. Good examples for comparison are specimens S-BM(168)-6 and SL(168)-11 - seam and seamless pipes of similar dimensions, with notches positioned in the base metal. On the other hand, the seamless specimen SL(89)-15 with diameter 88.9 mm, exhibits lower crack resistance in comparison to the one with larger diameter (ring SL(168)-11).

Figure 7.22 shows a comparison of crack growth curves for four seamless specimens with similar dimensions (diameter 168.3 mm, wall thickness 3.5-3.6 mm and ratio *W/B*=6). Just for reference, two more specimens are shown - both made from seam pipes, with notches in BM (S-BM(168)-6) or BM and WM (S-WM(168)-2).

A very good repeatability is obtained for three pre-cracked specimens. Two other things can be seen from this diagram. First, the dependence of crack growth resistance on initial stress concentrator size is rather low - this can be seen by comparing the curves SL(168)-12C, SL(168)-13C and SL(168)-14C, which are almost identical despite different *a/W* ratios: 0.43, 0.53 and 0.46, respectively. On the other hand, the

dependence on the stress concentrator shape exists, and the notched specimen exhibits higher resistance than the ones with a pre-crack.

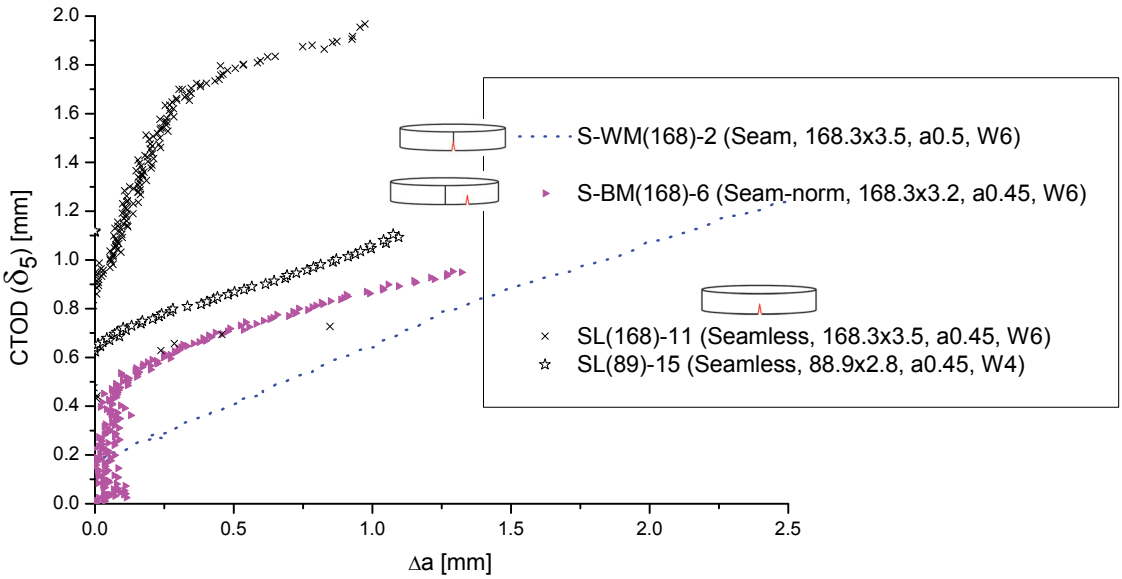

Figure 7.21. CTOD-Δa curves for seamless and seam rings with notches in the BM, as well as a seam ring with a notch in WM (specimen S-WM(168)-2)

The effect of crack length on fracture resistance was also non-pronounced on NIMOL 490K specimens from plate [92]. Generally, this can be seen as an advantage of PRNB geometry, since the fracture behaviour of standard fracture mechanics specimens often depends on the crack length. Mentioned example is analysed using the micromechanical model in the following chapter.

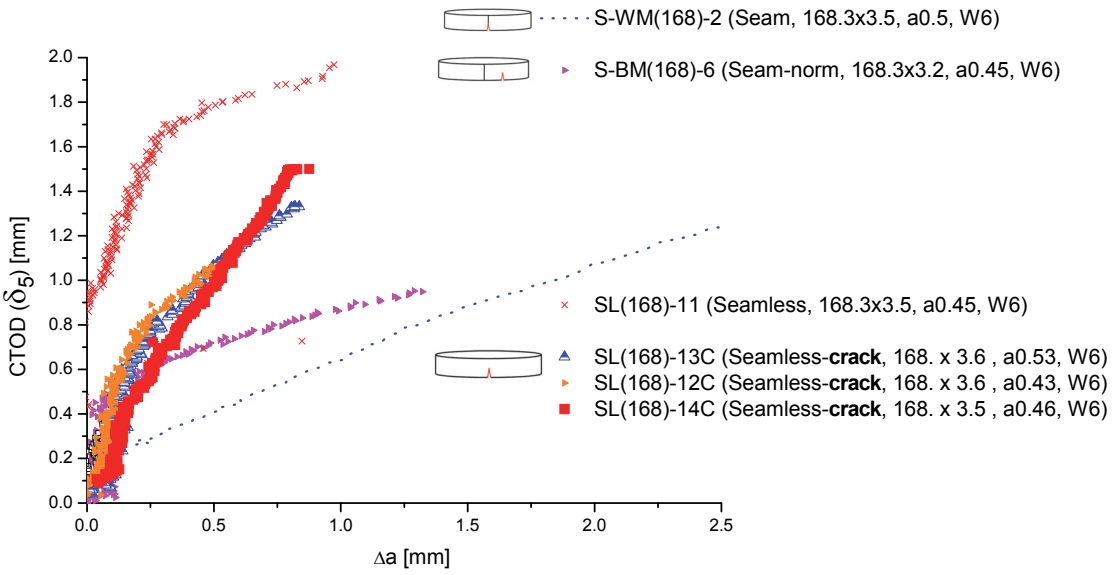

Figure 7.22. CTOD-Δa curves for seamless rings - notched and pre-cracked

The results can be related to dominant influence of material itself, instead of testing

geometry (defined by size of the specimen and size of the stress concentrator) - this is favourable for determining the fracture toughness of the pipeline material. On the examined pipes, the fracture properties determined by testing the PRNB specimens turned out to be different, despite quite similar tensile properties of the base metals.

Influence of *W/B* ratio on fracture resistance is shown in figure 7.23, for values of this ratio 4 (specimen 17) and 6 (specimens 20 and 21). It can be seen that the influence is very small. This is very important for fracture testing of thin-walled pipes by using PRNB specimens - e.g. for ratio *W/B*=2 (which is comparable with SENB specimens) the cracks may not grow. This is exactly what was obtained for specimens 22 and 23, which have ratio *W/B*=2, while their other dimensions are the same as those shown in figure 7.23. In other words, we will be able to measure the fracture resistance with the ratio *W/B* which may not correspond to a standard specimen.

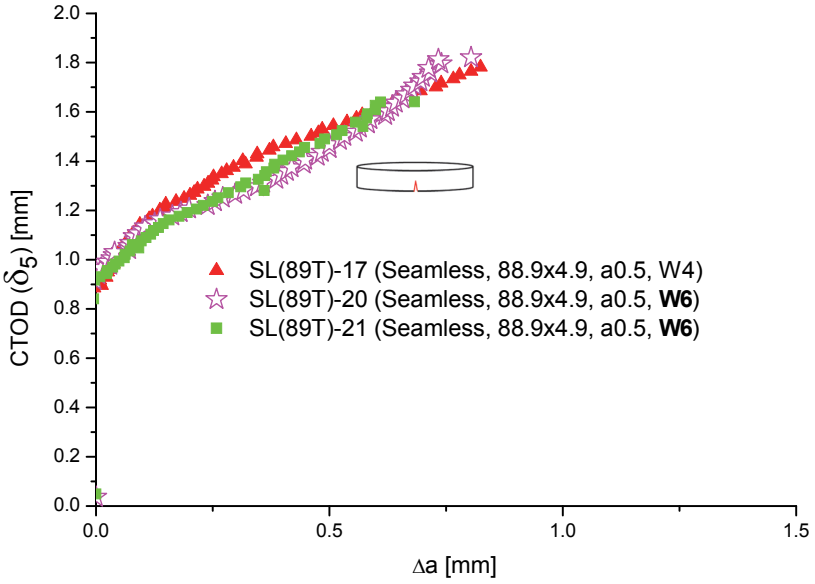

Figure 7.23. CTOD-Δa curves for seamless rings - influence of W/B ratio

Figure 7.24 show the final crack lengths on fracture surfaces, for some selected seam specimens. Two sides of the specimens are marked as "Aramis" side and "COD" side - due to the fact that stereometric displacement measurement is applied on the front side, while COD gauge is mounted on the back side. If the specimen contains a notch/crack in the seam, it is always on Aramis side of the specimen (S-WM(168)-1, S-WM(168)-2 and S-WM(168)-3). Seam pipes with *D*=168.3 mm, with one of the notches in seam exhibit a clear trend - larger crack growth in WM in comparison with BM, regardless of the fact that crack length in three specimens was different; figure 7.24.

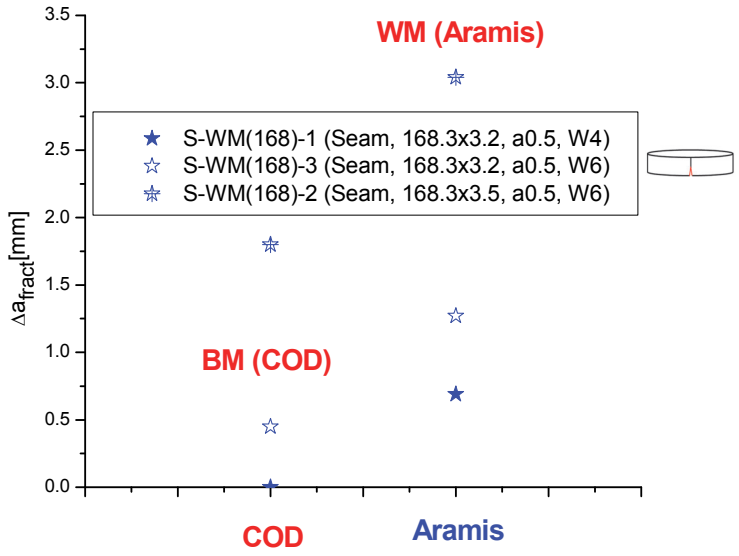

Figure 7.24. Final crack lengths measured on fracture surfaces - three seam rings

Crack lengths for several seamless pipes, D=168.3 and 88.9 mm, are shown in figure 7.25; there are no drastic differences in most cases when crack lengths on two specimen sides is considered (SL(89T)-17, SL(89)-15, SL(168)-11, SL(89T)-18 - very small crack growth generally).

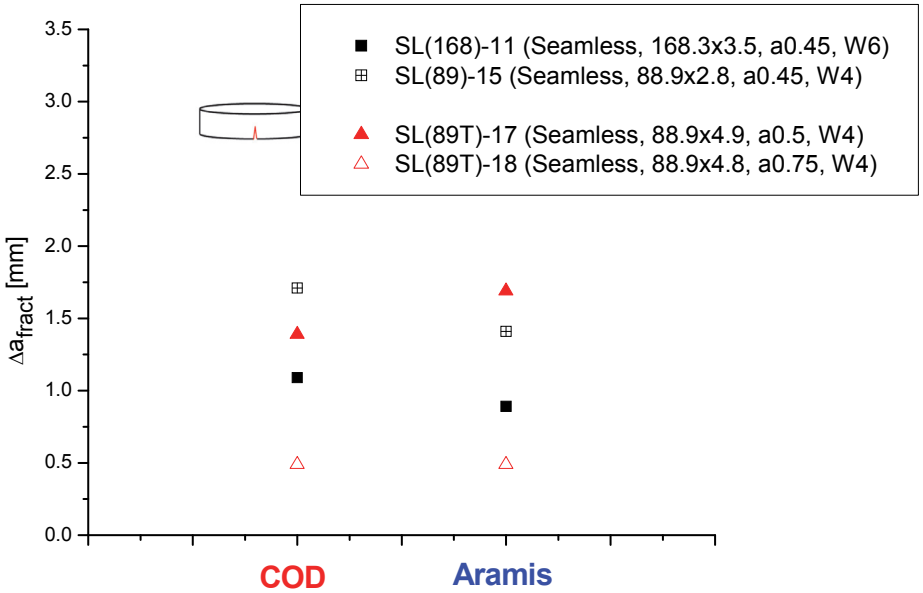

Figure 7.25. Final crack lengths measured on fracture surfaces - four seamless rings

As mentioned in the previous chapter, CT specimens were produced from one of the seamless pipes, with diameter 133 mm and wall thickness 11 mm. Having in mind larger wall thickness of this pipe, in comparison with the other ones, it was possible to fabricate the specimens for plane strain fracture reistance determination. Good repeatability is achieved, as shown in figure 7.26a. Fracture surface of one of the

specimens is shown in figure 7.26b.

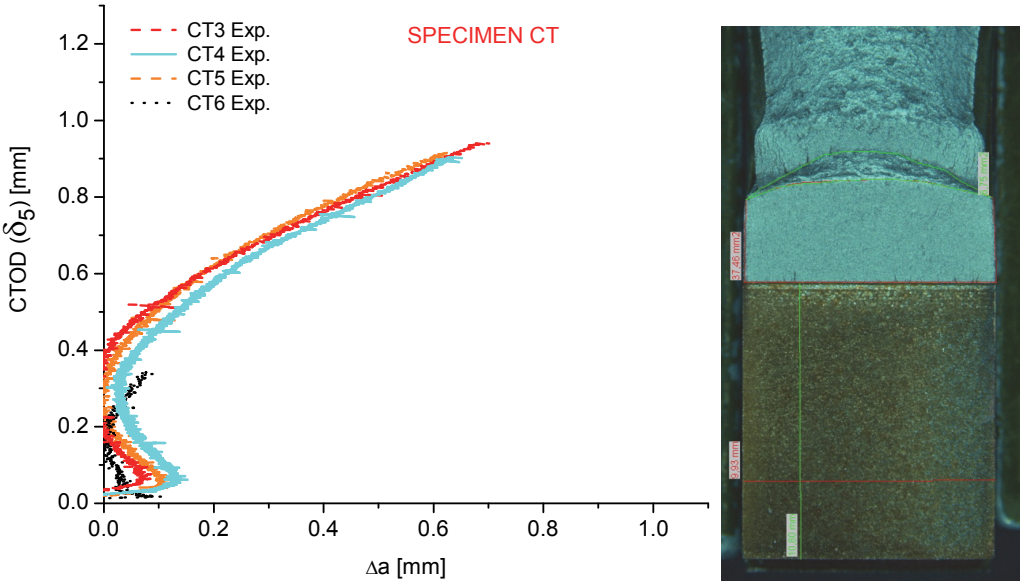

Figure 7.26. CTOD-Δa curves for CT specimens cut from the seamless pipe ∅133x11mm (a) and fracture surface (b)

Next, resistance to fracture initiation (crack growth onset) of the PRNB specimens is determined. Unlike the CT specimens, considered ring specimens do not have sufficient thickness for existence of dominant plane strain state; therefore, obtained values are called the critical values of the fracture mechanics parameter. Method from the procedure P2-92, and three characteristic values are determined: the one corresponding to the intersection of the crack growth curve and the blunting line $CTOD_{BL}$, for the crack growth 0.2 mm; parallel to the blunting line, $CTOD_{0.2/BL}$, and including the blunting, $J_{0.2}$. Although the values of these parameters are different, having in mind the different criteria, the trend clearly indicates a significant difference in behaviour of the examined materials, figure 7.27b.

Note: the blunting line is defined, in accordance with ESIS P2-92, as expression: $\delta = 1.87(R_m/R_{p0.2})\Delta a_B$.

Having in mind that the thin ring walls do not allow larger specimen thickness, the values obtained from figure 7.27 are not appropriate for fracture toughness determination in plane strain conditions. Therefore, micromechanical analysis is applied further in this chapter to determine the material plane strain fracture resistance, by forming of models of compact tensile specimens with the sufficient thickness and

material properties corresponding to the seam/seamless pipes.

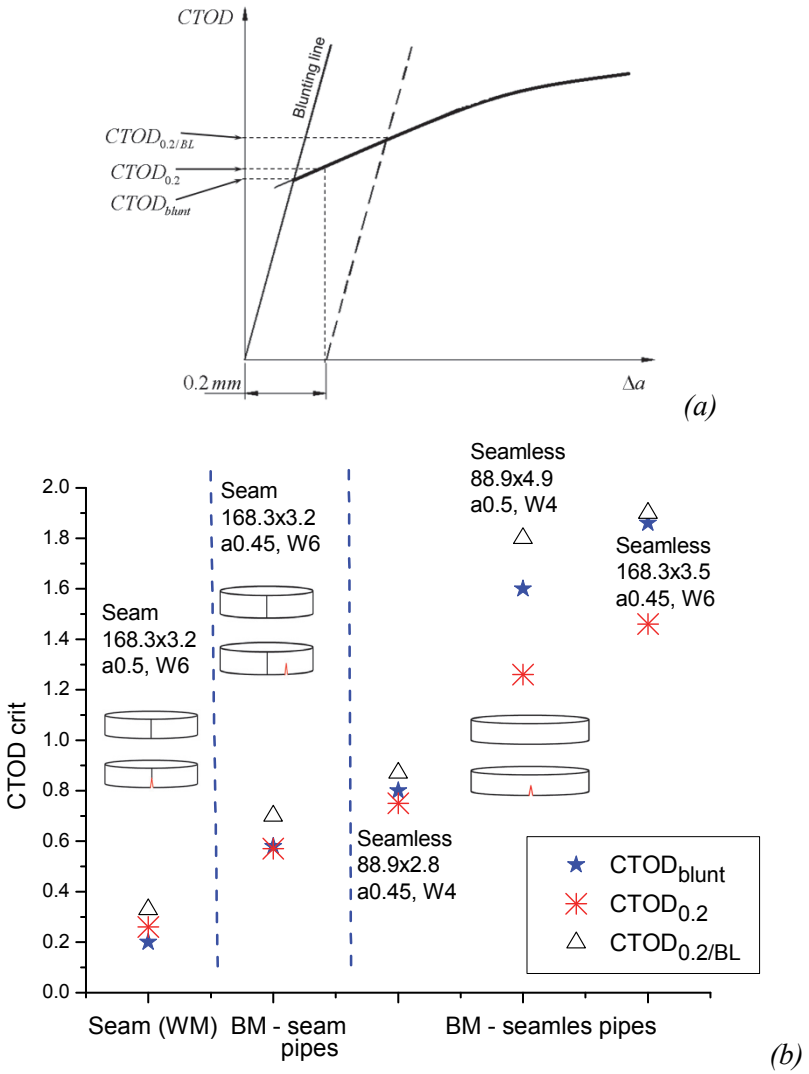

Figure 7.27. Critical CTOD values: determination scheme (a) and values obtained for ring specimens (b)

7.2 Tensile testing, hardness and microstructure

Testing of round tensile, RT, specimens fabricated from seam and seamless pipes resulted in ductile fracture of all specimens; necking is clearly visible on the specimen in figure 7.28. Nominal stress - strain curves are shown in figure 7.29. All specimens are fabricated with the same dimensions (nominal measures are shown in figure 6.13). All base materials, from seam and seamless pipe, are in relatively small range, while the welded joint (seam) has higher strength, on the example of the seam pipes with diameter 168 mm. Also, one specimen was fabricated from the hoop direction of the seamless

pipe with the highest wall thickness (133mm x 11mm), and it turned out that the tensile properties in this direction are very similat to the ones in axial direction.

Figure 7.28. A broken RT specimen

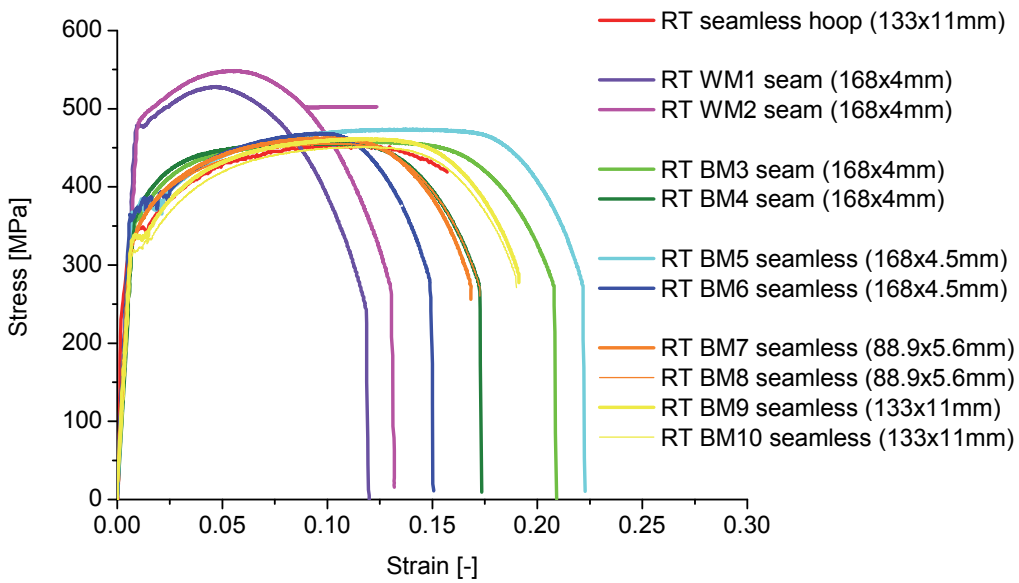

Figure 7.29. Stress - strain curves for seamless (P235GH) and seam (P235TR1) pipes

The curve obtained by tensile testing of high strength steel NIOMOL 490K is shown in figure 7.30. As mentioned previously, this thesis includes the micromechanical modeling of SENB and Ring specimens fabricated from this material. The strength is higher than the base materials of both seam and seamless pipes, and rather similar to the overmatched weld metal of the seam pipe. However, the ductility is much higher in comparison with the seam.

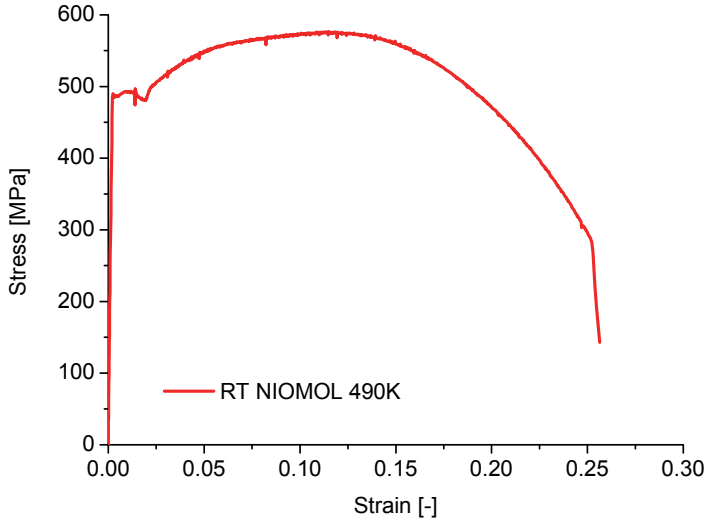

Figure 7.30. Stress - strain curves - NIOMOL 490K steel

Hardness profiles are determined for the seamless pipes, figure 7.31, and for the longitudinal weld (seam) region of the seam pipes, figure 7.32. For the seam pipe, it turned out that the hardness in the weld zone is higher than in the base metal, which is consistent with the results of tensile testing (overmatched joint). Also, seamless pipes generally have higher hardness values in comparison with the seam pipe base metal.

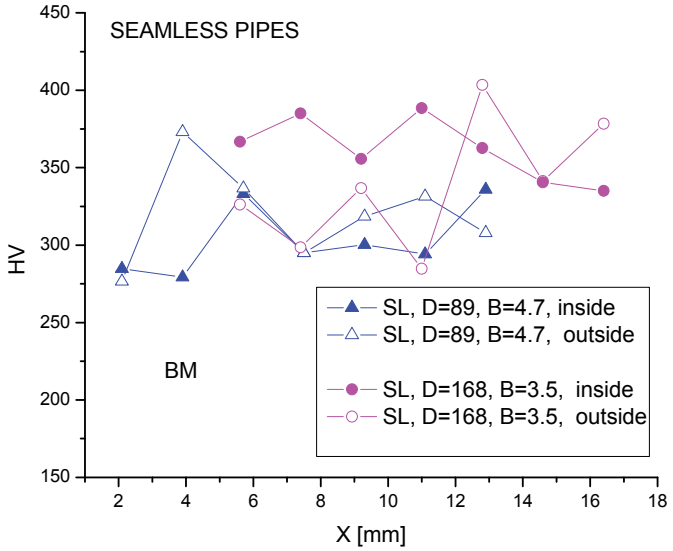

Figure 7.31. Hardness - seamless pipes

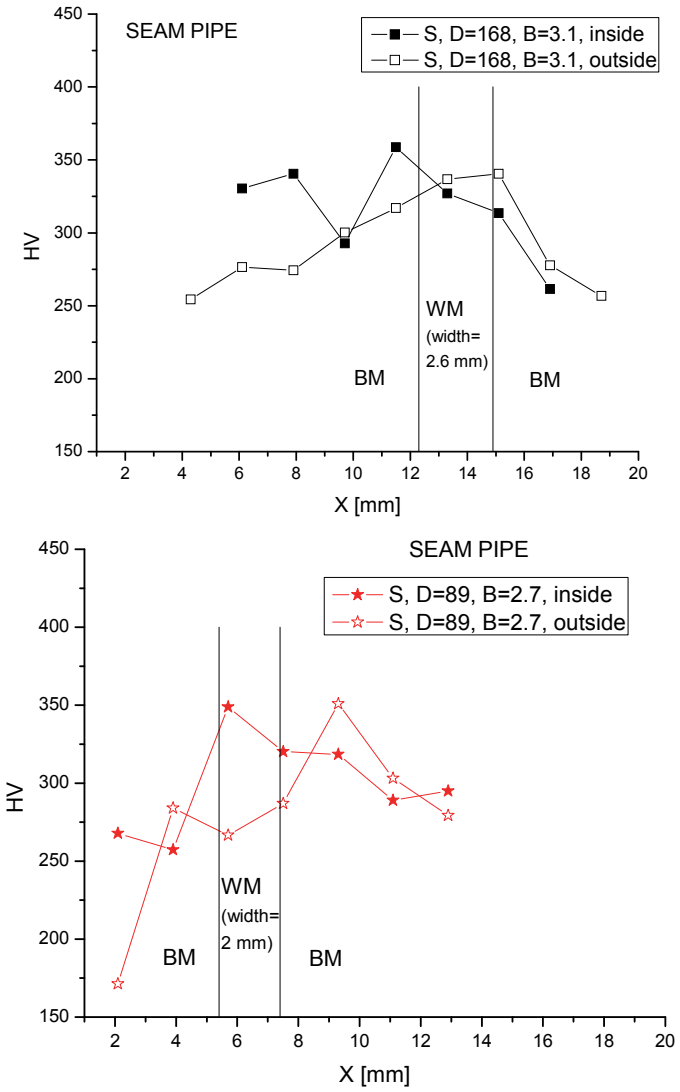

Figure 7.32. Hardness profile - seam pipes with D=168.3 mm and D=88.9 mm

The microstructure in the zone of the longitudinal weld (seam) is observed on the samples in the etched condition, figures 7.33- 7.38. Figures 7.33 - 7.35 correspond to the seam pipe with diameter 168.3 mm (which will be denoted as S168), while figures 7.36 and 7.38 correspond to the seam pipe with diameter 88.9 mm (which will be denoted as S89).

The base metal microstructure for both seam pipes (figures 7.33a and 7.36a) consists of two microconstituents. One microconstituent is ferrite, which can be seen on the light optical micrographs as white grains, while the second microconstituent is pearlite, represented as black colored islands at the boundaries of the ferrite grains. Similar microstructure is observed on the seamless pipe samples in etched condition.

On the other hand, the weld metal microstructure is shown in figures 7.33b and 7.36b. On the presented micrographs ferrite is observed in the form of side plates nucleated at the austenite grain boundaries, while the presence of the fine acicular ferrite and ferrite-carbide aggregates (pearlite) can also be found. Presence of the primary intragranular polygonal ferrite is, however, observed in the specimen S89 weld metal (figure 7.36b).

Figure 7.34a shows the transition between the base metal and HAZ for the pipe S168. A change of the grain size is observed and the beginning of the BM-HAZ transition is approximately marked. Figure 7.34b is enlarged view of a part of the same microphotograph. Similar structure of BM and HAZ is observed in this part of transition zone. Figures 7.35 and 7.38 show the entire HAZ width, which enabled estimation to approximately 0.35 and 0.4 mm for the specimens S168 and S89, respectively. Heat affected zone is significantly narrower than the weld metal, which is expected for the pipe fabrication procedures. It is previously mentioned that the structure of HAZ is similar to that of the BM; in figure 7.35 microstructure in HAZ similar to WM structure is observed only close to the fusion line.

The change in microstructure between the welded joint zones (examples are shown in figures 7.34, 7.35, 7.37 and 7.38) enabled determination of the weld metal and HAZ width. The average weld metal width is 2.6 mm for the pipes with diameter 168.3 mm (specimen S168) and 2 mm for the pipes with diameter 88.9 mm (specimen S89). As mentioned previously, estimate of the HAZ width is approximately 0.35 mm for S168 and 0.4 for S89. In the numerical models, HAZ is not taken into account, having in mind that crack growth occurs through the weld metal and HAZ dimensions are small; such configuration is typically treated as bimaterial BM-WM in the literature [102-106].

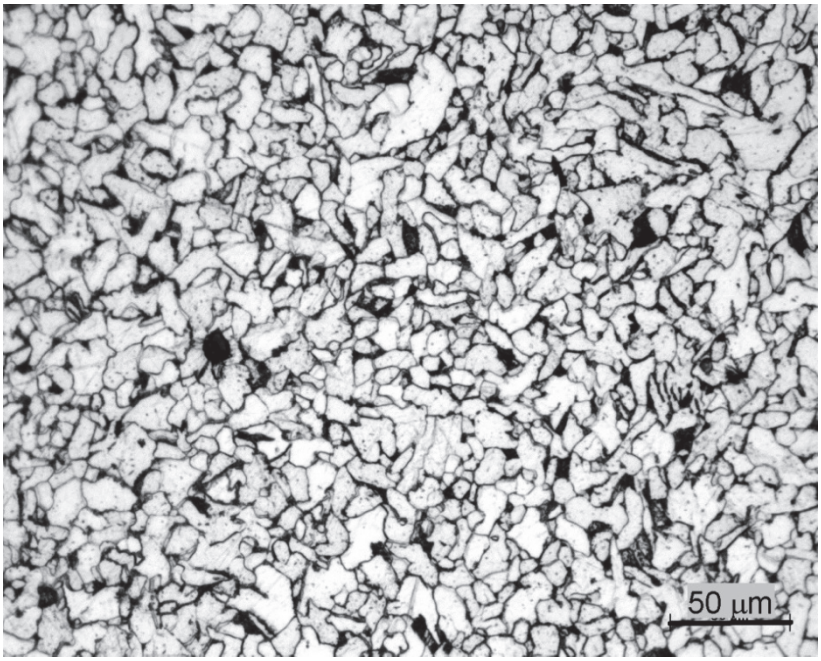

(a)

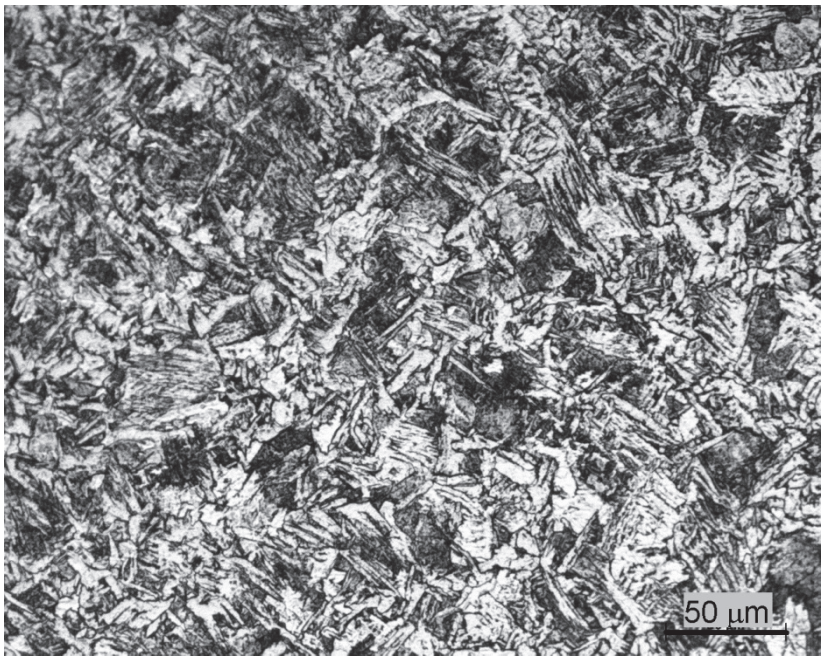

(b)

Figure 7.33. Base metal (a) and Weld metal (b) of a seam pipe - specimen S168

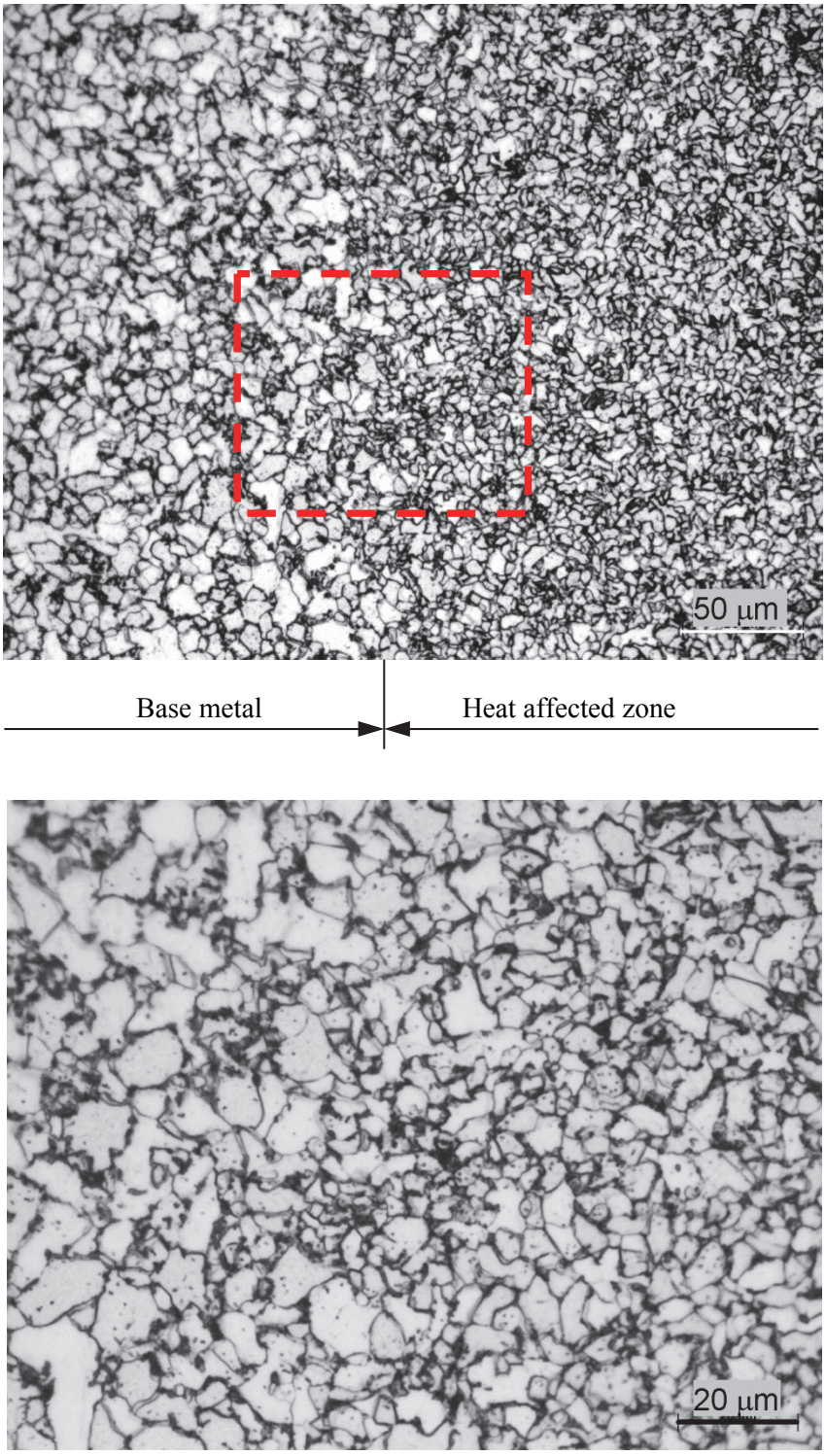

Figure 7.34. Transition Base metal - Heat-affected zone in a seam pipe (different magnifications) - specimen S168

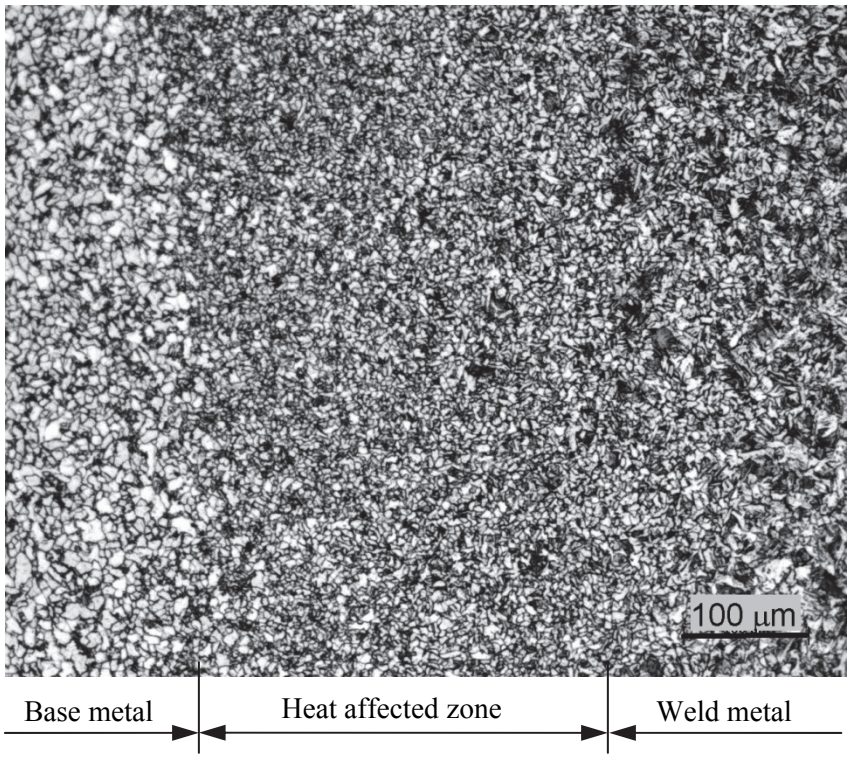

Figure 7.35. Transition Base metal - Heat-affected zone - Weld metal in a seam pipe - specimen S168

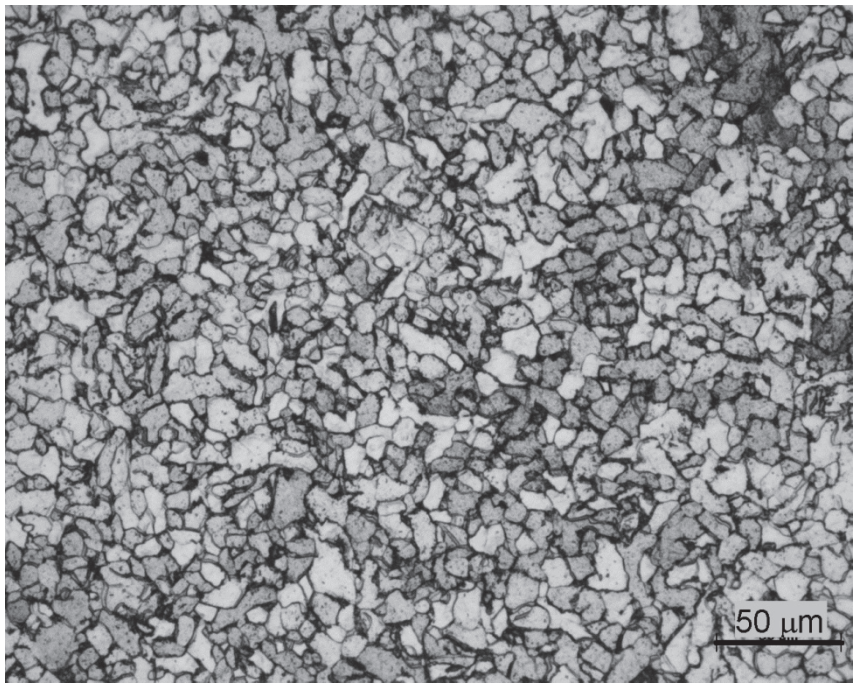

(a)

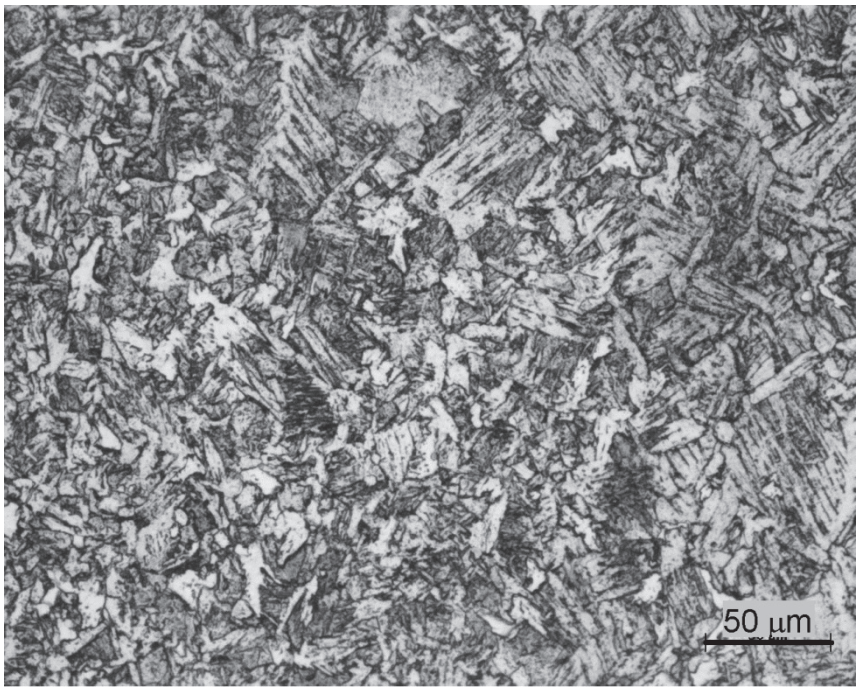

(b)

Figure 7.36. Base metal (a) and Weld metal (b) of a seam pipe - specimen S89

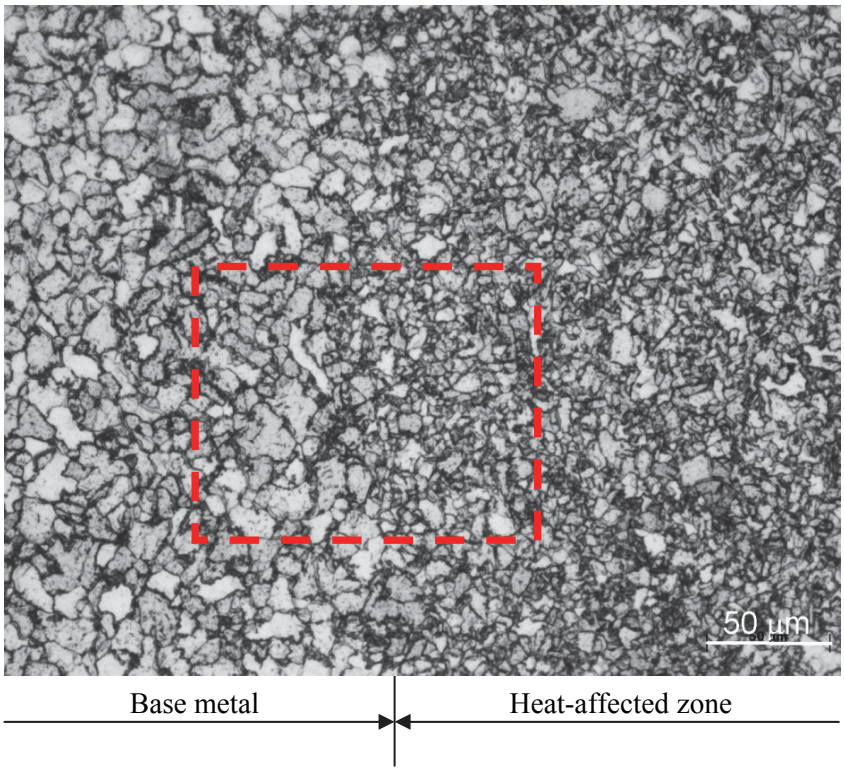

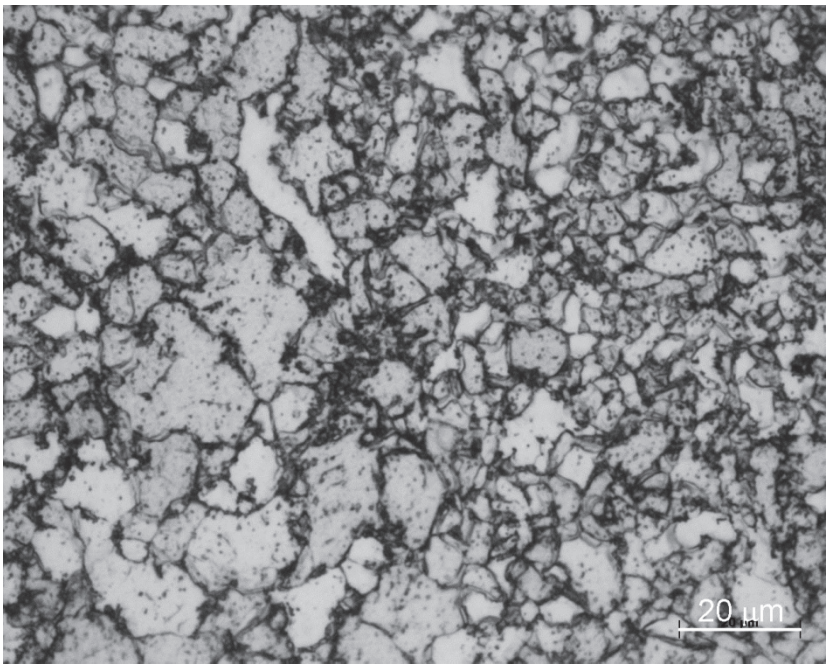

Figure 7.37. Transition Base metal - Heat-affected zone in a seam pipe (different magnifications) - specimen S89

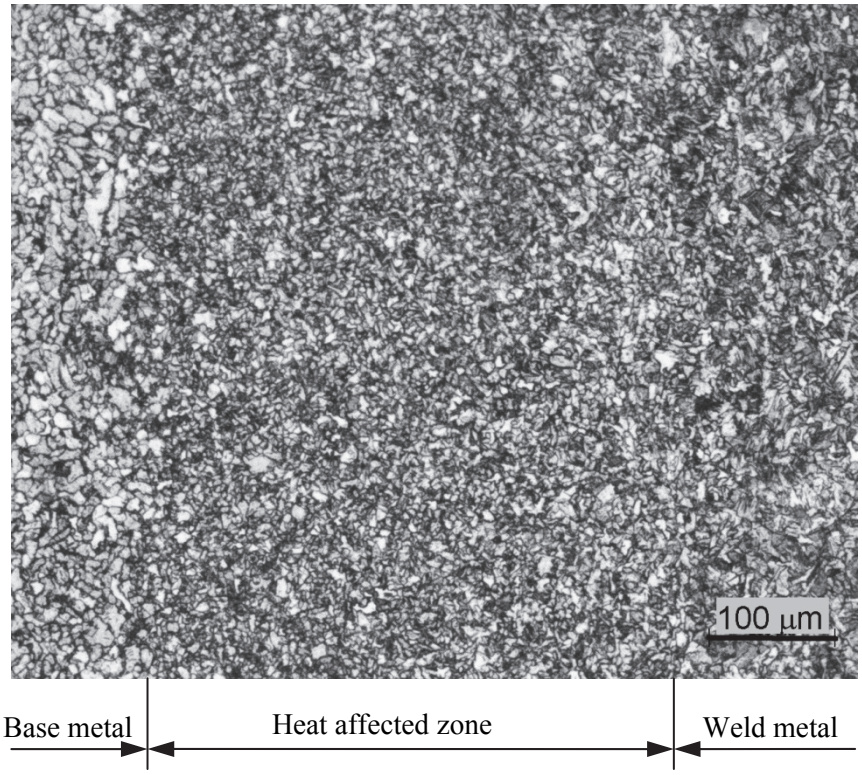

Figure 7.38. Transition Base metal - Heat-affected zone - Weld metal in a seam pipe - specimen S89

Volume fraction of inclusions in BM and WM of the seam pipes, as well as in the base metal of the seamless pipes, is determined by quantitative microstructural analysis (as-polished state of the surface, without etching). These values are applied in micromechanical analysis of fracture of rings, as initial values of the void volume fracture, i.e. damage parameter. Much larger content is observed in the seam pipe BM in comparison with the seamless one; the values are 2% and 0.7%, respectively. But, it turned out that the weld metal of the seam pipe contains significantly lower amount of inclusions - 0.7%, same as the seamless pipe base metal. The testing results are summed in table 7.1. In addition to the materials of the seam and seamless pipe, data for NIOMOL 490K are given.

Table 7.1. Micromechanical parameters of the seam pipe (base metal and weld metal), seamless pipe and plate material

	f_v [%]	f_v [-]	λ [μm]
Base metal (seam pipe S168)	2.02	0.0202	427
Weld metal (seam pipe S168)	0.72	0.0072	705
Seamless SL168	0.72	0.0072	640
NIOMOL 490K	0.94	0.0094	578

Next figures (7.39 - 7.41) show some characteristic examples of inclusions observed in the examined pipeline materials in the unetched as-polished state. Figures 7.39 and 7.40 are from the base material and weld metal of a seam pipe, while figure 7.41 corresponds to the base metal of a seamless pipe. It should be emphasized that these are only examples, while quantitative analysis is performed on a larger number of such images.

Most of inclusions observed on the microphotographs are sulphides and oxides, in both seam and seamless pipe samples. Sulfide inclusions, *i.e.* MnS, can be seen as elongate gray particles with rounded edges in the longitudinal plane on the base metal polished surface of a seam pipe (figure 7.39). On the other hand, exept sulfide inclusions presence on the weld metal polished surface of a seam pipe silicate inclusions are also identified in the form of clusters of individual inclusions (figure 7.40). On the micrographs representing the polished unetched surface of a seamless pipe (figure 7.41), exclusively sulfide and oxide inclusions can be seen.

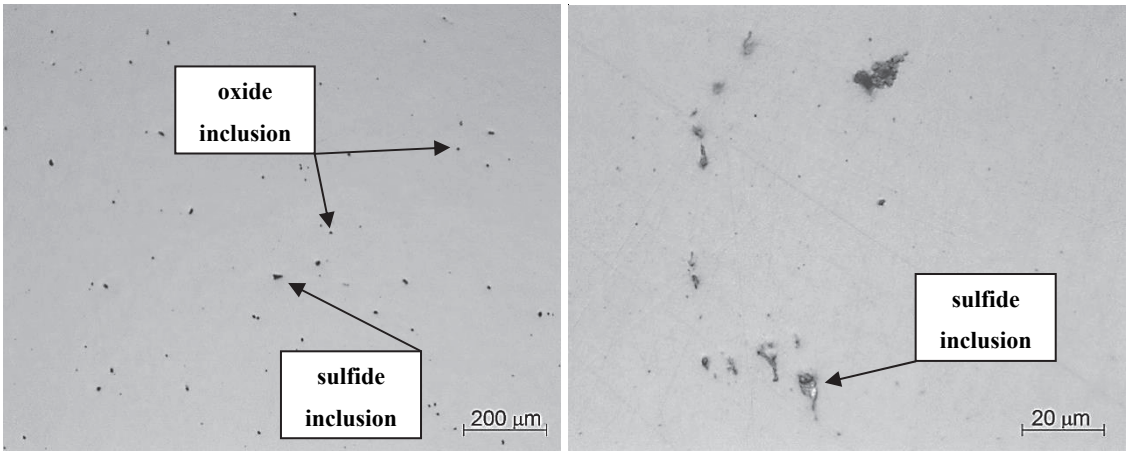

Figure 7.39 Base metal of a seam pipe (polished surface) - inclusions

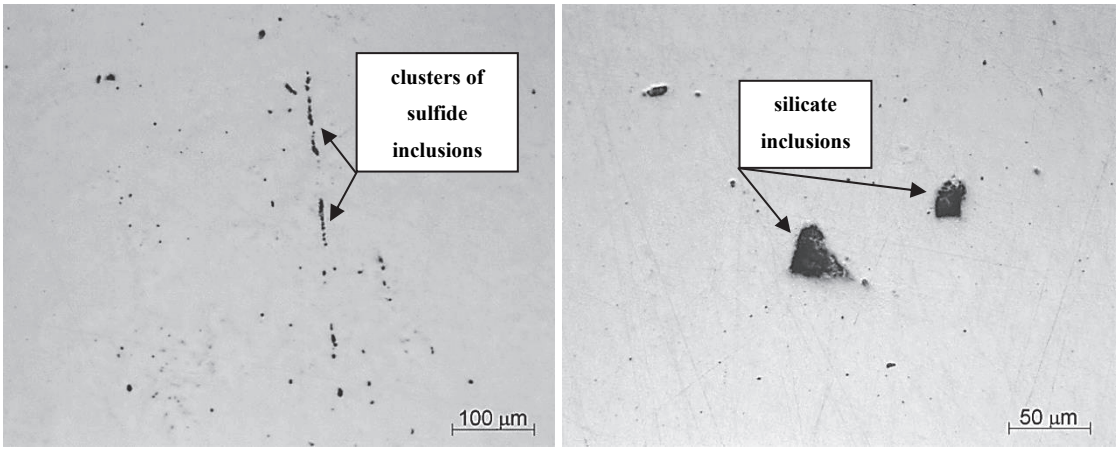

Figure 7.40. Weld metal of a seam pipe (polished surface) - inclusions

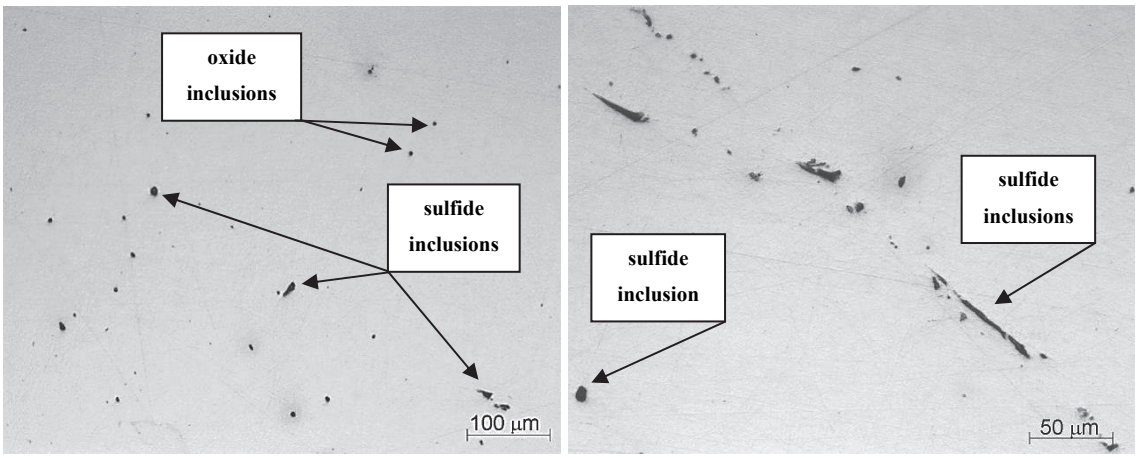

Figure 7.41. Material of a seamless pipe (polished surface) - inclusions

7.3 Ring-shaped specimens - micromechanical fracture analysis

In this chapter, the fracture of ring-shaped specimens is analysed using the micromechanical model CGM. The inputs for analysis of fracture are following experimentally determined data: stress - strain curve obtained from tensile testing and volume fraction of inclusions, determined by quantitative microstructural analysis (this value is used as the initial value of damage parameter).

7.3.1 High strength low alloyed steel NIOMOL 490

Micromechanical analysis is first done on the SENB and PRNB specimens cut from the steel plate (material NIOMOL 490); the aim was comparison of fracture conditions in these two specimen geometries. Their experimental testing is performed in the

dissertation of A. Likeb [92], and some of these results are also shown here, with added results of the numerical models.

Depencence of the external loading (force) on the crack tip opening displacement CTOD is given in figures 7.42 and 7.43. Examined SENB and Ring-shaped (PRNB) specimens had similar cross-section dimensions.

For each geometry, three specimens are tested. Since the results of the ring specimens practically coincide, one experimental line is shown in figure 7.43. The curves for SENB and PRNB specimens are similar with respect to their shape and the highest CTOD values.

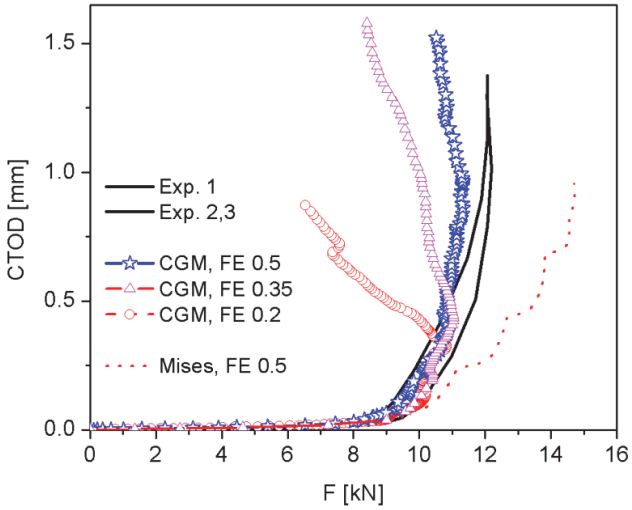

Figure 7.42. F-CTOD curves for SENB specimens - NIOMOL 490 [107]

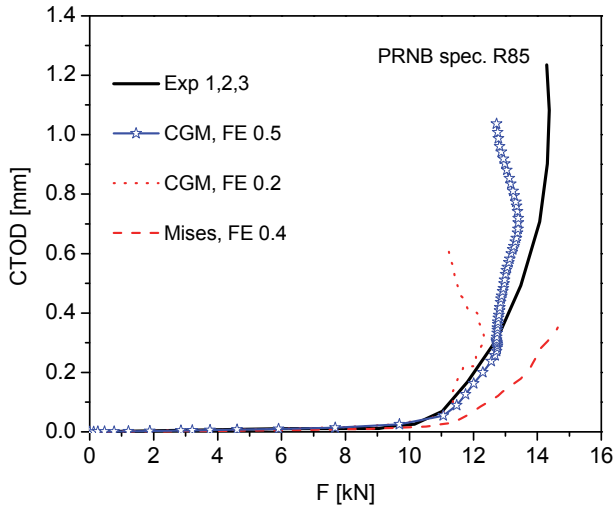

Figure 7.43. F-CTOD curves for PRNB specimens - NIOMOL 490 [107]

As for the micromechanical model, *F*-CTOD diagrams reveal that FE dimension 0.5

mm results in a reasonably good agreement with experiment. If finite element size is decreased, loss of load carrying capacity is much more rapid, figures 7.42 and 7.43. For von Mises plasticity (of course, this means that the crack is stationary), the load carrying capacity is overestimated.

When larger elements are considered (i.e. larger than 0.5 mm), smaller crack growth values are obtained, which does not correspond with experimental data. "This can be clearly seen by comparing the CTOD values corresponding to the fixed crack growth value Δa=0.7 mm, Table 7.2. Therefore, approximate element size 0.5 mm is selected as appropriate for the analysed material, and transferred to the ring geometries", [107, 108].

Table 7.2. CTOD values obtained for Δa=0.7 mm, for different FE sizes - SENB specimen

	SENB		
	Experiment	CGM (FE = 0.5 mm)	CGM (FE = 0.7 mm)
CTOD [mm] (for crack growth Δa=0.7 mm)	1.08	1.21	1.76
	1.17		
	1.32		

The element size obtained on SENB specimen is applied in analysis of fracture of ring geometries, i.e. it is transferred. To be more precise, it may be slightly different due to the particular model geometry, but it was always between 0.45 and 0.5 mm.

For the examined material, the most suitable size of the finite element approximates the mean free path between non-metallic inclusions (λ, Table 7.1). The relation between the FE size and material microstructure, expressed through λ, has been considered in many studies, including [109-114]. The FE size was determined as equal to λ in some of these studies, but this can not be regarded a rule. A more important conclusion from the mentioned studies, especially [109] and [110], is that the relationship between them exists - finite element size (as numerical parameter) depends on the mean free path between the inclusions (as microstructural parameter). This leads to transferability of the FE size, which is applied here, as mentioned previously.

Relatively large dimensions of FE obtained for NIOMOL 490, i.e. transferred from

SENB specimen (0.5 mm) actually had an effect on the model geometry of the Ring R85. Since the machined notch has radius of 0.25 mm, geometry of the notch could not be formed properly in the numerical model by using elements with size 0.5 mm. Therefore, the model of the notched specimen R85 is formed with a sharp crack.

Fracture resistance curves are shown in figures 7.44 and 7.45; for the Ring specimens, two points were obtained from experiment, one for crack growth initiation and one for final fracture.

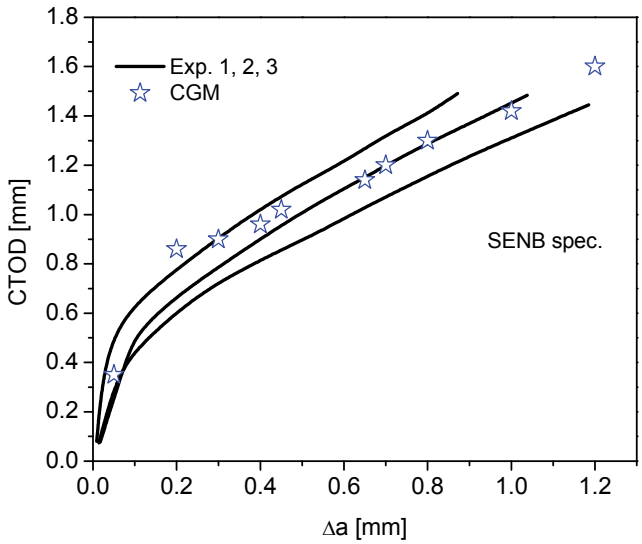

Figure 7.44. CTOD-Δa curves for SENB specimens [107]

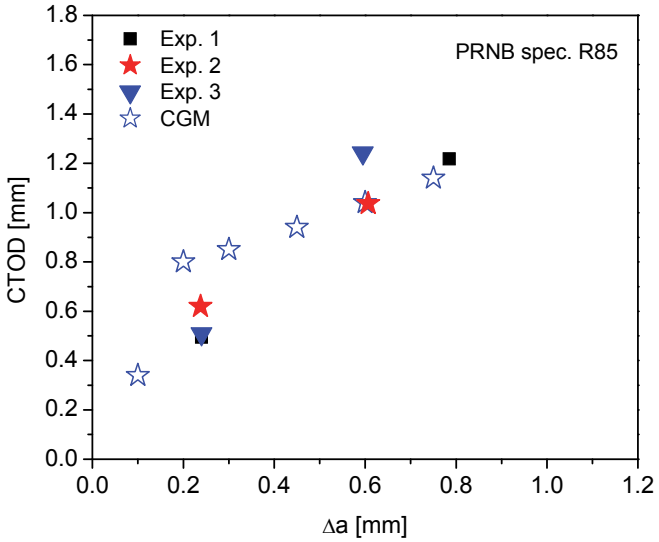

Figure 7.45. CTOD-Δa curves for Ring specimens [107]

Failure in any integration point is predicted when the damage parameter reaches the value f_F - void volume fraction at final fracture. In CGM, this value is calculated as:

0.15 + 2:f_0, as mentioned in the chapter dealing with micromechanical models. The crack initiation in the numerical model is shown in figure 7.46a; the field shown is the porosity, i.e. damage parameter of the Gurson-based micromechanical models. Stable crack growth in the model corresponds to the characteristic ductile fracture crack front shape, figure 7.46a. The increase of porosity in the mid-thickness position (position of growth initiation) is shown in figure 7.46b. It can be seen that a significant and rapid increase of porosity occurs after the critical value is reached, and that f_F is soon reached.

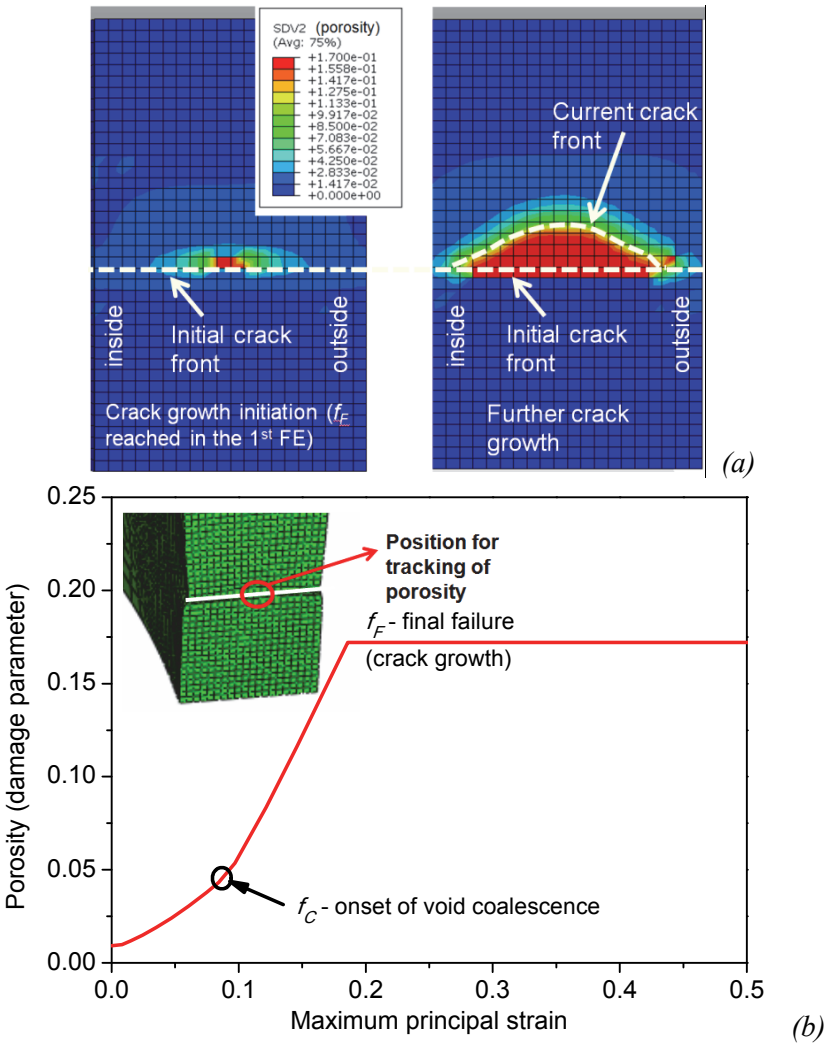

Figure 7.46. Damage parameter distribution (a) and change of damage parameter during the loading (b) - PRNB specimen

The results obtained from testing the SENB specimens and Ring specimens (R85) with the same cross-section suggest that their fracture conditions are similar. On force - CTOD curves, similar shape and maximum CTOD values are observed. Although two points (initiation and final failure) are obtained for rings on the crack growth curves, it

can be said that the trends in the range of crack growth of both specimen types are rather similar. Further, the stress triaxiality values in the middle of both specimens do not differ significantly, which is shown in the following text.

Next, PRNB specimens with different dimensions are examined. Different radius is used, but the ratio *R/B* was constant, i.e. decrease of radius leads to decrease of wall thickness. The force-CTOD curves in figure 7.47 show the effect of the dimensions of the specimen and defect. Although the stress concentrators are different for the two specimen sizes (R85 were notched, while R60 were pre-cracked), the trends of the curves are similar. The model predicts somewhat more pronounced loss of the load carrying capacity, especially for higher CTOD values.

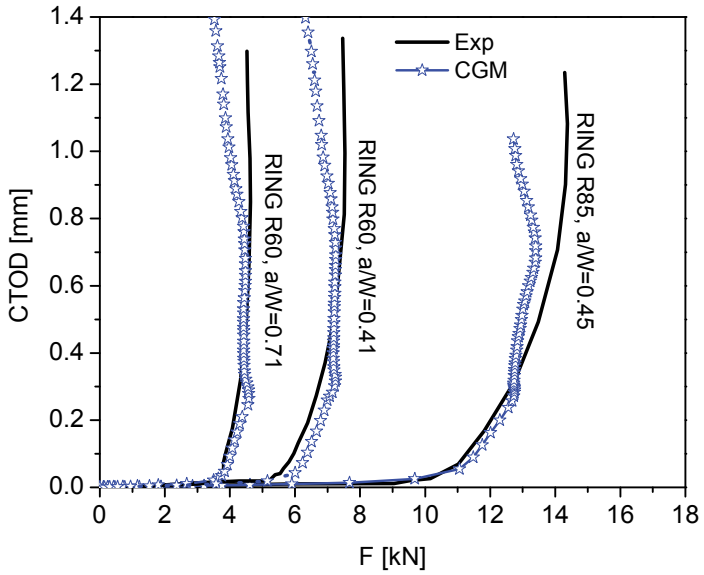

Figure 7.47. F-CTOD curves for PRNB specimens - influence of ring radius and crack/notch length

Stress triaxiality is also examined, as a very important quantity for ductile fracture. It is tracked at the finite element in the middle of the initial notch or crack front (just like porosity in figure 7.46b). All PRNB specimens (and also SENB specimen) have similar dependences of triaxiality on the maximum principal strain, figure 7.48.

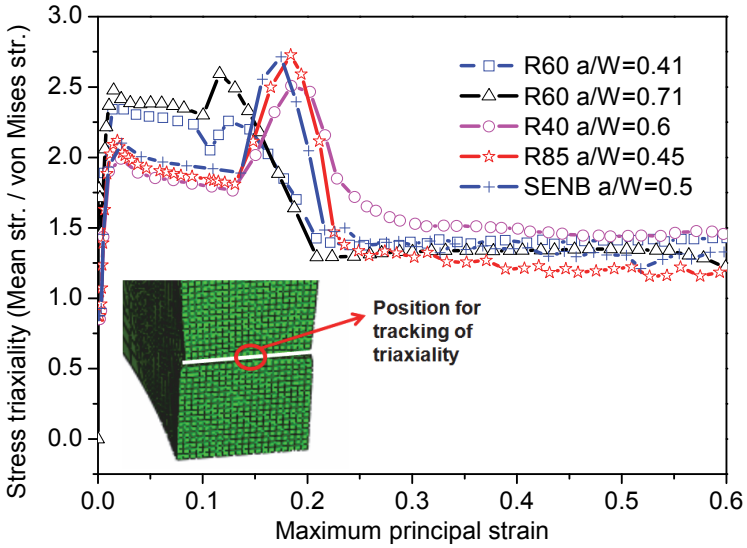

Figure 7.48. Stress triaxiality during the increase of loading

Experimental crack resistance curves are shown in figure 7.49a. As mentioned previously, only the growth onset and final fracture points are obtained (3 pairs of points for 3 specimens) for the notched R85 rings. Remaining curves are obtained by application of the normalisation procedure.

Prediction of fracture resistance curves obtained by the micromechanical model CGM is given in figure 7.49b. Pre-cracked specimens with radii 60 and 40 mm do not exhibit large differences, despite a wide range of a/W ratio - for R60 rings, 0.41 and 0.71. Just like in the experiment, notched specimen R85 has lower fracture resistance. However, this can not be taken as the isolated influence of the radius increase - because the ratio R/B was nearly constant for all geometries. With radius increase to 85 mm, thickness is also increased, which contributes to lower resistance to fracture initiation and development.

Crack resistance curves reveal some important data - specimen radius, initial defect shape and size do not have a very pronounced influence on fracture development. The influence of geometry of both specimen and stress concentrator on the crack growth resistance predicted by the micromechanical model corresponds to the experimentally determined trends, figure 7.49.

The critical value of void volume fraction f_c is calculated during the analysis if the CGM is applied, as mentioned in the chapter about the micromechanical modelling. The value of this parameter ahead of the initial crack front is shown in figure 7.50 (PRNB - R60).

The values are variable, which is not the case if GTN - Gurson-Tvergaard-Needleman model is used, where f_c is a material parameter.

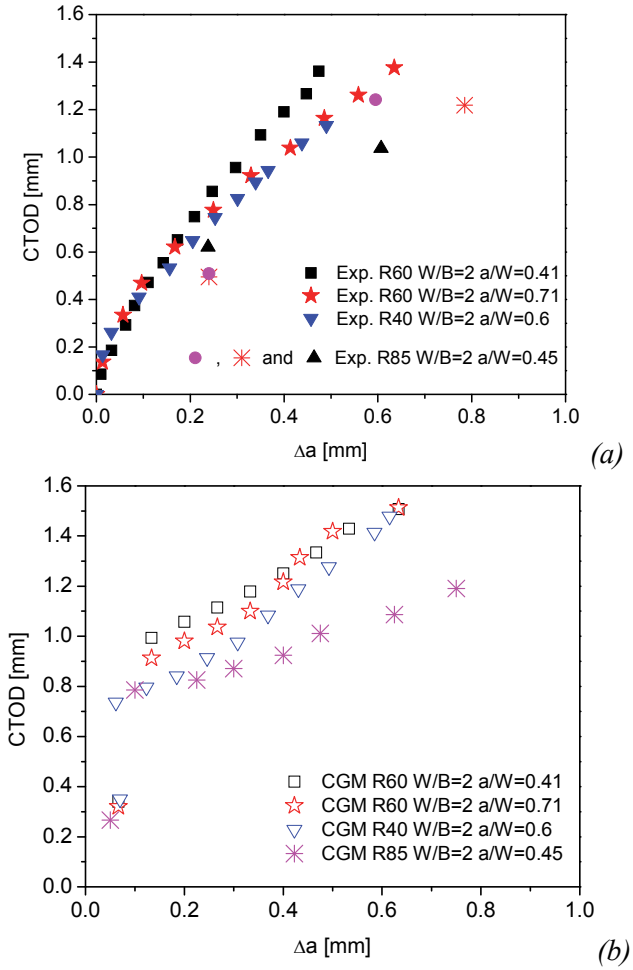

Figure 7.49. Crack growth curves for PRNB specimens: experimental (a) and obtained using the micromechanical model (CGM) (b)

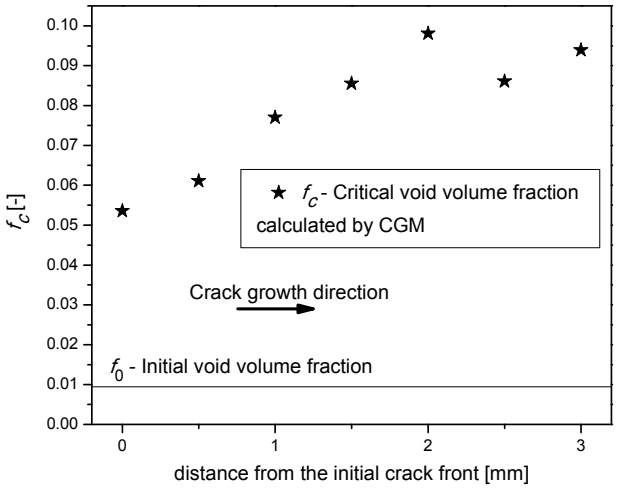

Figure 7.50. Critical void volume fraction ahead of the initial crack front obtained from CGM (PRNB R60 specimen)

Since fatigue pre-cracked specimens had uneven initial crack shape, the influence of this deviation is examined (figure 7.51b) by compating the straight crack front with two different modles with uneven crack front. Differences between the pre-crack lengths in the two models with uneven crack are 10 and 30%. In figure 7.51, it can be seen that 10% difference, corresponding to the examined specimens, does not cause significant influence on the crack front shape. However, for the third model there is a slight difference which can be seen through more pronounced growth on the external surface. On the curves *F*-CTOD, it can be seen that uneven pre-crack contributes to the increase of the load carrying capacity - figure 7.52, for larger CTOD values.

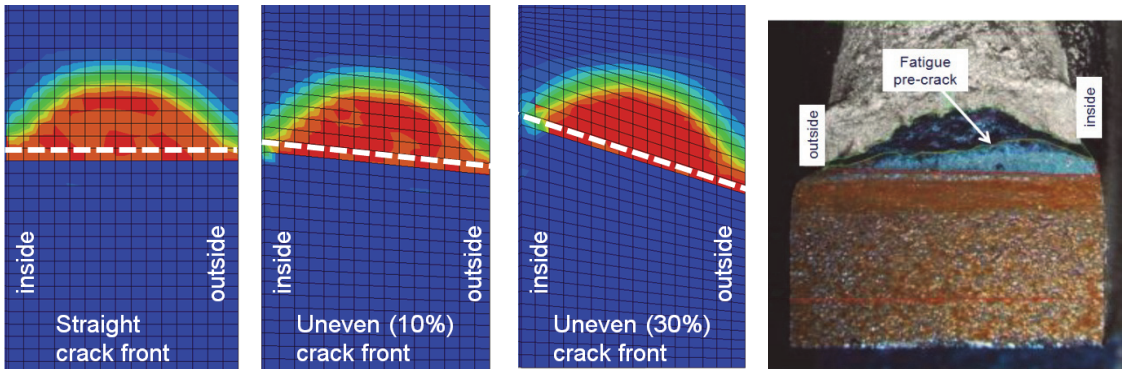

Figure 7.51. Crack growth for the straight and uneven crack front (a), and a photo of fatigue pre-cracked ring fracture surface (b)

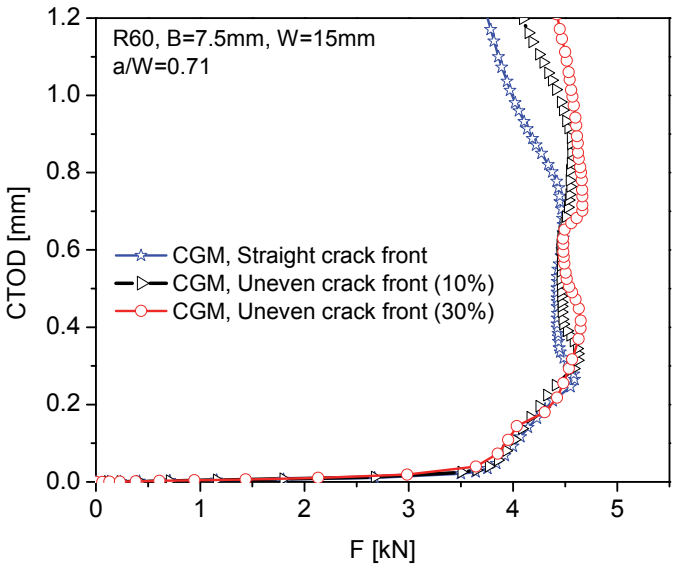

Figure 7.52. Influence of the crack front shape on F-CTOD curves for PRNB specimens

The influence of the ratio *W/B* (i.e. the specimen width *W*) on ductile fracture prediction using the micromechanical model is shown in figure 7.53. Actually, this influence is not

pronounced, since large difference in *W/B* (4 in comparison with 2) did not result in significant difference between the curves.

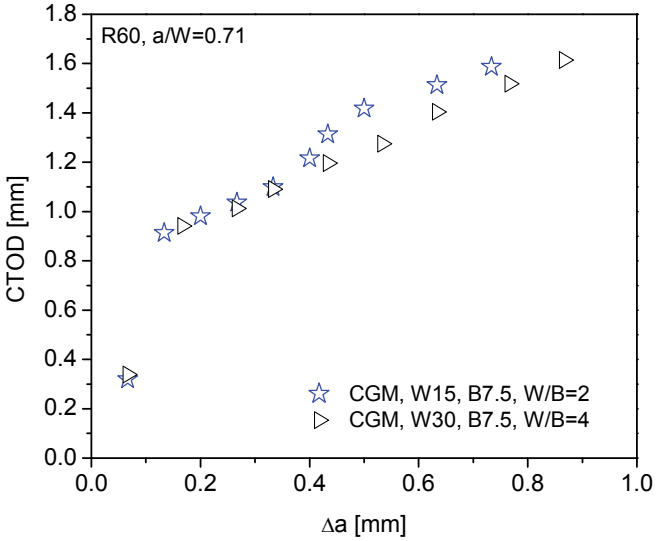

Figure 7.53. Influence of specimen width (W) on crack growth curves

The influence of thickness on fracture behaviour is also examined on the rings with radius 60 mm. In addition to the geometry with *B*=7.5 mm and *W*=15 mm, a model with increased thickness (12 mm) is created, figure 7.54. It can be seen that the length with the constant crack growth is larger, i.e. the region with dominating plane strain conditions is much wider.

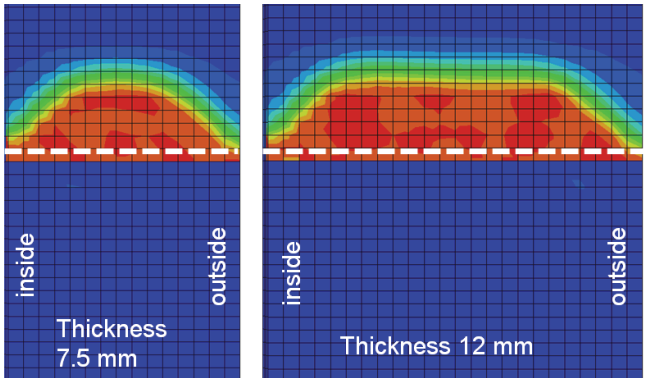

Figure 7.54. Crack growth for two models with different wall thickness and otherwise identical geometry

The crack growth curves in figure 7.55 present the resistance to crack growth for the specimens with different thicknesses (*B*=7.5 and 12 mm, *W*=15 mm). Therefore, it can be said that the constraint effect caused by wall thickness can be simulated by testing of the ring specimens.

Further, another model is introduced - with wall thickness 12 mm and same ratio W/B as initial models (W/B=2) - very similar trends are observed. Therefore, the assessment of crack growth for the ring with increased thickness also does not significantly depend on the ring width W.

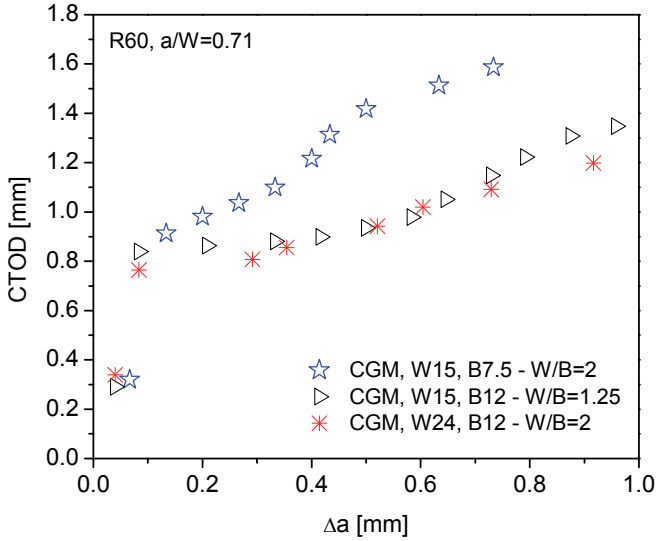

Figure 7.55. Influence of wall thickness on crack growth curves

7.3.2 Seam and seamless pipes - pressure vessel steel P235GH and P235TR1

Micromechanical analysis of fracture of PRNB specimens cut from seam and seamless pipes is also performed by application of the CGM model. Numerical models are formed either using two planes of symmetry or one plane of symmetry (one quarter or one half of the full specimen geometry). Models with half geometry were necessary in two cases: for the seam pipes with one of the notches/cracks in seam, and for specimens where a significant difference in crack length is observed.

Micromechanical model enabled tracking the damage development through the material, and forming the curves CTOD-Δa. As mentioned previously, CTOD values are determined by application of δ_5 concept, while the crack growth is determined by tracking the damage development in the ligament.

In analysis of fracture of seamless pipes, the initial step was micromechanical modelling of CT specimens fabricated from the pipe with dimensions 133x11mm (this was the only pipe size that had sufficient thickness for cutting of plane strain specimens). The

initial value of damage parameter is taken from table 7.1, as the value obtained for the seamless pipe. The FE size is varied (0.25 and 0.35 mm), and the fracture resistance curves are shown in figure 7.56. Smaller element underestimates the fracture resistance, while element size 0.35 mm is adequate for this material.

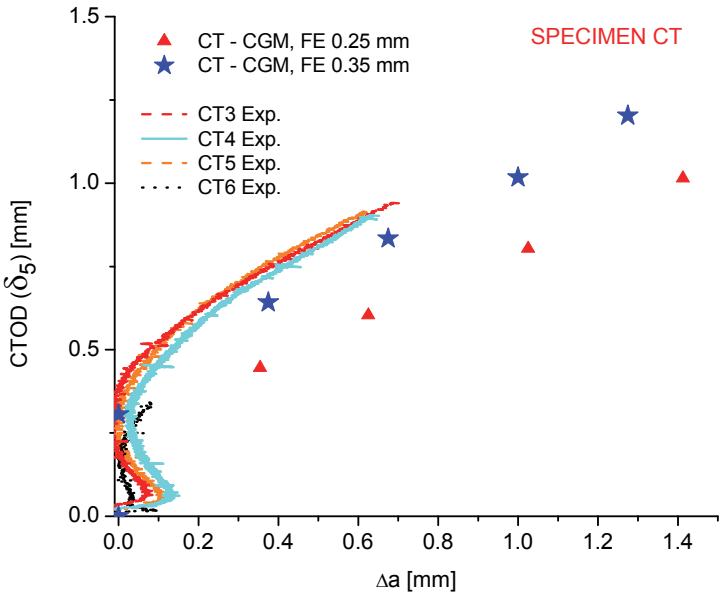

Figure 7.56. Crack resistance curves - CT specimens

When *F*-CMOD curves are considered, it can also be seen that the model with FE size 0.25 mm predicts much more pronounced force drop in comparison with the experimental values.

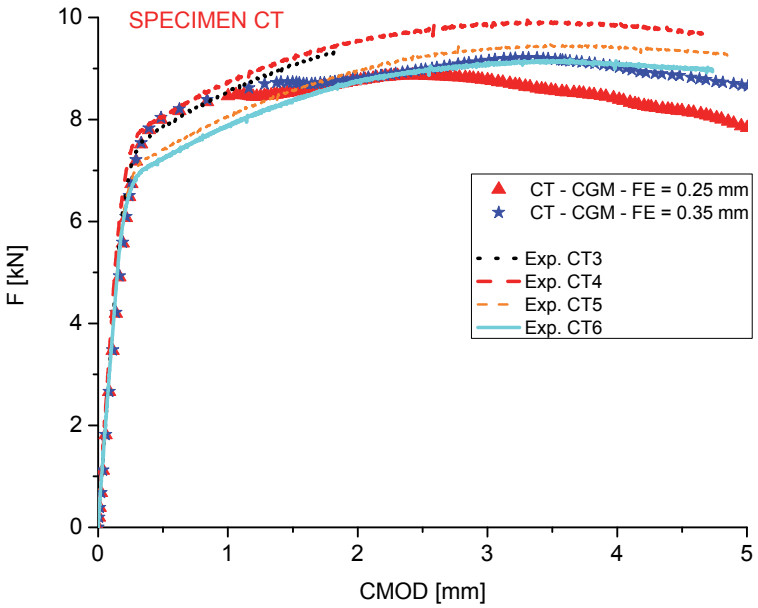

Figure 7.57. F-CMOD curves - CT specimens

When the same micromechanical parameters are transferred to the seamless pipe SL(168)-11, it turned out that the fracture behaviour is predicted correctly, i.e. the model does not show a significant deviation from experimental results on the fracture resistance curve, figure 7.58.

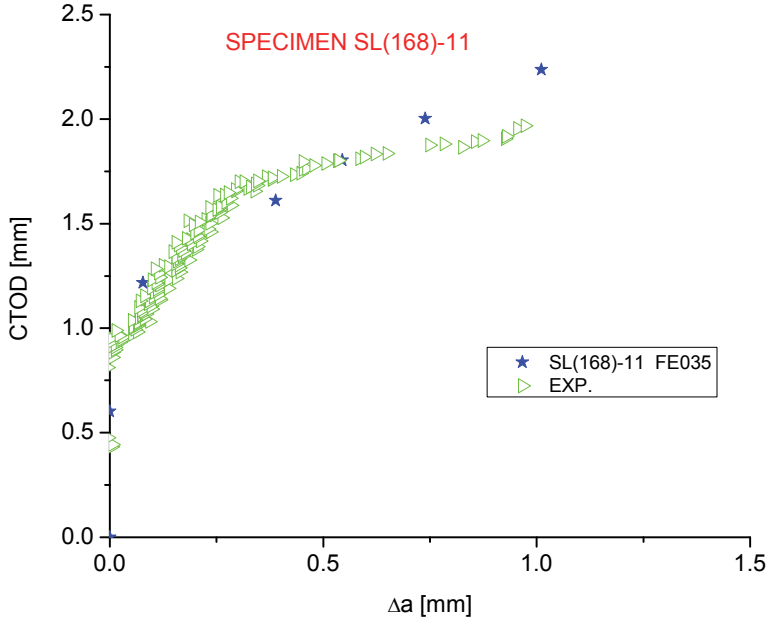

Figure 7.58. Crack resistance curves - specimen SL(168)-11

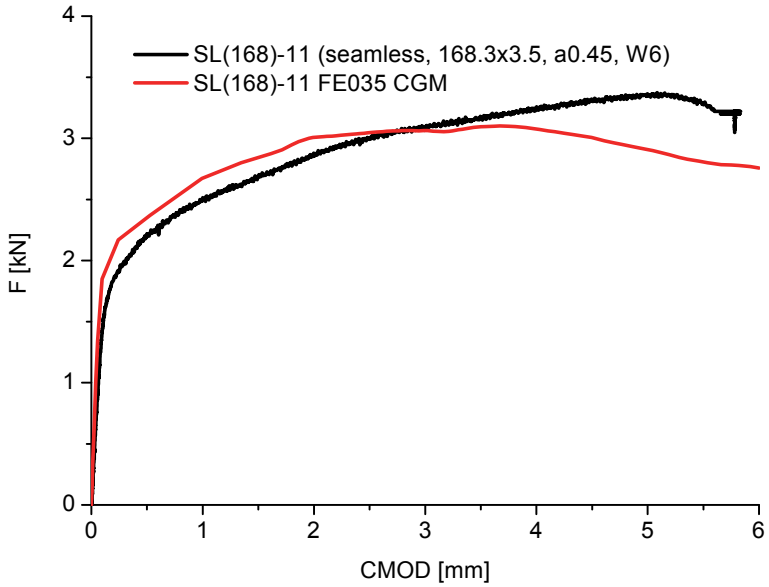

Figure 7.59. F-CMOD curves - specimen SL(168)-11

The next seamless pipe which was considered is SL(89T)-17; it has both smaller diameter and thicker wall. Again, a good agreement is obtained by using micromechanical parameters transferred from the CT specimen.

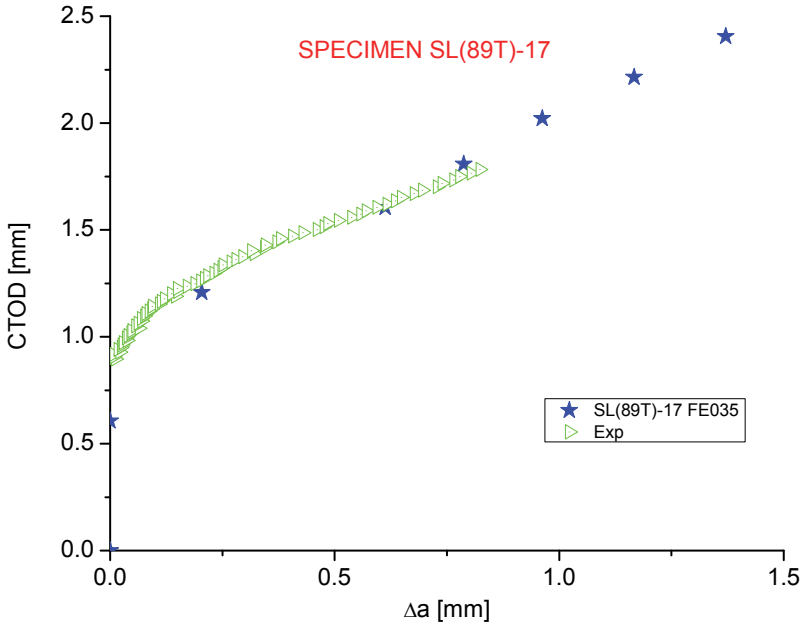

Figure 7.60.Crack resistance curves - specimen SL(89T)-17

On force - CMOD diagram, figure 7.61, another specimen is added - SL(89T)-18. It has the same dimensions as SL(89T)-17, except the notch length. Specimen SL(89T)-18 had the ratio *a/W* 0.75, i.e. the notch was rather long. There was almost no crack growth in this specimen, both in the model and during experimental examination, and therefore it is not shown in the previous figure.

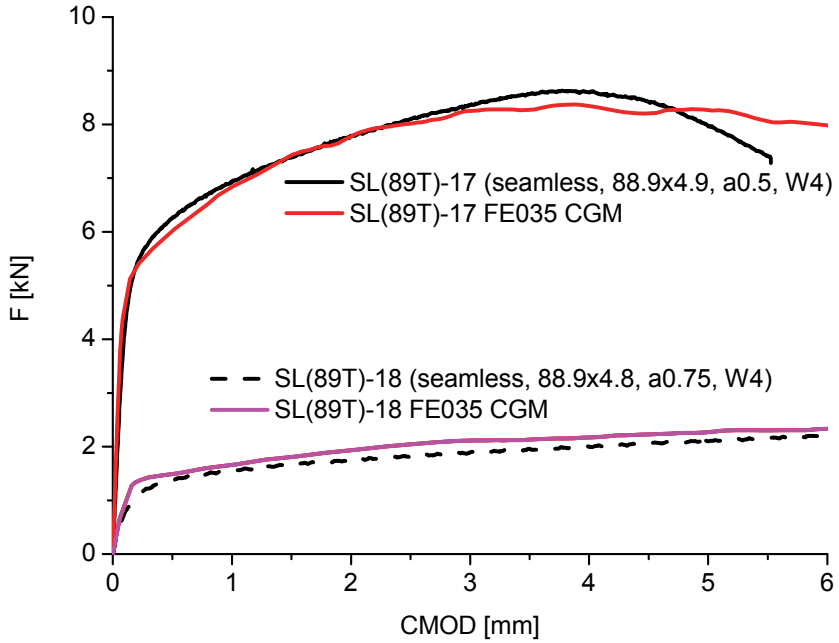

Figure 7.61. F-CMOD curves - specimens SL(89T)-17 and SL(89T)-18

However, analysis of PRNB specimens cut from the seamless pipes with dimensions

88.9x3.2 mm revealed significantly different behaviour - smaller finite element size turned out to be adequate. This is in agreement with their lower fracture resistance, determined experimentally, through fracture resistance curves and critical CTOD values in accordance with the procedure ESIS P2-92 (see figure 7.21 and 7.27). The difference is significant and points out to different behaviour of the materials of these two pipes; it is important to emphasize that different fracture resistance is revealed by using PRNB specimens, even though the material is nominally the same as for the other seamless pipes and CT specimens.

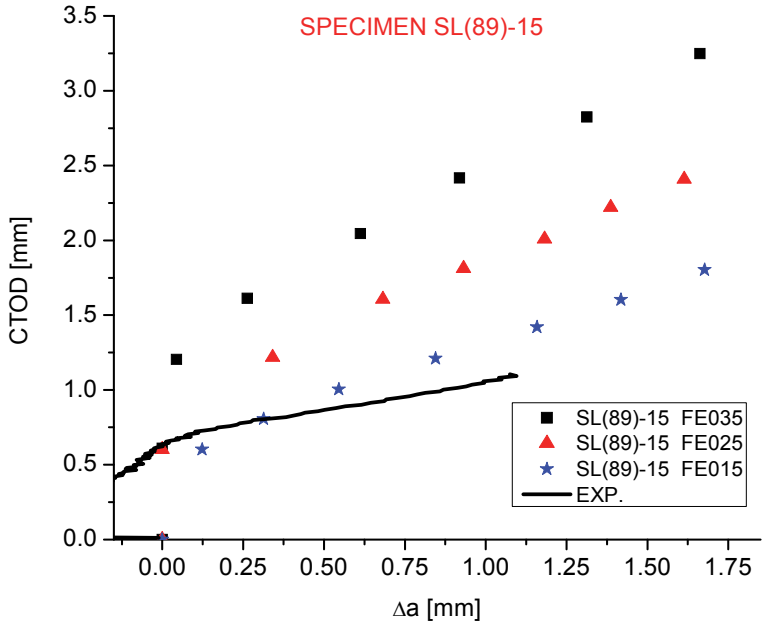

Figure 7.62.Crack resistance curves - specimen SL(89)-15

Figure 7.63 shows the influence of the secondary void nucleation. It can be seen that no significant change occurs if these voids are taken into account. Their volume fraction (f_N) is determined based on the chemical composition - i.e. lever rule [115], while two other void nucleation parameters important for this analysis are ε_N=0.3 and s_N=0.1 (these values are most often used in literature).

Unlike the most often used values of constitutive parameters q_1 and q_2 (1.5 and 1, respectively), there are some other suggestions in the literature. On the example of specimen SL(168)-11, the influence of decrease of q_1 from 1.5 to 1.2 is shown in figure 7.63. In the early stages of crack growth, fracture resistance becomes lower, and in the later stages it is higher in comparison with the results obtained for q_1=1.5.

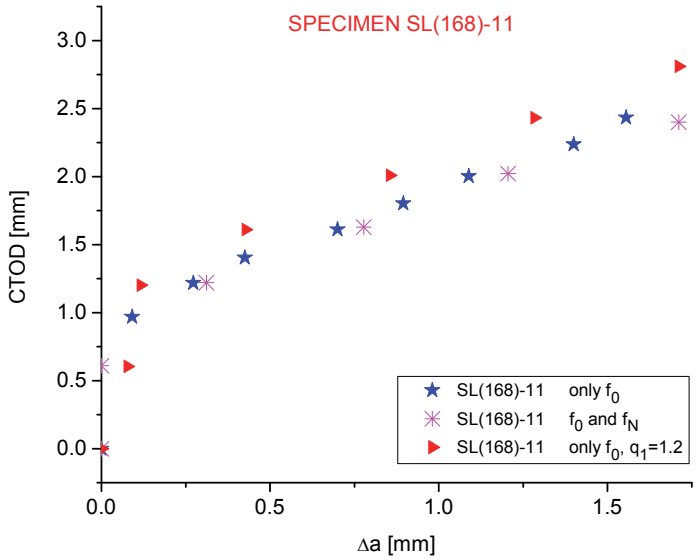

Figure 7.63. Crack resistance curves - model of specimen SL(168)-11 with a pre-crack - influence of secondary void nucleation and value of constitutive parameter q_1

In figure 7.64, micromechanical prediction of influence of the stress concentrator shape on fracture resistance is given. The difference is almost constant for the entire crack growth, and it can be said that it is caused by higher resistance to crack initiation of the notched geometry in comparison with the pre-cracked one.

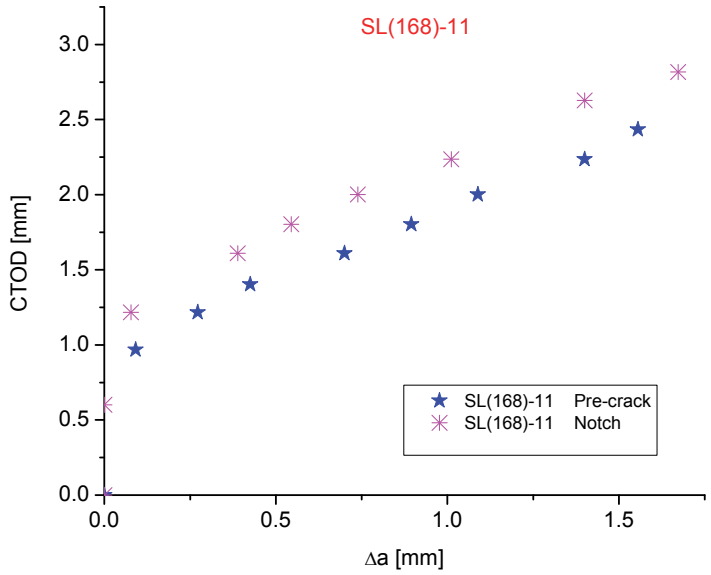

Figure 7.64. Crack resistance curves - specimen SL(168)-11 - influence of stress concentrator shape

On the example of another specimen with size Ø88.9x3.2mm, influence of difference in initial stress concentrator lengths on two sides of the specimen is analysed. On specimen SL(89)-16C (figure 7.65), fatigue loading lead to a significantly longer fatigue pre-crack on one side in comparison with the other side; ratios *a/W* are 0.65 and 0.35. It

should be emphasized that this is a limit case - most of the pre-cracked specimens had very similar crack lengths, while for this specimen the problem was a combination of small width, short machined notch and fabrication of the notch for fixing the COD gauge, which practically *cancelled* the initial machined damage and the fatigue crack growth almost did not occur.

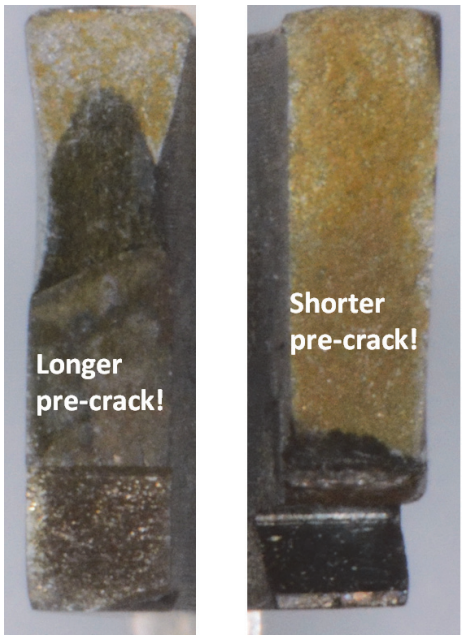

Figure 7.65.Fracture surfaces of the seamless specimen SL(89)-16C - different initial crack lengths and final crack lengths

Analysis of this model has shown that the boundary conditions are extremely important if the crack length difference exists. Namely, for the models where crack/notch lengths on both specimen sides are similar, displacement of the moving cylinder can be defined as translation (vertical, downwards). However, if this approach is applied to different crack lengths, neither the prediction of damage development, figure 7.66, nor force value redistriburion (figure 7.67) are obtained adequately. Therefore, it is important to introduce another freedom degree, which corresponds to the experimental setup - rotation of the moving cylinder around the horizontal axis normal to the notch/crack plane, figure 7.68.

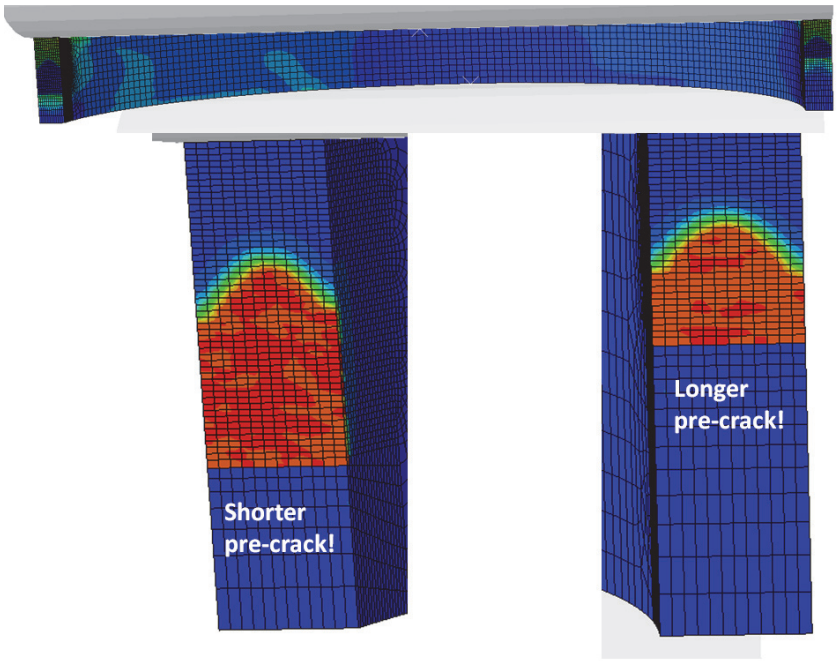

Figure 7.66. Prediction of crack growth for specimen SL(89)-16C - fixed loading pin

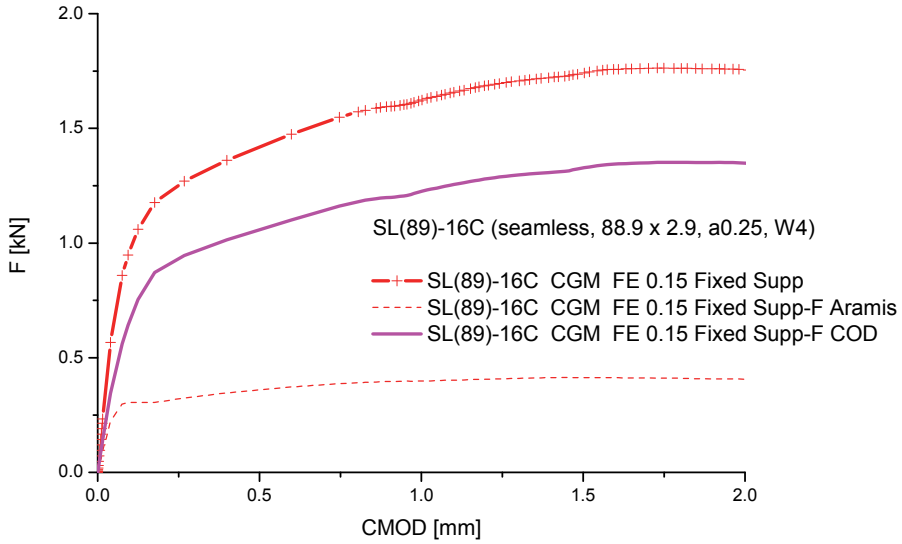

Figure 7.67. Prediction of force distributions on two sides of the specimen SL(89)-16C - fixed loading pin

Micromechanical analysis revealed that allowing the rotation of the upper cylinder (loading pin) enables prediction of damage development which corresponds to the experimentally determined, figure 7.69. Also, it is shown that the force value is split almost ideally into two equal parts on two specimen sides (figure 7.70), even in this case with very large difference in crack lengths. An important outcome from analysis of this example is that PRNB specimens are not sensitive to small differences in crack lengths, i.e. the force will be distributed evenly on the two sides of the specimen.

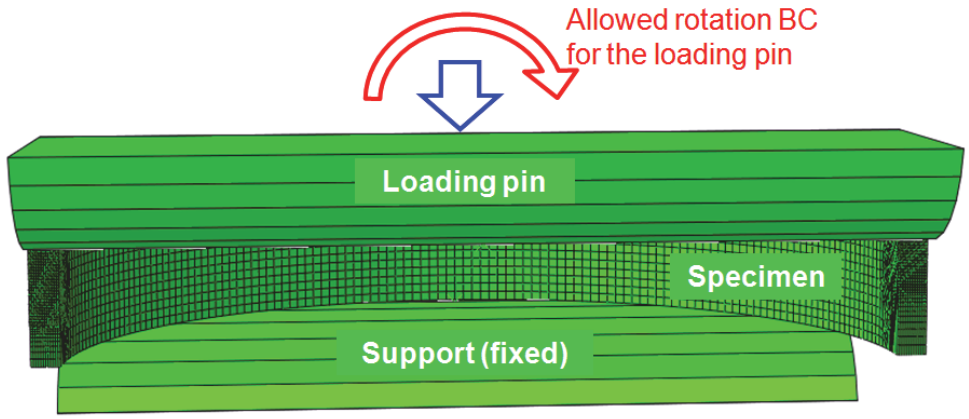

Figure 7.68. Allowed (unconstrained) rotation BC in the half-symmetrical ring specimen model

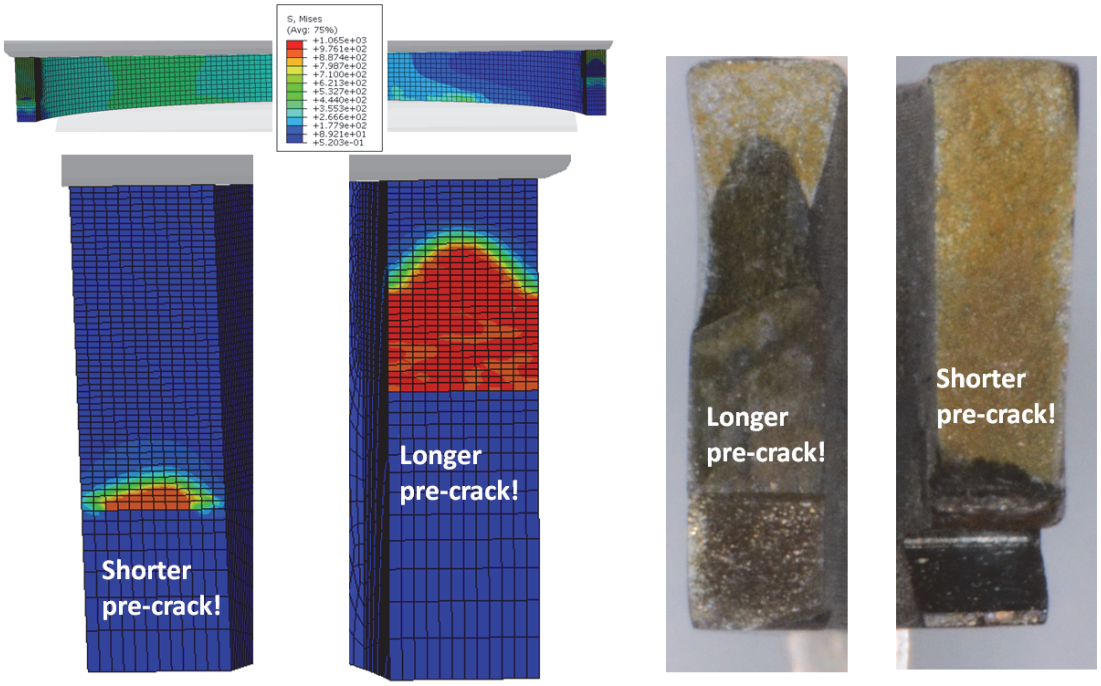

Figure 7.69. Prediction of crack growth for specimen SL(89)-16C - free loading pin rotation

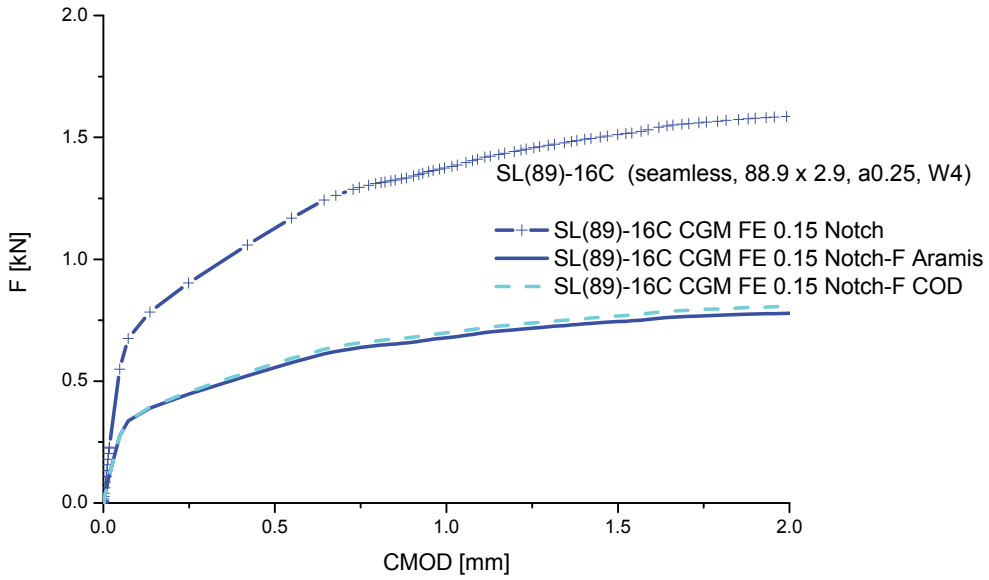

Figure 7.70. Prediction of force distributions on two sides of the specimen SL(89)-16C - free loading pin rotation

Micromechanical analysis of the fracture of seam pipe ring S-BM(168)-6 with both notches in the base metal (i.e. plane of the notches is at an angle of 90° with respect to the seam) has shown that significantly smaller element size is adequate for this material, in comparison with the seamless pipe of similar dimensions. Here, the appropriate value turned out to be 0.15 mm, as shown in figure 7.71.

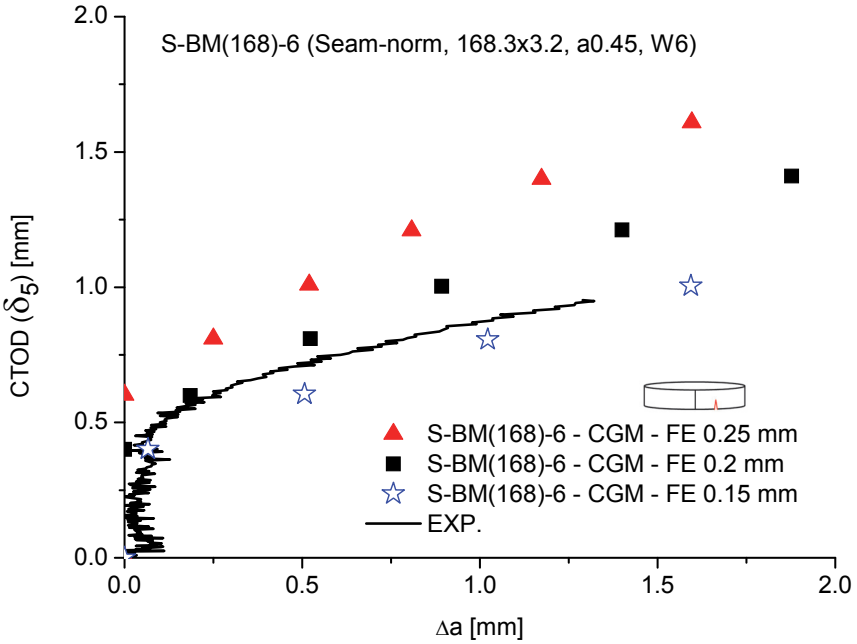

Figure 7.71. Crack resistance curves - specimen S-BM(168)-6 (base metal)

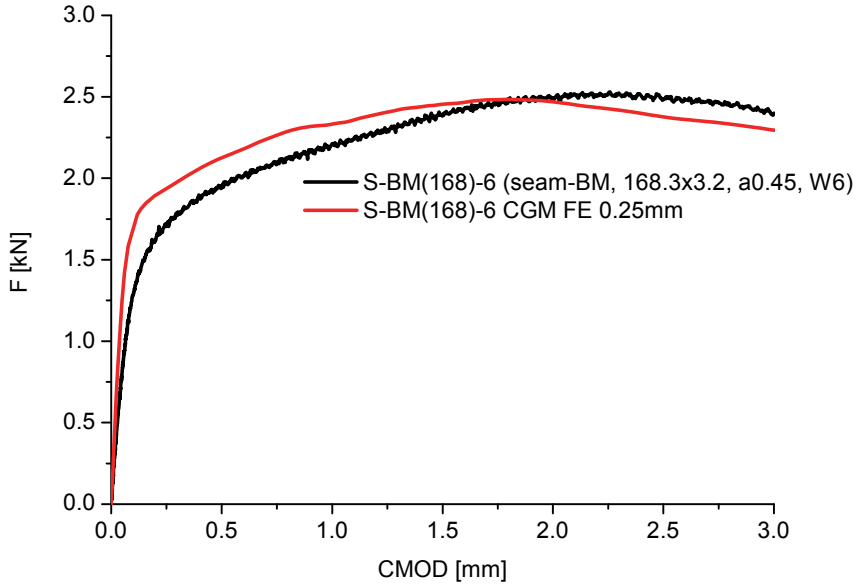

Figure 7.72. F-CMOD curves - specimen S-BM(168)-6

In figure 7.73, the effect of the stress concentrator shape on crack growth resistance of the seam pipe BM is shown. It can be seen that this influence is not large, and it is much less pronounced than in the case of the seamless pipe (figure 7.64, specimen SL(168)-11).

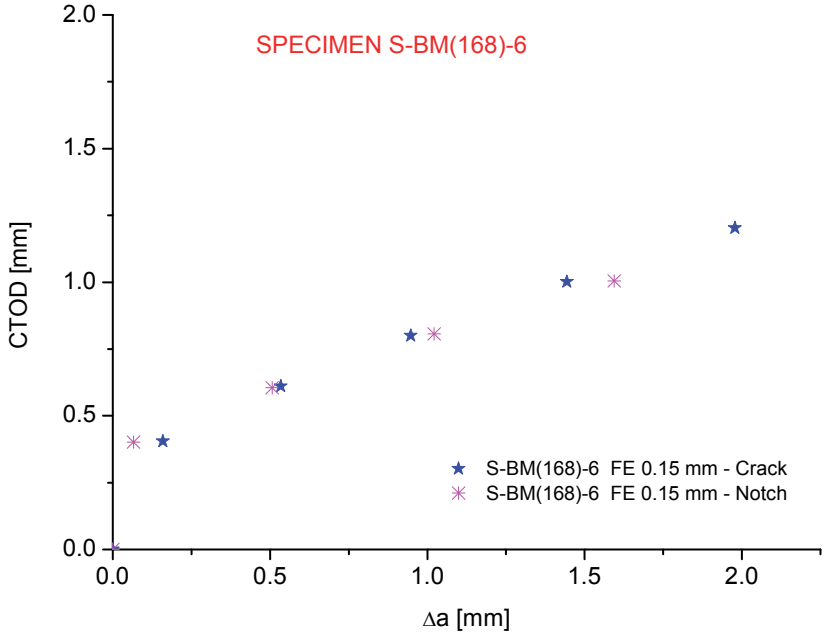

Figure 7.73. Crack resistance curves - specimen S-BM(168)-6 (base metal) - influence of the stress concentrator shape

This result, i.e. appropriate FE size, is utilised (transferred) in the analysis of the seam pipes with a notch in the seam and a notch in the weld metal. It was not possible to consider a quarter-geometry here, and each side of the specimen is modelled with its own appropriate element size and material properties.

It turns out that the weld metal requires three times smaller element then the base metal of the seam pipe - 0.05 mm in comparison with 0.15 mm for the base metal. The curves obtained using the CGM are shown in figure 7.74. Difference between the fracture resistance of BM and WM, experimentally determined by analysis of fracture surfaces and CTOD-Δa curves, is successfully modelled using the micromechanical model. Having in mind the calculation times, primarily due to the small element size in WM, a possibility of forming a simplified model with quarter-geometry is considered. This model would correspond to a hypothetical pipe with the same geometry, but with two weld metals. It turns out that this simplified model can successfully be used for prediction of damage development through the weld metal, with significant decrease in computation time and resources. Regarding the F-CMOD curves, figure 7.75, the model with quarter-geometry results in similar curve as the half-model; however, both of them overpredict the load carrying capacity in the initial testing stage (for small CMOD values).

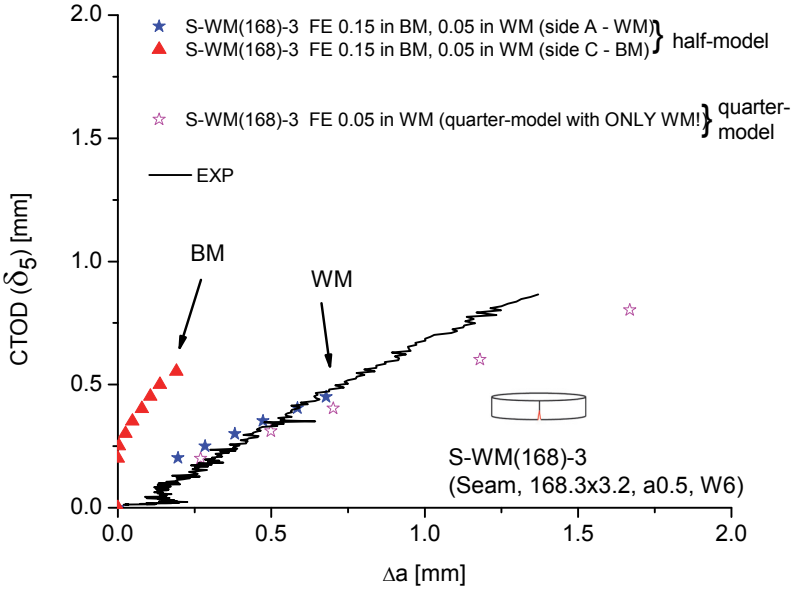

Figure 7.74. Crack resistance curves - specimen S-WM(168)-3 (notches in BM - side C, and WM, side A)

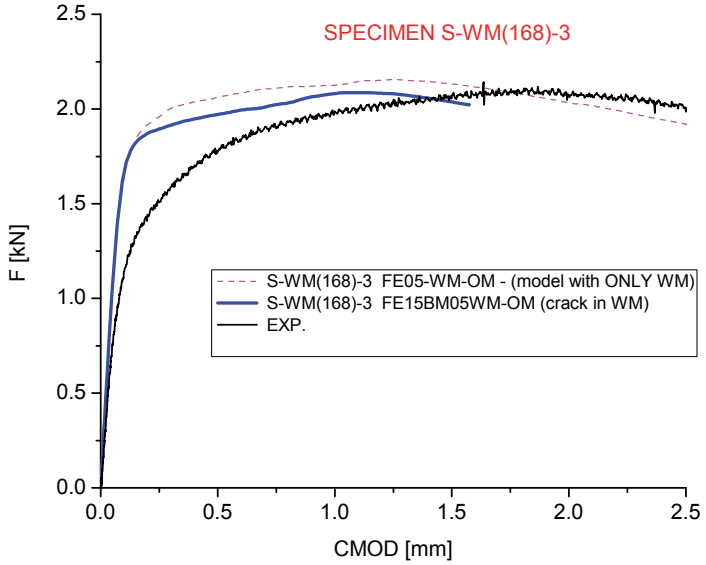

Figure 7.75. F-CMOD curves - specimen S-WM(168)-3 (base metal and weld metal)

Triaxiality (notch - crack comparison)

Triaxiality at the tip of the crack concentrators is analysed on two models with the same geometry and a crack (figure 7.76a) or a notch (figure 7.76b). The crack/notch length is varied, so the ratio *a/W* was from 0.25 to 0.75; all of these models are based on the geometry of the seamless specimens with diameter 88.9 mm. These are the models without the crack growth, i.e. obtained using the von Mises plasticity material model.

The values are much higher in the cracked specimens; this is certainly an explanation for the fact that the crack growth did not occur in some notched specimens - the triaxiality is not pronounced, so the conditions for ductile crack growth are satisfied later during loading, when the plastic deformation is significant.

However, the cracked specimens have a problem with the straightness of the initial crack, because the cracks produced by fatigue loading are more pronounced on the internal surface (due to the cylindrical geometry). Also, crack growth is observed in many notched specimens, and some of the final cracks were much longer in comparison with the ones in pre-cracked specimens. In other words, despite lower triaxiality, notched specimens can be used for fracture analysis of the pipeline material. The most pronounced condition for lack of crack growth is existence of very long notches (e.g. *a/W*=0.75) - crack growth often did not occur in these geometries, but it is

predominantly caused by lack of rigidity of the specimen - i.e. excessive deformations occur before the crack initiation and growth.

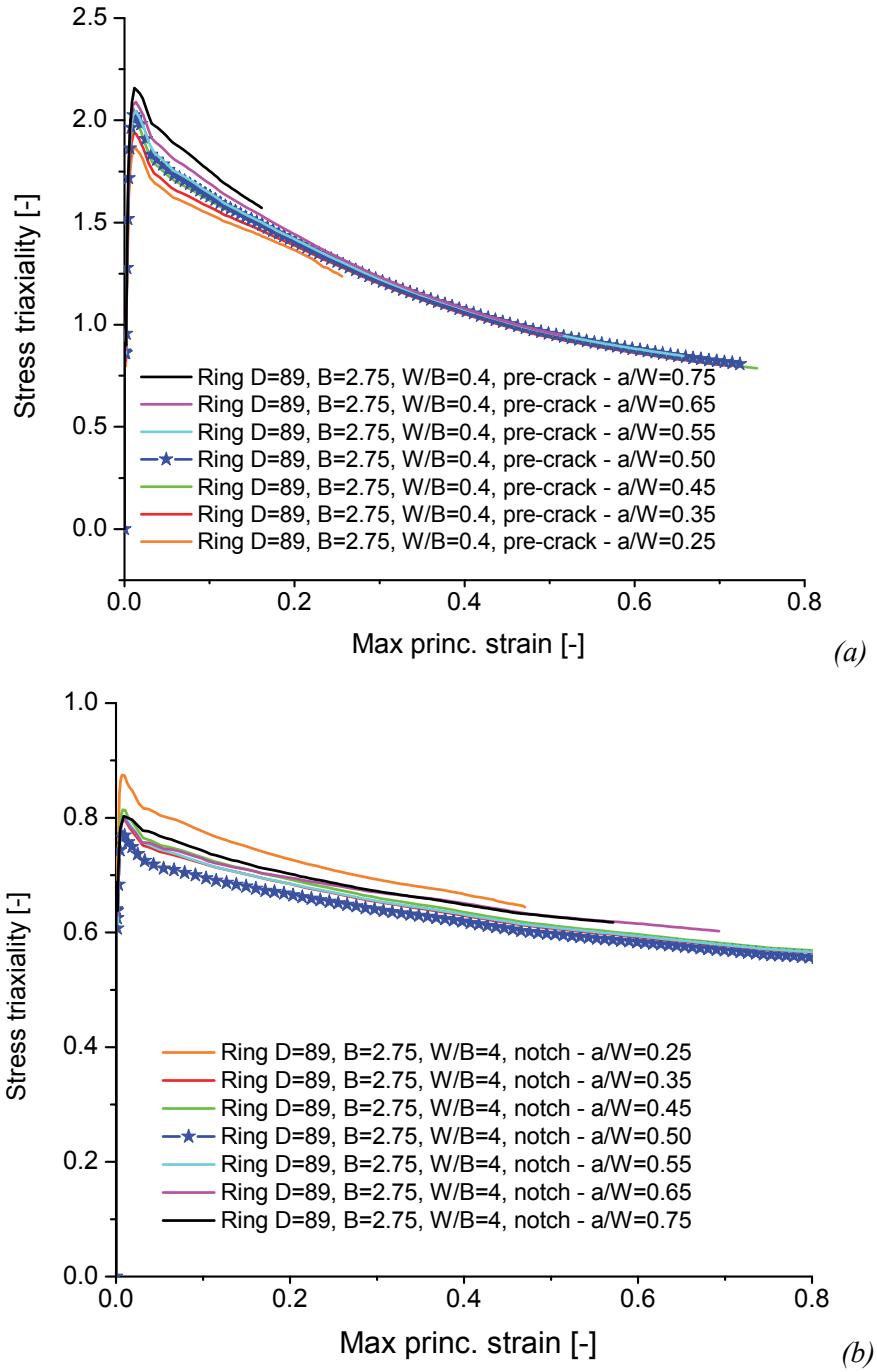

*Figure 7.76. Dependence of triaxiality on maximum strain, Rings D=88.9 mm, B=2.75 mm, W/B=4: **Crack** as stress concentrator (a) **Notch** as stress concentrator (b)*

In figure 7.76, it is shown that there is no significant influence of the crack length on triaxiality. Also, in the cracked specimens a trend can be noticed - increase of the crack length causes increase of triaxiality. On the other hand, notched specimens do not

exhibit such behaviour, and the lowest triaxiality is obtained for *a/W*=0.5. Either increase or decrease of this ratio slightly increases triaxiality. However, all these variations for both pre-cracked and notched specimens are rather low.

Next, the notch radius effect is examined, figure 7.77. It is shown that decrease of this radius below 0.25 mm (which is rather difficult to achieve in production, or practically imposible for *R*=0.02 mm) does not dramatically increase the stress triaxiality at the notch tip, i.e. the notches used in this work, with *R*=0.25 mm, can be regarded sufficient.

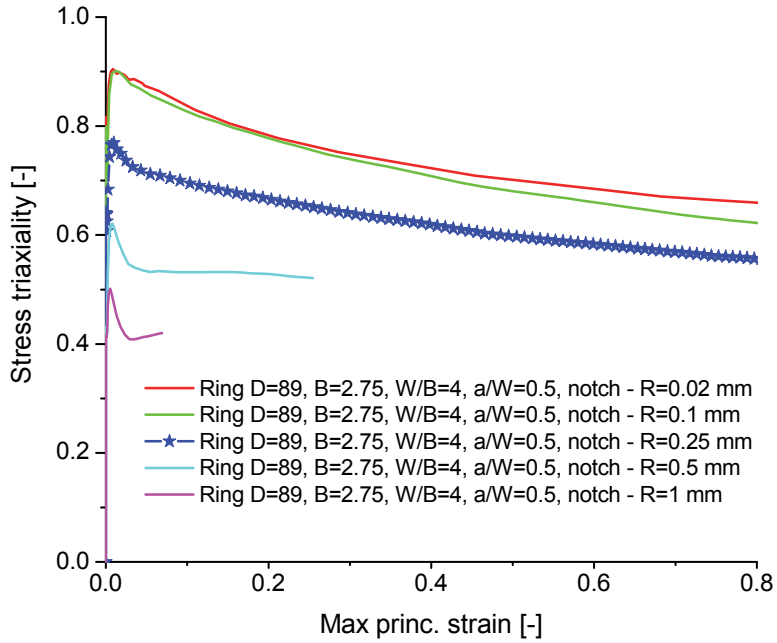

Figure 7.77. Dependence of triaxiality on notch diameter, Rings D=88.9 mm, B=2.75 mm, W/B=4, a/W=0.5, ***Notch*** *as stress concentrator*

7.3.3 Experimental-numerical procedure for determining the fracture resistance in plane strain conditions

Having in mind relatively small wall thickness of all examined ring shaped specimens fabricated from seamless and seam pipes, plane strain state could not be dominant during fracture, which is required for fracture toughness determination according to standards. Therefore, micromechanical analysis is applied to determine the fracture resistance curves in plane strain conditions. This is achieved by forming a series of models of CT20 specimens (dimensions are given in figure 6.19) with the material

properties and micromechanical parameters corresponding to the tested pipes. Besides one model of CT specimen which is experimentally examined (fabricated from the seamless pipe Ø133x11mm), additional models are also formed to match the base metal of the seam pipe Ø168.3x4 mm and welded joint of the seam pipe Ø168.3x4mm (these models can be considered as “hypothetical”). Also, one more additional model is formed - based on the seamless pipe Ø88.9x3.2mm, because experimental examination and micromechanical analysis lead to a conclusion that this pipe has lower fracture resistance in comparison with other seamless pipes. Based on the simulation of crack growth in these CT specimen models, crack growth curves in plane strain state are formed - which allow determination of plane strain fracture toughness.

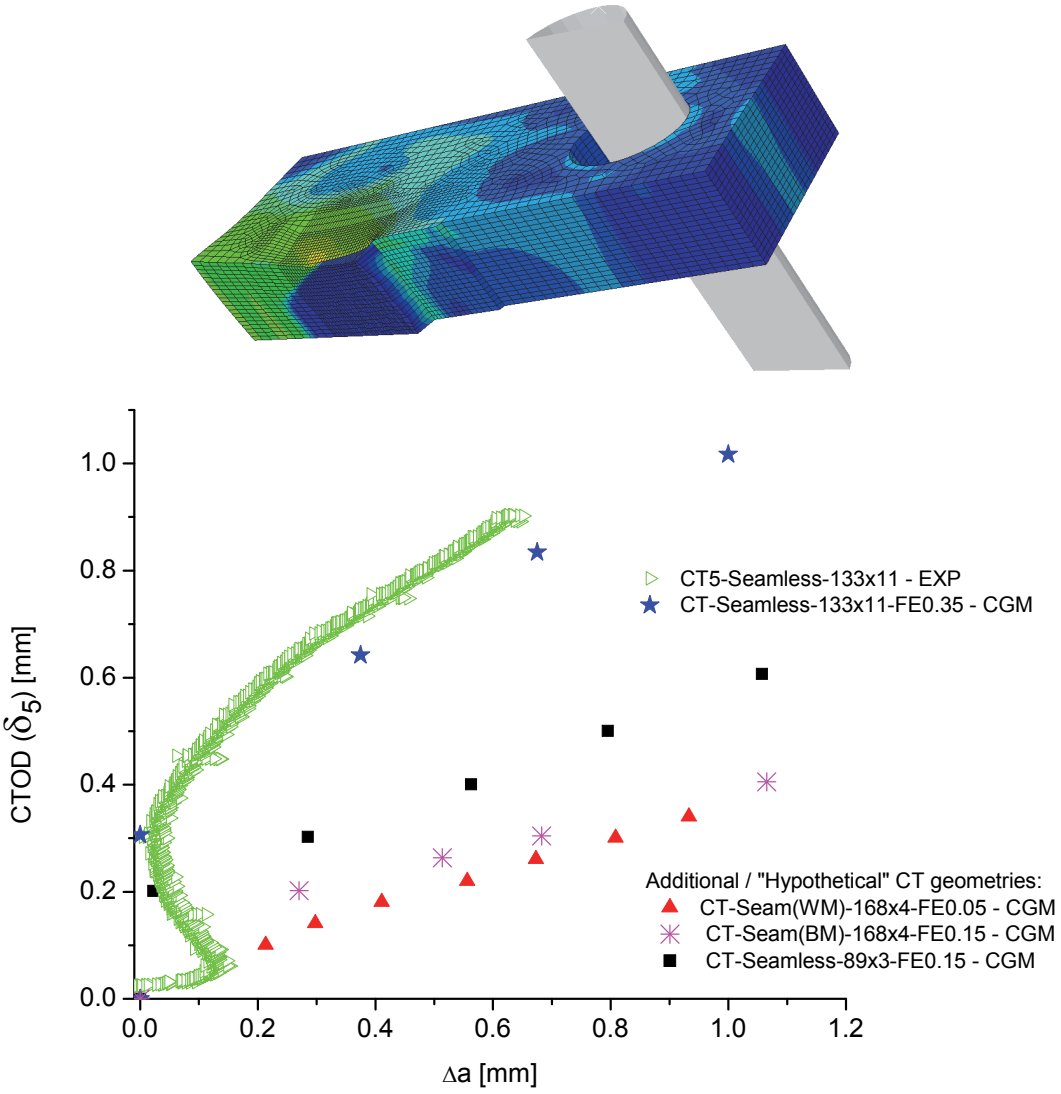

Figure 7.78.Equivalent von Mises stress field and Crack growth curves for additional CT specimens

It should be emphasised that additional models were not formed for all other SL pipes; because it was previously shown that the failure of these materials can be described by transferring the same micromechanical parameters from the CT specimen. This implies that all of them, except the pipe Ø88.9x3.2mm, have the similar fracture behaviour at the local level.

7.4 Ring-shaped specimens - plastic collapse analysis

Based on the experimental results (curves *F*-LLD), plastic collapse loads are determined for both specimens fabricated from the high strength low alloyed steel plates and pipes. Three methods which are often used in the literature are: TES (*twice elastic slope*), TED (*twice elastic displacement*) and TIS (*tangent inter-section*), chapter 3.7. These methods are based on tracking of global quantities - force and load line displacement, and in this work the first one is given an advantage here, because the value of the plastic collapse force is obtained with least uncertainty caused by the diagram analysis. For other two methods, it is necessary to estimate the value of elastic strain and slope of the force - LLD curve for large deformations, which inevitably includes a subjective estimate. For the method TES, the base is slope of the elastic part of the curve, which can be rather precisely determined from the diagram.

Analysis of failure by plastic collapse mechanism in numerical models is performed using von Mises yield criterion, figure 7.79.

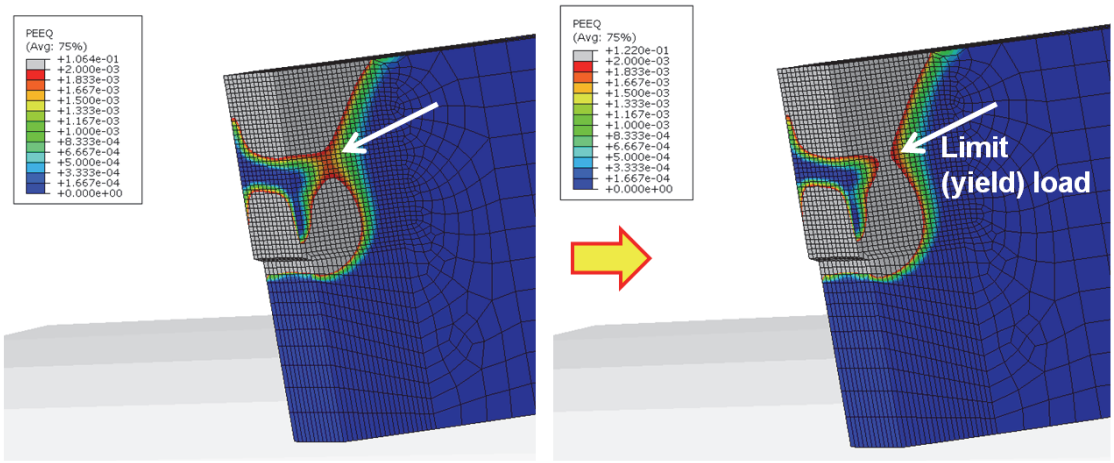

Figure 7.79. Joining the two parts of the plastic zone as criterion for plastic collapse

In three-dimensional finite element models of ring specimens, shape of the plastic zone in the ligament is tracked. The failure is predicted at the moment when equivalent plastic strain has reached the value 0.002 (i.e. 0.2%) in the entire ligament. This typically means that two plastic zones are joined; one of them is caused by the stress concentrator, while the other one originates from the position of the contact with the rigid body (loading pin).

7.4.1 High strength low alloyed steel NIOMOL 490

Plastic collapse loads for all analysed configurations are given in figure 7.80. Several important things can be seen from it. If we compare the values for 2D and 3D SENB specimens (a_0/W=0.5), they are similar; therefore, it can be said that much simpler and less complex 2D models can be used to determine the plastic collapse load. It can be seen that the plastic collapse loads have similar trends for SENB and PRNB specimens - they both decrease almost linearly.

Another important comparison can be made between the PRNB specimens with different defect geometry (crack and notch). The difference between them is also small, which means that the exact shape of the stress concentrator does not affect the plastic collapse load significantly (of course, if the sizes of the two defects are the same).

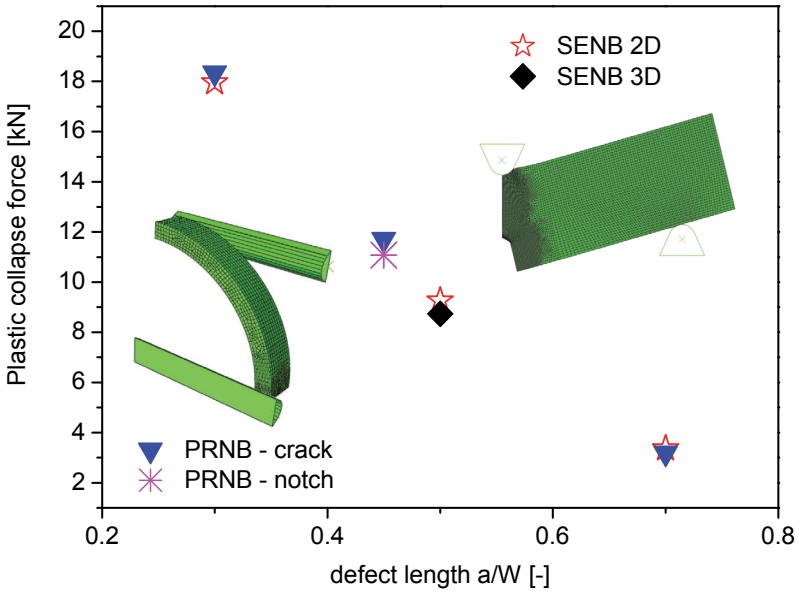

Figure 7.80: Dependence of plastic collapse load on defect length for SENB and PRNB specimens

In addition to those presented in figure 7.80, an additional radius of the specimen is considered (R = 60 mm, in addition to previously considered R = 85 mm). The influence of the ring radius on the plastic collapse loads is shown in Figure 7.81. The dependence of collapse loads on the ratio a/W is linear for both specimen sizes, but with a different slope.

All the results lead to conclusion that the PRNB specimens have similar behaviour as SENB specimens from the point of view of plastic collapse. Since this is previously shown for fracture mechanics testing (i.e. different failure mode - ductile fracture initiation and crack growth), it can be said that PRNB specimens are a good candidate for pipe material testing.

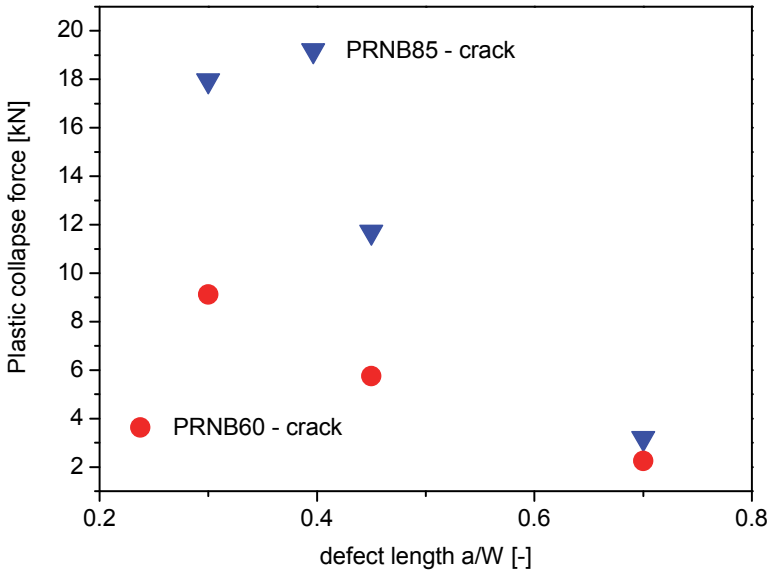

Figure 7.81 Influence of the ring specimen radius on plastic collapse load

In figure 7.82 and 7.83, presented trends are compared with experimental values. It can be seen that they are mostly in agreement, but the ring specimens with radius 60 mm exhibit different slope of experimentally and numerically obtained values, i.e. different rate of decrease of plastic limit load with increase of stress concentrator length.

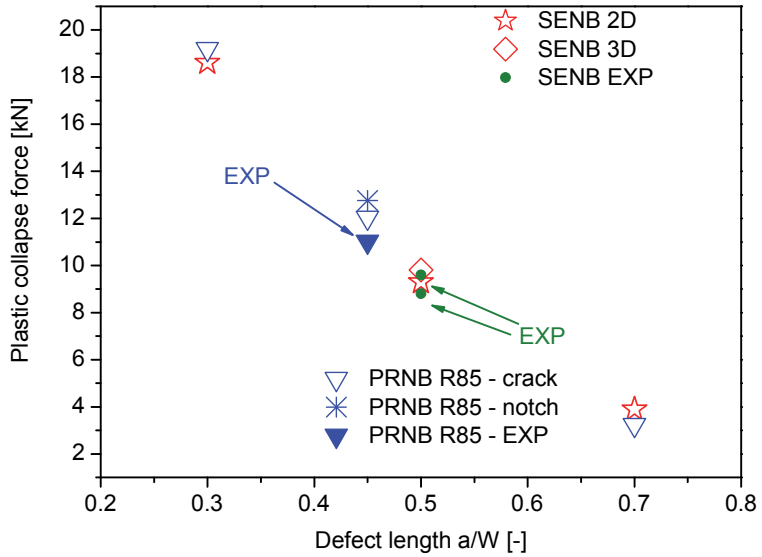

Figure 7.82. Plastic collapse load - SENB and PRNB specimens

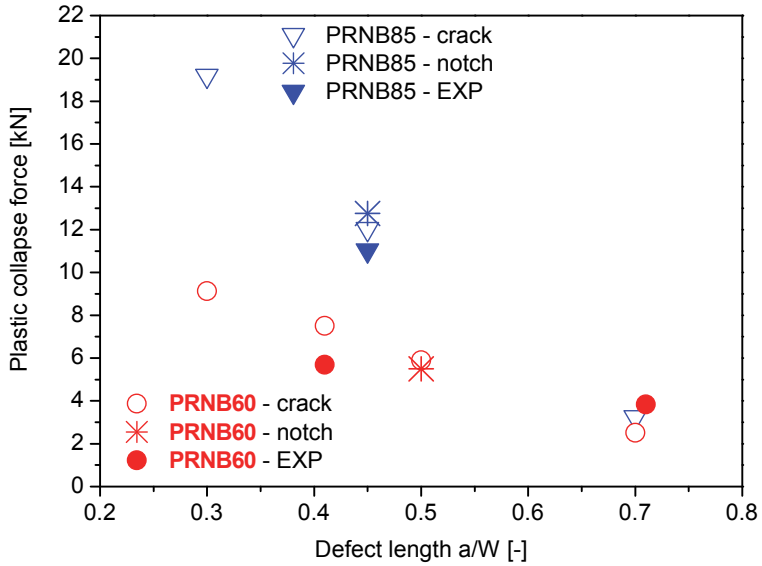

Figure 7.83. Plastic collapse load - PRNB specimens

7.4.2 Seam and seamless pipes - pressure vessel steel P235GH and P235TR1

In the next figures, dependence of plastic collapse load on geometry of the specimen and stress concentrator is shown for several combinations of seam and seamless rings. Figure 7.84 shows the influence of the defect length; the specimen with all dimensions besides the defect length approximately the same. Similar force drops are obtained for specimen diameter 168.3 mm, while more pronounced slope is obtained for the specimens with diameter 88.9 mm and thickness around 5 mm.

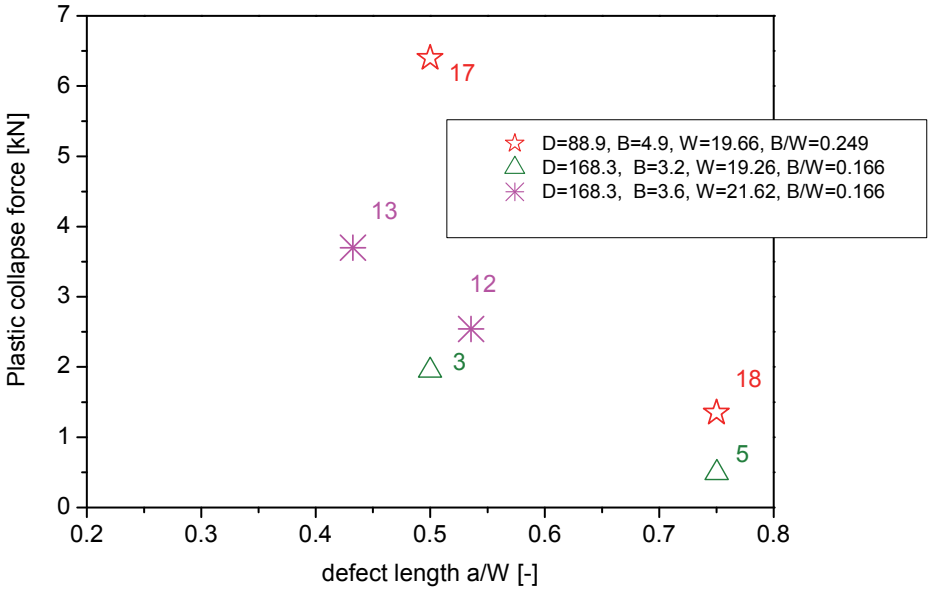

Figure 7.84. Dependence of plastic collapse load on defect length for PRNB specimens produced from seamless and seam pipes

Additional series of models are formed, corresponding to groups of fabricated specimens by size. On these models, the shape of the stress concentrator is varied (notches or cracks), as well as their length a; following values for the ratio a/W are used: 0.25, 0.35, 0.45, 0.5, 0.55, 0.65, 0.75. Dependence of plastic collapse load on the initial damage length is formed in the following figures.

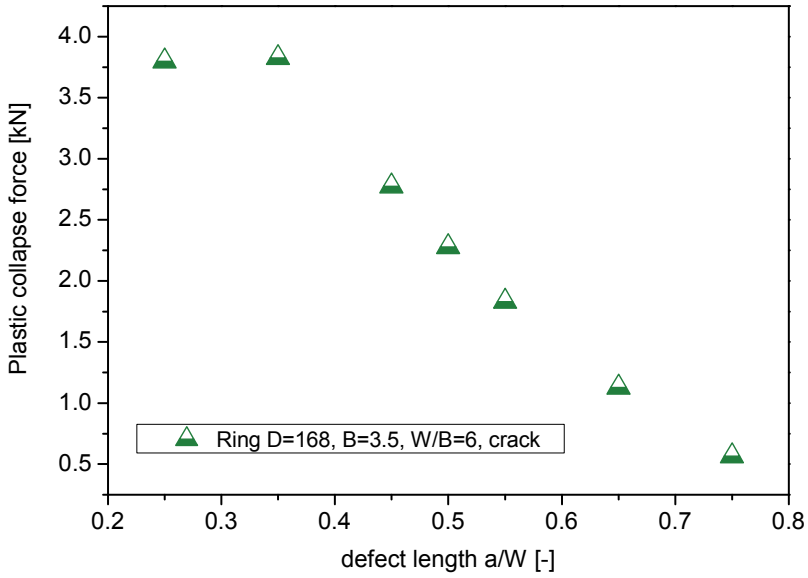

Figure 7.85. Dependence of plastic collapse load on defect length determined numerically - D=168.3 mm, B=3.5 mm, W/B=6, crack

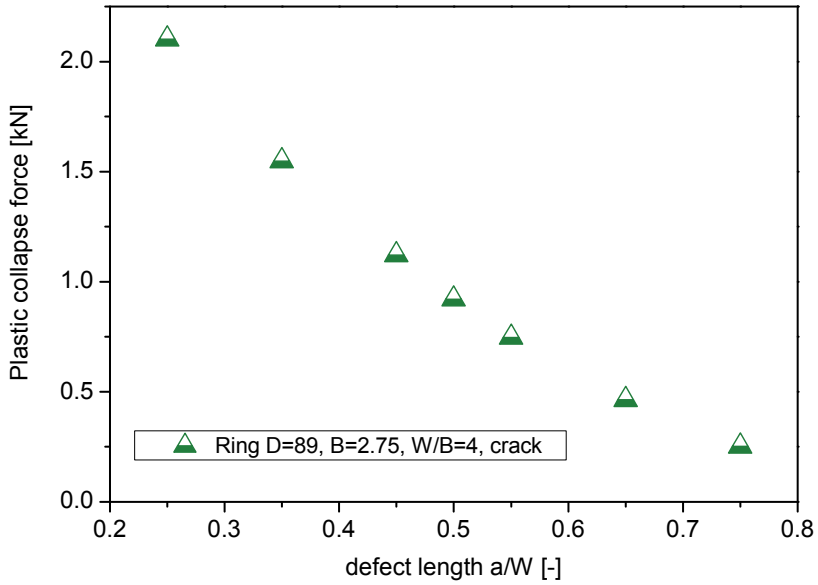

Figure 7.86. Dependence of plastic collapse load on defect length determined numerically - D=88.9 mm, B=2.75 mm, W/B=4, crack

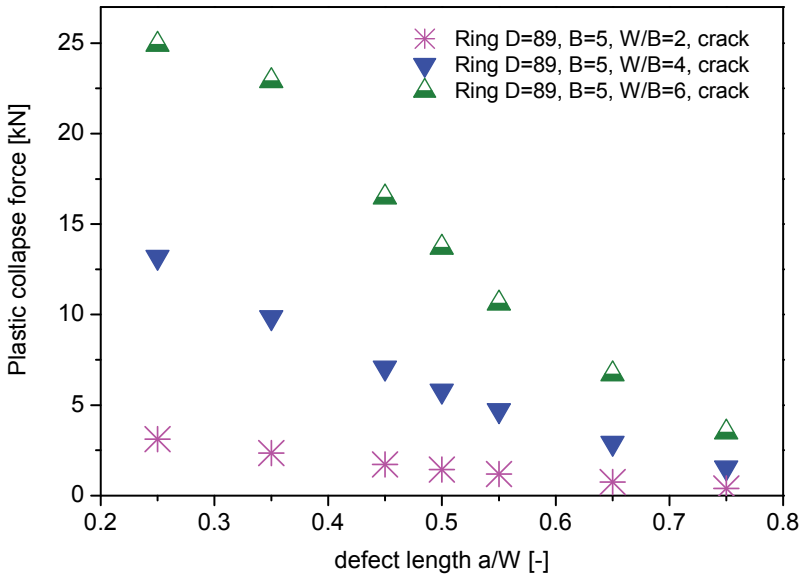

Figure 7.87. Dependence of plastic collapse load on defect length determined numerically - D=88.9 mm, B=5 mm, W/B=2,4 and 6, crack

It is concluded that small crack lengths do not give adequate results, and that they should be avoided. A possible reason is the equivalent plastic strain field, which is for some specimens characterised by a large difference between the outer and inner surface, as well as large values in the zones far from the stress concentration areas (crack/notch tip or contact). Irregularity becomes more pronounced with decrease of the wall thickness and increase of the specimen width.

The first example is shown in figures 7.88 and 7.89 - ring with diameter 168.3 mm, wall

thickness 3.5 mm and ratio *W/B*=6. For small crack lengths, *a/W* = 0.25 and 0.35, large plastic strain values are obtained far from the crack region, figure 7.88. For the crack with *a/W* = 0.25, plastic strain field around the crack is so irregular that the two parts of the plastic zone are not joined. On the other hand, for larger crack lengths (figure 7.89) plastic zones are rather regular, and large strain values are obtained only in the crack region.

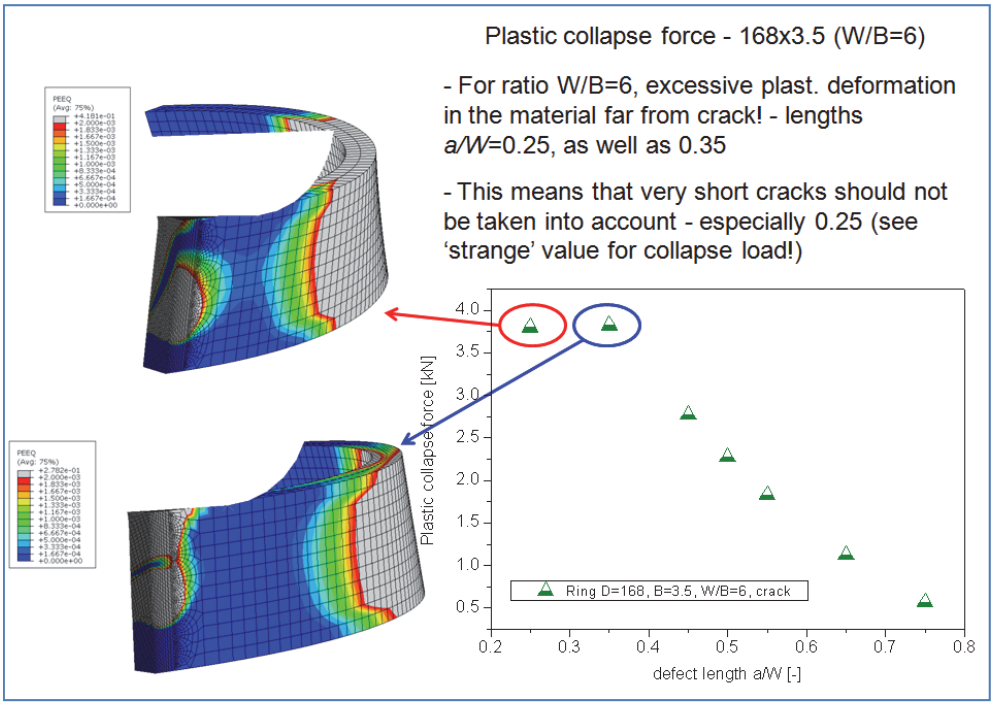

Figure 7.88. Plastic strain fields at plastic collapse for rings with D=168.3mm, B=3.5mm, W/B=6 - small a/W values

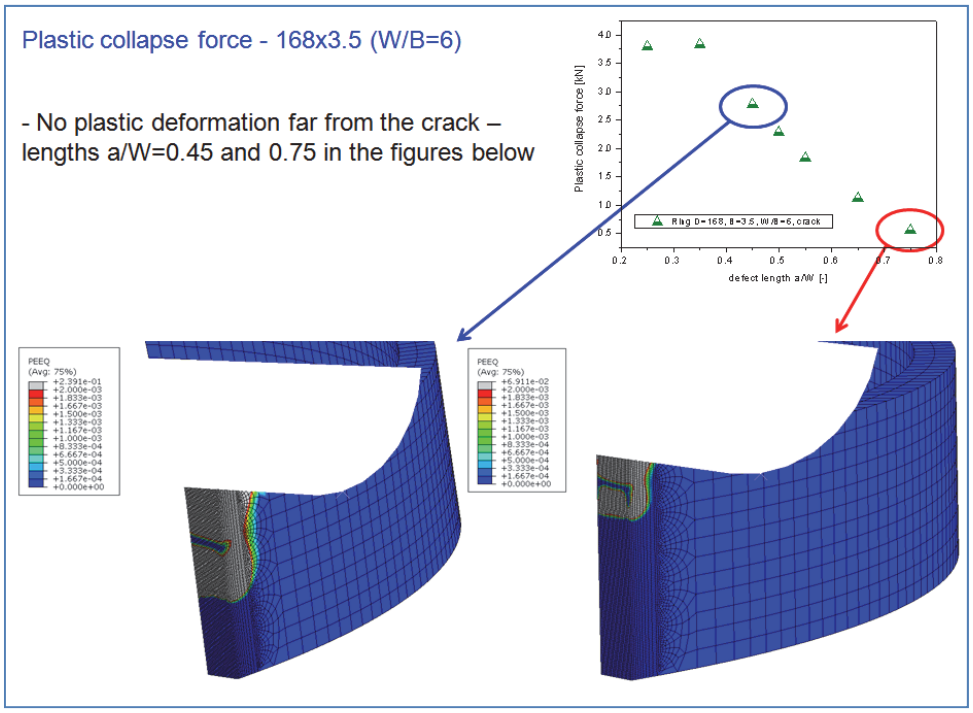

Figure 7.89. Plastic strain fields at plastic collapse for rings with D=168.3mm, B=3.5mm, W/B=6 - larger a/W values

In figures 7.90 and 7.91, it can be seen that the irregularity of the plastic strain field decreases with decrease of the ratio *W/B*.

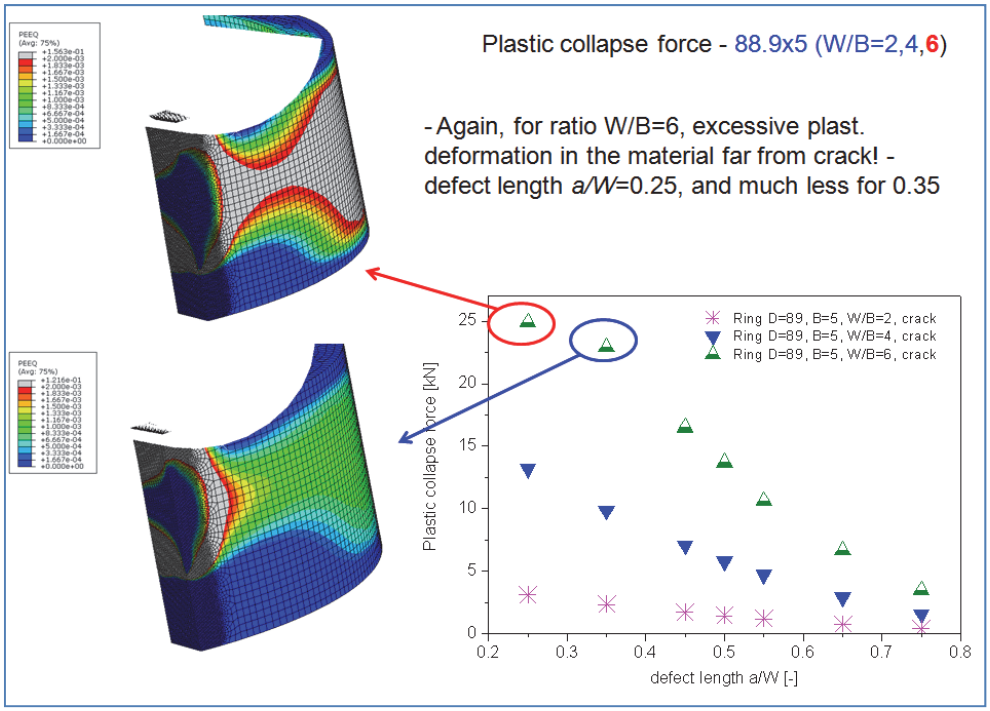

Figure 7.90. Plastic strain fields at plastic collapse for rings with D=88.9mm, B=5mm, W/B=6 - small a/W values

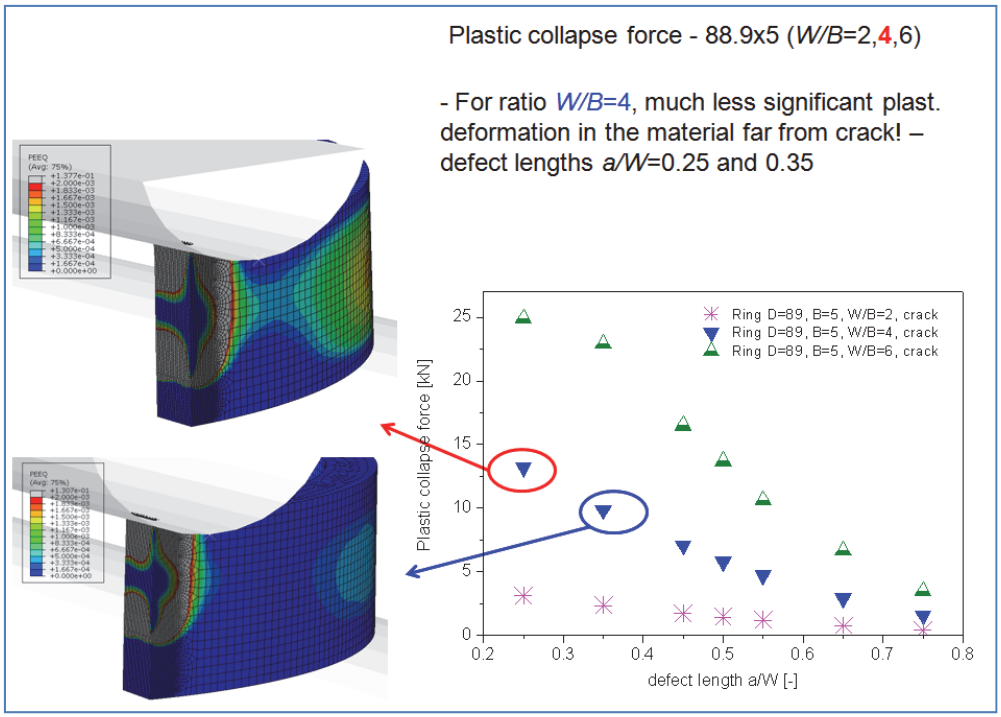

Figure 7.91. Plastic strain fields at plastic collapse for rings with D=88.9mm, B=5mm, W/B=4 - small a/W values

In further analysis, the plastic collapse loads are normalised by using the limit load of the ring with same dimensions, but without stress concentrators; this load is determined analytically [92]:

$$F_{Y0} = \frac{4\sigma_Y \cdot B \cdot W}{\sqrt{3 \cdot \left[1 + 12 \cdot \left(\frac{s}{W}\right)^2\right]}} \tag{7.1}$$

This enables determination of the influence of specimen geometry (primarily ratios *R/B* and *W/B*) on plastic collapse loads. The results are very similar, and the normalised curves almost coincide. Some new conclusions can be derived from these two figures. First, a significant increase of *W/B* ratio does not affect the material behaviour with respect to the normalised plastic collapse load, figure 7.92. Also, the change of wall thickness and ring diameter also do not cause the change of trends for the normalised plastic collapse loads, figure 7.93.

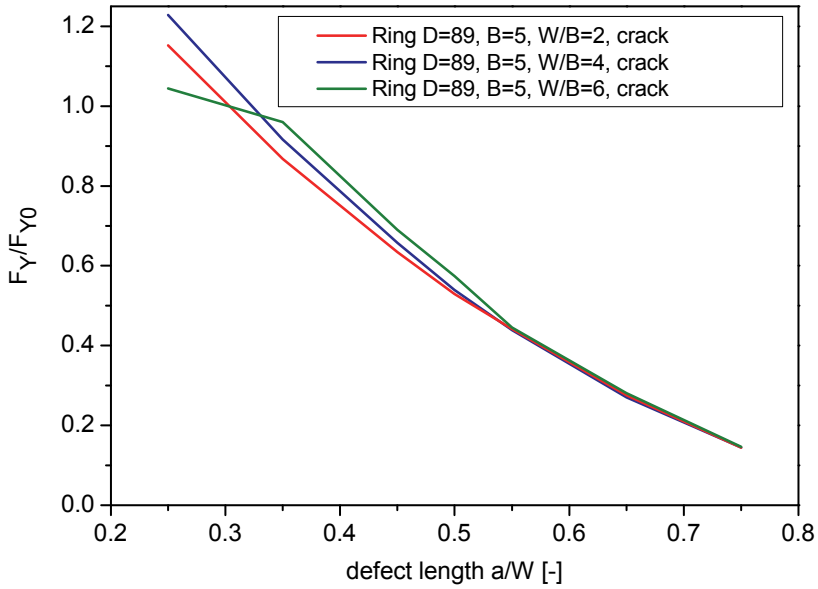

Figure 7.92. Normalised plastic collapse loads for D=88.9mm, B=5mm, W/B=2,4 and 6

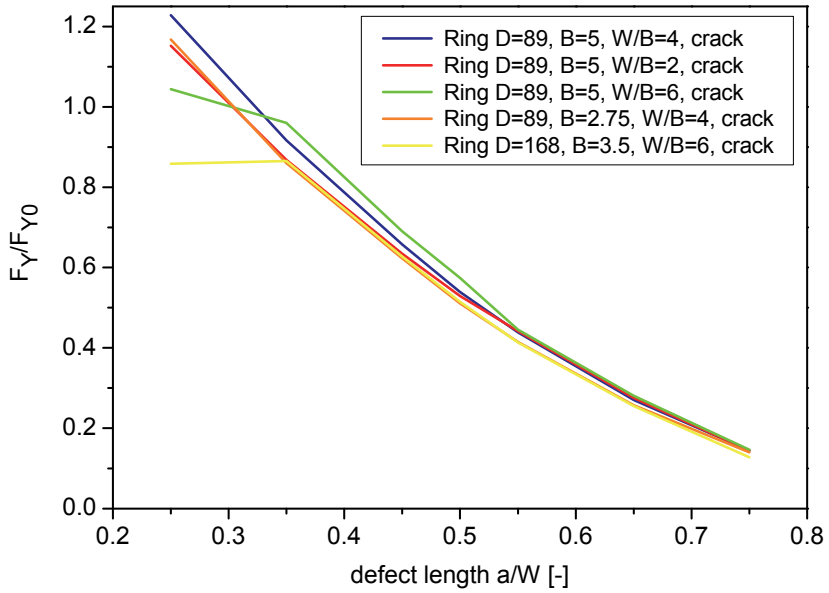

Figure 7.93. Normalised plastic collapse loads for five ring series

7.5 Ring-shaped specimens - determination of η_{plast} factor

On series of models with elastic-plastic material behaviour, the values of η_{plast} factor are determined (i.e. checked for the examined geometries). This factor is necessary for determining the J integral value based on the tracking of force and deformation of the specimen during testing. As measure of deformation, CMOD is often used (as shown in the following text and diagrams), but load line displacement can be used as well. The base for this procedure are diagrams F-CMOD, obtained through examination of a

series of models of specimens; all dimensions of the models in a series are the same, while the notch or crack length is varied. The range of ratios of the stress concentrator length and specimen width is a/W=0.25..0.75, which is broader in comparison with the range which is often used in the literature (a/W=0.45..0.55).

Based on the initial diagrams F-CMOD, diagrams F-CMOD$_{pl}$ are formed, by subtracting the elastic component of the crack mouth displacement from the total value.

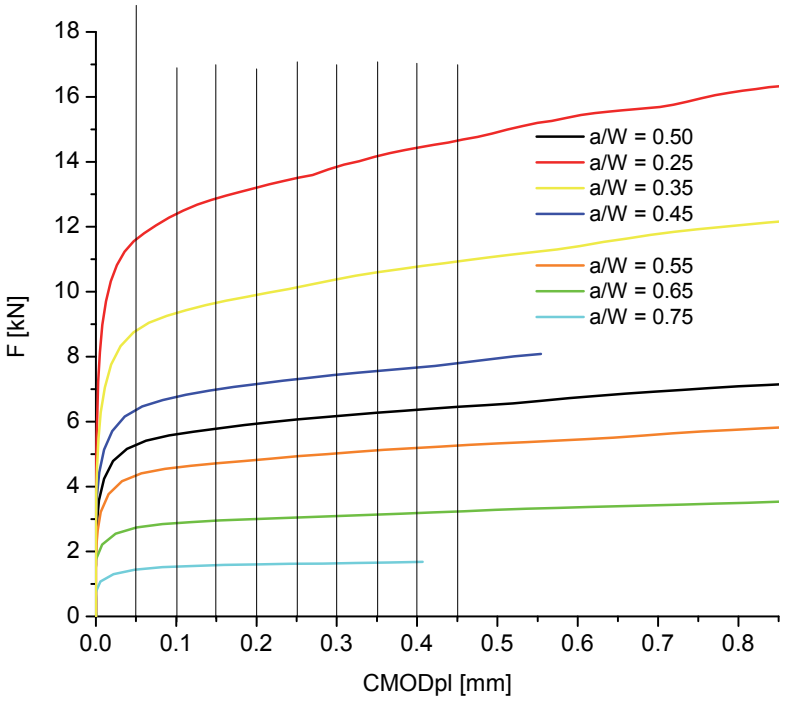

Figure 7.94 Dependence of the force value on the plastic component of CMOD

After that, dependence of the value S_{ij} on CMOD$_{pl}$ is drawn; S_{ij} represents the ratio of force values for two specimens with the same value of plastic component of CMOD. This value, even though it can vary significantly at the beginning of testing, becomes approximately constant with the increase of loading.

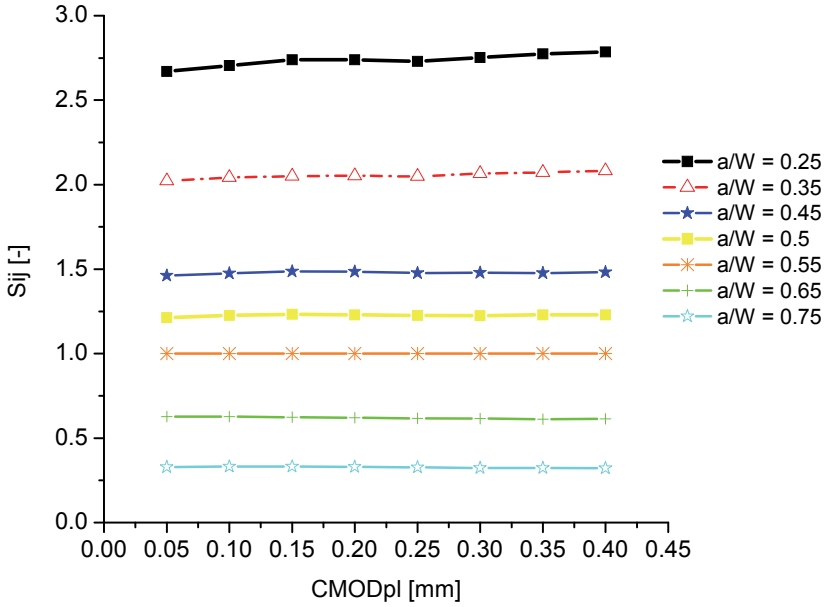

Figure 7.95 Dependence of the value S_{ij} on the plastic component of CMOD

The values from this figure are used for determination of the value of η_{plast} factor, which is actually the slope of the line (approximately straight) LogS_{ij} - Log(b/W), where b is the ligament length ($b=W-a \rightarrow b/W=1-a/W$). Forming of diagrams shown that the described methodology cannot be applied to cracks with length 25% of the specimen width - actually, they are not suitable for examination, which is also shown by plastic strain analysis, where large values are obtained far from the crack and the contact region.

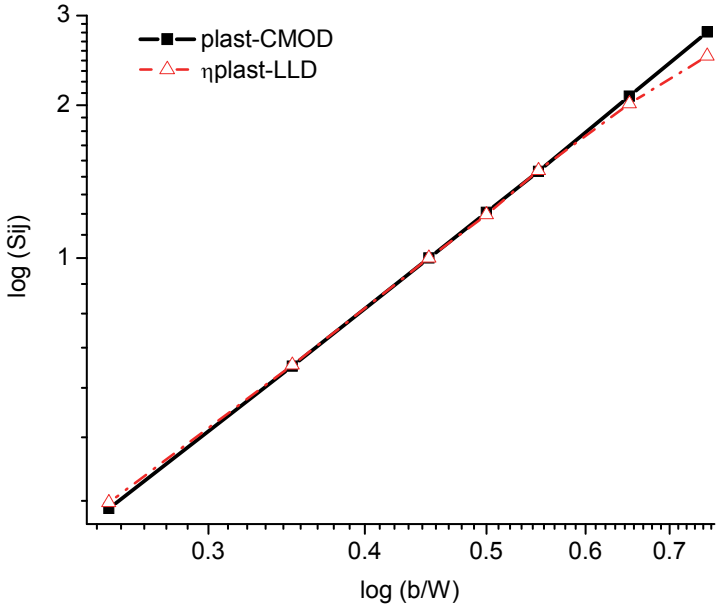

Figure 7.96 Log-log dependence of the value S_{ij} on ratio b/W (ligament length / specimen width)

Obtained values for η_{plast} factor are shown in table 7.3. Although certain dependences on characteristic dimensions, such as ratios *B/D* or *W/B* exist, they are not very pronounced.

It can be seen that the most of the results lie within the range obtained for crack and notch in [92,116] - between 1.9 and 2.07. However, it can be said that some specimens are not suitable for this procedure. Actually, the example is the same geometry which shown a very irregular plastic strain field and plastic collapse behaviour in figure 7.70 (small *a/W* ratio, diameter 168.3 mm, wall thickness 3.5 mm, ratio *W/B*=6).

A trend of general small decrease of values is observed for the series of specimens with thicker walls (diameter 88.9 mm, wall thickness 5 mm). In any case, if the values for *b/W* are from 0.25 to 0.55 (i.e. if *a/W* is between 0.45 and 0.75), it can be concluded that all the values of η_{plast} factor are close to 2, which is the value corresponding to SENB specimen. This can be considered as another similarity between these geometries.

In [92], even larger notch ratios are examined, resulting in larger values of η_{plast}. Such notches could further reduce the stress triaxiality, which makes the crack growth initiation less likely to occur, and they are not considered here. Also, the values of η_{plast} for determination of *J* integral using the F-v_{LL} curves are also given in the same work.

Table 7.3. Values of $\eta_{plast\text{-}CMOD}$ factor for different PRNB specimen geometries

	$\eta_{plast\text{-}CMOD}$ (*b/W*=0.25-0.45)	$\eta_{plast\text{-}CMOD}$ (*b/W*=0.45-0.55)	$\eta_{plast\text{-}CMOD}$ (*b/W*=0.55-0.75)
[92] - crack		2.07	
[92] - notch R0.25		1.90	
Ring168-35-06-crack	1.93	2.00	0.72
Ring89-275-04-crack	1.94	2.04	2.00
Ring89-275-04-notch	1.99	1.99	2.09
Ring89-5-02-crack	1.96	1.92	1.96
Ring89-5-04-crack	1.93	1.96	2.04
Ring89-5-06-crack	1.93	1.94	1.82

8. CONCLUSIONS

This thesis deals with damage and fracture characterisation of the pipeline material, through application of a recently proposed testing geometry - Pipe ring notched bend (PRNB) specimen. The research activities consisted of experimental and numerical part, and the most important conclusions are listed here. Numerical analysis is performed in software package Simulia Abaqus, including the application of the micromechanical model (Complete Gurson model - CGM) for ductile crack growth prediction. Geometry of the specimens and stress concentrators is varied; in addition to different sizes of the stress concentrators, different shapes were also considered - machined notch and pre-crack obtained by dynamic loading before the main test. In experimental testing, stereometric non-contact measurement system is applied for tracking the deformation of the specimen surface and values of fracture parameters CMOD and CTOD.

Examination of the ring specimens is first done on the specimens cut from the plate material (NIOMOL 490K), in order to be able to fabricate both standard specimens (SENB) and ring specimens (PRNB) with the same material history, cross-section dimensions and all other same conditions. Experimental part of this examination is done in a previous study, while micromechanical analysis of fracture is covered in this thesis. Parameters of the micromechanical model are determined by quantitative microstructural analysis and transferring from standard specimen geometry - SENB. The most important conclusion is that the geometry of the PRNB specimen has shown a similar behaviour to standard SENB specimen - in the conditions where the cross section is the same and the specimens are produced from the same piece of material. The quantities which are compared were: F-CMOD curves, final CMOD values, crack growth curves, trends on the plastic collapse loads. It is concluded that there is certain dependence of fracture resistance on the specimen size, which is not pronounced and relates primarily to the wall thickness, i.e. thicker walls decrease the resistance to ductile fracture. Small dependence of fracture resistance curves on the crack length (previously experimentally obtained) is confirmed, on the example of the specimen with

diameter 120 mm, with ratios *a/W* equal to 0.4 and 0.7.

Next part of the examination was experimental and numerical examination of failure of PRNB specimens cut from thin walled pipes, both seam (longitudinally welded) and seamless. Different pipe dimensions are considered; however, the ratios of these dimensions are actually more important: *R/B*, *W/B* and *a/W*. Most of the previous research has been performed on ring specimens cut from the plates, with ratios *R/B* = 8, *W/B* = 2. In this work, the ranges are extended, and maybe the most important dimension to emphasize is small wall thickness.

Crack growth curves are not severely influenced by the specimen radius, defect shape and defect initial size. The influence of the seam (welded joint) in the seam pipes is determined, based on the fracture resistance curves and fracture surfaces observed under optical microscope. Micromechanical model (CGM) can mostly successfully capture all the fracture development trends for both plate material and pipe materials. For plate material, the main aim was to show that PRNB specimen results correspond to SENB results if their cross-section is the same. However, the micromechanical analysis has also shown, just like the experimental results, that there is a difference among the materials of the pipes from the same group - on the example of seamless specimens with diameter 88.9 mm and wall thickness around 3 mm, the adequate FE size is significantly different in comparison with the other seamless pipes.

An experimental-numerical procedure for determining the fracture resistance in plane strain conditions despite the insufficient wall thickness is presented. Several numerical models of CT specimens are created, with properties corresponding to different pipe materials. Than, transferring the micromechanical parameters among these models and PRNB models enabled formation of crack resistance curves corresponding to the plane strain conditions (required by standards).

Regarding the plastic collapse loads, they were experimentally determined by using the TES (twice elastic slope) method, while analysis of plastic strain fiels is applied for numerical determination. Numerically determined values exhibit very similar trends as the experimental ones, when specimen dimensions are varied (crack length, wall thickness, specimen width). Somewhat smaller values are obtained by numerical analysis. It should be noted that, unlike the fracture behaviour, plastic collapse loads are

not significantly different when seam and seamless pipes are compared, due to the fact that it depends primarily on material tensile properties.

On series of models with elastic-plastic material behaviour, the values of η_{plast} factor are determined for the examined geometries of ring specimens. For ratios a/W between 0.45 and 0.75 (both for pre-cracks and notches with radius 0.25 mm), the values of η_{plast} factor are close to 2 in all cases, which is the value corresponding to SENB specimen.

If the two examined types of stress concentrators are compared, the notch is characterised by lower stress triaxiality, which is a possible cause for lack of stable crack growth in some geometries. However, the notched specimens are more convenient for fabrication and the final crack shape is symmetric. On the example of both notched and pre-cracked specimens, a good repeatability is obtained. Dependence of results on stress concentrator length, pipe wall thickness and specimen width is not pronounced.

The results have shown that PRNB specimens can be successfully used for assessment of failure resistance of the materials of the seam and seamless pipes; they also revealed some differences between the pipe groups, and even among the specimens from the same group. The heterogeneity effect of the welded joint (seam) in the seam pipes is determined. Also, developed experimental-numerical procedure enabled determination of crack growth prediction in plane strain conditions, despite the thin walls of the specimens.

LITERATURE

[1] V. Dias da Silva: *Mechanics and strength of materials*. Springer, Berlin (2006)

[2] C.E.Inglis: *Stresses in a plate due to the presence of cracks and sharp corners*. Transactions of the Institute of Naval Architects, Vol. 55 (1913) pp. 219-242

[3] A.A.Griffith: *The phenomena of rupture and flow in solids*. Philosophical Transactions of the Royal Society A, Vol. 221 (1920) pp. 163-198

[4] G.R. Irwin: *Plastic zone near a crack and fracture toughness*. Proceedings of the Sagamore Research Conference, Vol. 4. Syracuse University Research Institute, Syracuse, NY (1961) pp. 63-78

[5] D.S. Dugdale: *Yielding in steel sheets containing slits*. Journal of the Mechanics and Physics of Solids, Vol. 8 (1960) pp. 100-104

[6] A.A. Wells: *Unstable crack propagation in metals: cleavage and fast fracture.* Proceedings of the Crack Propagation Symposium, Vol. 1, Cranfield, UK, (1961) 210-223

[7] J.R. Rice: *A path independent integral and the approximate analysis of strain concentration by notches and cracks*. Journal of Applied Mechanics, Vol. 35 (1968) pp. 379-386

[8] J.D. Eshelby: *The continuum theory of lattice defects*. Solid State Physics, Vol. 3 (1956) pp. 79-144

[9] J.W. Hutchinson: *Singular behavior at the end of a tensile crack tip in a hardening material*. Journal of the Mechanics and Physics of Solids, Vol. 16 (1968) pp.13-31

[10] J.R. Rice, G.F. Rosengren: *Plane strain deformation near a crack tip in a power-law hardening material*. Journal of the Mechanics and Physics of Solids, Vol. 16 (1968) pp. 1-12

[11] J.A. Begley, J.D Landes: *The J-Integral as a fracture criterion*. ASTM STP 514, American Society for Testing and Materials - ASTM, Philadelphia, PA (1972) pp. 1-20

[12] H.M. Westergaard: *Bearing pressures and cracks*. Journal of Applied Mechanics, Vol. 6 (1939) pp. 49-53

[13] G.R. Irwin: *Analysis of stresses and strains near the end of a crack traversing a plate*. Journal of Applied Mechanics, Vol. 24 (1957) pp. 361-364

[14] I.N. Sneddon: *Distribution of stress in the neighbourhood of a crack in an elastic solid*. Proceedings of the Royal Society of London A, Vol. 187 (1946) pp. 229-260

[15] M.L. Williams: *On the stress distribution at the base of a stationary crack*. Journal of Applied Mechanics, Vol. 24 (1957) pp. 109-114

[16] T.L. Anderson: *Fracture mechanics*. CRC Press, London (1995)

[17] A. Sedmak: *Application of fracture mechanics to structural integrity*. Faculty of Mechanical Engineering, Belgrade (2003) in Serbian

[18] M. Berković: *Determining the stress intensity factors by using the finite element method* In: Monograph of the 1st International Fracture Mechanics Summer School, Faculty of Technology and Metallurgy - Goša Institute, Belgrade (1981) pp. 107-124, in Serbian

[19] *ESIS P2-92: Procedure for determining the fracture behaviour of materials*. European Structural Integrity Society - ESIS (1992)

[20] *EFAM GTP 94: Test procedure for determining the fracture behaviour of materials*. GKSS Research Center publication (1994)

[21] K.H. Schwalbe: *Basic engineering methods of fracture mechanics and fatigue*. GKSS Research Center, Geesthacht (2001)

[22] R. Narasimhan, A.J. Rosakis: *Three-dimensional effects near a crack tip in a ductile three-point bend specimen*: part I - a numerical investigation. Journal of Applied Mechanics, Vol. 57 (1990) pp. 607-617

[23] *Displacement gauge system for applications in fracture mechanics*. Patent Publication, GKSS Research Center, Geesthacht (1991)

[24] G.P. Nikishkov, J. Heerens, K.H. Schwalbe: *Transformation of CTOD δ_5 to CTOD δ_{BS} and J-integral for 3PB- and CT-specimens*. Engineering Fracture Mechanics, Vol. 63 (1999) pp. 573-589

[25] H. Andersson: *Finite element representation of stable crack growth*. Journal of the Mechanics and Physics of Solids, Vol. 21 (1973) pp. 337-356

[26] A.U. de Koning: *A contribution to the analysis of quasi static crack growth in steel materials*. Proceedings of the 4th International Conference on Fracture, Vol. 3, Waterloo, Canada (1977) pp. 25-31

[27] J.C. Newman J.r., M.A. James, U. Zerbst: *A review of the CTOA/CTOD fracture criterion*. Engineering Fracture Mechanics, Vol. 70 (2003) pp. 371-385

[28] U. Zerbst, M. Heinimann, C. Dalle Donne, D. Steglich: *Fracture and damage mechanics modelling of thin-walled structures - An overview*. Engineering Fracture Mechanics, Vol. 76 (2009) pp. 5-43

[29] J. Awerbuch: *Fundamentals of mechanical behavior of materials*. Wiley Custom Publishing, Philadelphia (2001)

[30] Đ. Drobnjak: *Physical metallurgy - Physics of strength and plasticity I*. University of Belgrade, Faculty of Technology and Metallurgy, Belgrade (1986) in Serbian

[31] G.E. Dieter: *Mechanical metallurgy*. Mc Graw-Hill, New York (1986)

[32] C.P. Cherepanov: *Crack propagation in continuous media*. Journal of Applied Mathematics and Mechanics, Vol. 31 (1967) pp. 503-512

[33] E. Budiansky, J.R. Rice: *Conservation laws and energy release rates*. Journal of Applied Mechanics, Vol. 40 (1973) pp. 201-203

[34] R.M. McMeeking: *Finite deformation analysis of crack tip opening in elastic-plastic materials and implications for fracture initiation*. Journal of the Mechanics and Physics of Solids, Vol. 25 (1977) pp. 357-381

[35] S. Saxena, N. Ramakrishnan, JS. Chouhan: *Establishing methodology to predict fracture behaviour of piping components by numerically predicting specimen fracture data using tensile specimen test*. Engineering Fracture Mechanics, Vol. 77 (2010) pp. 1058-1072

[36] Rakin M., Cvijović Z., Grabulov V., Putić S., Sedmak A.: *Prediction of ductile fracture initiation using micromechanical analysis*. Engineering Fracture Mechanics, Vol. 71 (2004) pp. 813-827

[37] F. McClintock: *On the plasticity of the growth of fatigue cracks.* In: Fracture of Solids. John Wiley and Sons (1963) pp. 65-102

[38] F. McClintock: *Ductile rupture by the growth of holes*. Journal of Applied Mechanics, Vol. 35 (1968) pp. 363-371

[39] A. Thompson, J. Williams: *Nuclei for ductile fracture in titanium*. Proceedings of the 4th International Conference on Fracture - ICF4, Vol. 2, Waterloo, Canada (1977) pp. 343-348

[40] S. Goods, L. Brown: *The nucleation of cavities by plastic deformation*. Acta Metallurgica, Vol. 27 (1979) pp. 1-15

[41] L. Babout, Y. Brechet, E. Maire, R. Fougeres: *On the competition between particle fracture and particle decohesion in metal matrix composites*. Acta Materialia, Vol. 52 (2004) 4517-4525

[42] W.T. Becker, D. McGarry: *Mechanisms and appearances of ductile and brittle fracture in metals.* In: ASM Handbook Vol. 11, Failure Analysis and Prevention. ASM International (2002) pp. 587-626

[43] C. Berg: *Plastic dilatation and void interaction*. In: Inelastic Behavior of Solids, McGraw-Hill, New York (1970) pp. 171-210

[44] J.R. Rice, D.M. Tracey: *On the ductile enlargement of voids in triaxial stress fields*. Journal of the Mechanics and Physics of Solids, Vol. 17 (1969) pp. 201-217

[45] H. Fresnel, P. Longère, V. Grolleau, P. Hardy, G. Rio: *Numerical prediction of the structural failure of airbag inflators in the destructive testing phase*. Engineering Failure Analysis, Vol. 16 (2009) pp. 2140-2152

[46] A. Pineau: *Physical mechanisms of damage*. In: Local Approach to Fracture, Presses de l’Ecole des Mines, Paris (2004) pp. 33-78

[47] A.A. Benzerga, J. Besson, A. Pineau: *Anisotropic ductile fracture. Part I: experiments*. Acta Materialia, Vol. 52 (2004) pp. 4623-4638

[48] M. Seidenfuss, M. Samal, E. Roos: *On critical assessment of the use of local and nonlocal damage models for prediction of ductile crack growth and crack path in various loading and boundary conditions*. International Journal of Solids and Structures, Vol. 48 (2011) pp. 3365-3381

[49] J. Liu, X. Hao, G. Li, G. Liu: *Microvoid evaluation of ferrite ductile iron under strain*. Materials Letters, Vol. 56 (2002) pp. 748-755

[50] P.F. Thomason: *Ductile fracture of metals*. Pergamon Press, Oxford (1990)

[51] F.M. Beremin. *Cavity formation from inclusions in ductile fracture of A508 steel*. Metallurgical Transactions, Vol. 12A (1981) pp. 723-731

[52] FM. Beremin: *Experimental and numerical study of the different stages in ductile rupture: application to crack initiation and stable crack growth*. In: Three-dimensional constitutive relations and ductile fracture. North-Holland Publ., Amsterdam (1981) pp. 157-172

[53] Y. Huang: *Accurate dilatation rates for spherical voids in triaxial stress fields*. Jurnal of Applied Mechanics - Transactions ASME, Vol. 58 (1991) pp. 1084-1086

[54] R. Chaouadi, P. De Meester, W. Vandermeulen: *Damage work as ductile criterion*. International Journal of Fracture, Vol. 66 (1994) pp. 155-164

[55] L. Bauvineau, H. Burlet, C. Eripret, A. Pineau: *Modelling ductile stable growth in a C-Mn steel with local approaches*. Proceedings of the Euromech-Mecamat Conference on Local Approach to Fracture 86-96. Fontainebleau, France (1996) p. 26-38

[56] T.C. Miller, T.L. Anderson: *A void growth model relating fracture toughness and constraint*. In: Landes JD et al., editors. Fracture Mechanics. ASTM STP 1207, vol. 24. Philadelphia: American Society for Testing and Materials; (1994) pp. 87-107

[57] W. Schmitt, E. Keim, G. Nagel, D.Z. Sun: *Engineering applications of the local approach*. In: Failure Assessment Concepts and Applications. Fraunhofer-Institut fuer Werkstoffmechanik (IWM); (1997) p. X-1390.

[58] A.L. Gurson: *Continuum theory of ductile rupture by void nucleation and growth*: part I - yield criteria and flow rules for porous ductile media. Journal of Engineering Materials and Technology - Transactions ASME, Vol. 99 (1977) pp. 2-15

[59] I. Scheider: *Derivation of separation laws for cohesive models in the course of ductile fracture*. Engineering Fracture Mechanics, Vol. 76 (2009) pp. 1450-1459

[60] Z.L. Zhang, C. Thaulow, J. Odegard: *A complete Gurson model approach for ductile fracture*. Engineering Fracture Mechanics, Vol. 67 (2000) pp.155-168

[61] M. Bergant, A. Yawny, J. Perez Ipiña: *Experimental determination of J-resistance curves of nuclear steam generator tubes*. Engineering Fracture Mechanics, Vol. 164 (2016) pp. 1-18

[62] P. Cambrésy: *Damage and fracture mechanisms investigations of an aluminium laser beam weld*. GKSS Research Center, Geesthacht (2006)

[63] I. Cvijović-Alagić: *Damage and fracture resistance of titanium based alloys for medical application,* University of Belgrade, Faculty of Technology and Metallurgy, PhD Dissertation (2013) in Serbian

[64] S. Feld-Payet, J. Besson, F. Feyel: *A continuous-discontinuous description of ductile fracture using adaptive remeshing strategies*. Proceedings of the IV European Conference on Computational Mechanics ECCM IV, Paris, France (2010) published on CD

[65] J. Mediavilla, R.H.J. Peerlings, M.G.D. Geers: *A robust and consistent remeshing-transfer operator for ductile fracture simulations*. Computers and Structures, Vol. 84 (2006) pp. 604-623

[66] P.O. Bouchard, F. Bay, Y. Chastel: *Numerical modelling of crack propagation: automatic remeshing and comparison of different criteria*. Computer Methods in Applied Mechanics and Engineering, Vol. 192 (2003) pp. 3887-3908

[67] L. Xia, C.F. Shih: *Ductile crack growth-I. A numerical study using computational cells with microstructurally-based length scales*. Journal of the Mechanics and Physics of Solids, Vol. 43 (1995) pp. 233-259

[68] X. Gao, J. Faleskog, C.F. Shih, R.H. Dodds: *Ductile tearing in part-through cracks*: experiments and cell-model predictions. Engineering Fracture Mechanics, Vol. 59 (1998) pp. 761-777

[69] P. Negre, D. Steglich, W. Brocks: *Crack extension at an interface: prediction of fracture toughness and simulation of crack path deviation*. International Journal of Fracture, Vol. 134 (2005) pp. 209-229

[70] O. Chabanet, D. Steglich, J. Besson, V. Heitmann, D. Hellmann, W. Brocks: *Predicting crack growth resistance of aluminium sheets*. Computational Materials Science, Vol. 26 (2003) pp. 1-12

[71] Y. Chen, S. Lambert: *Numerical modeling of ductile tearing for semi-elliptical surface cracks in wide plates.* International Journal of Pressure Vessels and Piping, Vol. 82 (2005) pp. 417-426

[72] V. Tvergaard, J.W. Hutchinson: *Two mechanisms of ductile fracture*: void by void growth versus multiple void interaction. International Journal of Solids and Structures, Vol. 39 (2002) pp. 3581-3597

[73] V. Tvergaard: *Discrete modelling of ductile crack growth by void growth to coalescence*. International Journal of Fracture, Vol. 148 (2007) pp. 1-12

[74] M. Rakin: *Local approach to ductile fracture of metallic materials*. Serbian Society of Metallurgical Engineers, Belgrade (2009) in Serbian

[75] V. Tvergaard, J.W. Hutchinson: *Effect of strain-dependent cohesive zone model on predictions of crack growth resistance*. International Journal of Solids and Structures, Vol. 33 (1996) pp. 3297-3308

[76] T. Siegmund, W. Brocks: *Prediction of the work of separation and implications to modeling*. International Journal of Fracture, Vol. 99 (1999) pp. 97-116

[77] I. Scheider, M. Schodel, W. Brocks, W. Schonfeld: *Crack propagation analyses with CTOA and cohesive model: Comparison and experimental validation*. Engineering Fracture Mechanics, Vol. 73 (2006) pp. 252-263

[78] A. Pineau: *Modeling ductile to brittle fracture transition in steels-micromechanical and physical challenges*. International Journal of Fracture, Vol. 150 (2008) pp. 129-156

[79] A. Hillerborg, M. Modeer, P.E. Petersson: *Analysis of crack formation and crack growth in concrete by means of fracture mechonics and finite elements.* Cement Concrete Research, Vol. 6 (1976) pp. 773-782

[80] I. Scheider, W. Brocks: *Simulation of cup-cone fracture using the cohesive model*. Engineering Fracture Mechanics, Vol. 70 (2003) pp. 1943-1961

[81] V. Tvergaard: *Crack growth predictions by cohesive zone model for ductile fracture*. Journal of the Mechanics and Physics of Solids, Vol. 49 (2001) pp. 2191-2207

[82] G. Hütter, L. Zybell, M. Kuna: *Micromechanical modeling of crack propagation in nodular cast iron with competing ductile and cleavage failure*. Engineering Fracture Mechanics Vol. 147 (2015) pp. 388-397

[83] *ASME B31.8S - Managing system integrity of gas pipelines*. American Society of Mechanical Engineers - ASME, New York (2016)

[84] L. Gajdos, M. Sperl: *Evaluating the integrity of pressure pipelines by fracture mechanics*. In: Applied Fracture Mechanics, InTech Publishing (2012)

[85] Z.L. Zhang, J. Xu, B. Nyhus, E. Østby: *SENT (single edge notch tension) methodology for pipeline applications.* Proceedings of the 18th European Conference on Fracture, Dresden, Germany, (2010), pp. 1-8, published on CD

[86] J. Xu, Z.L. Zhang, E. Østby, B. Nyhus, D.B. Sun: *Effects of crack depth and specimen size on ductile crack growth of SENT and SENB specimens for fracture mechanics evaluation of pipeline steels.* International Journal of Pressure Vessels and Piping, Vol. 86 (2009) pp. 787-797

[87] J. Xu, Z.L. Zhang, E. Østby, B. Nyhus, D.B. Sun: *Constraint effect on the ductile crack growth resistance of circumferentially cracked pipes*. Engineering Fracture Mechanics, Vol. 77 (2010) pp. 671-684

[88] G. Mahajan, S. Saxena, A. Mohanty: *Numerical characterization of compact pipe specimen for stretch zone width assessment*. Fatigue and Fracture of Engineering Materials and Structures, Vol. 39 (2016) pp. 859-865

[89] J.M. Koo, S. Park, C.S. Seok: *Evaluation of fracture toughness of nuclear piping using real pipe and tensile compact pipe specimens.* Nuclear Engineering and Design, Vol. 259 (2013) pp. 198-204

[90] M. Bergant, A. Yawny, J. Perez Ipiña: *Numerical study of the applicability of the g-factor method to J-resistance curve determination of steam generator tubes using non-standard specimens*. Engineering Fracture Mechanics, Vol. 146 (2015) pp. 109-120

[91] D. Angeles-Herrera, A. Albiter-Hernández, R. Cuamatzi-Meléndez, J.L. González-Velázquez: *Fracture toughness in the circumferential-longitudinal and circumferential-radial directions of longitudinal weld API 5L X52 pipeline using standard C(T) and nonstandard curved SE(B) specimens.* International Journal of Fracture, Vol. 188 (2014) pp. 251-256

[92] A. Likeb: *Suitability of pipe-ring specimen for determination of fracture toughness*. PhD Thesis, University of Maribor, Faculty of Mechanical Engineering, Slovenia, (2014) in Slovenian

[93] V. E. Lysaght: *Indentation hardness testing*. Reinhold, New York (1949)

[94] H. Czichos, T. Saito, L. Smith (Eds.): *Handbook of materials measurement methods*. Springer, Berlin (2006)

[95] E.E. Underwood: *Quantitative metallography*. In: ASM Metals Handbook, Vol. 9, ASM International (1986) pp. 123-134

[96] http://www.tamsteel.com

[97] J. Lozanović, N. Gubeljak, A. Sedmak: *Measurement of strain using stereometry*, Technical Gazette, Vol. 16 (2009) pp. 93-99

[98] N. Gubeljak, A. Likeb, Y. Matvienko: *Fracture toughness measurement by using pipe-ring specimens*. Procedia Materials Science, Vol. 3 (2014) pp. 1934-1940

[99] W. Musraty, B. Međo, N. Gubeljak, P. Štefane, Z. Radosavljević, Z. Burzić, M. Rakin: *Seam pipes for process industry - fracture analysis by using ring-shaped specimens*. Chemical Industry / Hemijska industrija, Vol. 72 (*2018*) pp. 39-46

[100] *ASTM E1820: Standard test method for measurement of fracture toughness*, American Society for Testing and Materials - ASTM (2015)

[101] Musrati, W., Međo, B., Gubeljak, N., Štefane, P., Veljić, D., Sedmak, A., Rakin, M.: *Fracture Analysis of Axially Flawed Ring-Shaped Bending Specimen*, Procedia Structural Integrity, Vol. 13 (2018) pp. 1828-1833

[102] M. Rakin, B. Medjo, N. Gubeljak, A. Sedmak*: Micromechanical assessment of mismatch effects on fracture of high-strength low alloyed steel welded joints*. Engineering Fracture Mechanics, Vol. 109 (2013) pp. 221-235

[103] I. Penuelas, C. Betegon, C. Rodriguez: *A ductile failure model applied to the determination of the fracture toughness of welded joints.* Numerical simulation and experimental validation. Engineering Fracture Mechanics, Vol. 73 (2006) pp. 2756-2773

[104] K.H. Schwalbe, R.A. Ainsworth, C. Eripret, C. Franco, P. Gilles, M. Koçak, al. et: *Common views on the effects of yield strength mis-match on testing and structural assessment*. In: Mis-matching of Interfaces and Welds. GKSS Research Center, Geesthacht (1997) pp. 99-132

[105] R. Chhibber, P. Biswas, N. Arora, S.R. Gupta, B.K. Dutta: *Micromechanical modelling of weldments using GTN model*. International Journal of Fracture, Vol. 167 (2011) pp. 71-82

[106] M. Rakin, N. Gubeljak, M. Dobrojević, A. Sedmak: *Modelling of Ductile fracture initiation in strength mismatched welded joint*. Engineering Fracture Mechanics, Vol. 75 (2008) 3499-3510

[107] B. Medjo, M. Rakin, N. Gubeljak, Y. Matvienko, M. Arsić, Ž. Šarkoćević, A. Sedmak: *Failure resistance of drilling rig casing pipes with an axial crack*. Engineering Failure Analysis, Vol. 58 (2015) pp. 429-440

[108] W. Musraty, B. Medjo, N. Gubeljak, A. Likeb, I. Cvijović-Alagić, A. Sedmak, M. Rakin: *Ductile fracture of pipe-ring notched bend specimens - micromechanical analysis*. Engineering Fracture Mechanics, Vol. 175 (2017) pp. 247-261

[109] D. Steglich, W. Brocks: *Micromechanical modeling of damage and fracture of ductile metals*. Fatigue and Fracture of Engineering Materials and Structures, Vol. 21 (1998) pp. 1175-1188

[110] F. Bron, J. Besson: *Simulation of the ductile tearing for two grades of 2024 aluminum alloy thin sheets*. Engineering Fracture Mechanics, Vol. 73 (2006) pp. 1531-1552

[111] C. Ruggieri, T.L. Panontin, R.H. Dodds: *Numerical modeling of ductile crack growth in 3-D using computational cell elements.* International Journal of Fracture, Vol. 82 (1996) pp. 67-95

[112] A. Nonn, W. Dahl, W. Bleck: *Numerical modelling of damage behaviour of laser-hybrid welds*. Engineering Fracture Mechanics, Vol. 75 (2008) pp. 3251-3263

[113] B.K. Dutta, S. Guin, M.K. Sahu, M.K. Samal: *A phenomenological form of the q_2 parameter in the Gurson model*. International Journal of Pressure Vessels and Piping, Vol. 85 (2008) pp. 199-210

[114] B. Younise, M. Rakin, N. Gubeljak, B. Međo, M. Burzić, M. Zrilić, A. Sedmak: *Micromechanical analysis of mechanical heterogeneity effect on the ductile tearing of weldments.* Materials and Design Vol. 37 (2012) pp. 193-201

[115] A.G. Franklin: *Comparison between a quantitative microscope and chemical methods for assessment of non-metallic inclusions*. Journal of Iron and Steel Institute, Vol. 207 (1969) pp. 181-186

[116] A. Likeb, N. Gubeljak, Y. Matvienko: *Finite element estimation of the plastic η_{pl} factors for pipe-ring notched bend specimen using the load separation method*. Fatigue and Fracture of Engineering Materials and Structures, Vol. 37 (2014) pp. 1319-1329

[117] *Abaqus analysis user's manual*. Simulia (2018)

APPENDIX: determining the locations of integration points in 3D finite elements in software package Abaqus

In many engineering problems, it is necessary to read the values of a variable from one or more integration points in an element (or a group of elements). An example is shown in figure 4.15, where damage parameter (porosity) is tracked in the element and integration point closest to the middle of the crack front on PRNB specimen.

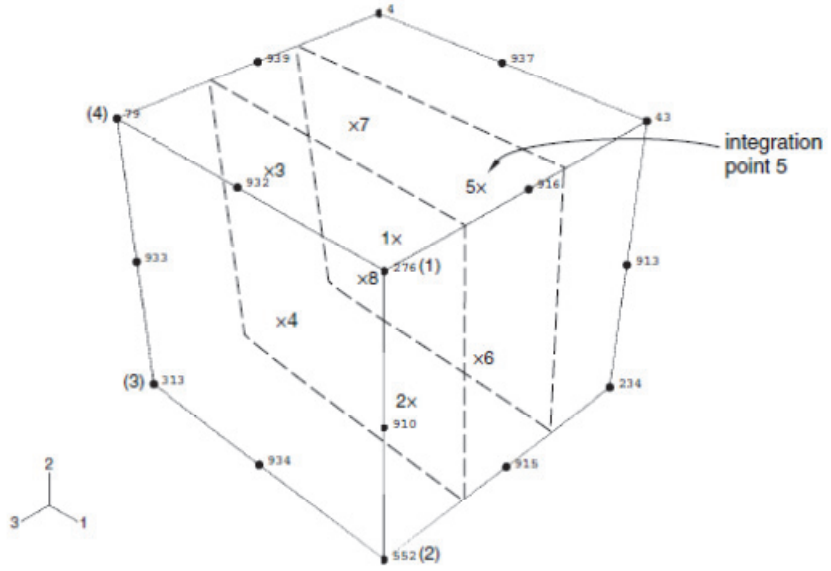

Figure A.1. *Locations of integration points in a finite element [117]*

To determine the integration point number:

1. In the **Display Group** toolbar, using the **Replace Selected** tool, the appropriate element is selected.

2. Next, the node labels should be made visible (if needed, **auto-fit** tool can be activated for better overview).

3. Using the **Query** tool, nodal connectivity for this element can be obtained (nodal connectivity is printed in the message area).

4. The nodal connectivity list should be compared with the figure of the used finite element from the Element library in Abaqus Analysis User's Manual [117], figure A.1.

5. After the global node numbers have been compared with the local numbers, appropriate integration point can be chosen.

CV of the candidate

Walid Mukhtar Musrati was born on March 8th, 1979, in AL-Khums, Lybia. In 2001, he graduated from the Faculty of Engineering of Almergheb University - Mechanical Engineering. In the period 2006-2008, he studied and finished Master academic studies on the Faculty for Mechanical Engineering and Technology at National Technical University "Kharkiv Polytechnical Institute" in Ukraine, in the field of Applied Materials Science. From 2009 to 2014, he worked as a lecturer at the Faculty of Engineering of Almergheb University. He enrolled the PhD studies at the University of Belgrade, Faculty of Technology and Metallurgy, in the school year 2014/15, and he passed all the exams in accordance with the study programme. He speaks English language and has basic knowledge of Russian.

Biografija kandidata

Walid Mukhtar Musrati je rođen 08. marta 1979. godine u AL-Khums, Libija. 2001. godine je diplomirao na Fakultetu za inženjerstvo Univerziteta Almergheb - usmerenje Mašinski Inženjer. U periodu 2006-2008. je studirao i završio Master akademske studije na Fakultetu za mašinstvo i tehnologiju pri Nacionalnom Tehničkom Univerzitetu "Kharkiv Polytechnical Institute" u Ukrajini, na usmerenju Primenjena nauka o materijalima. Od 2009. do 2014. godine je radio kao predavač na Fakultetu za inženjerstvo Univerziteta Almergheb. Doktorske studije na Tehnološko-metalurškom fakultetu Univerziteta u Beogradu je upisao školske 2014/15. godine, odslušao i položio sve ispite predviđene programom studija. Govori engleski jezik, služi se ruskim jezikom.

Изјава о ауторству

Име и презиме аутора: Walid Mukhtar Musrati

Број индекса: 4047/2014

Изјављујем

да је докторска дисертација под насловом

“Карактеризација оштећења и лома материјала цевовода коришћењем епрувета облика прстена” / “Characterisation of damage and fracture of pipeline material using ring-shaped specimens“

- резултат сопственог истраживачког рада;
- да дисертација у целини ни у деловима није била предложена за стицање друге дипломе према студијским програмима других високошколских установа;
- да су резултати коректно наведени и
- да нисам кршио/ла ауторска права и користио/ла интелектуалну својину других лица.

Потпис аутора

У Београду, _____

_____

Изјава о истоветности штампане и електронске верзије докторског рада

Име и презиме аутора: Walid Mukhtar Musrati

Број индекса: 4047/2014

Студијски програм: Инжењерство материјала

Наслов рада:

“Карактеризација оштећења и лома материјала цевовода коришћењем епрувета облика прстена” / “Characterisation of damage and fracture of pipeline material using ring-shaped specimens“

Ментор: проф. др Марко Ракин

Изјављујем да је штампана верзија мог докторског рада истоветна електронској верзији коју сам предао/ла ради похрањена у **Дигиталном репозиторијуму Универзитета у Београду.**

Дозвољавам да се објаве моји лични подаци везани за добијање академског назива доктора наука, као што су име и презиме, година и место рођења и датум одбране рада.

Ови лични подаци могу се објавити на мрежним страницама дигиталне библиотеке, у електронском каталогу и у публикацијама Универзитета у Београду.

Потпис аутора

У Београду, _____

_____

Изјава о коришћењу

Овлашћујем Универзитетску библиотеку „Светозар Марковић“ да у Дигитални репозиторијум Универзитета у Београду унесе моју докторску дисертацију под насловом:

“Карактеризација оштећења и лома материјала цевовода коришћењем епрувета облика прстена” / “Characterisation of damage and fracture of pipeline material using ring-shaped specimens“

која је моје ауторско дело.

Дисертацију са свим прилозима предао/ла сам у електронском формату погодном за трајно архивирање.

Моју докторску дисертацију похрањену у Дигиталном репозиторијуму Универзитета у Београду и доступну у отвореном приступу могу да користе сви који поштују одредбе садржане у одабраном типу лиценце Креативне заједнице (Creative Commons) за коју сам се одлучио/ла.

1. Ауторство (CC BY)

2. Ауторство – некомерцијално (CC BY-NC)

3. Ауторство – некомерцијално – без прерада (CC BY-NC-ND)

4. Ауторство – некомерцијално – делити под истим условима (CC BY-NC-SA)

5. Ауторство – без прерада (CC BY-ND)

6. Ауторство – делити под истим условима (CC BY-SA)

(Молимо да заокружите само једну од шест понуђених лиценци.
Кратак опис лиценци је саставни део ове изјаве).

Потпис аутора

У Београду, _____

_____

1. **Ауторство**. Дозвољавате умножавање, дистрибуцију и јавно саопштавање дела, и прераде, ако се наведе име аутора на начин одређен од стране аутора или даваоца лиценце, чак и у комерцијалне сврхе. Ово је најслободнија од свих лиценци.

2. **Ауторство – некомерцијално**. Дозвољавате умножавање, дистрибуцију и јавно саопштавање дела, и прераде, ако се наведе име аутора на начин одређен од стране аутора или даваоца лиценце. Ова лиценца не дозвољава комерцијалну употребу дела.

3. **Ауторство – некомерцијално – без прерада**. Дозвољавате умножавање, дистрибуцију и јавно саопштавање дела, без промена, преобликовања или употребе дела у свом делу, ако се наведе име аутора на начин одређен од стране аутора или даваоца лиценце. Ова лиценца не дозвољава комерцијалну употребу дела. У односу на све остале лиценце, овом лиценцом се ограничава највећи обим права коришћења дела.

4. **Ауторство – некомерцијално – делити под истим условима**. Дозвољавате умножавање, дистрибуцију и јавно саопштавање дела, и прераде, ако се наведе име аутора на начин одређен од стране аутора или даваоца лиценце и ако се прерада дистрибуира под истом или сличном лиценцом. Ова лиценца не дозвољава комерцијалну употребу дела и прерада.

5. **Ауторство – без прерада**. Дозвољавате умножавање, дистрибуцију и јавно саопштавање дела, без промена, преобликовања или употребе дела у свом делу, ако се наведе име аутора на начин одређен од стране аутора или даваоца лиценце. Ова лиценца дозвољава комерцијалну употребу дела.

6. **Ауторство – делити под истим условима**. Дозвољавате умножавање, дистрибуцију и јавно саопштавање дела, и прераде, ако се наведе име аутора на начин одређен од стране аутора или даваоца лиценце и ако се прерада дистрибуира под истом или сличном лиценцом. Ова лиценца дозвољава комерцијалну употребу дела и прерада. Слична је софтверским лиценцама, односно лиценцама отвореног кода.